# UNIVERSITÀ DEGLI STUDI DI CATANIA

## DIPARTIMENTO DI FISICA E ASTRONOMIA

### DOTTORATO IN FISICA XXIX CICLO


---

# Development and characterization of nanocarbon-based devices for sensing applications


**PhD student:**

**Salvatore Baldo**

**Tutors:**

**Prof. Giuseppe Falci (UNICT)**

**Dr. Silvia Scalese (CNR-IMM)**

**Coordinator:**

**Prof. Vincenzo Bellini**


---


**ANNO ACCADEMICO 2013 – 2014**

# Contents

**Introduction and motivations** ……..... I

## 1. Carbon Nanomaterials

1.1. Introduction ……. 1

1.2. Graphene……....…….. 4

1.2.1. Introduction…….……. 4

1.2.2. Graphene synthesis……..... 7

1.2.3. Graphene properties.……..…..... 15

1.3. Graphene oxide…….…..... 17

1.3.1. Introduction…….……. 17

1.3.2. Graphene oxide synthesis……....……... 19

1.3.3. Graphene oxide properties.……..... 21

1.4. Graphene oxide reduction……..... 26

1.5. Carbon nanotubes ……... 36

1.5.1. Introduction…….. 36

1.5.2. Carbon nanotubes synthesis……. 41

1.5.3. Carbon nanotubes properties.……..... 53

## 2. Carbon-based devices


2.1. Introduction ……..... 68

2.2. Carbon interconnects……... 70

2.3. Carbon nanotubes-based devices……. 73

2.3.1. CNTFET and state of the art in electronics applications…….. 73

2.3.1.1. CNTFET in CMOS technology... 85

2.3.1.2. CNTFET – TFT (Thin-Film Transistors)…….. 87

2.3.2. CNT-based devices and state of the art in sensing applications……. 91

2.3.2.1. CNT-based resistor…….. 93

2.3.2.2. CNT-based SAW resonators…… 95

2.3.2.3. CNT-based QCM devices…… 97

2.3.2.4. CNTFET as gas sensor: ChemFET……. 99

2.3.2.5. CNT-based devices in biosensing applications..... 104

2.3.2.6. CNT-based immunosensors……. 109

2.4. Graphene-based devices……... 116

2.4.1. Graphene-FET and state of the art in electronics applications…… 117

2.4.2. Graphene-FET and state of the art in sensing applications……. 121

## 3. Applications and results


3.1. Carbon-based devices development……. 129

3.1.1. Electrophoretic deposition..... 132

3.1.2. Dielectrophoretic deposition..... 137

3.1.3. Development of silicon devices in collaboration with STMicroelectronics…… 142

3.1.4. The issue of the parasitic capacitances in the dielectrophoresis process……... 146

3.1.5. Repeatability of the deposition process…... 149

3.2. Graphene oxide-based devices development…… 152

3.3. Development of the CNT-based immunosensor for Human Arginase-1 detection……..... 154

3.3.1. Immunosensors development..... 156

3.3.2. Human Arginase-1 detection..... 161

3.3.3. Arduino microcontroller-based system for protein detection……... 167

3.4. Graphene oxide-based sensors……..... 170

3.4.1. Electrical behavior for GO and rGO based devices in air and nitrogen environment….. 172

3.4.2. AC analysis: Impedance characterization.... 176

3.4.3. Gas detection test: the case of the ethanol... 179

**Conclusions**..... 181

**Appendix**..... 183

A1. Moore's Law..... 183

A2. Scanning electron microscopy (SEM)..... 185

A3. Optical lithography..... 187

A4. Immunoassay in biosensing field..... 194

A5. Code developed in “C” language for the Arduino microcontroller..... 200

**References**..... 210

**List of publications**..... 237

**Acknowledgements**..... 239

# Introduction and motivations

The development of methods and devices for identification of small amounts of material in a non-invasive, specific, portable and low cost way is one of the major challenges in the sensors field. In literature there are different way for identification and detection, but the electrical devices based on nanomaterials are emerging as a powerful and general class of ultrasensitive electrical sensors for the direct detection of biological/chemical species and physical quantities.

Nanostructure science and technology is a broad and interdisciplinary area of research and development activity that has been growing explosively worldwide in the past ten years. It has the potential for revolutionizing the ways in which materials and products are created and the range and nature of functionalities that can be accessed.

Nanotechnology-based devices, due to their very peculiar properties, have advantages in high sensitivity, low energy consumption and potentially highly miniaturized integration.

Already in 1961 Feynman enunciated his famous byword "*there's plenty of room at the bottom*", which somehow let us guess the potential of nano-science. But when is it possible to talk about "nano"? Nanostructure is a kind of structure whose size is certainly less than 100 nm while a nanostructured material contains substructures with that dimensionality.

Nanotechnologies include not just the techniques necessary to realize the nanostructures, but also all the investigation methods which allow the characterization.

Nanomaterials are very attractive because at nano scale unique optical, magnetic, electrical, and other properties emerge. These emergent properties have the potential for great impacts in electronics, medicine, and other fields.
The **Carbon nanotubes (CNTs)** are a typical example of nanomaterials. They are made by graphite planes (carbon atoms arranged in a hexagonal structure) rolled up to outline a cylindrical system. A single plane of graphite is called **graphene**, another very interesting nanomaterials studied today in different science fields. Due to their interesting properties, currently these materials are used in various technological applications, such as the automotive area, telecommunications, aerospace industry, biomedical field and even in the production of materials for sport. Moreover, in the last decade, microelectronics industries have shown a growing interest for CNTs and graphene because they could be a possible remedy for Moore's Law (in appendix more information about this law).
Thanks to the peculiar characteristics of the nanostructures in general, such as the high surface over volume ratio, they can be used as sensitive layers in gas or biomedical sensors by exploiting the changes of their electrical characteristics induced by surface chemical modifications. In fact, the development of methods for identification of specific bio-markers is one of the major challenges in the biosensor field and CNTs are a possible way to produce very attractive sensors. For example, the detection of proteins by immunoassays usually includes methods such as ELISA (enzyme-linked immunosorbent assay) and RIA (radioimmunoassay). However, most of these techniques require sophisticated instrumentation and time-consuming procedures and most of the reagents employed in immunoassays such as antibodies, enzymes, and fluorescence labels are very expensive. Therefore, there is an increasing interest for the development of new, simple, sensitive, reliable, and cheaper diagnostic methods.

Recent studies have established that CNTs can enhance the electrochemical reactivity of important biomolecules [1,2], and can promote the electron-transfer reactions of proteins [3,4]. For these reasons, CNTs are extremely attractive for a wide range of electrochemical biosensors such as amperometric enzyme electrodes, immunosensors and DNA hybridization biosensors.

Another very interesting nanomaterial is the **graphene oxide (GO)**. Usually, GO is used as a precursor to obtain graphene but, recently, it has received increasing attention in optoelectronic [5,6] and sensing [7] applications, due to its peculiar properties. GO can be viewed as a single sheet of graphene with many oxygen-containing groups, including hydroxyl, epoxy and carboxylic acid, bonded on the surface. The presence of these oxygen groups gives the possibility to tune the conductivity and enhances the hydrophilic property of GO. In particular, the hydrophilicity makes GO as an interesting material to produce humidity sensors. These last are in demand in the industrial, environmental, and structural monitoring fields. A lot of research has been conducted to fabricate high efficiency humidity sensors, based on either change in resistance [8,9] or mass [10,11], due to the presence of water molecules. In recent years, research has been conducted to achieve a high level of sensitivity and selectivity in sensors. In particular, carbon-based materials like graphene have raised great interest for the development of humidity and temperature sensors. However, pristine graphene is not useful in the sensors field, because the surface of pristine graphene is basically inert. Instead, in graphene oxide, the presence of several oxygen groups gives the possibility to making the graphene surface sensitive to the environment.

Moreover, due to the oxygen groups, the electrical conductivity of GO depends also on the temperature. However, a limited amount of work has been done with regards to humidity detection using graphene and graphene

oxide. Massera et al. reported using a graphene sheet as a humidity sensor, in which the graphene samples were prepared by the scotch-tape method [12]. Guo et al. used laser-reduced graphene-oxide films for humidity sensing [13], whereas a graphene oxide-silicon bilayer was used for humidity sensing by Yao et al. [14]. In these works a change in electrical resistance is reported as the mechanism for sensing humidity. Yao et al. demonstrated the sensitivity of graphene oxide to humidity by using it as a coating on quartz crystal microbalances, which is based on the concept of change in frequency due to a change in mass [15].

The subject of this PhD thesis has been the development and characterization of nanocarbon-based sensors, with particular attention to the use of easy and cheap methodologies and processes that are required for future large scale production. In the first part of the thesis the development of CNT-based devices for biosensing applications is reported and the tests on protein detection are shown. In the second part the development of GO-based devices is shown and the electrical behavior of the devices is investigated in different ambient conditions and for different oxygen functionalization (GO and reduced GO).

The thesis work is divided as follows:

In the first chapter the Carbon-like materials basics are recalled. In particular the types, the properties, and the main synthesis methods are described.

The second chapter introduces the FET/Resistor devices and then describes the most common CNTs/GO structures in literature.

In the third chapter, the methods for devices preparation are described with a focus on the dielectrophoretic process, used for the deposition of the carbon-based sensitive layers. Therefore, the characterization of the devices and the sensing properties achieved as immunosensors, or humidity/temperature and volatile organic compounds (VOC) sensors are shown and discussed.

Finally, in the conclusions the main results, work in progress, developments and future applications are discussed.

# CHAPTER 1

# Carbon Nanomaterials

## 1.1. Introduction

Nanotechnologies are a science branch which has as its main objective the achievement, the study and application of systems with dimensions below 100 nm. It is interesting underline that a nanometer is equivalent to 10 times the size of the hydrogen atom.

Nanomaterials can be defined as systems composed by nanometric or nanostructured units smaller than 100 nm, which are characterized by particular electrical, chemical, optical, mechanical and magnetic properties.

In the case of carbon**,** until 1985 there were known only two forms of crystalline carbon: the diamond three-dimensional form ($sp^3$) and the planar graphite form ($sp^2$), called **allotropic forms**.

Some studies performed by the American scientist Richard E. Smalley lead to the discovery (whereby he won the Nobel award) of a third form of regular arrangement of carbon atoms (another allotropic form): the **fullerenes**. They are "cages" roughly spherical formed by an ordered arrangement of hexagonals and pentagonals structures of carbon atoms.

The amount of polygons and their relative proportions defines the fullerene shape and size. The first fullerene discovered was the C60 (Fig. 1.1.1), which

has the same shape of a soccer ball, and for this is also known as "buckyball". Fullerenes took their name honoring to the architect Richard Buckminster Fuller, whose creations, called "geodetic domes" remember the fullerene structure (Fig. 1.1.1).

Fullerenes are produced artificially with a carbon vaporization system at high temperature but were also found in small percentages in a coal pit in Yinpinglang, China.

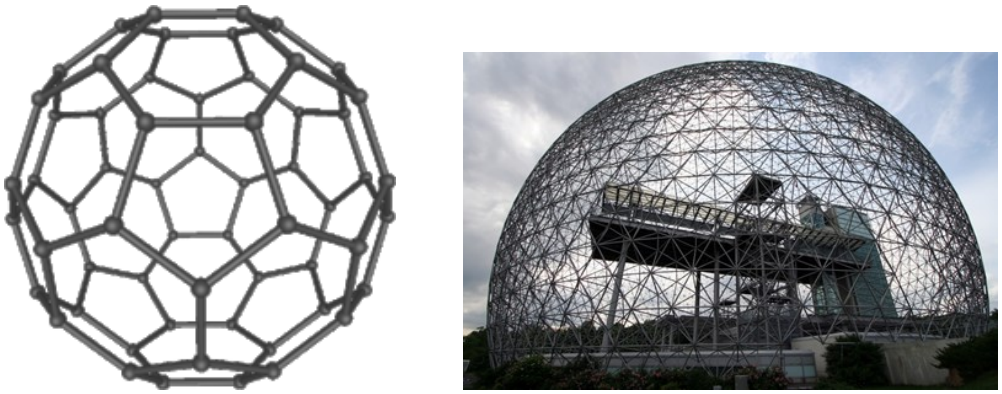

Fig. 1.1.1 - Fullerene C60 "buckyball" [wikipedia.org] (left) and the Montreal Biosphere by Buckminster Fuller [http://www.spatialagency.net/] (right)

In 1991, the Japanese researcher Sumio Iijima discovered accidentally another allotropic form among the secondary products of fullerenes: the **Carbon Nanotubes (CNTs)**.

The latter can be seen as a single graphite plane rolled up on itself to form a tubular shape.

A carbon atom has four free electrons, which are free to bind each other. In the diamond case, four electrons are regularly coupled with the electrons of other carbon atoms, forming a tetrahedral structure (i.e. in the shape of an equilateral triangular pyramid), with a carbon at the centre and other four at the corners, with the electrons in the middle. This bond is very strong and for

this reason the diamond is very hard. In the graphite, however, bind stably only three electrons, and the fourth remains free. In this way, each atom is bonded to three others, to form a triangular star. Many atoms all together give rise to a planar structure formed by hexagons whose vertices are carbon atoms. This planar structure is called **graphene**. Therefore, graphene is a material made of a monoatomic layer of carbon atoms (i.e., having a thickness equivalent to the size of a single atom).

Another example of Carbon-like materials is the **graphene oxide (GO),** a single sheet of graphite oxide that can be viewed as a two-dimension network of $sp^2$ and $sp^3$-bonded hybridized carbon atoms arranged in a dense honeycomb crystal structure. Many oxygen-containing groups, including hydroxyl, epoxy and carboxylic acid, are bonded to the two-dimensional network.

Therefore, today we know several allotropic form of the carbon, from the most famous bulk structures such as diamond and graphite to the nanostructured ones such as fullerenes, nanotubes and graphene (Fig. 1.1.2).

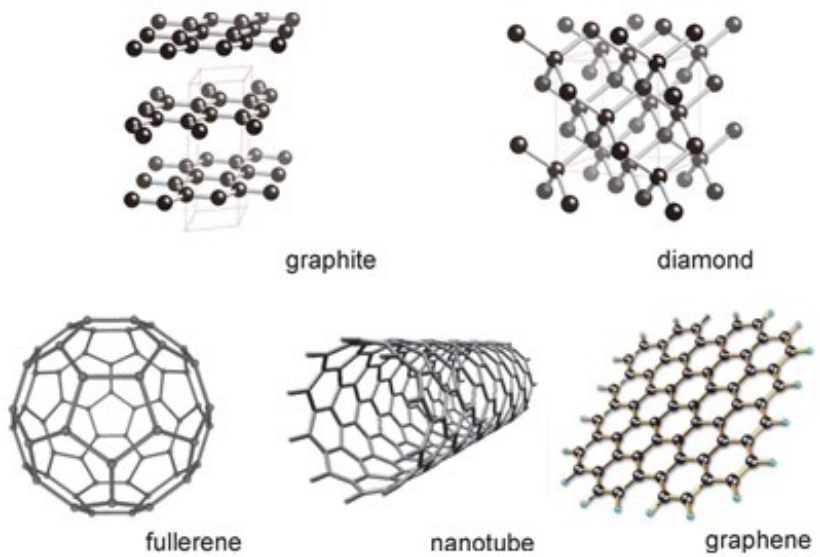


Fig 1.1.2 - Allotropic carbon forms [https://www.emaze.com/@AIWTLOZ/Carbon-]

# 1.2. Graphene

## 1.2.1. Introduction

Graphene, a two-dimensional sheet of $sp^2$ carbon atoms [16] (Fig. 1.2.1.1), has attracted worldwide interest from both fundamental science and device applications.

Among various intriguing properties, its extraordinary high carrier mobility [17] makes graphene a promising material for future electronic devices. Application to conductive composite materials [18] and ultra-high sensitive sensors [19] is also expected.

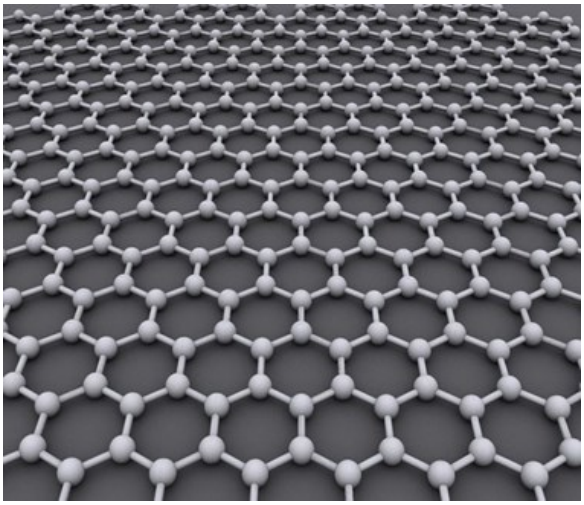

Fig. 1.2.1.1 - A graphene layer [www.wikipedia.org]

As the suggestion of the ending name -ene, the atoms are hybridized in the form $sp^2$, and will therefore have to form hexagons with angles of 120° (Fig. 1.2.1.2).

The Nobel Prize in Physics for 2010 was awarded to Andre Geim and Konstantin Novoselov at the University of Manchester "for groundbreaking experiments regarding the two-dimensional material graphene". In fact, in 2004, physicists at the University of Manchester and the Institute for Microelectronics Technology, Chernogolovka, Russia, first isolated individual graphene planes by using the **scotch tape** technique. They used adhesive tape to repeatedly split graphite crystals into increasingly thinner pieces until obtaining the graphene (see graphene synthesis paragraph).

Due to its free electrons, graphene shows excellent conduction characteristics and in the last years it has become one of the most studied materials for several technological applications.

Each carbon atom in graphene is covalently bonded to other three atoms with which it shares one electron forming $sp^2$ "σ-bonds". The fourth valence electron of a carbon atom occupies a $p^z$ orbital. The $p^z$ states mix together (π-bonds) forming delocalized electron states that are responsible for the electrical conductivity of graphene. In figure 1.2.1.2 primitive vectors of the hexagonal lattice of graphene and those of the reciprocal lattice are shown.

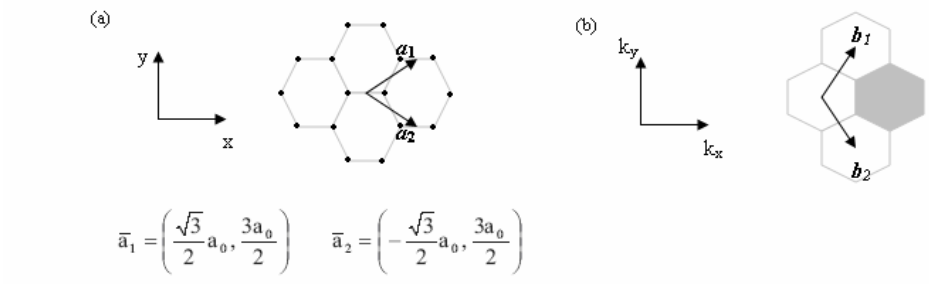


Fig. 1.2.1.2 - Direct lattice (a) and reciprocal lattice (b) of graphene. The grey hexagon represents the first Brillouin zone.

The energy dispersion relation for graphene $\boldsymbol{E(k_x, k_y)}$ is reported in Fig. 1.2.1.3: valence and conduction bands touch each other in six points (called "**K points**") coinciding with the corners of the hexagonal Brillouin zone.

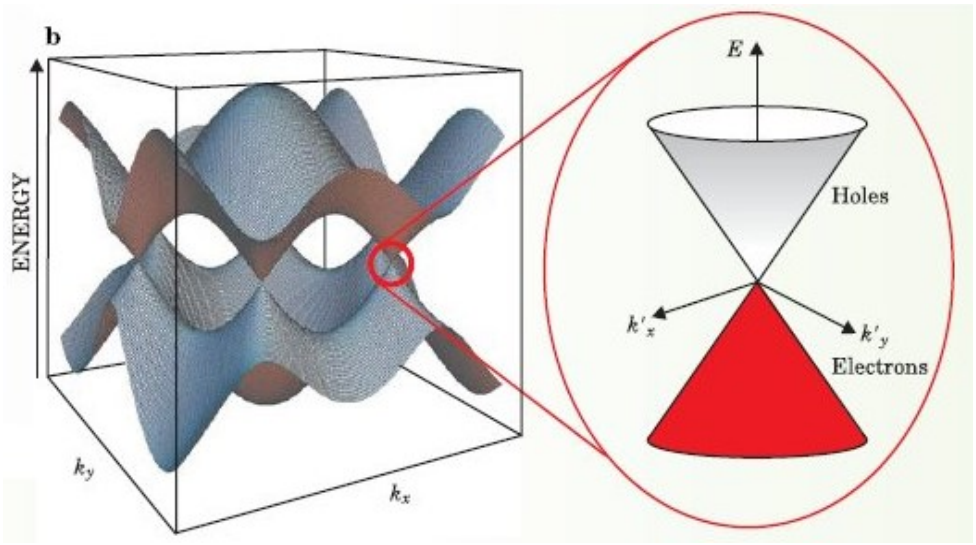


Fig. 1.2.1.3. - Valence and conduction bands of graphene. The conical shape of energy dispersion at the K-points is highlighted [M.Wilson et al., Phys. Today, 59, 2006, pp 21-23)]

Due to its particular band structure, graphene can be considered halfway between a metal and a semiconductor material, and therefore it is classified as a semi-metal or "**zero-gap**" semiconductor. For this reason, graphene is also used to produce transparent electrodes [20,21].

## 1.2.2. Graphene synthesis

Graphene can be produced by **exfoliation of highly ordered pyrolytic graphite (HOPG), epitaxial growth, chemical vapour deposition (CVD)** and the **reduction of graphene oxide**. The first three methods produce graphene with a relatively perfect structure and excellent properties, while in comparison, GO can be produced using inexpensive graphite as raw material by cost-effective chemical methods with high yield.

### Micromechanical Exfoliation – The "Scotch Tape Method"

As already mentioned, the first reported preparation of graphene was by Novoselov and Gaim in 2004 [22] by exfoliation of graphite using a simple adhesive tape.

After peeling it off the graphite, multiple-layer graphene remains on the tape. By repeated peeling the multiple-layer graphene is cleaved into various flakes of few-layer graphene. Afterwards the tape is attached on a substrate and the glue solved, e.g. by acetone, in order to detach the tape. Finally one last peeling with an unused tape is performed (Fig. 1.2.2.1).

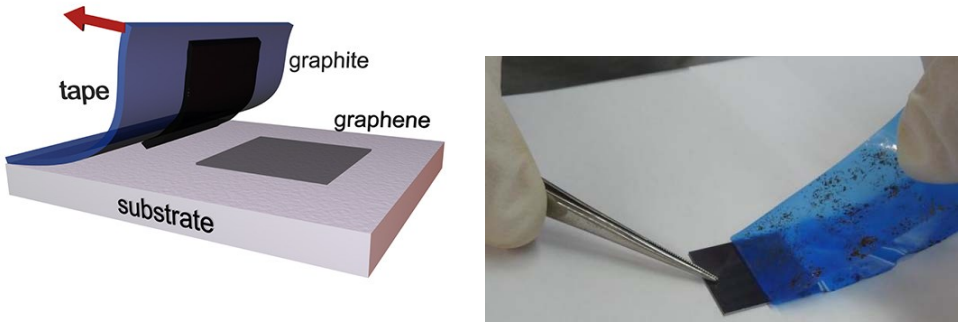


Fig. 1.2.2.1 – Schematization of the scotch tape method [http://www.graphene.ac.rs] (left), a real photo of the exfoliation process [https://www.sknust.de/wp-content/uploads/2014/03/graphene-exfoliation.png] (right)

The obtained flakes differ considerably in size and thickness, where the sizes range from nanometers to several tens of micrometers for single-layer graphene, depending on the preparation of the substrate used (Fig. 1.2.2.2). Single-layer graphene has an absorption rate of 2%, nevertheless it is possible to see it under an optical microscope on $SiO_2$/Si, due to interference effects [23].

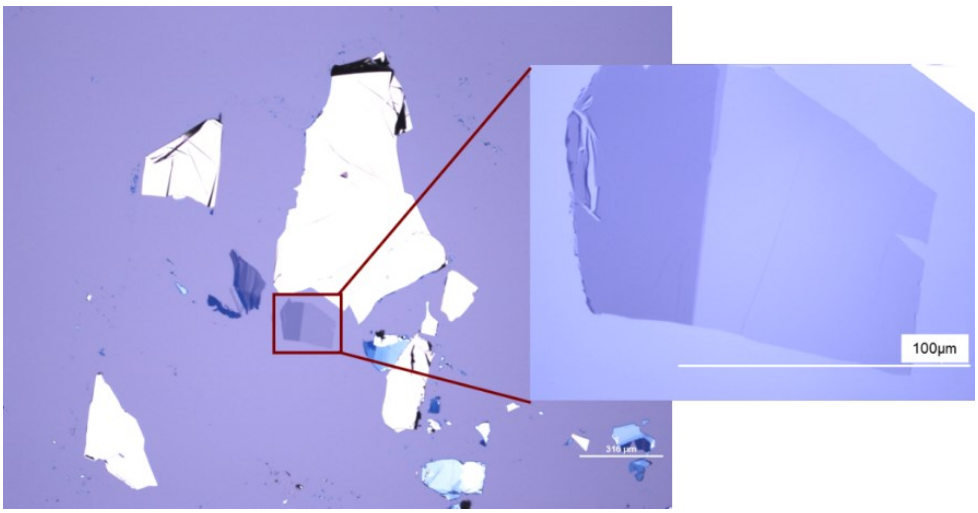


Fig. 1.2.2.2 - Optical image of the exfoliated graphene layers on 290 nm thick oxidized silicon wafers [http://dx.doi.org/10.5772/56640]

However, it is difficult to obtain larger amounts of graphene by this method, not even taking into account the lack of controllability. The complexity of this method is basically low, nevertheless the graphene flakes need to be found on the substrate surface, which is labour intensive. The quality of the prepared graphene is very high with almost no defects and nearly ideal mechanical and electrical properties.

## Liquid – phase exfoliation

Graphene can be prepared in liquid-phase. This allows upscaling the production, in order to obtain a much higher amount of graphene. The easiest method would be to disperse the graphite in an organic solvent with nearly the same surface energy as graphite. Thereby, the energy barrier is reduced, which has to be overcome in order to detach a graphene layer from the crystal. The solution is then sonicated in an ultrasound bath for several hours and centrifuged in order to dispose of the thicker flakes [24]. In another way, a DC voltage is applied between two electrode immersed in liquid to enhanced the exfoliation process **(Electrochemical Exfoliation)** [25] (Fig. 1.2.2.3).

The deposition of obtained graphene on a substrate can be performed by simple drop-casting. After the solvent evaporation, the graphene flakes remain on the surface. In order to achieve a more homogeneous coating, the sample can be rotated using the spin-coating method.

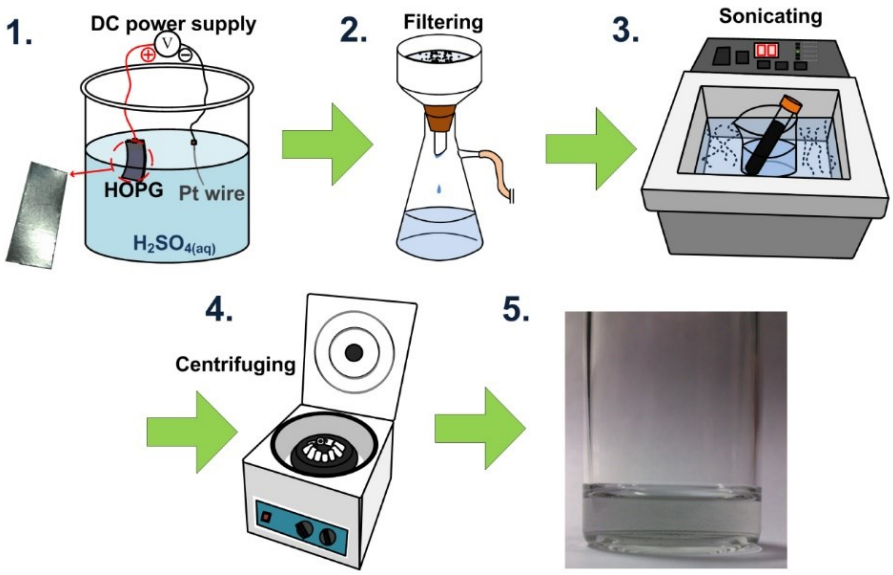


Fig. 1.2.2.3 - The liquid-phase exfoliation process [https://doi.org/10.1364/OME.3.001893]

The quality of the obtained graphene flakes is very high in accordance with the micromechanical exfoliation. Its size however is still very small, neither is the controllability given. On the other hand, the complexity is very low, and as mentioned above this method allows preparing large amounts of graphene.

## Growth on Surfaces - Epitaxial Growth

A totally different approach to obtaining graphene is to grow it directly on a surface. Consequently the size of the obtained layers are not dependent on the initial graphite crystal. The growth can occur in two different ways. Either the carbon already exists in the substrate **(epitaxial growth)** or it has to be added by **chemical vapour deposition**.

Epitaxial growth is a commonly used technique for creating high quality monolayer graphene. In this case, isolated monolayer of graphene is grown typically on a single-crystal of silicon carbide (SiC) by graphitization under UHV (Ultra High Vacuum) [26]. SiC is a wide-bandgap semiconductor which exists in various polytypes. For the production of epitaxial graphene, 3C- (cubic), 4H- and 6H-SiC (hexagonal) are the most commonly used polytypes. The graphitization of SiC was discovered in 1955, but it was regarded as unwelcome side effect instead of a method of preparing graphene [27].

Typically, in this growth process, under UHV annealing conditions (1200°C) the top layers of SiC crystals undergo thermal decomposition, Si atoms desorb and the carbon atoms remaining on the surface rearrange and re-bond to form epitaxial graphene layers [28-30] (Fig. 1.2.2.4.).

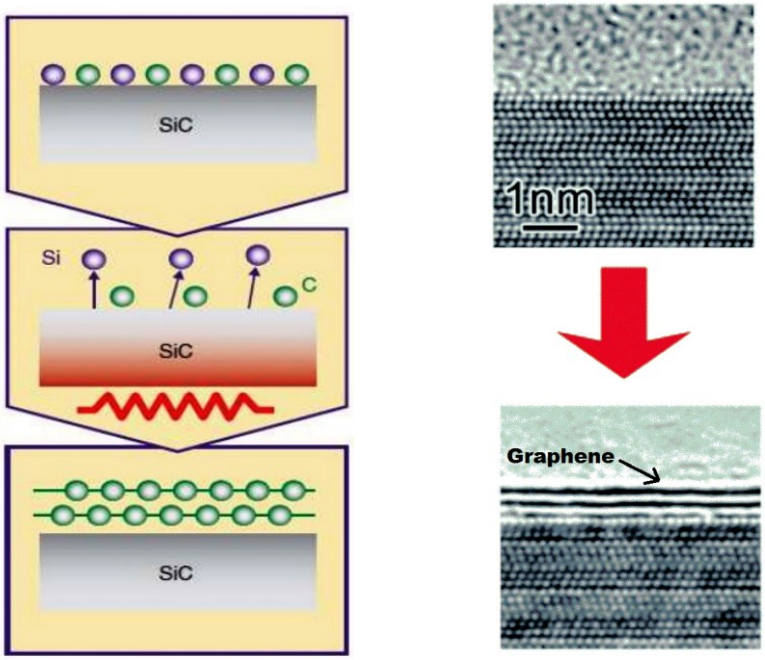


Fig. 1.2.2.4. – Epitaxial growth of graphene on SiC [Hiroki Hibino et al, Graphene growth on silicon carbide, NTT technical review, 2010] (left), TEM image of growth results [Wataru Norimatsu et al., 2014, DOI: 10.1039/C3CP54523G] (right)

The results are highly dependent on the parameters used, like temperature, heating rate, or pressure. Growth on the Si-face of hexagonal SiC wafers, under appropriate conditions exhibits manageable growth kinetics (contrary to the C-face growth) allowing better control over the number of graphene layers.

Usually, graphene is grown directly on SiC crystal but, in the last years, several modification on the epitaxy process were performed. For example, a thin Ni layer (111) can be evaporated onto a SiC crystal before of the epitaxial process. The Ni surface has a lattice structure very similar to the one of graphene, with a mismatch of the lattice constant at about 1.3% [27].

Upon heating the carbon diffuses through the Ni layer and forms a graphene or graphite layer on the surface, depending on the heating rate. The produced

graphene is easier to detach from the surface than the graphene produced by the growth on a simple SiC crystal without Ni [27].

The physical properties of graphene varied significantly between those grown epitaxially and exfoliated mechanically, due mainly to the influence of interfacial effects in epitaxial graphene.

Epitaxial growth of graphene can be performed also with metallic substrates, such as ruthenium (Ru) [31]. It is found that the (0001) faces of Ru crystals were able to grow epitaxial graphene layers, where a very sparse graphene nucleated at high temperatures. The first graphene layer coupled strongly to the Ru substrate and the second layer was free of the substrate interaction, which had an electronic structure similar to freestanding graphene. However, several hurdles must be overcome before real applications are found.

The possibility to produce large amounts of graphene by epitaxial growth is not as good as by liquid-phase exfoliation, but the controllability of the growth and graphene size in the epitaxial technique is better. In addition, depending on the applications, graphene grown on substrate can be used in situ without transfer to another substrate. However, in order to make graphene technologically viable, the transfer of graphene films to substrates appropriate for specific applications is required. For example, using a thermal release tape, dry transfer of epitaxial graphene from the C-face of 4H-SiC onto $SiO_2$, GaN and $Al_2O_3$ substrates was performed [32].

## Growth on Surfaces - Chemical Vapour Deposition

Chemical vapour deposition (CVD) is a process in which a substrate is exposed to gaseous compounds (see appendix for more information about CVD technique). These compounds decompose on the surface in order to grow a thin film, whereas the by-products evaporate. There are different

ways to achieve this. Graphene can be grown by exposing of a Ni substrate to a gas mixture of $H_2$, $CH_4$ and Ar at about 1000°C under low vacuum [33]. The methane decomposes on the surface, so that the hydrogene evaporates. The carbon diffuses into the Ni and, after cooling down in an Ar atomosphere, a graphene layer grows on the surface (Fig. 1.2.2.5).

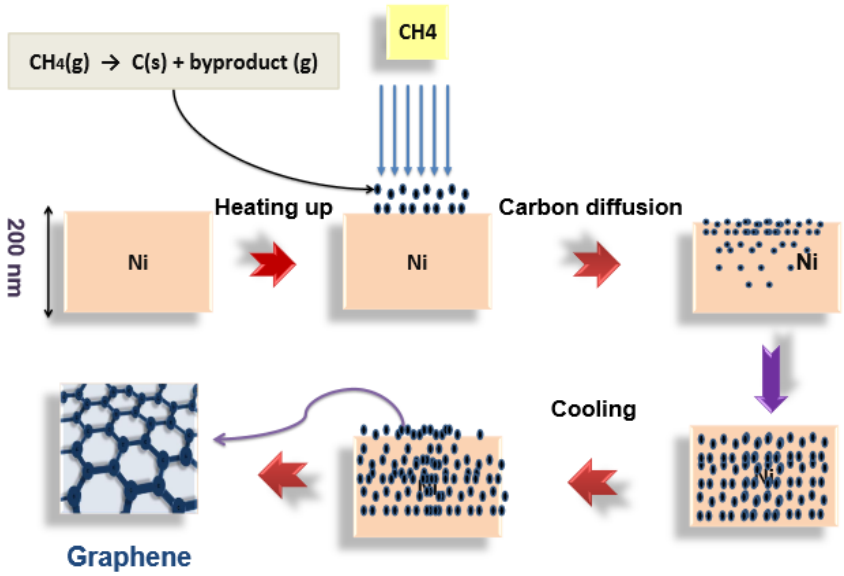


Fig. 1.2.2.5 - CVD graphene growth mechanism on nickel
[https://www.comsol.com/paper/download/194707/alshurman_poster.pdf]

The average number of layers depends on the Ni thickness and can be controlled in this way. Furthermore, the shape of the graphene can also be controlled by patterning of the Ni layer.

Using copper instead of nickel as growing substrate results in single-layer graphene with less than 5% of few-layer graphene, which do not grow larger with time [34]. This behavior is supposed to be due to the low solubility of carbon in Cu.

CVD graphene is more likely to carry impurities due to the various materials required. However, research has shown that such impurities can be sufficiently minimized to create graphene as pure as exfoliated flakes [35].

Additionally, the CVD graphene tends to wrinkle due to the difference in thermal expansion between graphene and substrate. This is decreased via proper annealing, but is still an ongoing research challenge [36]. Most importantly, graphene from CVD is a contiguous film as large as the underlying metal substrate, in contrast to the random micron-sized flakes from the scotch tape method.

After the synthesis, graphene can be transferred to an arbitrary substrate via polymer support, which can be attached onto the top of the graphene. After etching of the Ni or Cu, the graphene can be stamped onto the required substrate and the polymer support gets peeled off or etched away (Fig. 1.2.2.6).

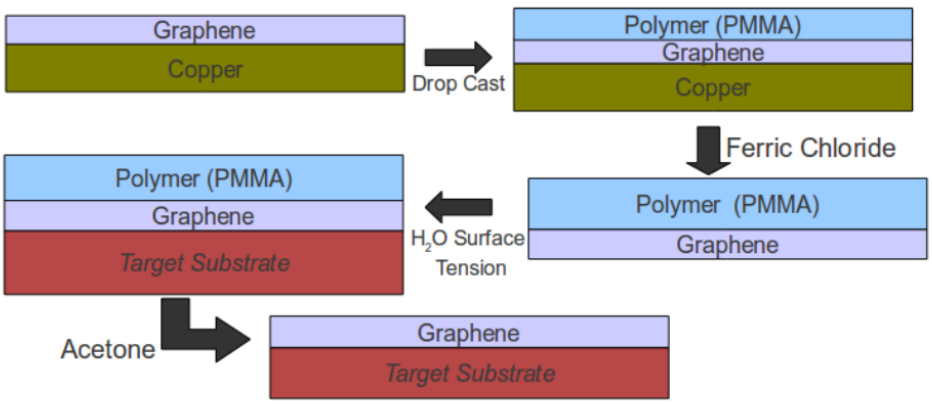


Fig. 1.2.2.6 - Schematic diagram of the transfer process to an arbitrary substrate [Dissertation of Benjamin Pollard, Department of Physics, Pomona College, 2011].

Using this method several layers of graphene can be stamped onto each other in order to decrease the resistance.

## 1.2.3. Graphene properties

The following properties of graphene are extracted from a "Scientific Background on the Nobel Prize in Physics 2010 – GRAPHENE, compiled by the Class for Physics of the Royal Swedish Academy of Sciences, 5 October 2010"

### *Density*

*The unit hexagonal cell of graphene contains two carbon atoms and has an area of 0.052 $nm^2$. We can calculate its density as being 0.77 $mg/m^2$. A hypothetical hammock measuring 1$m^2$ made from graphene would thus weigh 0.77 mg.*

### *Optical transparency*

*Graphene is almost transparent; it absorbs only 2.3% of the light intensity, independent of the wavelength in the optical domain. This number is given by πα, where α is the fine structure constant. Thus suspended graphene does not have any colour.*

### *Strength*

*Graphene has a breaking strength of 42N/m. Steel has a breaking strength in the range of 250-1200 MPa= 0.25-1.2x$10^9$ $N/m^2$. For a hypothetical steel film of the same thickness as graphene (which can be taken to be 3.35Å, i.e. the layer thickness in graphite), this would give a 2D breaking strength of*

*0.084-0.40 N/m. Thus graphene is more than 100 times stronger than the strongest steel. In a 1m$^2$ hammock tied between two trees you could place a weight of approximately 4 kg before it would break.*

## *Electrical conductivity*

*The sheet conductivity of a 2D material is given by $\sigma=en\mu$. The mobility is theoretically limited to $\mu=200{,}000\ cm^2V^{-1}s^{-1}$ by acoustic phonons at a carrier density of $n=10^{12}\ cm^{-2}$. The 2D sheet resistivity, also called the resistance per square, is then 31 Ω. The fictional hammock measuring 1m$^2$ would thus have a resistance of 31 Ω.*
*Using the layer thickness we get a bulk conductivity of $0.96x10^6\ \Omega^{-1}cm^{-1}$ for graphene. This is somewhat higher than the conductivity of copper which is $0.60x10^6\ \Omega^{-1}cm^{-1}$.*

## *Thermal conductivity*

*The thermal conductivity of graphene is dominated by phonons and has been measured to be approximately 5000 $Wm^{-1}K^{-1}$. Copper at room temperature has a thermal conductivity of 401 $Wm^{-1}K^{-1}$. Thus graphene conducts heat 10 times better than copper.*

# 1.3. Graphene oxide

## 1.3.1. Introduction

Graphite oxide has a similar layered structure to graphite, but the plane of carbon atoms in graphite oxide is heavily decorated by oxygen-containing groups, which not only expand the interlayer distance but also make the atomic-thick layers hydrophilic. As a result, these oxidized layers can be exfoliated in water under moderate ultrasonication. If the exfoliated sheets contain only one or few layers of carbon atoms like graphene, these sheets are named **graphene oxide (GO).** This material can be viewed as a two-dimensional network of $sp^2$ and $sp^3$-bonded hybridized carbon atoms arranged in a dense honeycomb crystal structure. Many oxygen-containing groups, including hydroxyl, epoxy and carboxylic acid, were bonded to the two-dimensional network. The precise chemical structure of GO is still not quite clear, which contributes to the complexity of GO due to its partial amorphous character. Several early investigations have proposed structural models of GO and the widely accepted GO model was proposed by Lerf and Klinowski (Fig. 1.3.1.1)

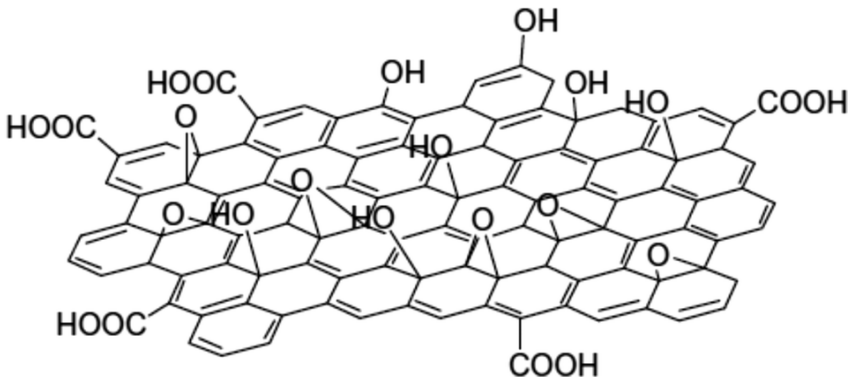


Fig. 1.3.1.1 – Graphene oxide structure [Mahmoud Nasrollahzadeh et al., 2015, DOI: 10.1039/C4RA12552E]

The presence of oxygen-containing groups gives the possibility to tune the conductivity and enhance the hydrophilicity property of GO.

As mentioned in the introduction, graphene oxide has received increasing attentions in several application, due to its inherent electrical and mechanical properties.

Recently, exploring the feasibility of integrating GO into graphene-based electronic devices has motivated immense studies on the intrinsic electrical [37,38] and mechanical [39,40] properties of GO. It is well known that the electrical properties of GO would be influenced by some external stimulations, including reducibility reagent [41], electric field [42-44], temperature [45,46], light [47], etc. Due to the tunable electrical property, GO is considered as a potential electrical material candidate for graphene-based electronic devices.

## 1.3.2. Graphene oxide synthesis

The history of the evolution of synthesis methods and chemical structure of GO has been extensively reviewed by Dreyer et al. [48] and Compton and Nguyen [49]. The route to prepare GO involves two main steps (Fig. 1.3.2.1). Firstly, graphite powder is oxidized to produce graphite oxide, which can be readily dispersed in water or another polar solvent due to the presence of hydroxyl and epoxide groups across the basal planes of graphite oxide and carbonyl and carboxyl groups located at the edges [50–52]. Secondly, the bulk graphite oxide can be exfoliated by sonication to form colloidal suspensions of monolayer, bilayer or few-layer GO sheets in different solvents [53].

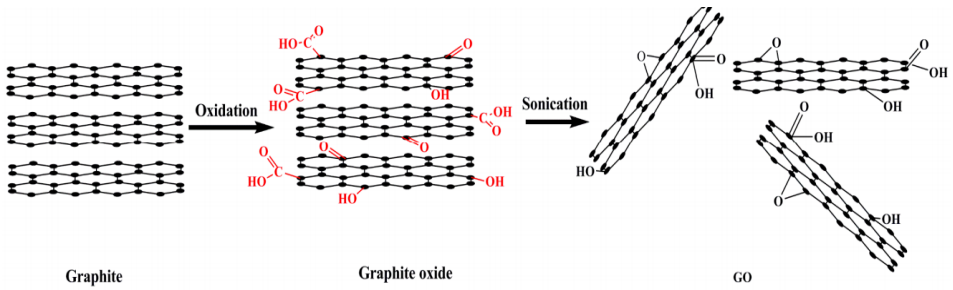


Fig. 1.3.2.1 – Synthesis of graphene oxide [Lubricants 2014, *2*, 137-161, DOI:10.3390/lubricants2030137]

The critical point of preparing GO is the selection of suitable oxidizing agents to oxidize graphite. Reviewing the origin of the preparation of graphite oxide, it has had more than 150 years of history since the first report from **Brodie** [54] in 1859. The oxidation process was performed by adding $KClO_3$ in a single addition to a slurry of graphite in fuming $HNO_3$. The C/H/O ratio of the oxidation product was determined to be 2.19/1.00/0.80, which is the typical composition of graphite oxide [55]. About 40 years later, **Staudenmaier** [56] modified the Brodie method by using concentrated

$H_2SO_4$ and fuming $HNO_3$ as the oxidizing agents. Additionally, the $KClO_3$ was added slowly and carefully over a period of one week in the procedure. In the following decades, many other similar methods have been reported [57,58]. The method most commonly used today was reported by **Hummers and Offeman** in 1958 [59]. In the Hummers method, the oxidation of graphite to graphite oxide is accomplished by treating graphite with essentially a water-free mixture of concentrated $H_2SO_4$, $NaNO_3$ and $KMnO_4$. Compared to the Brodie-Staudenmaier methods, the Hummers method requires less than 2 h for completion at temperatures below 45° and can be carried out safely. These three methods are the primary routes to prepare graphite oxide from graphite and have been reviewed extensively by Ruoff and co-workers [60,61]. However, all three reactions involve the liberation of toxic gas NOx and/or $ClO_2$. Some modifications based on the Hummers method have been proposed. Kovtyukhova [62] added a pre-oxidized procedure using $H_2SO_4$, $K_2S_2O_8$, and $P_2O_5$. The C/O ratio of the oxidation product was 4.0/3.1, illustrating that this was richer in oxygen than the graphite oxide prepared by the Hummers method. The method proposed by Kovtyukhova is defined as a typical **modified Hummers method** and has been cited by many researchers in recent years [63–65].

## 1.3.3. Graphene oxide properties

### Electrical properties

The properties of GO are different than pristine graphene due to the presence of the oxygen-containing groups. In particular, the quantity, the type of these groups and the environment play an important role in the electrical conductivity.

Intrinsic properties, such as the oxygen sites in GO and the dependence between conductivity (σ) and oxygen concentration have been investigated [66–77]. Several conduction mechanisms, such as Mott variable range hopping (VRH) [70–73], Efros–Shklovskii (ES) VRH (the modified VRH model that considers the Coulomb gap) [74], Arrhenius behavior [75,76], and fluctuation-induced tunneling (FIT) [77] conduction have been suggested.

Kazuto Hatakeyama et al. studied the GO conduction finding that, in GO with high amount of functional groups, the electrical transport is basically an $H^+$ proton transport. They show that, in air environment, the conductivities (σ) of multilayer graphene oxide films (assembled by the drop-cast method) are larger than those of single-layer GO (prepared in the same way). In particular, at 60 % relative humidity (RH), the σ value increases from $1x10^{-6}$ S $cm^{-1}$ in single-layer GO to $1x10^{-4}$ and 4 $x10^{-4}$ S $cm^{-1}$ for 60 and 200 nm thick multilayer films, respectively [78]. As described by Anderson's proton conductivity model [79], at a low RH, only a small amount of water molecules is adsorbed onto the surface active hydrophilic groups (i.e., hydroxyl) of GO sheets through hydrogen bonding, and hence, the GO surface is not completely water-covered. With the increasing adsorption of water molecules, hopping proton mechanism plays an important role. Protons

($H^+$) arising from hydroxyl of GO is bonded to excess adsorbed water molecules to form hydronium ($H_3O^+$) ion. However, the hydronium ions formed by charged carriers were alone and not enough to yield the continuous conduction path due to insufficient adsorption of water molecules. However, the increasing formation of hydronium ions can be seen as an accumulate layer, promoting the formation of an ions conduction path. [80] (Fig. 1.3.3.1)

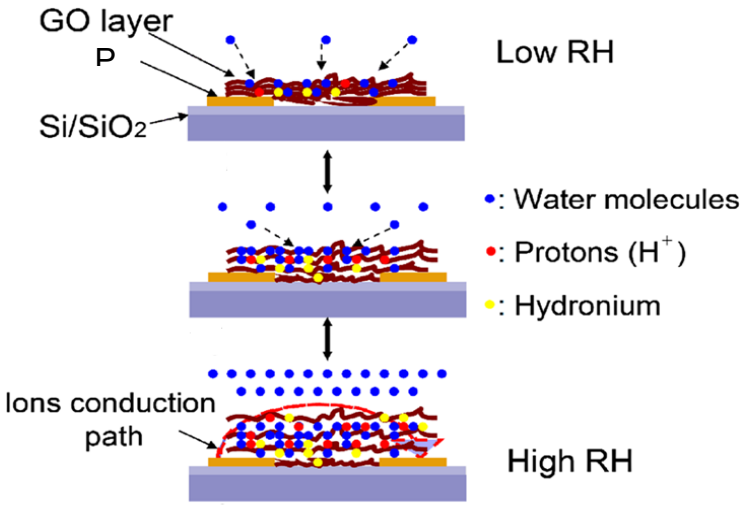


Fig. 1.3.3.1 – The electrical interaction mechanism between GO films and water molecules [80]

A proposed mechanism for proton conductivity in GO is shown in Fig. 1.3.3.2. In multilayer GO, mobilized protons can change path from one layer to the surrounding layers through nanopores, which results in increased conductivity. Proton mobility and hydrogen bond reformation in single and multilayer GO films is supported by single and double GO walls, respectively [78].

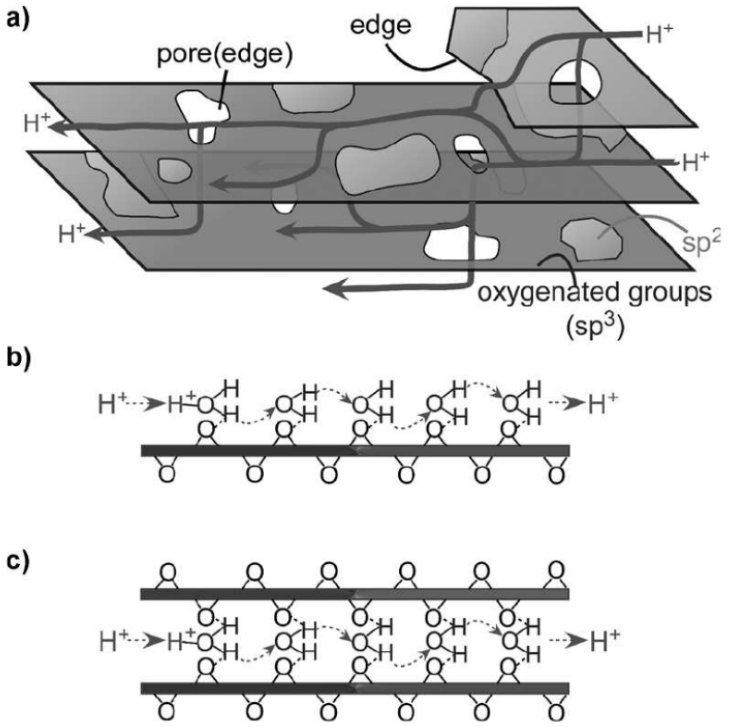


Fig. 1.3.3.2 – Proposed mechanism for proton conductivity. a) In multilayer GO, protons can change from the conduction path in one layer to another through nanopores. The $sp^3$ - and $sp^2$ -hybridized areas are denoted in dark grey and light grey, respectively. Proton transfer supported by single (b) and double (c) GO walls, respectively [78].

As GO bears various hydrophilic functional groups, it is necessary to identify the main factors that influence proton conductivity in GO. It was observed strong electrostatic attractions between the negatively charged epoxy groups of GO and transition metal ions [81].

Based on this observation, Kazuto Hatakeyama et al. described how the epoxy sites could be successfully blocked with ethylenediamine, obtaining a functionalized GO also called enGO. A decrease in the enGO conductivity was observed confirmed that the epoxy sites act as the major vehicle for proton transport in GO [78].

Totally different behaviour is shown in the case of GO with lower amount of functional groups. Meihua Jin et al. found that the GO with a band gap of 1.7 eV showed a p-type semiconducting behaviour at room temperature in air environment, while the GO with a band gap of 2.1 eV showed insulating characteristics. The band gap was tuned via the oxidation time, resulting in strong correlation with the atomic ratio of O/C. The conductance of the 1.7 eV band gap graphene oxides increased with temperature, again confirming semiconducting behaviour [82]. These results showed that in the case of GO with lower amount of functional groups (typical case of reduced GO, see below) the electrical transport is not a proton transport.

## AC analysis – Impedance Spectroscopy

An evaluation of the electrical transport properties in AC voltage could provide useful information about the material. A typical electrical characterization in AC is the **impedance spectroscopy**. In this technique the impedance of the material is measured over a range of frequencies typically from 20Hz to 1MHz using an LCR meter. The results are shown in a Nyquist plot, where the imaginary part of the impedance is in the y axis and the real part is in the x axis. Yao et al. found that GO exhibit two types of impedance: **semicircle-type impedance** and **straight line-type impedance**.

The semicircle-type impedance is associated with the bulk impedance of GO films, and it can be electrically equivalent to a parallel circuit of a resistor $R_{GO}$ and a capacitor $C_{GO}$, as shown in Fig. 1.3.3.3., where $R_{GO}$ and $C_{GO}$ represent the bulk resistor and geometric capacitance of the GO films, respectively. Instead, the straight line-type impedance is due to the **Warburg impedance**, caused by the diffusion of ions across the interface between the GO films and the electrodes. Warburg impedance can be modelled as

additional impedance Zw, as shown in Fig. 1.3.3.3. [80]. Typically, the straight line-type impedance is present in GO with high amount of oxygen-containing groups (in which is present a proton transport) while the semicircle-type impedance is present in GO with low quantities of oxygen-containing groups.

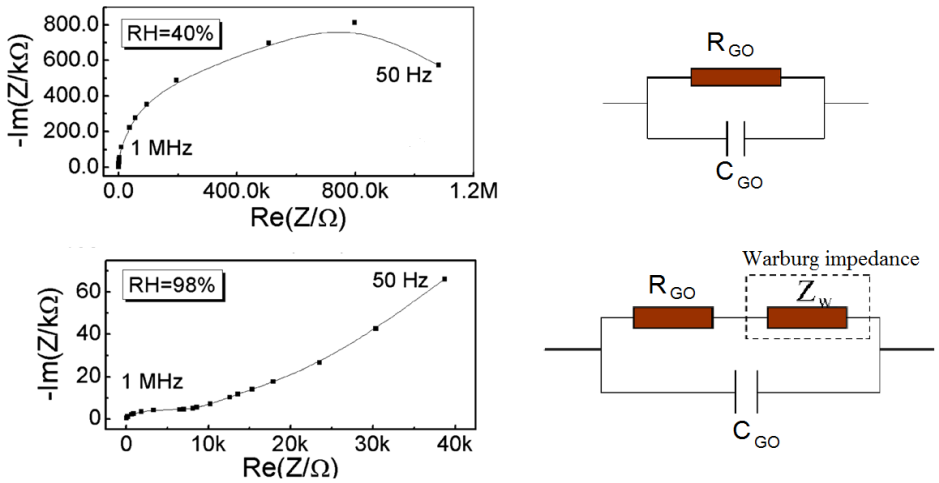


Fig. 1.3.3.3. – Impedance analysis of GO film in the case of semicircle-type impedance (up) and in the case of straight line-type impedance (down) [80]

## 1.4. Graphene oxide reduction

One of the attractive property of GO is that it can be reduced to graphene-like sheets by removing the oxygen-containing groups with the recovery of a conjugated structure. The **reduced GO (rGO)** sheets are usually considered as one kind of chemically derived graphene. The very important goal in the reduction process is to obtain graphene-like materials similar to the pristine graphene. However, reduction approach produces disordered graphene-like materials and not all $sp^3$ carbon atoms are converted to $sp^2$. This is mainly because the decomposition of oxygen-containing groups also removes carbon atoms from the carbon plane, which splits the graphene sheets into small pieces and results in the distortion of the carbon plane. Defects inevitably affect the electronic properties of the material by decreasing the transport path and introducing scattering centres. Therefore, rGO has much lower mobility than the exfoliated graphene, mainly because plenty of defect remain in rGO. The conductivity of monolayer graphene mainly relies on carrier transport within the carbon plane, as a result, functional groups attached to the plane are the main influencing factor on its conductivity, while functional groups attached to the edge have less influence. Consequently, the reduction of GO can be obtained removing epoxy and hydroxyl groups on the plane, while other groups, e.g. carboxyl, carbonyl and ester groups, present at the edges or defective areas only have a limited influence on the conductivity of an rGO sheet.

There are many approaches available to achieve reduction of GO, such as **thermal, chemical and optical method.**

## Thermal annealing

GO can be reduced to graphene-like sheets by heat treatment and the process is named **thermal annealing reduction**. There are several ways to obtain a heating, for example through a furnace, a hot plate or also by optical or electromagnetic irradiation.

The heating temperature significantly affects the reduction on GO.

Schniepp et al. [83] found that if the temperature was less than 500 °C, the C/O ratio was no more than 7, while if the temperature reached 750 °C, the C/O ratio could be higher than 13.

Wang et al. [84] annealed GO thin films at different temperatures, showed that the electrical conductivity of the reduced GO film obtained at 500 °C was only 50 S/cm, while at 700 °C and 1100 °C it could be 100 S/cm and 550 S/cm, respectively (Fig. 1.4.1).

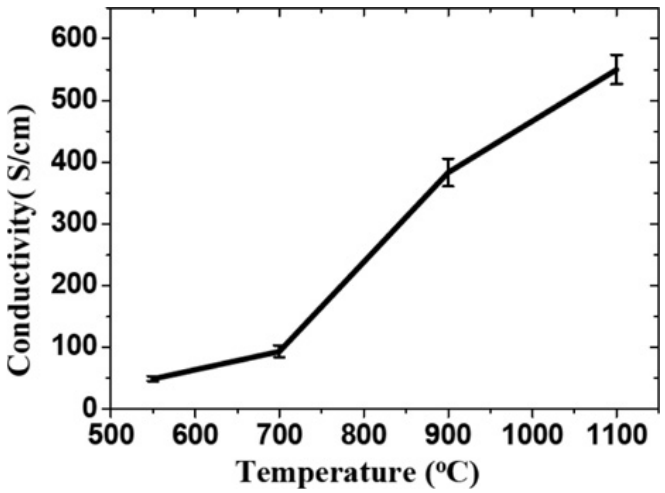


Fig. 1.4.1. - Increase of the average conductivity of graphene films from 49, 93, 383 to 550 S/cm, along with the temperature increasing from 550 °C, 700 °C, 900 °C to 1100 °C, respectively [84].

Most important is the atmosphere in which the thermal annealing reduction of GO is performed. Since the etching of oxygen will be increased at high temperatures, oxygen gas should be excluded during annealing. For this reason, annealing reduction is usually carried out in vacuum [85], in inert [84] or in reducing atmosphere [86].

In the first case, Becerril et al. [85] reduced GO films by thermal annealing at 1000 °C, and found that a quality vacuum ($<10^{-5}$ Torr) is a key-factor for the recovery of GO, otherwise the films can be quickly lost through reaction with residual oxygen in the system. The same consideration can be done in inert atmospheres.

For the third case, a reducing gas such as $H_2$ is added to consume the residual oxygen in the atmosphere. Moreover, because of the high reducing ability of hydrogen at elevated temperatures, the reduction of GO can be performed at low temperature in a $H_2$ atmosphere. For example, Wu et al. reported that GO can be reduced at 450 °C for 2 h in an $Ar/H_2$ (1:1) mixture with a resulting C/O ratio of 14.9 and conductivity of $\sim 1 \cdot 10^3$ S/cm.

Based on the above results, in general the reduction of GO by high temperature annealing is desired but, high temperature means large energy consumption and critical treatment conditions. For example, some applications need to have GO on substrates, but high reduction temperature cannot be used for GO films on substrates with a low melting-point, such as glass or plastic.

The binding energy between graphene and different oxygen-containing functional groups can be an important index to evaluate the reducibility of each group attached to the carbon sheet. Using density functional theory (DFT) calculation, Kim et al. [89] obtained the binding energy of an epoxy group (62 kcal/mol) and a hydroxyl group (15.4 kcal/mol) to a 32-carbon-atom graphene unit, which indicates that epoxy groups are much more stable

than hydroxyl groups in GO. In a calculation by Gao et al. [90] (Fig. 1.4.2.), the epoxy and hydroxyl groups in GO are divided into two types for their different locations at the interior of an aromatic domain of GO (A, B) and at the edge of an aromatic domain (A', B').

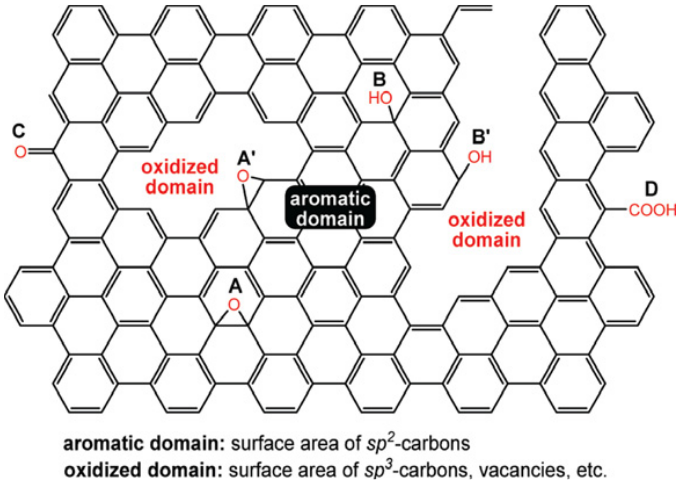


Fig. 1.4.2 – Schematic of oxygen-containing groups in GO: A, epoxy groups located at the interior of an aromatic domain of GO; A', epoxy groups located at the edge of an aromatic domain; B, hydroxyl located at the interior of an aromatic domain; B', hydroxyl at the edge of an aromatic domain; C, carbonyl at the edge of an aromatic domain; and D, carboxyl at the edge of an aromatic domain [90].

Due to the low binding energy, a single hydroxyl group attached to the interior aromatic domain is not stable and is subject to dissociation at room temperature, while a hydroxyl group attached to the edge is stable at room temperature. As a result, hydroxyl groups attached to the inner aromatic domains of GO are expected to dissociate or migrate to the edges of aromatic domains.

Jeong et al. [92] has investigated the thermal stability of graphite oxide. According to their results, most of the oxygen- containing groups can be removed by annealing at 200 °C in low-pressure argon (550 mTorr). After annealing for 6 h, according to the results of Fourier-transformed infrared

spectroscopy (FTIR), the peaks representing epoxy and carboxyl groups obviously decrease, and the peak for hydroxyl groups totally disappears. These phenomena become even more pronounced after annealing for 10 h, and the reduced graphite oxide can have a C/O ratio of 10.

Ultimately, as the experimental work has discovered, a large number of functional groups can be removed by moderate heating above 200 °C with enough time, but the full deoxygenation of GO solely by thermal annealing is rather difficult even at temperatures as high as 1200 °C.

## Microwave and photo reduction

There are several alternative to perform thermal reduction, including **microwave irradiation (MWI)** [93,94] and **photo-irradiation** [95,96]. The main advantage of MWI over conventional heating methods is heating substances uniformly and rapidly. By treating graphite oxide powders in a commercial microwave oven, rGO can be readily obtained within 1min in ambient conditions [93].

Flash reduction [95] of GO films can be performed with a single flash from a xenon lamp. The photo energy emitted by the flash lamp at a close distance (<2mm: ~1 J/cm$^2$) can provide 9 times the thermal energy needed for heating GO (thickness ~1 μm) over 100°C, which should be more than enough to induce deoxygenating reactions, and suggests that flash irradiation could lead to a much higher degree of reduction of GO. The GO films typically expand tens of times after flash reduction because of rapid degassing, and the electrical conductivity of the expanded film is around 10 S/cm using its maximum expanded thickness in the calculation. Because the light can be easily shielded, rGO patterns can be easily fabricated with photomasks,

which facilitates the direct fabrication of electronic devices based on rGO films, as shown in Fig. 1.4.3.a.

A further improvement of the photo-reduction and patterned film fabrication was carried out with **femtosecond laser irradiation** as proposed by Zhang et al. [96]. The focused laser beam (laser pulse of 790 nm central wavelength, 120 fs pulse width, 80 MHz repetition rate, focused by a 100x objective lens) has even higher power density than a xenon lamp flash and the heated area in a GO film is very localized with a line width in the range of $10^{-1}$–10 μm. As a result, the laser reduction can produce rGO films with a much higher conductivity of 256 S/cm, and the rGO film patterns can be drawn directly by a pre-programmed laser on the GO film to form more complicated and delicate circuits as shown in Fig. 1.4.3. b,c,d,e.

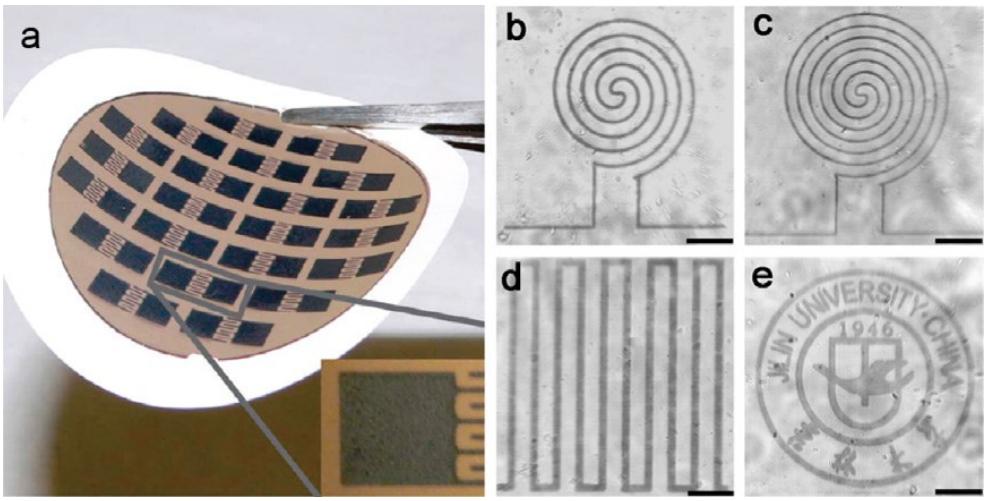


Fig. 1.4.3. – Patterned rGO film obtained by (a) flash reduction [95] and (b-e) femtosecond laser reduction [96]. The black parts in the films are the reduced GO patterns.

The reduction of GO by **visible laser irradiation** depends on many experimental parameters. Maria A Buccheri et al. show that the laser irradiation of GO samples mainly caused a variation in the type of oxygen functional groups and a decreasing of GO planes dimension respect to the

effective reduction of oxygen moieties [97]. In this work the solution of GO was irradiated by the second harmonic (532 nm) radiation of a Nd:YAG pulsed laser system operating with a pulse duration of 5 ns and a repetition rate of 10 Hz. Pulsed visible laser irradiation of GO solution in water does not produce a large reduction in the oxygen content, but creates defects in the GO structures, as indicated by the shift of the G band position (creation of divacancies in the graphene structure) and the small decrease in the $I_G/I_D$ ratio in the Raman spectra. In agreement with the Raman results, XPS analysis shows that the irradiation reduces the $sp^2$ component while the signals related to the oxygen configurations that are stable on defects (C=O, COOH and C–OH) increase, suggesting the creation of more holes or edges. DLS analysis on irradiated and initial samples confirmed that the average size of the irradiated samples is about half the value of initial GO, confirming a reduction in the size after laser irradiation. The SEM image of the irradiated sample shows a series of much smaller objects, with irregular edges. Summarizing, the pulsed visible laser irradiation of the GO solution in water produces more defects in the GO structures with the creation of a population of GO flakes with reduced dimensions and irregular shape. These results are different from other literature data [98] that report the reduction of the oxygen content in GO flakes irradiated by pulsed visible laser. The main differences are the GO concentration and the irradiated volume of GO as well as the frequency and energy of the pulsed laser, suggesting a dependence on these parameters for the modification of the content and type of oxygen functionalities of GO.

## Chemical reduction

Reduction by chemical reagents is based on their chemical reactions with GO. Usually, the reduction can be performed at room temperature or by moderate heating. As a result, the requirement for equipment and environment is not as critical as that of thermal annealing treatment, which makes chemical reduction a cheaper and easily available way for the mass production of graphene compared with thermal reduction.

The reduction of graphite oxide by hydrazine was used before the discovery of graphene [99], while the use of hydrazine to prepare chemically derived graphene was first reported by Stankovich et al. [100,101]. These reports an easy way for the mass-production of graphene. The reduction by hydrazine and its derivatives, e.g. hydrazine hydrate and dimethylhydrazine [102], can be achieved by adding the liquid reagents to a GO aqueous dispersion, which results in agglomerated graphene-based nanosheets due to the increase of hydrophobility. When dried, an electrically conductive black powder with C/O ratio around 10 [101] can be obtained. The highest conductivity of rGO films produced solely by hydrazine reduction is 99.6 S/cm combined with a C/O ratio of around 12.5 [103].

In another way, GO can be reduced keeping it in colloidal state in water by adding soluble polymers [100] as surfactant, in order to change the charge state of rGO sheets. The graphene sheets suspended in colloidal solutions can be used to assemble macroscopic structures by simple solution processes like filtration [104].

Metal hydrides, such as sodium borohydride ($NaBH_4$) has been also used as strong reducing reagents, resulting more effective than hydrazine as a reductant of GO [105]. However, $NaBH_4$ reacts with water, which is the main solvent for the exfoliation and dispersion of GO. In alternative way, Ascorbic

acid (Vitamin C, VC) was recently reported as reducing reagent for GO, which is considered to be an ideal substitute for hydrazine [103]. Fernandez-Merino et al. shown that GO reduced by VC could achieve a C/O ratio of about 12.5 and a conductivity of 77 S/cm, comparable with hydrazine reduction. In addition, VC is non-toxicity (in contrast to hydrazine) and it is chemically stable in water than $NaBH_4$.

Finally, Pei et al. [106] reported another reducing reagent, hydroiodic acid (HI), for GO. The investigations report C/O ratio around 15 and the conductivity of the rGO films around 300 S/cm, both better than obtained by other chemical reduction methods. The reduction by HI can be perdormed using GO in colloid form, powder or film in a gas or solution environment, even at room temperature [107].

## Photocatalyst reduction

GO can be reduced also by photo-chemical reactions with the assistance of a photocatalyst like $TiO_2$. Recently, Williams et al. reported the reduction of GO in a colloid state with the assistance of $TiO_2$ particles under ultraviolet (UV) irradiation. As shown in Fig. 1.4.4, a change in color from light brown to dark brown can be seen as the reduction of GO proceeds [108]. This color change suggested as partial restoration of the conjugated network in the carbon plane like that in chemical reduction processes. According to the formula shown in Fig. 1.4.4, upon UV-irradiation, charge separation occurs on the surface of $TiO_2$ particles. In the presence of ethanol the holes produce ethoxy radicals, thus leaving the electrons to accumulate within the $TiO_2$ particles. The accumulated electrons interact with GO sheets to reduce functional groups.


$$TiO_2 + h\nu \rightarrow TiO_2(h + e) \xrightarrow{C_2H_5OH} TiO_2(e) + {}^{\bullet}C_2H_4OH + H^+ \quad (1)$$

$$TiO_2(e) + \text{graphene oxide (GO)} \rightarrow TiO_2 + \text{graphene reduced (GR)} \quad (2)$$

Fig. 1.4.4 – Color change of a 10mM solution of TiO2 nanoparticles with 0.5 mg/mL GO before and after UV irradiation for 2 h in ethanol. A suspension of 10 mM TiO2 nanoparticles is also shown for comparison [108].

## Electrochemical reduction

Another method for the GO reduction is based on the electrochemical removal of oxygen functionalities [109–112]. Electrochemical reduction of GO sheets can be carried out in a normal electrochemical cell using an aqueous buffer solution at room temperature. The reduction is due to the electron exchange between GO and electrodes. In particular, after depositing GO on a substrate, an electrode is placed opposite the GO film in an electrochemical cell and reducing occurs during charging of the cell.

Zhou et al. [109] reported the best reduction effect using an electrochemical method. Elemental analysis of the resultant rGO revealed a C/O ratio of 23.9, and the conductivity of the rGO film produced was measured to be approximately 85 S/cm. They found also that the reduction can be controlled by the pH of the buffer solution.

Finally, An et al. [111] used electrophoretic deposition (EPD) to make GO films. They found that GO sheets can be reduced also on the anode surface during EPD.

# 1.5. Carbon nanotubes

## 1.5.1. Introduction

It is very difficult to give a unique definition of carbon nanotubes, especially due to the huge variety of sizes and shapes that they may have. Overall, the CNTs can be divided in two large families: **single-walled CNTs**, or **SWCNT** and **multi-walled CNTs**, or **MWCNT**.
The SWCNT can be regarded, for conformation and structure, belonging to the fullerene family, while MWCNTs to the nanowires family, which represent a particular case.

### SWCNT

The first SWCNTs were produced in 1993 through an arc discharge system (which we will discuss later) with electrodes composed by a coal-cobalt mixture.
An ideal SWCNT can be described as a carbon tube formed by a layer of graphene rolled up on itself to form a cylinder, closed at both ends by two hemispherical caps (Fig. 1.5.1.1 a). The nanotubes body is formed just by hexagons, while the closing structures (its hemispheres) are formed by hexagons and pentagons, as regular fullerenes. For this reason the SWCNT can be considered as a sort of “giant fullerenes”, and for this reason are also called “buckytubes”.

In the reality, the CNTs have got often structural defects or imperfections in the geometric structure (e.g. the presence of pentagonal or heptagonal defects on the tube walls) which deform the cylinder.

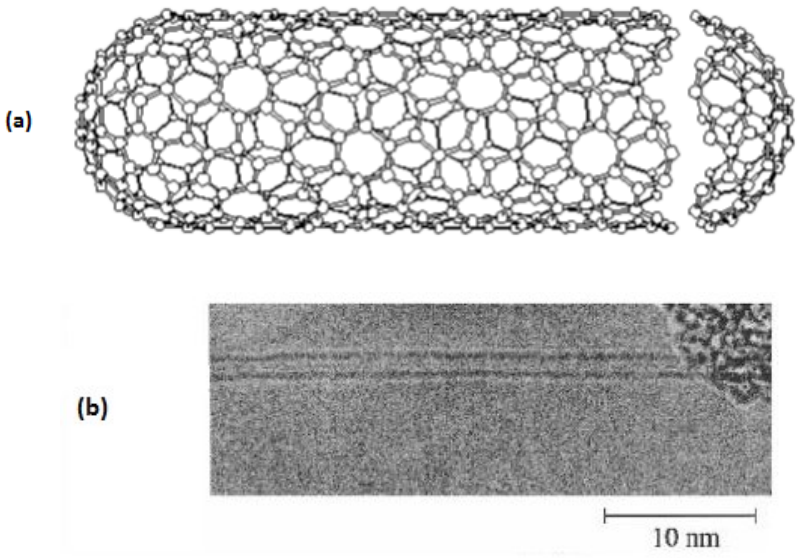


Fig. 1.5.1.1 – (a) An Ideal SWCNT closed by two semi-fullerenes [http://www.phys.ttu.edu/], (b) SWCNT TEM image [Iijima et al.,1993, doi:10.1038/363603a0]

The SWCNT diameter is included between a minimum of 0.7 nm (consistent to twice of the graphite interplanar distance) and a maximum of 10 nm, but in most cases, the diameter is less than 2 nm.

The high ratio ($10^4$ - $10^5$) between length and diameter of the SWCNT allows to consider them virtually as one-dimensional nanostructures, and gives to these molecules some specifics properties, which we will see later.

The graphene sheet "rolled up" can be described by a "**chiral vector**" **C** (or **helicity**), which connects two crystallographically equivalent sites and it is

expressed as the sum of two **unit vectors $\mathbf{a_1}$** and $\mathbf{a_2}$ so that $\mathbf{C = na_1 + ma_2}$ (Fig. 1.5.1.2).

The values of n and m cause the **diameter d** and the **chiral tube angle θ:**

- is zero (θ=0°) if n (or m) is null, then I have a **SWCNT Zig Zag;**
- θ=30° if n = m, then I have a **SWCNT Armchair;**
- 0°<θ<30° if n≠m≠0, then I have a **SWCNT Chiral.**

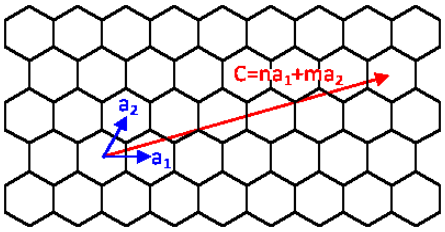


Fig. 1.5.1.2 – Chiral vector representation [http://ykkato.t.utokyo.ac.jp/nanotubechirality.en.html]

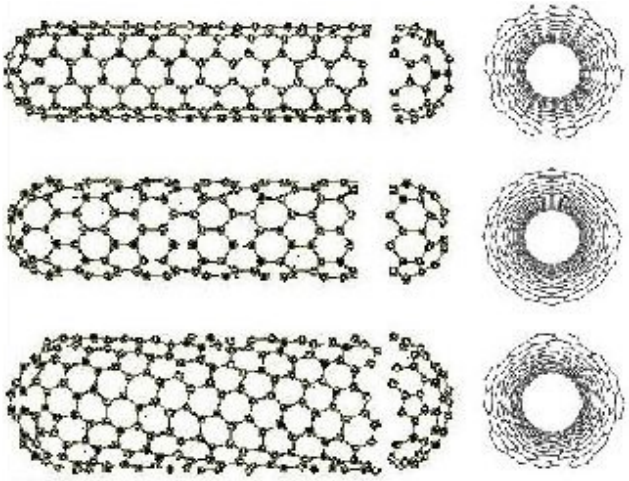

Fig. 1.5.1.3 – SWCNT schematic models: CNT "armchair" (5,5) (high), CNT "zigzag" (9,0) (center), CNT chirale (10,5) (down) [http://ipn2.epfl.ch]

The angle θ changes according to the law:

$$\theta = arctan\left[\frac{\sqrt{3}m}{2n+m}\right]$$

The diameter d is proportional to n and m according to the law:

$$d = \frac{a}{\pi}\sqrt{m^2 + n^2 + mn}$$

where **a** is the graphite lattice constant (a = 0.25 nm).

Therefore we can conclude that the geometrical properties of SWCNT are completely determined by the chiral vector (i.e. from the numbers n and m).

## MWCNT

**Multi-wall carbon nanotubes (MWCNTs)** are formed by several coaxial SWCNTs, and the distance between two neighbor walls is equal to the distance between two graphitic planes in graphite. Their outer diameter usually ranges between 10 and 20 nm, depending on the number of walls. Each "tube" contained in a MWCNT can have different diameter and chirality and therefore different properties, and most importantly interacts with the adjacent tubes (Fig. 1.5.1.4). The border between a multi-walled nanotube and a nanowire is not well defined, and a large size MWCNT can be considered as a specific case of tubular fiber.

The MWCNTs often present a large number of structural imperfections, and show an extreme variety of configuration in their terminal zones.

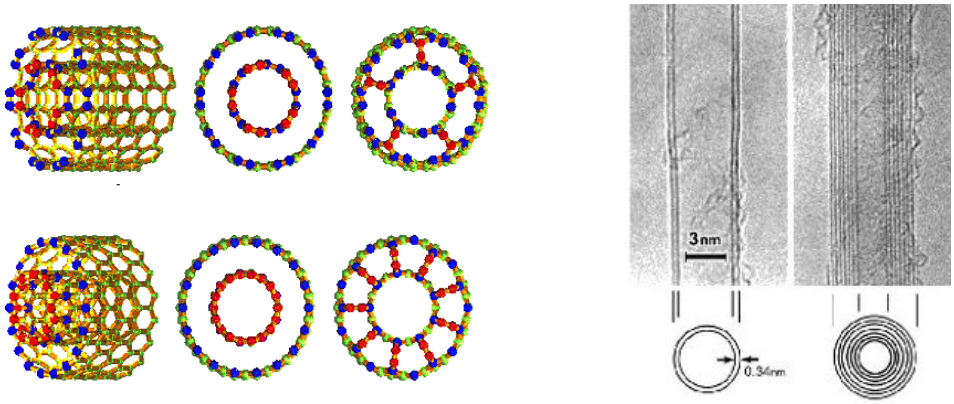


**(a)** **(b)**

Fig. 1.5.1.4 - (a) different types of MWCNT [www.maranza.com], (b) TEM images of double-wall CNT (DWCNT) and a MWCNT [www.intechopen.com]

## 1.5.2. Carbon nanotubes synthesis

One of the CNTs synthesis techniques is the **arc discharge technique** which allowed Iijima to observe for the first time the CNTs. The Japanese scientist observed tubular fullerenic structures by using a transmission electron microscope (TEM) in the soot produced in an arc discharge between two graphite electrodes. Since 1991, the CNTs discovery year, several other synthesis techniques were introduced, such as **laser ablation** and **chemical vapor deposition (CVD)**.

Along with the CNTs other species can form in a synthesis process, from catalytic metal particles to amorphous carbon and non-tubular fullerenes, which require a later purification.

### CNTs by Arc Discharge

The schematic diagram of the arc discharge system is shown in figure 1.5.2.1. Two graphite rods are used as electrodes within a vacuum chamber in the presence of inert gas.

When the pressure inside the chamber is stabilized, a voltage is applied between the graphite rods and the two rods are approached until the discharge turns on. In order to maintain the discharge on, the positive electrode is gradually approached to the negative one such a way that the gap between the anode and cathode is constant, while the anode is consuming. The energy is sufficient to vaporize the anode and a plasma is formed between the electrodes. The temperature in the plasma region can reach thousands degrees and C atoms and small agglomerates, called cluster, condense in CNT and other structures, depositing on the negative electrode and on the chamber walls.

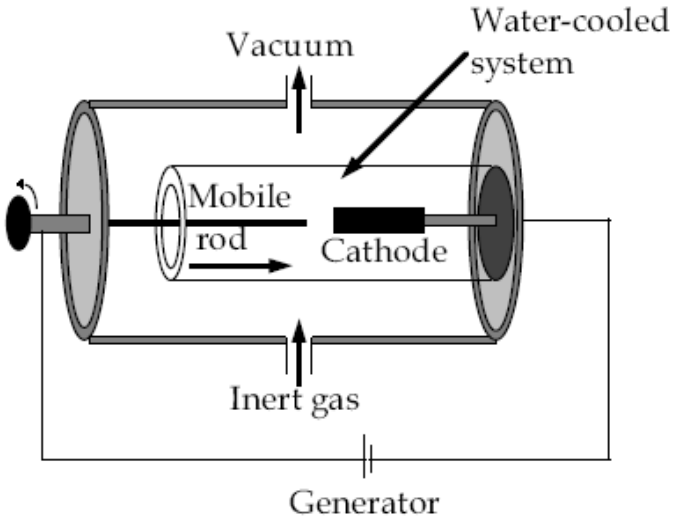


Fig. 1.5.2.1 – Schematic diagram of Arc discharge
[http://lem.ch.unito.it/didattica/infochimica/2006_Nanotubi/frame-sintesi.html]

The two most important parameters in the arc discharge synthesis are the arc current control and the inert gas pressure, which determine the deposition speed.

The growth temperatures are higher than all other CNTs synthesis methods, which guarantees the best crystallinity and perfection of the tubes. Moreover, this technique allows a high CNT production yield, but it has poor process control, and it does not permits the direct the growth on substrates.

If both electrodes are produced in graphite, the main arc discharge products are MWCNTs. The catalytic particles absence avoids purification processes using heavy acid, so the MWCNT are free of defects.

To obtain SWCNT, the electrodes are doped with a small amount of catalytic metal particles which thus, are found in the deposited material together with other impurities.

Using a gaseous mixture of methane at 10 torr and argon at 40 torr, a current of 200A and a voltage of 20V, Iijima and Ichihashi have synthesized for the

first time SWCNTs, with diameter of about 1 nm [113]. Subsequently using carbon electrodes and catalytic particles of Co, Ni, and Fe, with a current of 95-105A and helium at 100-500 torr, SWCNT with diameter of about 1.2 nm have been synthesized by using catalytic particles of Co [114]. The quantity and quality of the nanotubes obtained depends on various parameters, such as the metal concentration, the gas type, the discharge current and the geometry of the system.

The catalytic metal particles concentration affects the CNTs quality, because the presence of these particles in the reaction product requires a purification process which alter the tubes structure.

The high particles concentration, especially if these are Co and Mo, also affects the tubes diameter, which is reduced between 0.6 and 1.2 nm [115].

The inert gas choice allows to control lightly the SWCNT diameter because the thermal conductivity and the gas diffusion coefficient affect the carbon atoms and metal condensation near to the cathode.

For example, it has been observed that the CNTs diameter decreases about 0.2 nm if the argon-helium ratio increases of the 10%, compared to the only argon presence which contributes to the SWCNT formation with a diameter of 1.2 nm [116].

Over the years various type of arc discharge techniques have been introduced allowing to obtain MWCNTs with a high purity degree, low cost and in large scale.

**The arc discharge in liquid nitrogen (LN$_2$ Arc discharge)** (Fig. 1.5.2.2), for example, allows to synthesize MWCNT highly crystalline with the possibility of mass production without the necessity to use inert gas and vacuum systems.

The reaction product could contain up to 70% MWCNT [117].

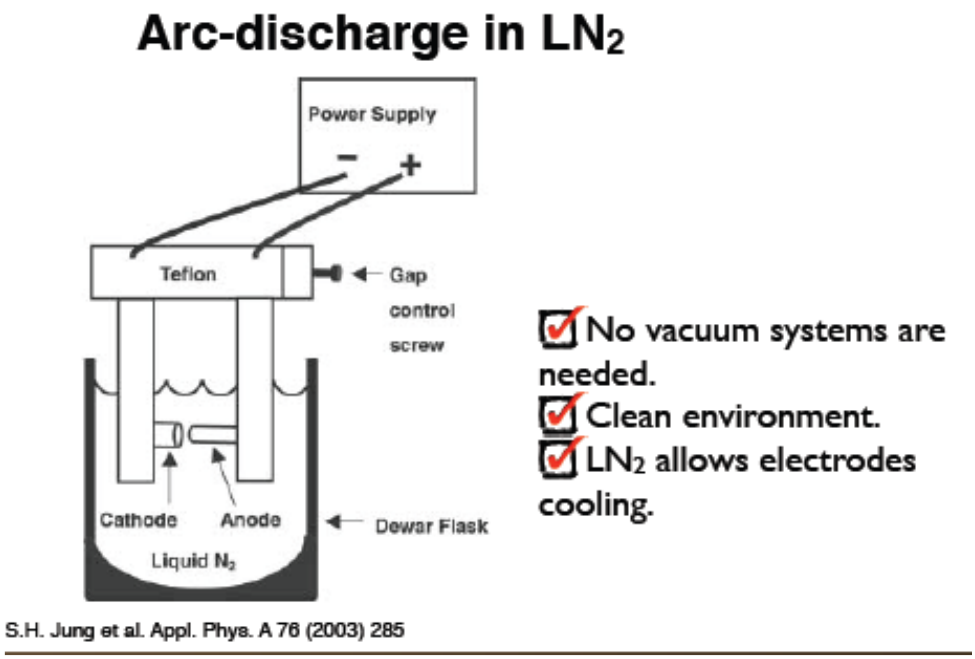


Fig. 1.5.2.2 - Arc discharge in liquid nitrogen

## CNTs by Chemical Vapor Deposition (CVD)

The CNTs large scale production is often more convenient with **Chemical Vapor Deposition (CVD)** technique. The CNTs are formed by the hydrocarbon decomposition at the vapor state in the catalyst presence, using an energy source which is typically an electron beam, a plasma or a resistive coil heated for Joule effect. It is a continuous process in which the carbon source is continuously replaced by the flowing gas.

The energy source shatters the molecules in reactive radical species, at temperatures between 500 and 1200 °C. The reactive species diffuse to a substrate, heated and covered with catalyst particles, to which remain linked forming carbon nanotubes. The technique was used in 1959 for the production of fibers and filaments of carbon, and after CNTs discovery by

Iijima, it was used for the CNTs synthesis using benzene, acetylene, ethylene, methane as hydrocarbons, and nanoparticles of Ni, Fe, Co and Mo as catalysts. The catalytic particles size and type, the hydrocarbon used and the temperature, are the main parameters of the CNTs growth.

The experiments show that the MWCNT growth is favored by most of the hydrocarbons used, at temperatures between 600 and 900 °C, while the SWCNT formation requires the use of stable hydrocarbons (including CO and $CH_4$) at temperatures between 900 and 1200 °C, presumably because their diameter is smaller and leads to a greater curvature and formation energy. Increasing temperatures also increase the CNTs density and the growth speed.

The catalytic particles are generally of Fe, Ni or Co or organometallic solids as ferracene, cobaltocene and nichelocene. Their sizes are found to affect the CNTs diameter. Compared to the arc discharge, the growth on substrates is possible, but for both MWCNTs and SWCNTs catalytic particles are required. Moreover, because of the chemical process nature and low temperatures (compared to the arc discharge), the CNTs grow with many defects.

## CNTs Growth mechanism in CVD synthesis

The CNT growth mechanism is still not very clear and in the literature there are many different opinions.

In general, the catalyst-based growth process (as the CVD) can be of two types: **root growth** and **tip growth.**

## Root growth

In this model, the carbon gas is deposited around the catalyst and, after forming a graphitic shell on it, the tubular structure grows leaving the catalyst at the base.

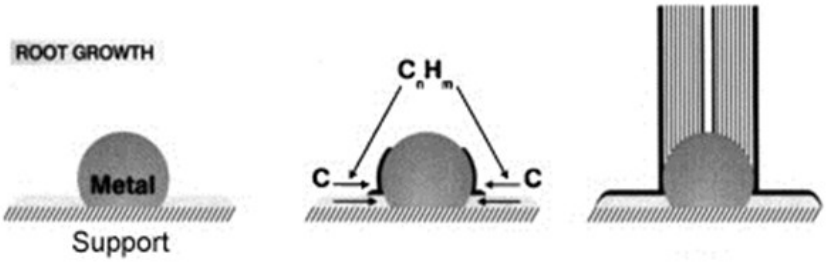


Fig. 1.5.2.3 - CNT root growth [http://students.chem.tue.nl]

## Tip growth

In this case, the carbon gas is deposited on the catalyst forming a solid solution. After solution saturation, the carbon precipitates on the catalyst surface, binds to the substrate and begins to grow in a tubular shape, dragging up the catalyst.

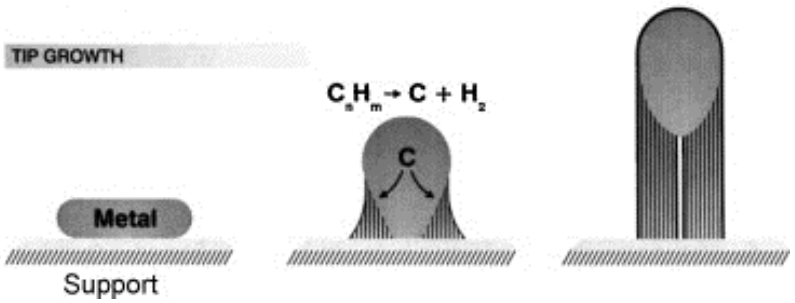


Fig. 1.5.2.4 - CNT tip growth [http://students.chem.tue.nl]

In figure 1.5.2.5 is shown a MWCNT with a catalytic particle inside.

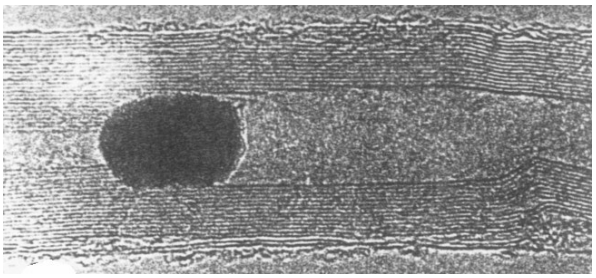

Fig. 1.5.2.5 – A TEM image were a MWCNT with a catalytic particle inside is shown [Ivanov V., et al., 33, 1727-1738 (1995)].

## CNTs by Plasma Enhancement CVD (PE-CVD)

The CNTs synthesis with CVD stimulated by plasma (**Plasma Enhancement CVD**) consists in glow discharge producing inside a chamber or into a reaction furnace, through a high-frequency alternate voltage applied between two electrodes (Fig. 1.5.2.6).

The CNT growth happens through the glow discharge (caused by high-frequency generator) on the nanometric catalytic particles (prepared by the catalyst sputtering on the substrate).

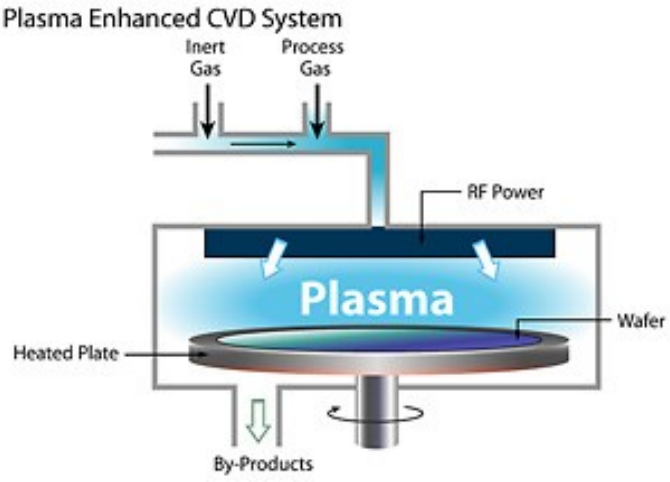


Fig. 1.5.2.6 - PE-CVD schematization [http://www.dowcorning.com]

The catalyst material has a strong influence on the diameter, on the growth speed, and on the CNT structure.

Using a $CO_2$ and $CH_4$ compound as reaction gas and Fe catalytic particles on a Si substrate, at temperatures between 300 and 350 °C, the synthesized of MWCNTs lined up vertically with a 15 nm diameter has been shown. The highest percentage (50%) of nanotubes in the reaction products, is obtained at temperatures lower than 330 °C [118].

## CNTs by Thermal CVD

In this case, a metal catalyst (Fe, Ni, Co, or their alloy) is deposited on a substrate and subsequently etched in a HF solution (in distilled water) in order to obtain a discontinuous layer. Then it is inserted into a quartz tube inside a furnace. Heating the metal film catalyst at a temperature between 750 and 1050 °C, there is the formation on the substrate of nanometric catalytic particles on which occurs the MWCNT growth.

Using Fe as a catalyst, the CNTs diameter depends on the film thickness, and it changes between 30 and 40 nm or between 100 and 200 nm, respectively, for a thickness of 13 nm and 27 nm [119].

## CNTs by Laser Ablation

The **laser ablation technique** (or laser vaporization technique) for the CNTs synthesis was used for the first time in 1996 by Smalley et al. [120]. Etching a carbon target with intense laser pulses, mass spectroscopy put previously in evidence the fullerenes presence.

Smalley's group was able to produce large quantities of fullerenes C60 only in a high temperature furnace, leading subsequently to the SWCNT

production. In figure 1.5.2.7. a schematics of a laser ablation system is reported.

A laser beam, usually a YAG or a $CO_2$ laser, is introduced through a window inside a quartz tube, and focused towards a graphite target (eventually doped with Co, Ni, Fe or Y catalytic particles) located in the tube at the center of the furnace. The target is vaporized in the presence of an inert gas at high temperature (500-1200 °C). Pressure and gas flow are kept constant by a control system, typically at 1cm/s and 500 torr.

The CNTs produced during the graphite vaporization, together with the catalytic particles and other impurities, are conveyed and collected on a water cooled trap, while the vaporization surface is kept as cool as possible moving the laser focus or moving the target.

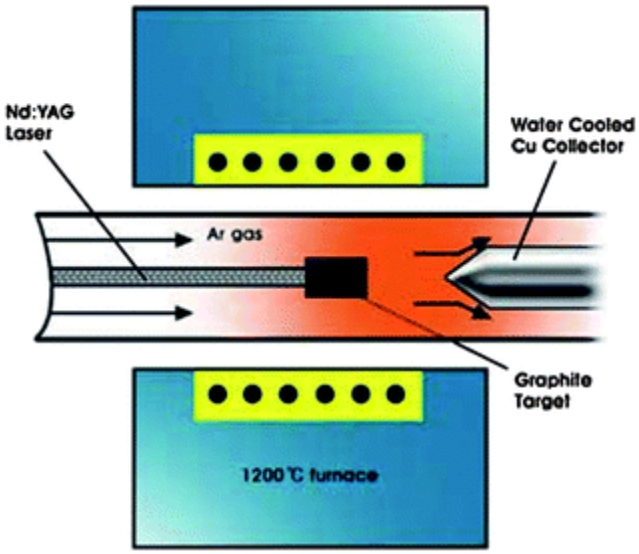


Fig. 1.5.2.7 – A laser ablation system diagram [http://students.chem.tue.nl]

When the graphite steam cools, the molecules and the carbon atoms condense quickly forming clusters containing fullerenes. The catalytic particles condense less rapidly and attack the cluster impeding their closure in closed structures and opening even those which are already formed. From these

clusters the formation and the growth of the carbon nanotubes take place, until the catalytic particles will become too large, the cooling would not allow more carbon diffusion along the catalytic particles surface, or the particles have been coated by carbon, so that it cannot absorb further. As for the arc discharge technique, the SWCNT synthesis requires, compared to the MWCNT synthesis, the use of catalytic particles, usually of Co, Ni, Fe or Y. The SWCNT diameter can be controlled setting the furnace temperature, the catalytic particles nature and the gas flow in the tube. The laser ablation is an expensive technique, which makes it rarely used especially in the MWCNT synthesis.

## CNTs Purification

It is predicted theoretically and observed experimentally that CNTs possess excellent physical and chemical properties and have wide-range potential applications. However, only some of these properties and applications have been verified. To a great extent, this situation can be ascribed to the difficulties in getting high-purity CNTs. Because as-prepared CNTs are usually accompanied by carbonaceous or metallic impurities, purification is an essential issue to be addressed.

Considerable progress in the purification of CNTs has been made and a number of purification methods including chemical oxidation, physical separation, and combinations of chemical and physical techniques have been developed for obtaining CNTs with desired purity.

Carbonaceous impurities typically include amorphous carbon, fullerenes, and carbon nanoparticles (CNPs) (as shown in Fig. 1.5.2.8). Because the carbon source in arc discharge and laser ablation comes from the vaporization of graphite rods, some un-vaporized graphitic particles that have fallen from the

graphite rods often exist as impurity in the final product. In addition, graphitic polyhedrons with enclosed metal particles also coexist with CNTs synthesized by arc discharge and laser ablation as well as high temperature (>1000 °C) CVD. Fullerenes can be easily removed owing to their solubility in certain organic solvents. Amorphous carbon is also relatively easy to eliminate because of its high density of defects, which allows it to be oxidized under gentle conditions. The most knotty problem is how to remove polyhedral carbons and graphitic particles that have a similar oxidation rate to CNTs, especially SWCNT.

Metal impurities are usually residues from the transition metal catalysts. These metal particles are sometimes encapsulated by carbon layers (varying from disordered carbon layers to graphitic shells, as shown in Fig. 1.5.2.8 b and c making them impervious and unable to dissolve in acids.

Another problem that needs to be overcome is that carbonaceous and metal impurities have very wide particle size distributions and different amounts of defects or curvature depending on synthesis conditions, which makes it rather difficult to develop a unified purification method to obtain reproducibly high-purity CNT materials.

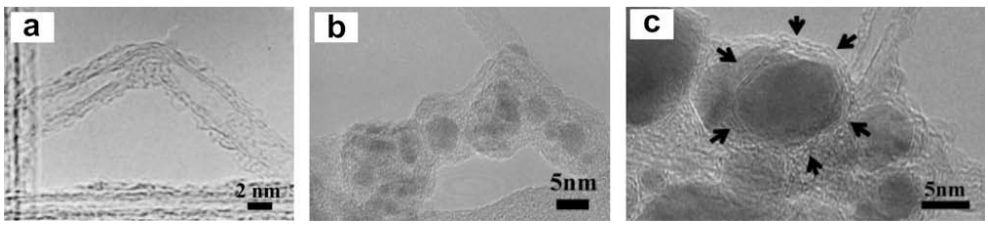


Fig. 1.5.2.8 - TEM images of (a) amorphous carbon and fullerene molecules on the surface of CNTs, (b) metal nanoparticles covered by amorphous carbon layer, (c) metal nanoparticles covered by graphitic carbon multi-layer [Fang HT et al., Chem Mater 2004;16(26):5744–50]

## CNTs Oxidation

The carbonaceous impurities co-existing with as-synthesized CNTs are mainly amorphous carbon and CNPs. Compared with CNTs, these impurities usually have higher oxidation activity. The high oxidative activity demonstrated by amorphous carbon is due to the presence of more dangling bonds and structural defects which tend to be easily oxidized; meanwhile the high reactivity of the CNPs can be attributed to their large curvature and pentagonal carbon rings [121]. Therefore, chemical oxidation purification is based on the idea of selective oxidation etching, wherein carbonaceous impurities are oxidized at a faster rate than CNTs.

In general, chemical oxidation includes **gas phase oxidation** (using air, $O_2$, $Cl_2$, $H_2O$, etc.), **liquid phase oxidation** (acid treatment and refluxing, etc.), and **electrochemical oxidation**. The disadvantages of this method are that it often opens the end of CNTs, cuts CNTs, damages surface structure and **introduces oxygenated functional groups** (–OH, –C=O, and –COOH) on CNTs (Fig. 1.5.2.9). As a result, the purified CNTs in turn can serve as chemical reactors or a starting point for subsequent nanotube surface chemistry [122].

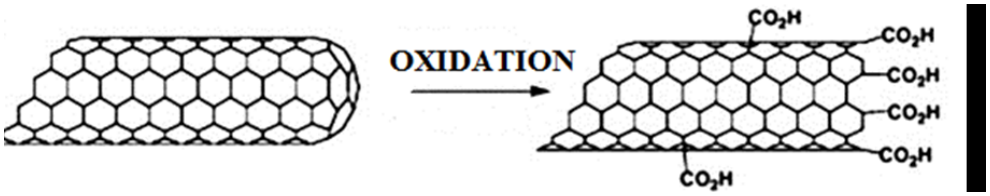


Fig. 1.5.2.9 – Birth of -COOH group after CNTs oxidation [M. Prato et al., 2008, Chemical Research, 41(1), 60-68.]

## 1.5.3. Carbon nanotubes properties

Since the discovery of CNTs by Iijima, several studies have been performed to investigate, from both theoretical and experimental point of view, their physical, chemical, and electrical properties.

### Electrical and Electronic properties

The remarkable electrical performances of carbon nanotubes have their origin in the electronic structure that can be derived from the band structure of graphene by imposing boundary conditions along the nanotube circumference. Anyway, the electrical transport within the CNTs can be "disturbed" and drastically affected by the presence of defects and lattice vibrations.

### CNTs band theory

The carbon nanotube band structure can be derived from the one of graphene by imposing boundary conditions along the nanotube circumference.
The wave vector **k** = ($k_x$,$k_y$) along the tube's girth is quantized:

$$\boldsymbol{k\,C} = 2\pi q$$

where C is the chiral vector and q an integer number
In terms of $k_x$ and $k_y$:

$$(na_{1x} + ma_{2x})k_x + \left(na_{1y} + ma_{2y}\right)k_y = 2\pi q$$

from which, taking as reference the choice of primitive vectors of the hexagonal lattice shown in Fig 1.2.1.2, we get

$$k_x = \frac{4\pi q}{a(n+m)\sqrt{3}} - \frac{n-m}{(n+m)\sqrt{3}} k_y$$

Then, in the reciprocal lattice space some quantization lines appear spaced in width by a value

$$\Delta k = \frac{2\pi}{a|C|\sqrt{3}} = \frac{2}{d}$$

which depends exclusively on the nanotube diameter d and then from its helicity.

In figure 1.5.3.1 the wave vectors eligible for each type of nanotube are shown.

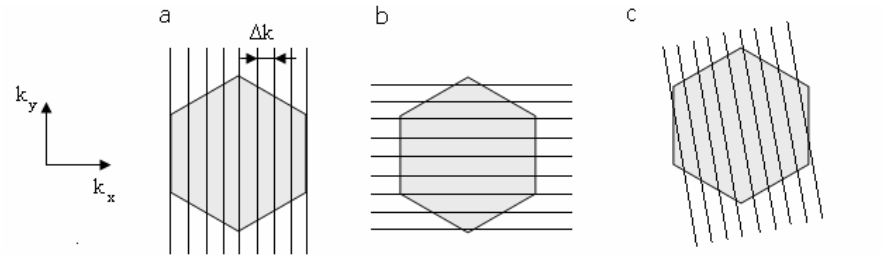


Fig. 1.5.3.1 - Wave vectors allowed for a nanotube (a) armchair, (b) zig-zag and (c) chiral.

The dispersion equation in terms of kx and ky is

$$E_{2D}(k_x, k_y) = \pm\gamma \sqrt{1 + 4cos\left(\frac{k_x a\sqrt{3}}{2}\right) cos\left(\frac{k_y a}{2}\right) + 4cos^2\left(\frac{k_y a}{2}\right)}$$

where a = 0.25nm is the graphite lattice constant and γ = 2.7 ± 0.1 eV is the C-C tight bonding overlap energy.

If the quantization lines relating to the graphene sheet, cross the hexagon vertices where the valence and conduction bands are touching, the nanotube shows a metallic behavior because it is characterized by a null band-gap.
Otherwise it behaves as a semiconductor. Especially, it is proved that the nanotube has metallic behavior if n - m = 3q with q positive integer or zero, while performs as semiconductor if n - m ≠ 3q [123].
In semiconducting nanotubes, the distance between the minimum of the conduction band and the maximum of the valence band corresponds to the energy gap

$$E_g = \frac{2a_{cc}\gamma}{d}$$

where $\mathbf{a_{cc}}$ is the nearest neighbor C-C distance (0.142nm).
At this point it is clear that from the nanotube helicity we obtain the diameter and the energy band gap.
In a MWCNT, the situation is obviously much more complex because each tube can have a chirality and therefore electrical properties different from the other tubes forming the same MWCNT. In general, a MWCNT tend to be semi-metal such as graphite due to the band-gap reduced (particularly for larger diameters). In any case it is clear that the helicity of the structure is a very important feature that can be engineered, which makes the topic "nanotubes" extremely fascinating.
Up to now, however, the synthesis of nanotubes with controlled helicity is not easily achieved, and therefore by the same synthesis experiment nanotubes with different electronic properties are produced.
The electronic transport properties of conventional three-dimensional metals are successfully described by Fermi-liquid theory. But when the dimensionality of such a system is reduced to one, as in the carbon nanotubes, the Fermi-liquid state becomes unstable to Coulomb interactions,

and the conduction electrons should instead behave according to **Tomonaga–Luttinger-liquid** theory. In particular, carbon nanotubes show two different electrical behaviors depending of the range of temperature: **ballistic current transport** at room temperature and **Coulomb blockade phenomena** at low temperatures. Ballistic transport (see later) is showed when the distance between the electrodes, where voltage is applied, is shorter than the mean free path. Coulomb blockade occurs when the electrons go in and out from a single atom between two electrodes due to a high contact electrical resistance. However, these electrical transport described are visible only in a single nanotubes. In fact, in the case of several SWCNTs or MWCNTs (with many SWCNTs), a typical electrical transport of the metal is shown. Metallic multiwall CNT can support a current density of $10^8$ A/cm$^2$ and can dissipate a power of 1.82 mW [124]. Moreover, they have high dielectric constant, while semiconducting carbon nanotubes have low dielectric constant [125, 126, 127].

Usually, during the synthesis of carbon nanotubes, both metallic and semiconducting carbon nanotubes are obtained [128], forming groups of carbon nanotubes called **bundles,** held together by van der Waals interactions. A bundle with several hundred of nanotubes is instead named **rope**. The presence of multiple carbon nanotubes can substantially reduce the electrical resistance compared with the electrical resistance of an individual nanotube.

Typically, the electrical transport in a bundle has a metallic behaviour (the resistivity increased with the temperature) and can be modified by the applied electrical field.

In the case of semiconducting nanotubes, the applied electrical field produces band gap closure, while for metallic nanotubes it produces a band gap opening.

## CNTs conductance

The 1D nature of the CNT leads to a new type of quantized resistance related to its contacts with three dimensional macroscopic objects such as metal electrodes [129].

The electron confinement in CNT around its circumference produces a small number of discrete states (modes) that overlap the continuous states of the metal electrodes. This mismatch of the number of states, that can transport the current in CNT, and the electrodes lead to a **quantized contact resistance**, **Rq**.

The resistance value is determined by the number of modes, M, in carbon nanotubes with energies lying between the Fermi's levels of the electrodes.

For a CNT, the conductance is:

$$G = G_0 M = \frac{4\pi e^2}{h} M$$

where $G_0$ = (12.9 kΩ)$^{-1}$ and M takes into account any processes influencing the conduction. For a perfect SWCNT M = 2, and the conductance value is (6.45kΩ)$^{-1}$.

The resistivity measured for a MWCNT decreases according to the temperature and the values (at room temperature) are compatible or lower than the graphite resistivity (~ 0.4 Ωm).

## Ballistic conduction

An ideal nanotube, should behave as a ballistic conductor: if an electron is injected by an ideal contact in "ballistic wire" and if the wire has another ideal contact, the electron injected will come out from the second contact. This behavior implies that there are no backscattering phenomena in the wire.

If you study a "ballistic tube" the theory predicts the existence of two independent automodes, then the conductance will be exactly the double.

It is noted that the resistance is not zero, as in the case of a superconductor, but is independent from the length of the tube, in contrast with the law of Ohm.

In other words, the electrons can move inside a nanotube without heating that [130]. These properties make the CNTs very attractive for the development of nanoelectronics, where silicon can be replaced by "nanowires" or "quantum wires". To do this, however, synthesis and manipulation techniques have still to be improved in order to get a suitable control of the CNT structural and electronic properties. In the literature there are some examples that suggest a ballistic behavior even for the MWCNT. For example, in Fig. 1.5.3.2 a typical example of a ballistic behavior is shown [131]. In this case, the counter electrode is a film of liquid mercury, and it is observed that soaking the nanotubes in the liquid are obtained the plateau in the conductance of the system which therefore is ballistic, i.e. independent from nanotubes submerged length.

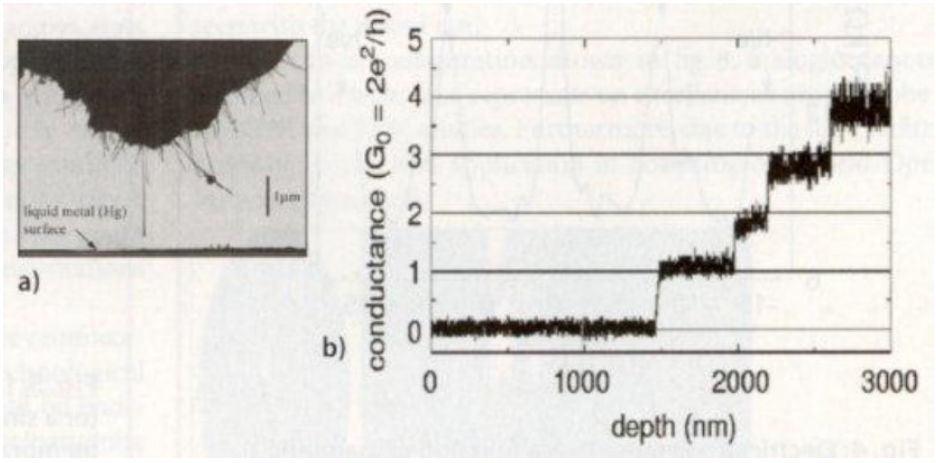


Fig. 1.5.3.2 - CNTs ballistic behavior [http://www3.nd.edu/]

## CNT doping

The nanotubes conduction properties can be adjusted "doping them", i.e. by inserting in their structure nitrogen and boron atoms (Fig. 1.5.3.3). Among the most interesting results in this field there is a "nanodiode" made up of two nanotubes (one of which is conductor and the other one semiconductor) melted together on one end, that acts as a normal diode, with current by passing in one direction and not in the other [132].

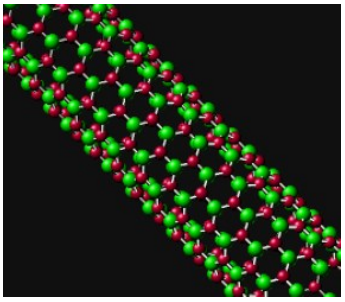

Fig. 1.5.3.3. – Image realized with computer that shows a nanotube formed by nitrogen and boron atoms.[132]

## Field emission

CNTs produce field emission [133]. The electrons emission due to the presence of the high electrostatic fields is a phenomenon known since the late years of the XIX century. But its proper interpretation was possible only after the development of quantum theory and it is due to the physicists Fowler and Nordheim, who developed the theory of field emission in 1928. The theory interprets the field emission as a special case of tunnel effect (Fig. 1.5.3.4).

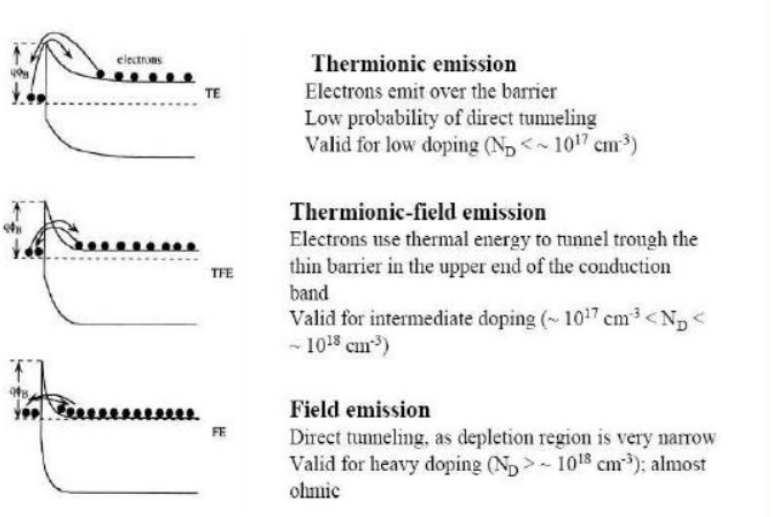


Figure 1.5.3.4. - Thermionic effect and field-effect: band diagram [133]

The most important parameter to characterize this emission is the **threshold field** that represents the minimum electric field required to activate the emission. An efficient material will have a lower threshold field.

For these studies, besides the precision in measuring the emitted current, that usually are very weak (less than a billionth of Ampere), it is also very important to evaluate precisely the distance between the emitting cathode and the anode.

Thanks to the technology developed for tunnel effect microscopes, some field effect characterization systems exist which allow to measure, with the accuracy of some tens of nanometers, the anode-cathode distance. The intensity of the emitted current in the field emission phenomenon depends, of course, on the applied field gradient, according to the Fowler-Nordheim model.

In nanotubes, the field emission occurs applying a potential of just a few hundred volts. They are able to emit high currents of the order of 0.1 mA, a current density exceptional for such a small object. Currently the field emission phenomenon in CNTs is widely studied.

## Mechanical and elastic properties

The crystal mechanical resistance depends on several factors, among which the most important are the force of the atom-atom constructive material bond and the absence of structural defects in the crystalline lattice. To bring a defect-free nanotube to breakage all the covalent carbon-carbon bonds that compose it (C-C $sp^2$) have to be broken up.

These bonds are the strongest known in nature, it follows that the nanotubes should have an extremely high mechanical strength. A fiber formed by carbon nanotubes would be then not just the strongest ever made, but even the most resistant one [134].

It was calculated that the theoretical Young's modulus of CNT can reach up to 4 TPa, and its tensile strength should be about 220 GPa (100 times larger than that of steel, but in front of a weight 6 times minor) [135].

The nanotubes are not only extremely resistant to fracture under tensile stress, but also very flexible and they can be bent repeatedly up to about 90° without breaking or become damaged (Fig. 1.5.3.5) [136].

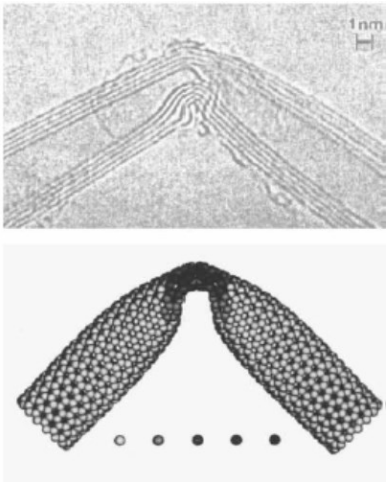


Fig. 1.5.3.5 - CNT deformation at 90° (TEM image) [136]

In this kind of measurement, there are two main difficulties: the first is to isolate a single nanotube, the second is the enormous difficulty to manipulate nanometer sized objects. For this reason it is often necessary to resort to computer simulations, which, however, are strongly influenced by approximations and theoretical models used in the simulations.

A relatively simple method to measure the mechanical and elastic properties of nanotubes is to deposit them on an alumina surface, obtained using a membrane with a few hundred nanometers pore size. In Fig. 1.5.3.6 you can see how the use of an atomic force microscope and a good amount of luckiness allows the mechanical characterization of the material, in particular, once you have located a nanotube that luckily is suspended above an alumina pore, we can proceed with strength measures. Jean-Paul Salvetat devised this novel technique, along with co-workers from the École Polytechnique Fédérale de Lausanne (EPFL) in Switzerland.

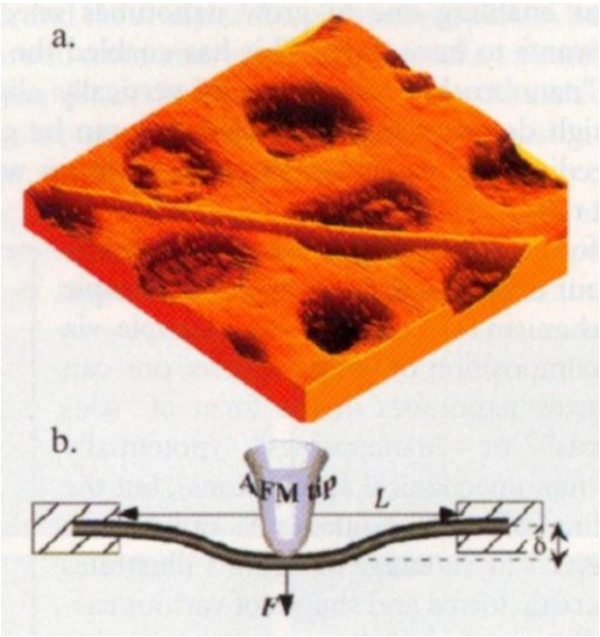


Fig. 1.5.3.6 – CNT elasticity measurement with AFM [http://www3.nd.edu/]

The same group also determined that the deflection is inversely proportional to the Young's modulus. For nanotubes produced with arc discharge it was found that the Young's modulus is around 0.8 TPa but in the case of nanotubes grown up with catalytic methods the Young's modulus is smaller even two orders of magnitude. These results clearly indicate us that the growth process quality is reflected in an important way to the quality of the nanotubes produced (defects!).

The extreme nanotubes strength, coupled with their flexibility, would make them ideally suited for use as reinforcing fibers in high-performance composite materials, in place of regular carbon fibers, Kevlar or glass fibers. The technological problem about the construction of such fibers persists, however, given that currently it is not possible to build macroscopic fibers constituted by nanotubes. Thanks to their small sizes and their mechanical strength properties the nanotubes can also be used for special high level applications, as for example probe for scanning tunneling microscopes (STM).

## Thermal Properties

All nanotubes types show typical physical characteristics of solids and must therefore be seen as graphite microcrystals and not as new molecular species of carbon. By molecular dynamics calculations, the estimated value of thermal conductivity at room temperature for a single-walled nanotube (10,10) is 6600W/mK (3320W/mK for isotopically pure diamond) and therefore it can be defined the best heat conductor known. Furthermore, the nanotubes have got a high thermal stability (up to 2800°C in vacuum and 750°C in the atmosphere) [137].

One of the possible applications to utilize these excellent thermal properties can be the implementation of internal connections in integrated circuits. The connecting cables in the traditional microchip circuits shall be approximately 250 nm, we would like them much smaller in order to be able to pack more devices in the same area. But there are two problems that prevent the attempts to miniaturization: first, conventional cables bundled up tightly overheat, second, while the cables will gradually reduce, the electrons flow is intense enough to melt them. The nanotubes could solve this problem: it has been estimated a1 billion amps per square centimeter of current carrying capacity, compared to copper wires that melt at about 1 million amperes per square centimeter [138].

## Chemical properties

Because of their tubular form, nanotubes show strong capillarity properties and their great surface/volume ratio makes them theoretically ideal for the adsorption of gases and liquids [139]. The ends of the closed carbon nanotubes, are chemically more reactive than the walls of the tubes, for the presence of pentagons or metallic catalysts in the caps that close the nanotubes, and also for their higher bending radius. The opening of the CNT caps can be done for example by oxidation with oxygen [140]. After these reactions some carboxylic groups (-COOH), hydroxyl (-OH) or other functional groups remain attached at the tubes ends, but in general also on the tube walls (Fig. 1.5.3.7).

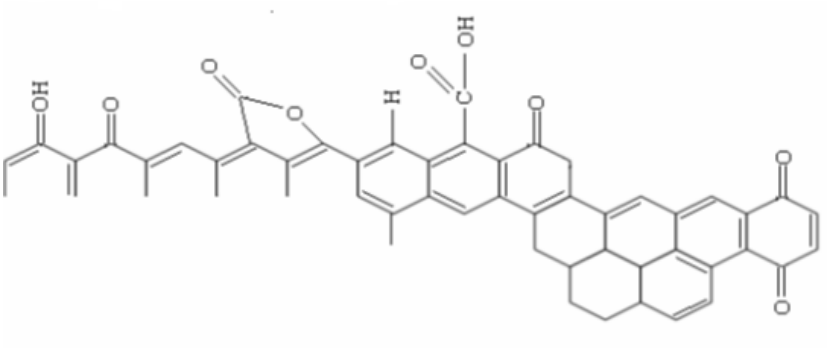


Fig. 1.5.3.7 - Possible chemical groups at the nanotube surface.

Nanotubes can be plunged in $HNO_3$, S, Cs, Rb, Se solution, and different oxides such as Pb and $Bi_2O_2$, while they are hydrophobic and show no aptitude for baths in watery solvents. For their structure they are characterized by high property of capillarity, for which it is possible to insert these agents within the tubes by capillary pressure, proportional to 1/d.

Regarding the adsorption, notable oxygen absorption capacity have already been experimentally observed, and theoretical studies related to the adsorption of various other gaseous molecules show that the adsorption depends on the sites and on the gas molecule. The adsorption of some molecules affects the electronic tubes structure, modifying the Fermi's level, the density of states and then the CNT conductance. This makes the CNTs suitable to be used as chemical sensors. The CNTs adsorption properties have been studied in the case of $O_2$, $C_6H_{12}$, $NH_3$, $NO_2$ and also hydrogen, especially in view of its possible use in "fuel cell". In fact, all the systems used up to now for hydrogen storage (tanks, hydrides, active carbons) require to work at high pressure and low temperature in order to store a sufficient amount of hydrogen. Of great interest were some experiments on hydrogen adsorption on carbon nanotubes "doped" with lithium or potassium [141].

## Defects in CNTs

In general nanostructures show often vacancies, interstitials, dislocations and geometrical imperfections. The displacements of C atoms from the graphitic lattice sites of the CNTs cause the formation of vacancies in the hexagonal lattice and the atoms endowed of enough energy could leak from the CNTs surface. Therefore the birth of pentagonal and heptagonal defects take place (Fig. 1.5.3.8).

Particularly interesting is the **Stone-Wales transformation** [142] which forms pentagonal structures and from the simulations it seems to occur also in CNTs during mechanical deformation (Fig. 1.5.3.9).

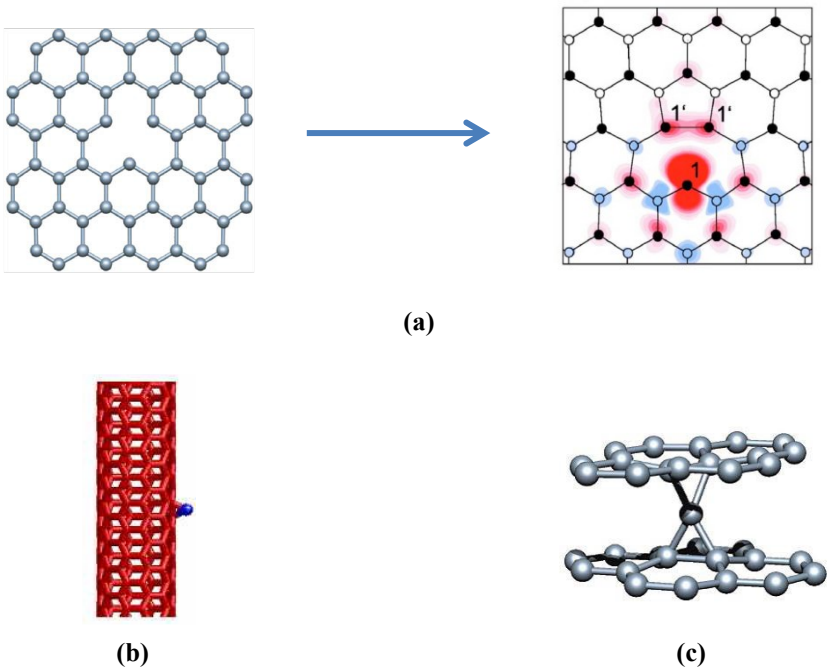


Fig. 1.5.3.8 – Point defect: (a) Birth of pentagonal structures, (b) Atom leakage from CNTs (c) Interstitiality into the structure [http://www.fis.unipr.it]

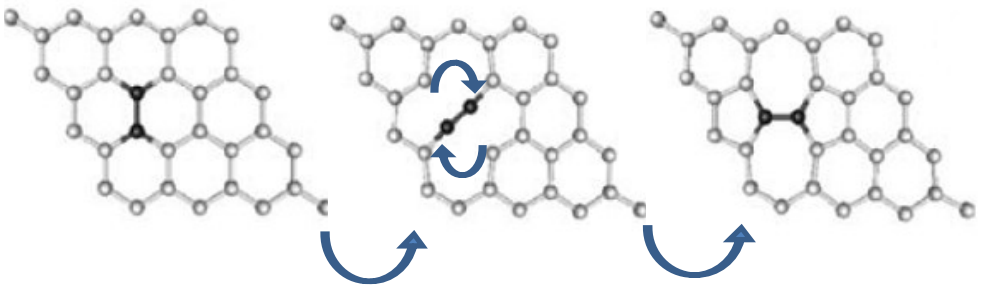

Fig. 1.5.3.9 – Point defect: Stone-Wales transformation [http://www.fis.unipr.it]

The defectivity of a CNT might derive from several factors.

We can differentiate defects caused by synthesis processing, electrical current flowing through the CNT and Ion implantation/electron irradiation.

The CNT structural defects have a very important role in the sensing properties. Experimental observations and theoretical calculations, in fact, show that several compounds can enter inside the tubes or in their defective sites, improving the transfer and store of electrochemical charging**.**

The defects affect the electron transport in nanotubes. Valentini et al. [143] achieved a CNTs film with PE-CVD technique. Exposing the film to $NO_2$ they observed that the CNT defects created during the growth, are responsible of a strong $NO_2$ absorption compared to defect-free CNTs. Due to the strong carbon-carbon bonding within CNTs, the interaction between the defect-free CNT walls and gas molecules was expected to be relatively weak and, consequently, the electronic transport properties of the nanotubes were insensitive to the exposure of CNTs to various molecules. In general, defect sites can give rise to stronger interactions with adsorbed molecules [144].

# CHAPTER 2

# Carbon-based devices

## 2.1. Introduction

With the reduction in power consumption and size chip, the electronic industry has been searching novel strategies to overcome these constraints with an optimal performance.

Carbon nanomaterials, due to their extremely desirable electrical and thermal properties, have been considered for their applicability in VLSI (Very Large Scale Integration) electronics.

In the case of carbon nanotubes the main applications in electronics are gas/biochemical sensors, data storage, RF applications, logic circuits and/or semiconductor materials [145].

As active part of electronic devices, the CNTs have been used to control their electrical properties. In this manner, carbon nanotubes can implement electronic devices such as diodes, transistors, Schottky rectifiers [146], supercapacitors [147], solar cells [148], organic light-emitting diodes and sensors.

Different strategies and topologies have been proposed with the aim of improving their performance. For example, transistors and Schottky rectifiers can be obtained by means of metallic-semiconducting junctions using CNTs-

metal interface [149]. Moreover, the high surface/volume ratio and the possibilities of functionalization makes CNTs ideal for sensing applications.

Today, also graphene and its derivatives, such as graphene oxide and graphene nanoribbons (GNRs) (strip made from graphene sheets with widths going from a few nanometers to tens of nanometers and lengths from nanometers to micrometers) are presented as attractive candidate for next-generation of integrated circuit applications due to their very interesting properties.

The size of GNRs allows the control of the band gap. In this way, the band gap can be changed in an electronic device generating a wide versatility of design [150].

The use of graphene as electronic material resides in the reduction of energy consumption, linear energy dispersion, carriers with zero mass, linear current-voltage characteristic, very low channel electrical resistance, mobilities and saturation velocities for a high current-carrying capability (6 orders higher than copper), low density of states, and the increase of frequency operation in ON/OFF switching [151]. Due to its nature structurally malleable, the electrical properties of the graphene can be favorably modified by mechanical strain and stress [152].

## 2.2. Carbon interconnects

In integrated circuits, all of the individual elements (transistors, diodes, capacity, etc...) are connected to each other through the metal interconnections. Usually, copper or aluminum are used but, with the need to increasingly reduce the scale of integration, these materials begin to give problems due to high power dissipation, electromigration, high RC delays that reduce the operation speed of ICs etc ... For this reason, research is looking to find an alternative to these materials.

CNTs and graphene can be used in integrated interconnects [153] (Fig. 2.2.1).

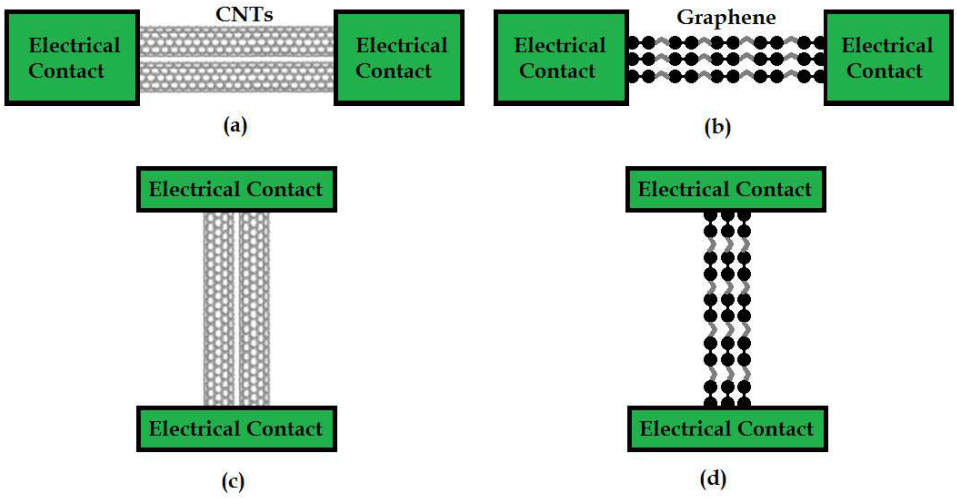


Fig. 2.2.1 - (a) electrical interconnects based on carbon nanotubes, (b) interconnects based on graphene, (c) vias based on carbon nanotubes, and (d) vias based on graphene [http://cdn.intechopen.com/pdfs-wm/26722.pdf]

Carbon nanotubes can be integrated into multilevel interconnects to meet emerging needs: delay, lifetime, parasitic resistance, inductive effects, bandwidth density, electromigration [154], energy efficiency, power dissipation, and lowering temperature of the interconnection. Additionally,

the use of carbon nanotubes makes possible the development of three-dimensional hyper-integration architectures.

For a perfect SWCNT, with perfect contacts, the best electrical resistance is about of 6.45 KΩ. This value is high to be used in interconnects, therefore, carbon nanotubes are placed in parallel in large numbers (a bundle) with the aim of reducing the total electrical resistance. A CNTs bundle is generally a mixture CNTs, both SWCNTs and MWCNTs.

CNTs bundle gives the possibility to produce ICs interconnections and also via (vertical interconnect access) at the local level for VLSI circuits. A via is an electrical connection between layers in an integrated electronic circuit that goes through the plane of one or more adjacent layers.

Within integrated circuit, usually the capacities and inductances are made by using the interconnections. For example, to make an inductor, just implement the spiral-shaped paths. For this reason, the length to diameter ratio of the CNT interconnects have significant implications for the design of on-chip capacitors and inductors [155].

Due to the very high frequencies used to carry signals in the integrated circuits, the ballistic transport presented by carbon nanotubes and graphene allow us to design advanced interconnect networks.

Tube-tube junctions involve physical contact, with small structural deformation, between two tubes and these are not chemically bonded. This type of junction is found in interconnections between ropes, MWCNTs, and crossed-over tubes [156]. The electrical transport is realized by means of tunneling transport between tubes, producing an alteration in electrical transport of the individual tubes involved in the junction, due to the weak electrical coupling.

Graphene presents a higher conductance respect to Cu for interconnects in the range of nanometers. Among the properties exploited of the graphene for

interconnects are: high carrier mobility at room temperature, thermal conductivity, higher mechanical strength, reduced capacitance coupling between adjacent wires, width-dependent transport gap, temperature coefficient, and ballistic transport. When line widths of the graphene nanoribbons are reduced below 8 nm, the resistivity of GNRs is insignificant. The use of CNT and graphene in interconnects extends the life of high performance for silicon-based integrated circuit technology. In fact, these materials allow us to cool heat flux, to remove hot-spots, and to spread lateral heat [157]. For this reason, the mechanical and thermal properties of CNTs and graphene must be taking into account in the design of interconnects.

## 2.3. Carbon nanotubes-based devices

Since CNTs were discovered and studied, research went straight forward creating different types of electronic devices for both the digital and analog electronics and even in the sensors filed. Regarding the digital and analog electronics, in literature there are many topologies of electronic devices based on CNTs but, in general, can be grouped together in the category of **Carbon nanotubes-based FET** (field-effect transistor). CNTFET is a transistor in which the active channel is formed by one or many CNTs. There are different topologies of CNTFET and they will be discussed in the next paragraphs. As for the field of sensors, instead, in addition to CNTFET (often called in this case **chemFET**), are also popular **Carbon nanotubes-based resistors (also called MOX, Metal Oxide Resistor)**, **CNT-based SAW resonators** and the **CNT-based QCM devices**.

### 2.3.1. CNTFET and state of the art in electronics applications

In general, a CNTFET is a device with three terminal in which the nanomaterial is deposited between two electrodes on a substrate typically used as a third electrodes (back-gated topology, see later). In this way, the current through the nanomaterial can be modulate by the electrical field applied with the gate electrode. If there is not the third electrode, i.e. the substrate is not conductive or simply it leads to zero potential, we obtain a **Carbon nanotubes-based resistor**, because the device is a resistor with the equivalent resistance of the CNTs. Usually, CNTFET refers to a field-effect transistor that utilizes a single carbon nanotube or an array of carbon

nanotubes as the channel material instead of bulk silicon in the traditional JFET or MOSFET structure. To understand the CNTFET working the operation of the most common MOSFETs will be recalled briefly.

## MOSFET

The MOSFET (Metal Oxide Semiconductor Field Effect Transistor) is a device generally accessible through four terminals, called "bulk", "drain", "gate" and "source". In Fig. 2.3.1.1 an N - channel MOSFET (Enhancement) structure is shown.

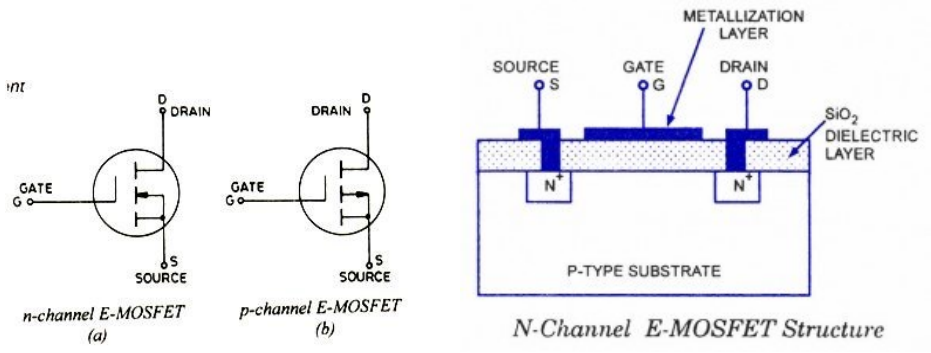


Fig. 2.3.1.1 - Enhancement MOSFET: N-channel and P-channel symbol (left)[http://www.transtutors.com], N-channel E-MOSFET section view (right) [http://www.circuitstoday.com]

In the MOSFET, the channel conductivity modulation is performed through the control of **metal-oxide-semiconductor** interface. This last makes negligible the current absorbed by the gate terminal. Initially, between source and drain there are two pn junctions inversely polarized. In this situation, the channel conductivity is very limited. Acting on the gate terminal is possible to cause the inversion of population into the channel (strong inversion), a situation in which the channel conductivity can be very high and generally associated to the on state device.

Therefore, the MOSFET operation depends on the gate voltage. Considering an N - channel MOSFET in common-source configuration, the output characteristics are the following (Fig. 2.3.1.2):

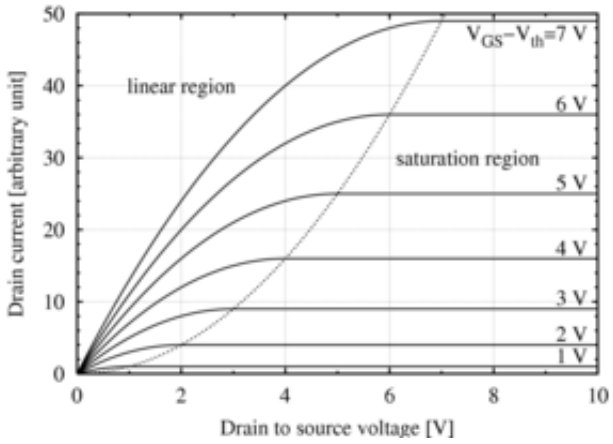


Fig. 2.3.1.2 - Output characteristic: IV curves of an N - channel MOSFET common source [http://upload.wikimedia.org/wikipedia]

## CNTFET

CNTFET first demonstrated in 1998 by Dekker group. [158]. According to Moore's law, the dimensions of individual devices in an integrated circuit have been decreased by a factor of approximately two every two years. This scaling down of devices has been the driving force in technological advances since late 20th century. However, as noted by ITRS 2009 edition, further scaling down has faced serious limits related to fabrication technology and device performances as the critical dimension shrunk down to sub-22 nm range. The limits involve electron tunneling through short channels and thin insulator films, the associated leakage currents, passive power dissipation, short channel effects, and variations in device structure and doping. These limits can be overcome to some extent and facilitate further scaling down of

device dimensions by modifying the channel material in the traditional bulk MOSFET structure with a single carbon nanotube or an array of carbon nanotubes.

Different electrode configurations (geometry and position of the electrodes) can be chosen for a CNTFET, depending on the application. In general, there are four topologies of CNTFET: **Back-gated** CNTFET**, top-gated** CNTFET**, wrap-around gate** CNTFET **and suspended** CNTFET**.**

- **Back-gated CNTFET**

The earliest techniques for fabricating carbon nanotube field-effect transistors involved pre-patterning parallel strips of metal across a silicon dioxide substrate, and then depositing the CNTs on top in a random pattern [158].

The semiconducting CNTs that happened to fall across two metal strips meet all the requirements necessary for a rudimentary field-effect transistor. One metal strip is the "source" contact while the other is the "drain" contact. The silicon oxide substrate can be used as a gate contact (if the substrate is doped) adding a metal contact on the back of the substrate (Fig. 2.3.1.3).

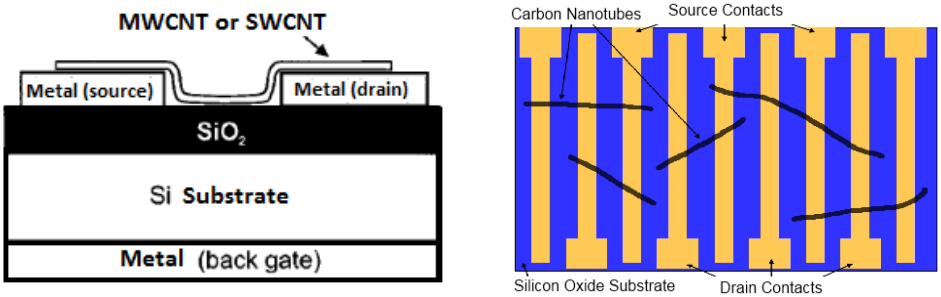


Fig. 2.3.1.3 - Back-gated CNTFET- Side view (left), Top view (right) [www.wikipedia.org]

This structure suffered from several drawbacks. The first was the metal contact, which actually had very little contact to the CNT, since the nanotube just lay on top of it and the contact area was therefore very small.

Also, due to the semiconducting nature of the CNT, a Schottkey Barrier forms at the metal-semiconductor interface [159], increasing the contact resistance. CNT - metal interface was investigated and high work function metals such as Palladium or Platinum were found to provide Ohmic contacts to p-type CNTs in ambient conditions [160].

The second drawback was due to the back-gate device geometry. Its thickness made it difficult to switch the devices ON and OFF using low voltages, and the fabrication process led to poor contact between the gate dielectric and CNT [161]. However, recently ultra-thin high-κ gate dielectrics have been produced, such as $ZrO_2$ and $HfO_2$, obtaining a better coupling with the gate in small channel devices [162].

One of the main advantages of the back-gated devices is to be able to use these devices as sensors, because the CNTs that form the channel are exposed to the environment.

- **Top-gated CNTFET**

Eventually, researchers migrated from the back-gate approach to a more advanced top-gate fabrication process [161]. In the first step, single-walled carbon nanotubes are solution deposited onto a silicon oxide substrate.

Individual nanotubes are then located via atomic force microscope (AFM) or scanning electron microscope (SEM). After an individual tube

is isolated, source and drain contacts are defined and patterned using high resolution electron beam lithography. A high temperature anneal step reduces the contact resistance by improving adhesion between the contacts and CNT. A thin top-gate dielectric is then deposited on top of the nanotube, either via evaporation or atomic layer deposition. Finally, the top gate contact is deposited on the gate dielectric, completing the process (Fig. 2.3.1.4).

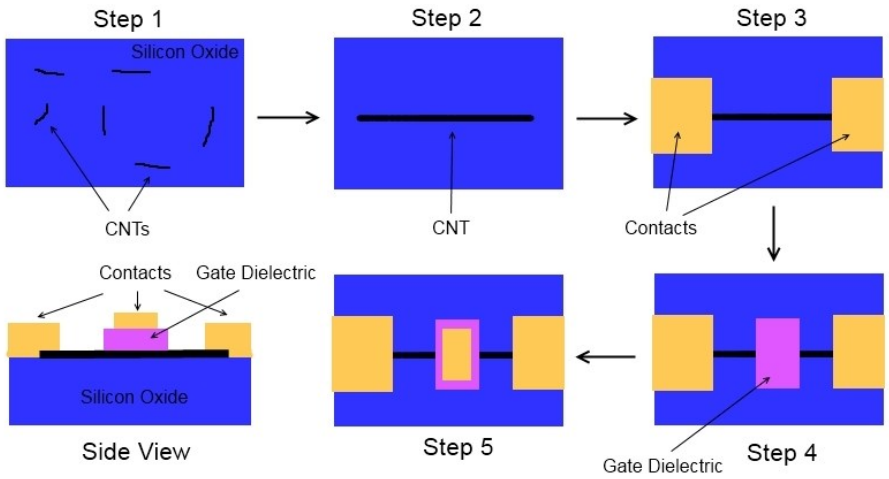


Fig. 2.3.1.4 - The process for fabricating a top-gated CNTFET [http://en.wikipedia.org]

Arrays of top-gated CNTFETs can be fabricated on the same wafer, since the gate contacts are electrically isolated from each other, unlike in the back-gated case. Moreover, due to the thinness of the gate dielectric, a larger electric field can be generated respect to the nanotube using a lower gate voltage.

These advantages mean top-gated devices are generally preferred over back-gated CNTFET, despite their more complex fabrication process. However, there are many problem to use top-gated devices as a gas/bio-sensors because the CNTs which constitutes the channel are covered by the gate contact. Indeed, today there are some applications in the field of biosensors that use this topology. In particular, a solution (usually PBS or

water) with inside the analyte is pipetted on the active channel and subsequently, an electrode is placed in contact with the drop operates as gate electrode [163]

- **Wrap-around gate CNTFET**

Wrap-around gate CNTFETs, also known as gate-all-around CNTFETs were developed in 2008 [164] and are a further improvement upon the top-gate device geometry. In this device, instead of gating just the part of the CNT that is closer to the metal gate contact, the entire circumference of the nanotube is gated (Fig. 2.3.1.5).

This should ideally improve the electrical performance of the CNTFET, reducing leakage current and improving the device on/off ratio.

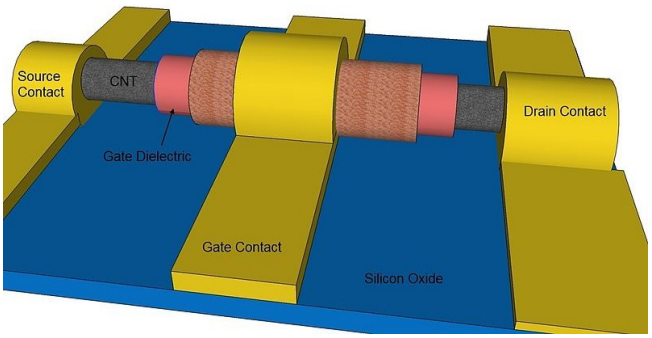


Fig. 2.3.1.5 - Wrap-around gate CNTFET [http://en.wikipedia.org]

Device fabrication begins by first wrapping CNTs in a gate dielectric and gate contact via atomic layer deposition [165].

These wrapped nanotubes are then solution-deposited on an insulating substrate, where the wrappings are partially etched off, exposing the ends of the nanotube. The source, drain, and gate contacts are then deposited onto the CNT ends and the metallic outer gate wrapping.

- **Suspended CNTFET**

Yet another CNTFET device geometry involves suspending the nanotube over a trench to reduce contact with the substrate and gate oxide (Fig. 2.3.1.6) [166]. This technique has the advantage of reduced scattering at the CNT-substrate interface, improving device performance. There are many methods used to fabricate suspended CNTFETs, ranging from growing them over trenches using catalyst particles [166], transferring them onto a substrate and then under-etching the dielectric beneath [167], and transfer-printing onto a trenched substrate [168].

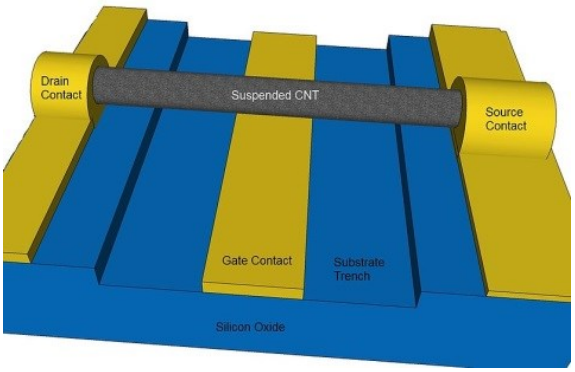


Fig. 2.3.1.6 - A suspended CNTFET device [http://en.wikipedia.org]

The main problem suffered by suspended CNTFETs is that they have very limited material options for use as a gate dielectric (generally air or vacuum), and applying a gate bias has the effect of pulling the nanotube closer to the gate, which places an upper limit on how much the nanotube can be gated. This technique will also only work for shorter nanotubes, as longer tubes will flex in the middle and droop towards the gate, possibly making touching the metal contact and shorting the device. In general, suspended CNTFETs can be useful for studying the intrinsic properties of clean nanotubes.

Due to the CNTs properties, CNTFETs show high mobility, high ON/OFF ratios ($10^4$ – $10^6$) and low OFF-currents, very useful properties in digital electronics.

Four electrical transport behavior can be found in CNTFET, and differ from one another on according to the length of the nanotube, compared with their mean free path, and by the type of contact between the nanotubes and the source/drain electrodes:

- **ohmic-contact ballistic**, when charge injection by the source and drain contacts is performed into the carbon nanotubes and vice versa, producing a high drain-source current;
- **ohmic-contact diffusive**, when in the charge transport happens scattering between source/drain and carbon nanotubes, limiting the drain-source current;
- **Schottky-barrier ballistic**, when the gate voltage controls the potential barrier and the drain-source voltage can reduce the barrier producing bidirectional high drain-source current (in ON-state, electrons tunneling from the source while in OFF-state the holes tunneling form the drain);
- **Schottky-barrier diffusive**, when the combination of gate and drain voltages reduces the Schottky barrier and in the charge transport happens scattering producing a reduced drain-source current [169].

Two important parameters to consider in CNTFET are the **transconductance (gm)** and **sub-threshold swing**. Transconductance indicates how drain-source current ($I_{DS}$) changes respect the gate voltage ($V_G$) when the drain-source voltage ($V_{DS}$) is constant, while sub-threshold swing indicates the change needed in gate voltage for a change in drain-source current of an order of magnitude. High gm and a low sub-threshold swing are needed for high-speed digital electronics.

Usually, CNTFET has an **ambipolar** behaviour, in which there is an injection, from the source and drain, of either electrons or holes, or of both carriers simultaneously. Consequently, there is an inversion of the charge carriers sign in function of the applied gate voltage sign (electrons for positive $V_G$ and holes for negative $V_G$). Accordingly, the $V_G$-$I_{DS}$ characteristic of a CNTFET is ambipolar, i.e. changes the sign according to the gate voltage (Fig. 2.3.1.7). For this reason, the height of the Schottky barrier, between CNT and source/drain, becomes a critical factor. In fact, to obtain a unipolar behavior, as in the standard MOSFET, can be change the metals of the electrodes in order to obtain Schottky barriers more high for a type of carrier or using two different gate, one to control the height of the barriers and the other to control the type of conduction.

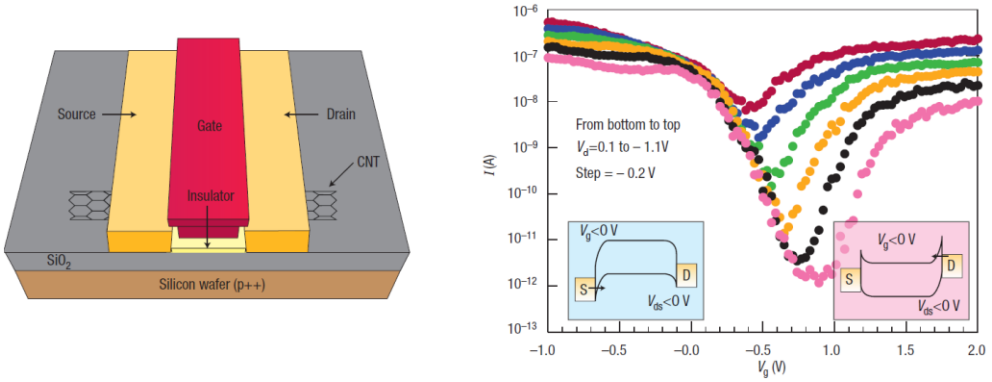


Fig. 2.3.1.7 – (left) a schematic of a typical structure of CNTFET top gate, (right) ambipolar transfer characteristics (current versus gate voltage) of a top gate FET in figure. In the inset the schematization of the band structure: under negative gate bias (letf) the holes are injected from the source (S) while under positive gate bias (right) electrons are injected from the drain (D) [Ph. Avouris et al. Nature Nanotech. 2, 605 - 615 (2007)]

## CNTFET disadvantages

- **Lifetime (degradation)**

The carbon nanotubes degrades in a few days when exposed to oxygen. To solve this issues different polymers can be used to passivate the CNTs, improving the lifetime [170].

- **Reliability**

Carbon nanotubes have shown reliability issues when operated under high electric field or temperature gradients. Avalanche breakdown occurs in semiconducting CNT and joule breakdown in metallic CNT. Unlike avalanche behavior in silicon, avalanche in CNTs is negligibly temperature-dependent. Applying high voltages beyond avalanche point results in Joule heating and eventual breakdown in CNTs [171]. This reliability issue has been studied, and it is noticed that the multi-channeled structure can improve the reliability of the CNTFET. The multi-channeled CNTFETs can keep a stable performance after several months, while the single-channeled CNTFETs are usually out of work after a few weeks in the ambient atmosphere [172]. The multi-channeled CNTFETs keep operating when some channels break down, this won't happen in the single-channeled ones.

- **Difficulties in mass production, production cost**

Although CNTs have unique properties such as stiffness, strength, and tenacity compared to other materials especially to silicon, single

CNTFETs have not yet advanced into commercial technology mainly due to the not heterogeneity performance, mass production in a controlled way and high production cost. To overcome the fabrication difficulties, several methods have been studied such as direct growth, solution dropping, deposition by electrophoresis technique and various transfer printing techniques [173].

### 2.3.1.1. CNTFET in CMOS technology

CMOS (complementary-MOS) inverter (NOT logic gate) consist of pairs of p-type and n-type transistors connected in order to obtain a digital circuit that invert the input signal from bit 0 to bit 1 and vice versa. This behaviour is obtained since the transistors simultaneously change their operating status. In this system, the power dissipation is very low because there is a current flow only at the instant of transition from the OFF state to ON state and vice versa. CMOS inverter is the main circuit of the digital electronics and several studies have been performed in order to use the CNTFETs to achieve it.

Usually, CNTFETs have p-type electrical transport while, achieve n-type doping in CNTs is a little more complicated. Early demonstrations of logic gates, such as inverters and NOR gates, was achieved making a n-type CNTs by using a low work function metal electrode such as Al [174] or by doping with Potassium [175]. In this last case, a single nanotube bundle was positioned over two gold electrodes to produce two p-type CNTFETs in series. The device was covered by PMMA and a window was opened by e-beam lithography to expose part of the nanotube. Potassium was then evaporated through this window to produce an n-CNTFET, while the other CNTFET remains p-type (Fig. 2.3.1.1.1).

Ambipolar CNTFETs can also been used in logic gates. However, the threshold voltages for the n-type and p-type side must be precisely controlled by using different work function gate electrodes.

The difficulty to control the threshold voltage has led to investigate other architectures. For example, pass-transistor logic was recently used to produce carbon-based digital electronics, such as digital adders production, using six CNTFET [176].

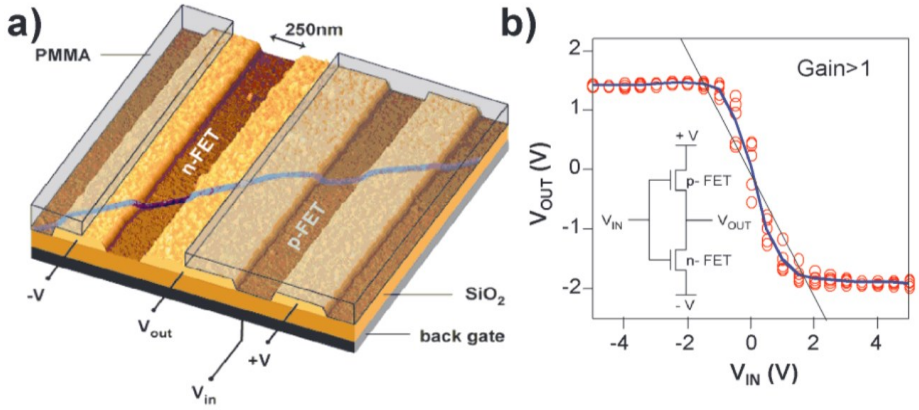


Fig. 2.3.1.1.1 - a) Image of the CNT-based inverter. (b) IN/OUT voltage characteristics: data for five different measurements on the same device (red), average of these five measurements (blu) [V. Derycke et al.,Nano Lett.,Vol. 1, No. 9,2001].

## 2.3.1.2. CNTFET – TFT (Thin-Film Transistors)

A **thin-film transistor** (**TFT**) is a kind of FET produced by depositing a thin films of an active semiconductor, a dielectric layer and metallic contacts on a non-conductive substrate. (Fig. 2.3.1.2.1). Typically, the substrate is glass, because the first application of TFTs was in liquid-crystal displays (LCD). TFTs differs from the conventional transistor, where the semiconductor material typically is the substrate, such as a silicon wafer.

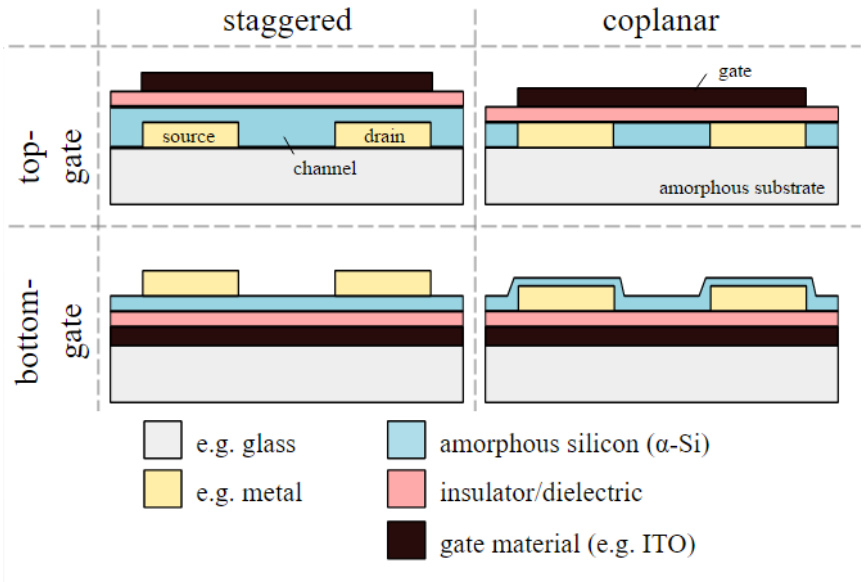


Fig. 2.3.1.2.1 – Typical structure of TFT [Wikipedia.org]

In recent years, portable consumer electronics has motivated researchers to develop semiconductor materials that can be incorporated in flexible electronics. For this reason, today are developing various technologies to produce TFTs on plastic and flexible substrates. TFT based on amorphous Si and several organic and inorganic semiconductors are already used in electronic devices, sensors, and flexible displays [177].

Of course, also the CNTs can be used as semiconducting layer in a TFT. In particular, CNT-based TFTs (Fig 2.3.1.2.2a) have shown similar field-effect mobility than most of the organic and inorganic semiconductors used for these applications [177]. In addition, CNTs have attractive mechanical and optical properties useful for flexible and transparent electronics. In the early studies of CNTTFTs, as-grown CNT networks on oxide gate dielectrics with a back-gate geometry were produced [178]. This device has a field-effect mobility of 270 $cm^2/Vs$ and ON/OFF ratio of $10^4$. Several studies and applications have followed. Wang et. al., developed a very interesting CNTTFT on flexible substrates (polyimide) used for digital and analog application (Fig 2.3.1.2.2) [179]. The TFT exhibits highly uniform device performance with on-current of 15μA/μm, transconductance up to 4μS/μm and mobility around 50 $cm^2/Vs$. [179].

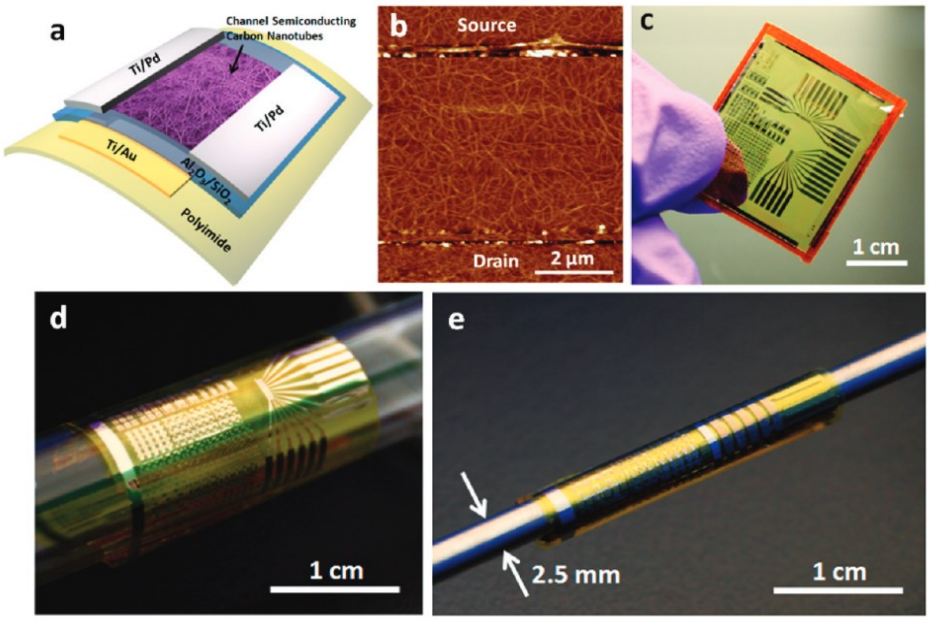


Fig. 2.3.1.2.2 (a) Schematic diagram of the CNTTFT on a flexible substrate. (b) AFM image showing the CNTs networks. (c) Flexible nanotube circuit with a size of 2.5 × 3$cm^2$, (d,e) Photos showing the bendability of the circuits produced, where the samples are being rolled onto a tube with a diameter of 10 mm (d), and a metal rod with a diameter of 2.5 mm (e) [179].

In CNTTFTs, charge transport was found to be dominated by percolation effects as confirmed by simulations and experiments. Moreover, the channel resistance changes with channel length (Fig. 2.3.1.2.3 a,b) [180,181].

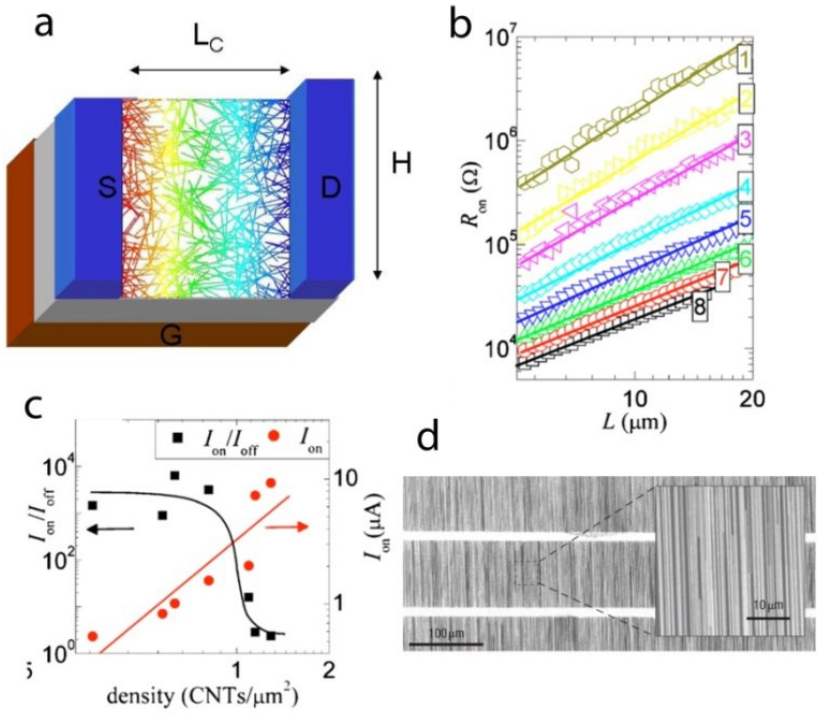


Fig. 2.3.1.2.3 - a) Schematic of a CNTTFT with a percolating network of CNTs. The color variation from drain to source shows the simulated electrostatic potential with percolation theory [180], b) Variation of the channel resistance with the channel length ($L$) for CNT density increasing from top (1) to bottom (8) [181], c) trade-off between on/off ratio and on-current as a function of CNT density [181] d) aligned CNTs grown by CVD [184].

The field-effect mobility of CNTTFTs (usually < 300 cm$^2$/Vs) is significantly less than that for a single CNT (> 10,000 cm$^2$/Vs) mainly for the following reasons.

First, the equivalent capacitance of the CNT network affect the mobility then the single CNT but the main motivation is the CNT-CNT contact resistance

in the CNT network [182]. The contact between a metallic CNT and a semiconducting CNT is approximately 1000 times more resistive than two metallic or two semiconducting CNTs [182].

In the CNTs, there is a trade-off between ON-state current (and thus field-effect mobility) and ON/OFF ratio (Fig. 2.3.1.2.3 c) due to increase the percolation of metallic CNTs in thicker films [181]

In the fabrication of CNTFET, it is important to control the CNT position or of the CNTs film. Therefore, in addition to as-grown random CNT networks, also aligned CNTs can be used in TFTs.

There are several way to align the CNTs, directly grown or deposited subsequently. In the second case, dielectrophoresis is the most common technique used for align CNT deposition. This technique will be described in detail later.

Regarding the directly grown, aligned CNTs have been grown by CVD on miscut quartz substrates [183-185] (Fig. 2.3.1.2.3 d). Subsequently, printing methods have also been developed to transfer aligned CNT arrays on plastic substrates [183].

Ref. [184] show that aligned CNT films improves the currents and the mobility, while the ON/OFF ratio can be altered due to the presence of metallic CNTs. To solve this problem, several studies have been done, including selective removal of metallic CNTs.

For example, metallic CNTs from random CNT thin films can be selectively etched by methane plasma etching [186].

A successful method for sorting CNTs is centrifugal sorting in density gradients. This method, named **density gradient ultracentrifugation (DGU)**, allows the separation by diameter and/or electronic type by varying the surfactant concentration [187].

### 2.3.2. CNT-based device and state of the art in sensing applications

The CNTs electrical properties are extremely sensitive to the mechanisms of charge transfer and to structural changes caused by external agents. For example, in presence of molecules characterized by a tendency to accept (e.g. $NO_2$) or donate (e.g. $NH_3$) electrons, the interaction with the nanotubes leads to a change in the carrier concentration on the CNT walls with a consequent conductivity modulation.This property, together with the high surface/volume ratio and the possibility of functionalization, has led to the use of carbon nanotubes for the sensors production. Generally, sensors have the following properties:

- **Sensitivity**: indicates how much the device appears sensitive to the presence or to the action of the analyte. This feature depends on how much a sensor property (typically resistance or capacitance) is affected by the presence of a target;
- **Selectivity**: the sensor response will be influenced by the presence of different molecules types. The selectivity is the sensor ability to reject the "noise" and provide a measure exclusively linked to the target;
- **Dynamic response**: characterized by the reaction time (time interval after which the system response is complete or partially complete according to the definition) and the recovery time (time required for the device to return to the response basis line);
- **Stability:** the sensor response does not changes over the time.
- **Reversibility**: is the sensor ability to return to its default state (pre-exposure), after a specified time.

The sensors based on pristine CNTs (i.e. non-functionalized) are often characterized by low sensitivity and selectivity, high recovery times and

irreversibility. The functionalization processes, which allow to suitably modify the CNTs structure, can lead to overcome some limitations, increasing both the sensitivity and the selectivity, and thus improve the sensor performance.

In the case of CNTs chemical sensors (usually gas and biosensor), there are many configurations, such as the **CNT resistor**, **SAW** (Surface Acoustic Wave) resonator devices, **QCM** (Quartz Cristal Microbalance) and the most common **CNTFET**.

## 2.3.2.1. CNT-based resistor

As described above, usually the CNTs-based devices are FET structure but, if the gate is connected to the ground potential, the device is named simply CNT-resistor.

In a chemical CNT-resistor (Fig 2.3.2.1.1) a single CNT or a CNTs network connect the two electrodes. The bond created between the analyte and the CNTs surface alters the electrical characteristics of the CNT-resistor, due to a resistance variation. Generally, a heater can be positioned on the sensor backside and it allows to heat the sensor at the desired working temperature.

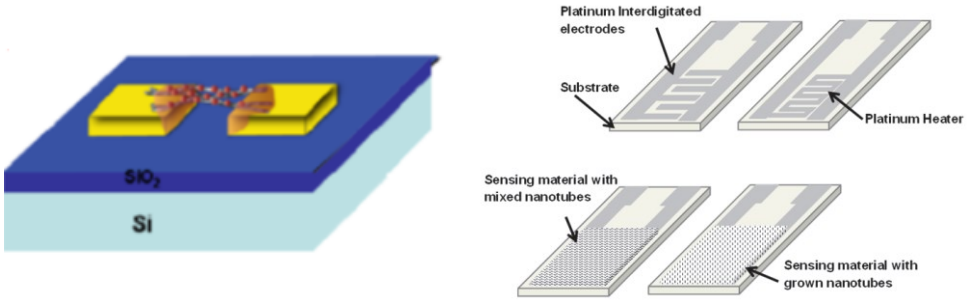


Fig. 2.3.2.1.1 - Planar structure of chemoresistive sensor with top side coated thick/thin film and heater on the backside [Donato N. et al., "Novel Carbon Nanotubes-Based Hybrid Composites for Sensing Applications " (2011)]

Most of this type of sensors use films based on metal oxides such as $SnO_2$, ZnO (**Metal Oxide Semiconductor device, MOX**) or conducting polymers. In the first type of sensors, power supply is generally required to heat the sensitive layer deposited on the interdigitated contacts to an operating temperature from 200° C to 1000° C, through the back heater. The conducting polymers, instead, operate at lower temperatures but their life time is limited. In general, the sensing material should lead a good trade-off between sensor performance and power consumption (lower operating temperatures).

The use of CNTs can improve the performance of this kind of devices. In particular, thanks to their above-mentioned properties, it is possible to increase the sensitivity and selectivity to a specific analyte also working at room temperature. There are several works in the literature related to these devices. For example, Hoël Guerinet et al. reported a gas sensing resistor fabricated by direct integration of horizontal CNT arrays between metal electrodes through a directional and selective catalytic CVD growth process activated in-situ [188]. Hoël Guerinet measured that upon exposure to $H_2$, but also for other gases such as $NH_3$, toluene or ethanol, the CNT resistors responses are drastically influenced by the CNT metal-interface. Changing the materials used for the electrodes (Pt, Pd), they have detected up to 10 ppm of toluene and ethanol at room temperature.

Since the CNTs greatly increase the performance of these devices, it is possible to eliminate the back heater by operating the device at room temperature.

Anyway the back heater, could also be useful to release easily the analyte after being captured. This may increase the repeatability of the measurement. However, the heating can drastically reduce the average life time of CNTs.

## 2.3.2.2. CNT-based SAW resonators

**SAW (Surface Acoustic Wave) resonator** are a class of micro-devices in which a surface acoustic wave can be modulated by physical phenomenon. The acoustic wave spreads on the surface of piezoelectric crystal, in which the stresses and strains of the wave are coupled to electric fields. The basic surface acoustic wave device consists of a piezoelectric substrate, an input interdigitated transducer (IDT) on one side of the surface of the substrate, and a second, output interdigitated transducer on the other side of the substrate. The space between the IDTs, across which the surface acoustic wave will propagate, is known as the delay-line. This region is called the delay line because the signal, which is a mechanical wave at this point, moves much slower than its electromagnetic form, thus causing an appreciable delay.

Due to the piezoelectric effect, the sensor transduces an electrical signal applied in the input IDT into a mechanical wave that, unlike an electrical signal, can be easily influenced by physical phenomena. This influenced wave is detected by the second IDT and changes in amplitude, phase, frequency, or time-delay, between the input and output electrical signals, can be correlated with the external influence (Fig. 2.3.2.2.1).

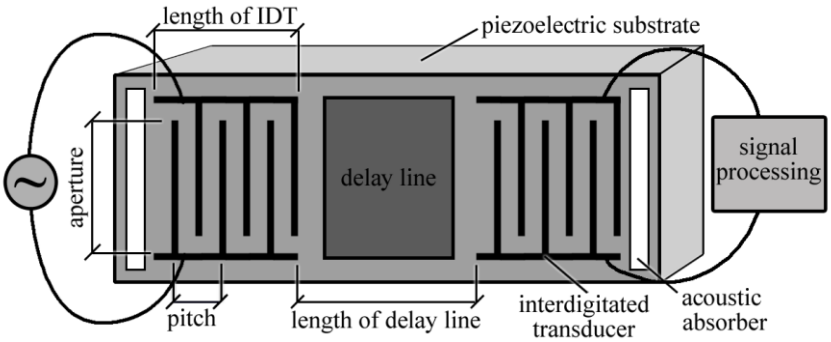


Fig. 2.3.2.2.1 – Schematization of SAW device [Wikipedia.org]

Of course, the delay-line region can be functionalized in order to detect a specific target. In fact, any change in the piezoelectric crystal results in a change of wave properties. For example, in the literature there are many works on CNT-based SAW devices for the detection of **Volatile Organic Compounds (VOC),** such as ethanol, methanol, acetone, m-xylene, toluene and ethylacetate. In ref [189], a SAW device with MWCNTs films was produced, detecting up to 10 ppm of ethanol, 40 ppm of methanol and 150ppm of acetone.

### 2.3.2.3. CNT-based QCM devices

**QCM (Quartz Crystal Micro-balance)** is a resonant device that uses the piezoelectric effect of a quartz crystal to generate an electrical signal at a well-defined frequency. Usually it is formed by a quartz crystal with two electrodes attached to the sides of the crystal (Fig. 2.3.2.3.1).

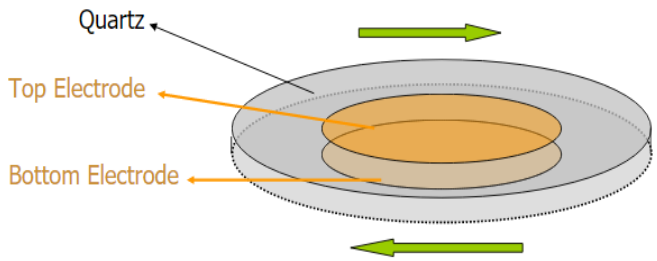


Addition of mass on the surface of the resonator causes changes in its resonance frequency.

Sauerbrey Equation $\Delta f = -\left(2f_0^2 / A\sqrt{\rho_q \mu_q}\right)\Delta m$

Fig. 2.3.2.3.1. – QCM device schematization and the Sauerbrey equation to link the shift in frequency with the mass change on a surface [http://slideplayer.com/slide/8256440/]

When the device is connected to an appropriate electrical circuit, in the output of this circuit a sinusoidal signal is generated with the same oscillation frequency of the crystal quartz. If one or both quartz sides are influenced by any particle the resonance frequency changes according to the **Sauerbrey** law (see Fig. 2.3.2.3.1). Through this law is thus possible to associate the mass variation on the device surface to the oscillation frequency variation (from which the name microbalance). Obviously it is possible to functionalize the sides of the crystal (usually with organic films on the electrodes) in order to detect a particular target.

QCM devices can be functionalized with CNTs in order to improve the features. As shown before, the **VOC** sensing applications are much investigated. In ref [190] a QCM gas sensor coated with carbon nanotubes CNTs layered films was produced in order to detect ethanol, methanol, acetone, m-xylene, toluene and ethylacetate in a wide range of concentration from 10 to 800 ppm. In particular, the sensor exhibit high sensitivity (5.55 Hz/ppm to m-xylene) at room temperature, fast response, linearity, reversibility, repeatability, low drift of the baseline frequency, and potential sub-ppm range detection limit.

## 2.3.2.4. CNTFET as gas sensor: ChemFET

Typically, the **chemFET** is a back-gated CNTFET. The presence of the third electrode (gate) allows the conductivity modulation and usually is used to improve the sensitive.

The study of gas adsorption on CNTs is currently at the centre of an intense experimental and theoretical activity since the adsorption of gas on carbon nanotubes modifies sensibly their electronic properties.

One of the earliest reports of gas sensors based on single CNTFETs was performed by Kong et al. in 2000 [191]. Kong et al. produced a back-gated device using a single SWCNT (10.0), showing that the electrical conductivity of the SWCNT changes under gas exposure, such as $NO_2$ and $NH_3$. According to Kong et al., the CNTs conductance increases during exposure to $NO_2$ while decreases with $NH_3$.The sensitivity (defined as ratio of resistance before and after gas exposure) changes from 100 to 1000 with response times of a few seconds to one minute. A shift in the transfer characteristic is shown in Fig. 2.3.2.4.1 under gas exposure.

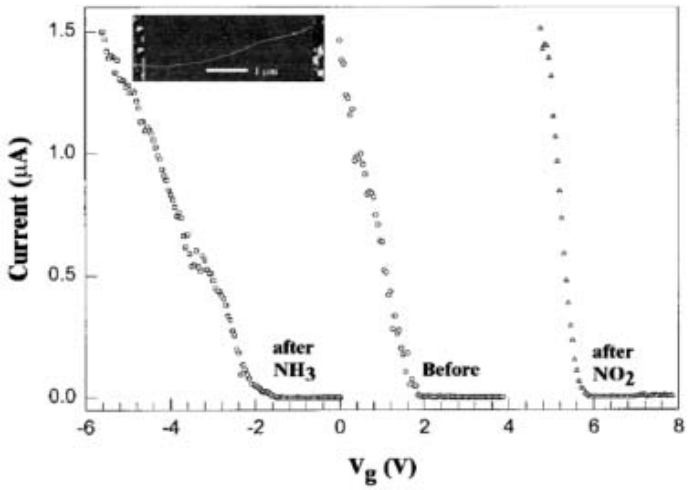


Fig. 2.3.2.4.1 - Transfer characteristics of a single semiconducting SWCNT FET (AFM image in inset) before and after exposure to $NH_3$ and $NO_2$ [191]

These results showed that single CNT devices outperformed commercially available metal oxide or conducting polymer sensors [192]. It is possible to explain this sensing behavior because $NO_2$ is an electro-attractor and thus increases the holes concentration while $NH_3$ is a Lewis base, with an electron pair that can be donated. However, the theory show that there is no interaction between pure CNT and $NH_3$. Probably the interaction occurs with other agents adsorbed by CNT (e.g. $O_2$) (Fig. 2.3.2.4.2).

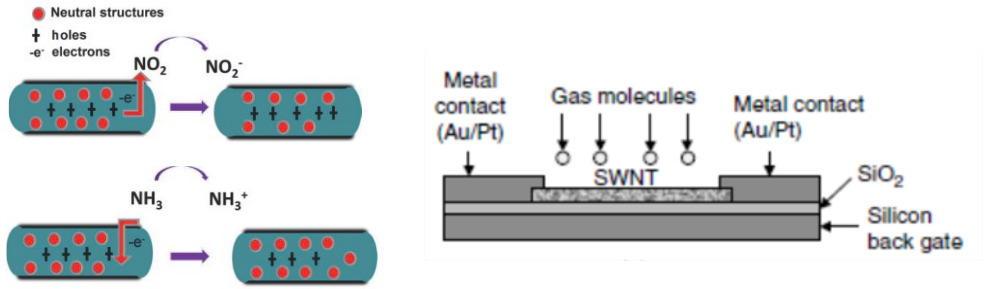


Fig. 2.3.2.4.2 – Back-gated CNTFET (left), Gas sensing mechanism operating on p-type CNT semiconductors with $NO_2$ and $NH_3$ gas (right) [Donato N. et al., "Novel Carbon Nanotubes-Based Hybrid Composites for Sensing Applications " (2011)]

As described in the first chapter, the CNTs purification with chemical methods (the most used) induces the attachment of –COOH, -OH groups on the CNTs surface (Fig. 2.3.2.4.3).

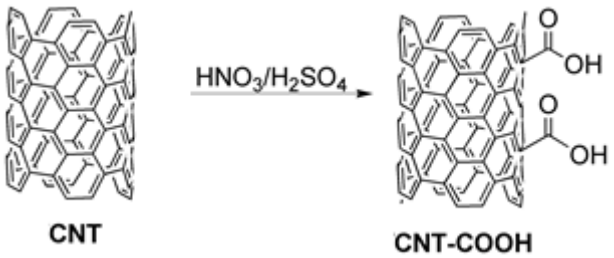


Fig. 2.3.2.4.3. – Purification example with –OH group birth

The presence of -COOH groups enhances the interaction between the CNTs and the $NH_3$ molecules, by formation of hydrogen bonds from polar $NH_3$ molecules with oxygen-containing groups on the CNT.

The adsorption of $NH_3$ on the nanotube surface donates electrons to the valence band, decreasing the number of holes, thereby increasing the separation between the Fermi level and valence band. It forms a space charge region at the surface of p-type semiconducting CNT, increasing the electrical resistance (Fig 2.3.2.4.4).

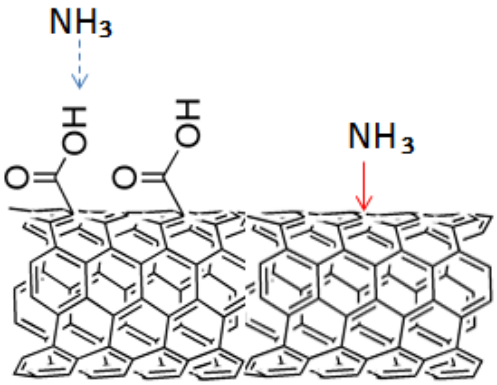


Fig. 2.3.2.4.4 – Interaction between $NH_3$ and -OH group

One of the major issues with CNTs for sensing applications is the difficulty to handle them. CNTs tend to aggregate in bundles through strong attractive interactions (due to the nanostructured nature), which are very difficult to disrupt. As grown, pristine CNTs have highly hydrophobic surfaces and are not soluble in water or any common solvents. Introduction of functional groups on the surface of CNTs (for example through purification with chemical methods) may promote their solubility and facilitate their study and use [193]. In particular, the functional groups make the CNTs electrically charged and thus an electrostatic repulsion is obtained.

In order to understand the sensing mechanism, other analytes was studied, such as alcohols [194], oxygen [195], and hydrogen [196]. Regarding the

sensing mechanism, some research groups showed that, beyond the already described mechanisms, semiconducting CNTs can act as Schottky barrier transistors. In particular, the barrier between the source/drain electrodes and nanotubes can be tuned by the metal work function. The latter can be modulated by local dipoles induced by adsorbed gas molecules and thus threshold voltage and polarity of CNTFETs correspondingly change as a function of the adsorbed gas molecules [197]. Instead, in the metal CNTs, chemically induced Schottky barrier produces a lower variation in resistivity and thus reduced sensitivity. In this case, to obtain high sensitivity, a stronger chemical interaction (covalent interaction) is needed. For example, Collins et al. developed a functionalization where a controlled density of defects was created on a CNT (metallic or semiconducting) via an electrochemical redox reaction [198]. Therefore, a specific functionalization of various chemical species can be obtained through defect sites. In another approach, the selectivity can be improved using polymers around the CNTs. For example, polyethyleneimine (PEI)-coated CNTFETs are selectively sensitive to $NO_2$, while Nafion-coated devices are selective towards $NH_3$ [199]. However, recently it developed a new method to increase the selectivity using semiconducting SWCNTs encapsulated with single-stranded DNA (ss-DNA) as shown in Fig. 2.3.2.4.5. The DNA sequences were chosen to have specific binding with methanol, propionic acid, trimethylamine (TMA), dinitrotoluene (DNT), and dimethyl methylphosphonate (DMMP) [200]. The ss-DNA functionalized CNT devices showed a current modulation as high as 30% versus 0-1% in bare control CNT devices at the same exposure dose [200, 201]. Different studies for hydrogen detection have been carried out. In particular, studies focused on arrays of semiconductor CNT (sorted via selective dispersion and DGU) devices, showing that CNTs with diameter

distributions near 1.4 nm have a good sensitivity to hydrogen (Fig. 2.3.2.4.6) [202].

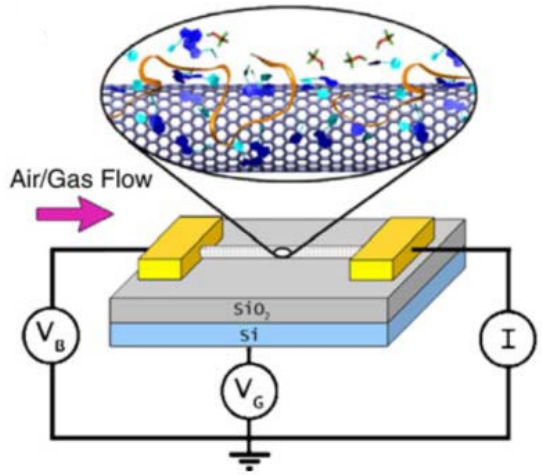


Fig. 2.3.2.4.5. - Schematic of a single CNTFET non-covalently functionalized with ss-DNA molecules for selective detection of nerve agents such as DMMP [200]

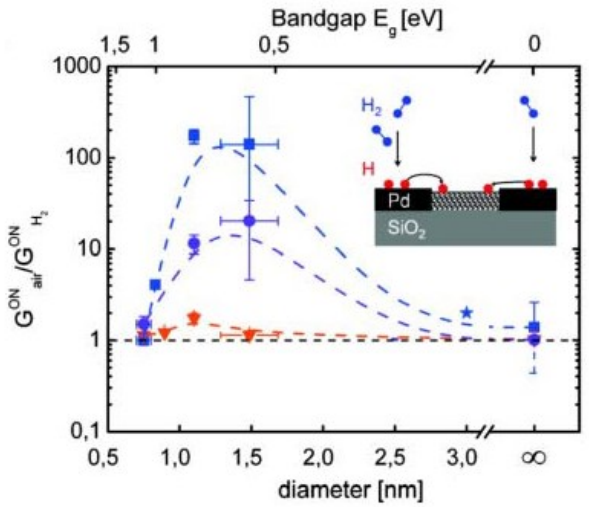


Fig. 2.3.2.4.6. – Sensitivity of CNTFET devices vs SWCNT diameter d and electronic band gap. The conductance in air and in 100 ppm $H_2$ in Ar has been measured. Three types of CNTFETs have been investigated: SWCNT/Pd FETs on Si/SiO2 (blue squares), SWCNT/Au FETs on Si/SiO2 (red triangles), and SWCNT/Pd FETs on Parylene-C coated Si/SiO2 (purple circles). The dashed lines are guides to the eye, indicating an optimum sensitivity at d≈1-1.5 nm. The inset shows the device under investigation and illustrates the formation of atomic hydrogen on the Pd surface, its diffusion and the chemisorption on SWNTs [202]

## 2.3.2.5. CNT-based devices in biosensing applications

The development of CNT-based biosensors has allowed to explore new range of sensitivity that with the standard methods of analysis cannot be obtained. For example, several cancer biomarkers indicate the presence of the disease when their concentration in blood is very low, in the order of picograms / millilitres. These levels of sensitivity can be achieved thanks to the interesting properties of CNT integrated in the new biosensor systems.

CNT-biosensors have been developed to detect a wide variety of cancer biomarkers through conjugation or complexation of DNA or aptamers, antibodies, proteins, or enzymes [203,204].

Depending on the sensing mechanism, biosensors can be subdivided in **electrochemical CNT-biosensors**, **immunosensors**, and **optical CNT-based biosensors**.

In the following we recall some definitions of biological species that will be used in the discussion below.

**Amino acid:**

The amino acids are molecules composed of an amino functional group (amine) (-$NH_2$) and a carboxylic acid functional group (carboxylic acid) (-COOH).

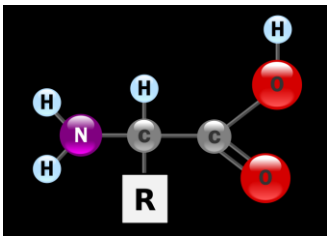


**Protein:**

Proteins are macromolecules consisting of chains of amino acids linked together by a peptide bond (i.e. a bond between the amino group of an amino acid and the carboxyl group of the other amino acid, via loss of a water molecule). Proteins perform many functions in living organisms, including

the catalysis of metabolic reactions, DNA replication, response to stimuli and the transport of molecules from one place to another. The proteins differ from each other mainly in their amino acid sequence, which depends on the nucleotide sequence conserved in the genes and which usually results in a protein folding into a specific three-dimensional structure that determines its activity.

**Nucleic acids:**

Nucleic acids are macromolecules storing and transporting genetic information. They are linear polymeric macromolecules formed by a series of nucleotides. The latter are formed by a sugar, a nitrogenous base and some phosphate groups. The nucleic acids are produced starting from nucleotides for dehydration.

**Aptamers**:

Aptamers are nucleic acids having the property to bind to a molecule or a protein.

**Enzyme**:

An enzyme is a catalyst of biological processes. The majority of enzymes are proteins. A small minority of enzymes are of particular RNA molecules.

The catalysis process induced by an enzyme (as from any other catalyst) consists of an increase of the rate of reaction and then in a more rapid achievement of the state of thermodynamic equilibrium.

**Antibodies**:

An antibody is a protein with a peculiar quaternary structure that gives it a shape of a "Y". The antibodies have the function, in the context of the

immune system, to neutralize foreign bodies such as viruses and bacteria, recognizing each antigen as a target. This is because at the end of the arms of the "Y" there is a structure able to "close" the segments of the body to recognize. Each clasp has a different key, consists of the original antigenic determinant. When the "key" (the antigen) is inserted, the antibody is activated. The production of antibodies is the main function of the humoral immune system.

## Electrochemical and Electronic CNT Biosensors

Typically, most of biosensors are electrochemical, due to their low-cost, fast response times and small size.

The mechanism of transduction can be amperometric, potentiometric, conductometric, voltametric and piezoelectric. Potentiometric biosensors measure the oxido-reduction potential of an electrochemical reaction that produce or absorb hydrogen ions, causing a change in pH, measureable as an electrical signal at the surface of a pH-meter probe. Amperometric biosensors measure a current due to a voltage applied between two electrodes. In this way it can detect electro-active species present in the biological samples that change this current.

Piezo-electric biosensors have the resonance frequency proportional to the mass of adsorbed material on itself (see QCM paragraph).

Enzyme-coupled electrochemical biosensors are based on enzymatic catalysis of a reaction that produces electro-active species and then a measurable electric signal. Generally, these biosensors are formed by a reference electrode, a working electrode and a counter electrode. The target is detected by enzymes immobilized on the working electrode. The catalytic activity

cause an electron transfer producing a measurable current or voltage. (Fig. 2.3.2.5.1 a).

Enzymes show excellent selectivity for their target and have high catalytic activity. In order to improve the sensing performances, CNTs, thanks to their interesting properties, can be used in these applications.

Several electrochemical CNT-based biosensors have been developed to detect ions or protein biomarkers [205]. For example, CNT-glucose biosensor based on conjugation of glucose oxidase have been produced [206, 207].

Patolsky et al. showed alignment of glucose oxidase (GOx) on electrodes using SWCNTs as electrical connectors between the enzyme redox centers and the electrode (Fig. 2.3.2.5.1.b) [207].

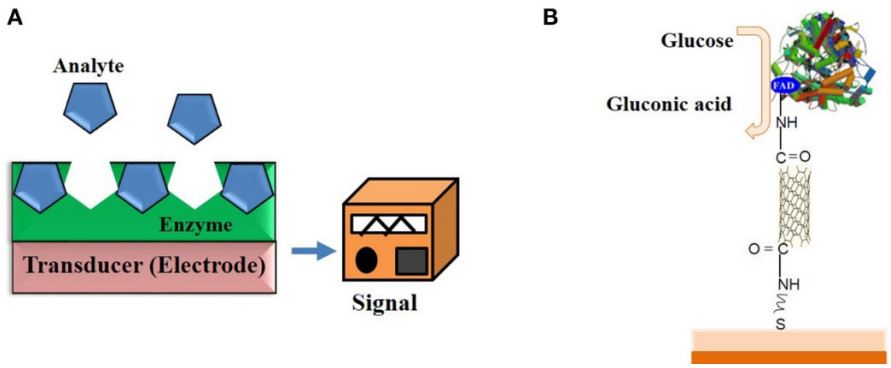


Fig. 2.3.2.5.1 – a) Typical design of an enzyme-based electrochemical biosensor. b) SWCNT electrically-contacted glucose oxidase electrode [Carmen-Mihaela Tîlmaciu 2015, doi: 10.3389/fchem.2015.00059]

Electrochemical biosensors based on functionalized CNTs were also used for detection of nitric oxide [208], and dopamine monitoring in rat striatum [209].

Regarding amperometric CNT-based biosensors, Fei et al. carried out detection of cysteine on Pt/CNT electrodes by cyclic voltammetry [210].

Moreover, array of CNTs-electrodes coated with anti-PSA (prostate specific antigen) antibodies were used to detect PSA [211] (Fig. 2.3.2.5.2).

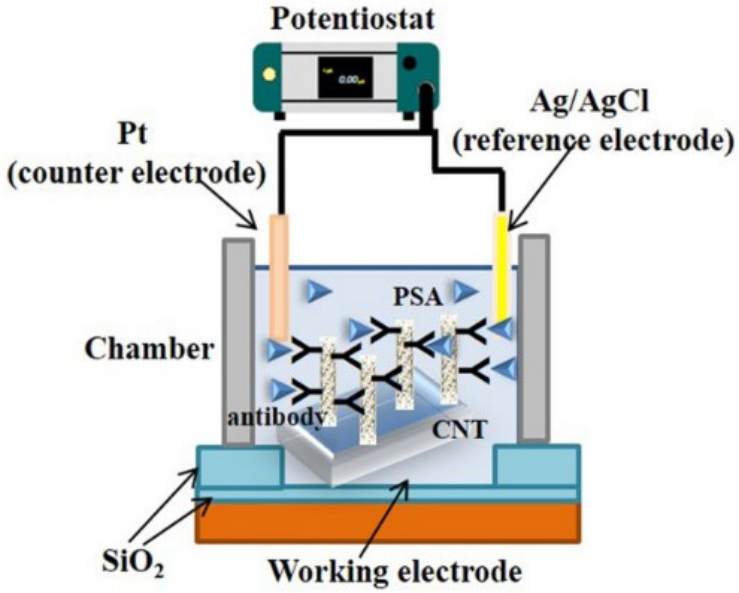


Fig. 2.3.2.5.2 - Schematic illustration of an amperometric biosensor for PSA detection [Carmen-Mihaela Tîlmaciu 2015, doi: 10.3389/fchem.2015.00059]

## 2.3.2.6. CNT-based immunosensors

Immunosensors are compact analytical biosensors that yield measurable signals in response to specific antibody–antigen interactions. A large number of immunosensors have been developed using different sensing mechanism such as changes in mass, heat, electrochemical interactions, or optical properties [212]. In particular, electrical detection technique has several advantages such as simple and fast measurements, which enables miniaturized and inexpensive biosensors [213,214]. Typically, electrical immunosensor consists in a substrate in which the electrical conductivity changes after the antibody–antigen interaction (Fig. 2.3.2.6.1).

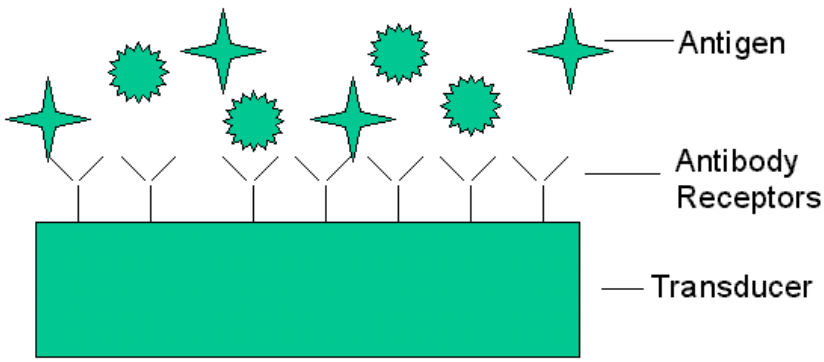


Fig. 2.3.2.6.1 – A scheme of electrical immunosensor [http://www.tms.org/pubs/journals/JOM/0010/Kumar/Kumar-0010.html].

Electrical immunosensors are a relatively modern technology and there are few works in the literature. Among the electrical immunosensors we can distinguish those based on functionalization of electrodes and those based on nanostructured materials (also functionalized) such as carbon nanotubes.

The reagents used in immunoassays (see Appendix) such as antibodies, enzymes, and fluorescence labels are very expensive. Therefore, the miniaturization of the diagnostic systems without affecting their properties is

highly desired. The use of carbon nanotubes (CNTs) can improve the sensitivity in the electrical immunosensors [215]. In fact, the electrical/structural properties of CNTs make them very promising for developing ultrasensitive and miniaturized immunosensors. The typical structure of a CNT-based immunosensor is shown in Fig. 2.3.2.6.2. The need of using the BSA (bovine serum albumin) and a functionalization to bind the antibodies to nanotubes will be explained in the following paragraphs.

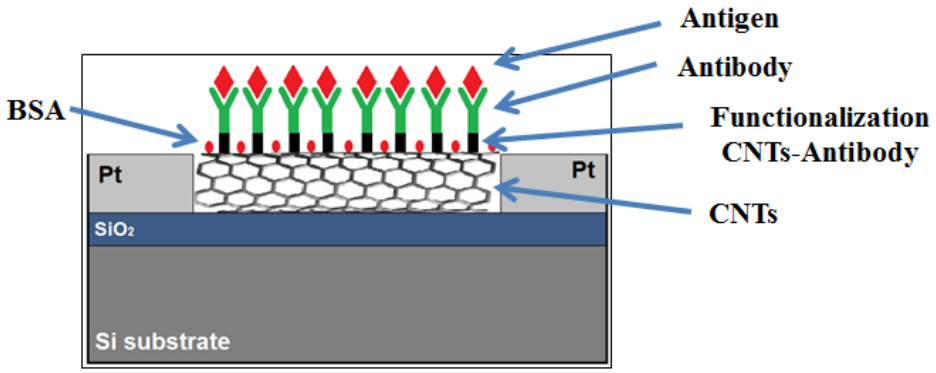


Fig. 2.3.2.6.2 – Schematization of CNT-based immunosensor.

It is very important to underline that this type of devices are **label-free**, i.e. the antibodies or the antigens are not bound to markers (labels), because the sensing is associated with the electric type variations induced by the bonds between the proteins and the nanotubes.

As mentioned above, CNTs cannot be directly used to detect biomolecules but it is always necessary an appropriate functionalization in order to obtain a specific interaction. In order to produce a CNT-based immunosensor, is necessary to introduce a molecular recognition function in the CNTs so that they can specifically recognize and detect biomolecules from biological samples. Several approach have been studied in this sense. The basic idea for CNT functionalization is to attach the antibodies or the antigens, on the

surface of the CNTs. In general there are three possible ways: (1) the first approach is to grow CNTs directly on a substrate and subsequently bind the antibody; (2) in the second case, instead, the CNTs are deposited on the substrate according to various techniques such as DGU and dielectrophoresis and then the antibody is bound to the CNT; (3) the last approach is to induce the CNT-antibody binding interaction directly in solution and subsequently deposit the functionalized nanotubes on the substrate.

In the last two cases, the lack of solubility of the CNTs in solutions is one of the main difficulties. To overcome this problem, several studies have been performed [216,217].

One way is to make CNTs from hydrophobic to hydrophilic for example by oxidation treatments [218]. However, this covalent method changes the electrical conductivity of the nanotubes. For this reason, in order to maintain the electronic properties ($sp^2$ nanotube structure), a non-covalent method is usually preferred. In this case, a common approach to increase the CNT solubility in solution is to use detergents or surfactant such as sodium dodecyl sulfate (SDS) and Triton-X 100 [219]. Another method of solubilization is an ultrasonication of CNTs in the presence of phosphotungstic acid [220].

**CNT-antibody interaction**

Regardless of how the CNTs are prepared, it is interesting to understand the interaction between the antibodies and the nanotubes.

In fact, the major challenge in the immunosensors production is to attach antibodies or antigens to the CNTs. This can be performed by using either covalent or noncovalent methods.

**Non-covalent Attachment of the Antibodies to the CNTs.**

Several studies revealed that enzymes and other proteins can adsorb spontaneously on the sidewalls of acid-oxidized CNTs [221,222].
For example, O'Connor et al. [223] reported a method of antibody adsorption on SWCNTs deposited on a graphite disk electrode. At pH 7.2, anti-biotin antibody was incubated on SWCNT surface for 3 h, followed by washing in PBS to remove the excess. With a concentration of 0.5 mg/mL of antibody, the nanotube surface was completely covered.
The relative size of the antibody respect to the CNT have an important role in the adsorption mechanism. For example, the size of immunoglobulins (7-8 nm, human IgG, 150 kDa) compared to the diameter of SWCNTs (1-10 nm) can create problems for the complete adsorption on the nanotube [224]. Also another protein such as ferritin was found not to be able to directly adsorb on the SWCNT [225]. It is clear that several investigations have yet to be done in this direction, especially regarding the spontaneous interaction between proteins and CNTs. Although the non-covalent absorption is less invasive on the CNT surface, it is clear that the CNT-antibody interaction is not very effective respect the covalent interaction. Moreover, a spontaneous adsorption of protein can be a problem in the case of immunosensors because can degrade the specificity of the sensors.

**Covalent Antibodies-CNTs interaction**

As mentioned above, non-covalent absorption on CNTs can be a problem for nonspecific binding between proteins and CNTs. To solve this issue, it is necessary to create a covalent antibodies-CNTs interaction and avoid non-specific adsorption of the antigens with the nanotubes. In fact, the interaction

must be the only CNT-antibody and then antibody-antigen. Several techniques have been developed in this direction. One way is to bind antibodies to CNTs after attaching them with some functional groups [226]. For example, a carboxylic acid group can be added to either sidewall or the tips of the CNTs by acid oxidization. Subsequently, these groups can be activated using 1-ethyl-3-(3-dimethylaminopropyl) carbodiimide hydrochloride (EDC) as a coupling agent [227]. The EDC treatment leads to the formation of a highly reactive and unstable acylurea derivative. It then forms a more stable active ester in the presence of *N*-hydroxysuccinimide (NHS). As a result, the antibody can be linked to the CNT through a nucleophilic substitution reaction between the active ester and the amine group of the antibody, forming an amide bond. In Fig. 2.3.2.6.3 a schematization of this reaction in the case of insulin detection is shown.

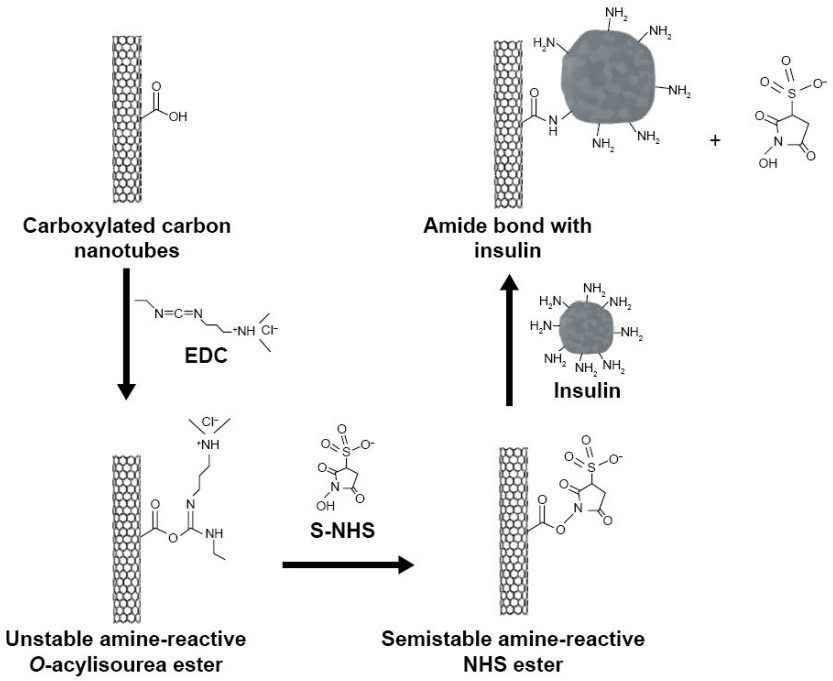


Fig. 2.3.2.6.3 – Functionalization of CNTs through EDC and NHS in order to link the antibodies to the nanotubes [https://dx.doi.org/10.2147/IJN.S98726].

**CNT-antibody binding through streptavidin-biotin interaction**

Another strategy to bind the antibodies on the CNTs is to exploit the streptavidin-biotin interaction. Streptavidin is a protein (52.8 KDa) with a very high affinity for biotin. This last (also known as vitamin B7 or vitamin H) is a small molecule that can be conjugated to many proteins without losing or altering the activity. Streptavidin-biotin biological interaction is the strongest non-covalent binding known.

The methods to link the antibodies on the CNTs, that exploits the streptavidin-biotin interaction, involves in tying the streptavidin on the surface of functionalized nanotubes by the EDC coupling chemistry, followed by the addition of biotinylated antibodies (i.e. antibodies linked with the biotin) [228]. The strong specificity of streptavidin-biotin interaction leads to the immobilization of antibodies on the CNT surface, without affecting the properties of the antibody to capture the antigen. Sun's group used this strategy to produce immunosensor for *E. coli* detection [229]

**Nonspecific Binding of Proteins to CNTs: issues and solutions**

Usually, in the biological samples there are numerous types of proteins and other molecules. One of the problems in development of biosensors is the non-specific binding of undesired molecules from the biological sample.

The non-specific binding is due to the spontaneous adsorption of the proteins in the CNTs surface. To get rid of this problem, several surfactants such as poly ethylene oxide (PEO) and poly ethylene glycol (PEG) have been tested [230, 231]. PEO and PEG are biocompatible polymers well-known for their protein-repelling properties. They act forming a highly hydrophilic and neutrally charged layer at the surface. For example, Shim et al. [232] found

that the adsorption of Triton (surfactant with hydrophilic poly ethylene chain) and PEG on SWCNTs is highly effective in preventing nonspecific adsorption of streptavidin to nanotubes.

Another method to prevent the non-specific binding is to use of BSA (bovine serum albumin), a common blocking agent used in ELISA tests [222, 223]. In the case of NHS covalent bind between CNTs and antibodies, BSA can be used to block the NHS sites where are not bound the antibodies. In this way, the following antigens will bind only with the respective antibodies, avoiding non-specific binding with the CNTs.

## 2.4. Graphene-based devices

With the introduction of graphene as active material for electronic devices, new field-effect transistors were introduced, called **Graphene (G) FETs**. As illustrated for the carbon nanotubes, also in this case there are four types of GFETs: **back-gated GFETs**, **top-gated GFETs**, **wrap around gate GFETs** and **suspended GFETs**. Back-gated GFETs present large parasitic capacitances and poor gate control. However, when smooth edges of the graphene nanoribbons are achieved, ON/OFF ratios as high as $10^6$ are obtained, which is attractive for digital applications (see later). Moreover, this structure can be used as a sensor, because the graphene (that form the channel) is exposed to the environment. Top-gated GFETs are the preferred option for analogical practical applications. In wrap-around gate GFETs, the gate can act on the entire rectangle of the graphene nanoribbon, improving the ON/OFF ratio. However, wrap-around gate and suspend gate GFETs are today still under study, due to technological production issues.

## 2.4.1. Graphene-FET and state of the art in electronics applications

The electrical properties of graphene make it very useful for digital electronics. The high mobility allows faster switching circuits, while the low contact resistance of graphene, in contrast to CNTs, allows high conductance devices production. However, the lack of a band gap (and then low ON/OFF ratio) compromises the development of graphene-based digital electronics, in which an ON/OFF ratio of at least $10^4$ is necessary.
In all the possible bias condition, graphene shows a minimum conductivity of 4 $e^2/h$ and thus it cannot be turned off completely. Therefore, in order to use the graphene in digital electronics are needed methods to obtain a band gap in graphene. Usually, a band gap can be obtained through quantum confinement, chemical treatment and using bilayer graphene structure.

- **Band gap through quantum confinement**

  A band gap can be obtained through quantum confinement in narrow **graphene nanoribbons (GNRs)** (strip of graphene sheets with widths of few nanometers and lengths of few micrometers) (Fig. 2.4.1.1 a) [233]. In particular, the confinement-induced band gap is inversely proportional to the GNR width and depends on the type of GNR edge (i.e., zig-zag or armchair) [234, 235]
  Using chemical exfoliation of graphene, X. Li et al. produced sub-10 nm GNR, achieving a GNRFETs with an ON/OFF ratio up to $10^6$ and mobility of 100-200 $cm^2/Vs$ (Fig. 2.4.1.1b) [236].

- **Band gap through chemical treatment**

One way to obtain a band gap in graphene is to treat it with chemical agent. For example, as already described in the first chapter, is possible to obtain a band gap in graphene oxide, which can be more or less changed according to the quantity and type of functional groups. Another method to "dope" the graphene is to use hydrogen, obtaining a material that is called "**graphane**" [237]. In this case, a band gap of 3.5eV was obtained. In another case, fluorinated graphene (fluorographene) was produced obtaining, through reaction with xenon difluoride, a band gap of 3 eV [238].

- **Band gap in bilayer graphene (BLG)**

**Bilayer graphene (BLG)** consists of Bernal stacking of two graphene layers where half of the carbon atoms in one layer align with carbon atoms in other layer, and the other half of the atoms occupy the centers of the hexagons (Fig. 2.4.1.1c) [239]. As the graphene, intrinsic BLG don't have band gap and the valence and conductance bands touch each other at the K point (Fig. 2.4.1.1.a) [240]. However, if a vertically electric field is applied, a change in the bands is shown, obtaining a finite gap (Fig. 2.4.1.1a,c,d) [239, 241, 242]. Using this technique, a band gap of more than 100 meV was observed (Fig. 2.4.1.1d) [239].

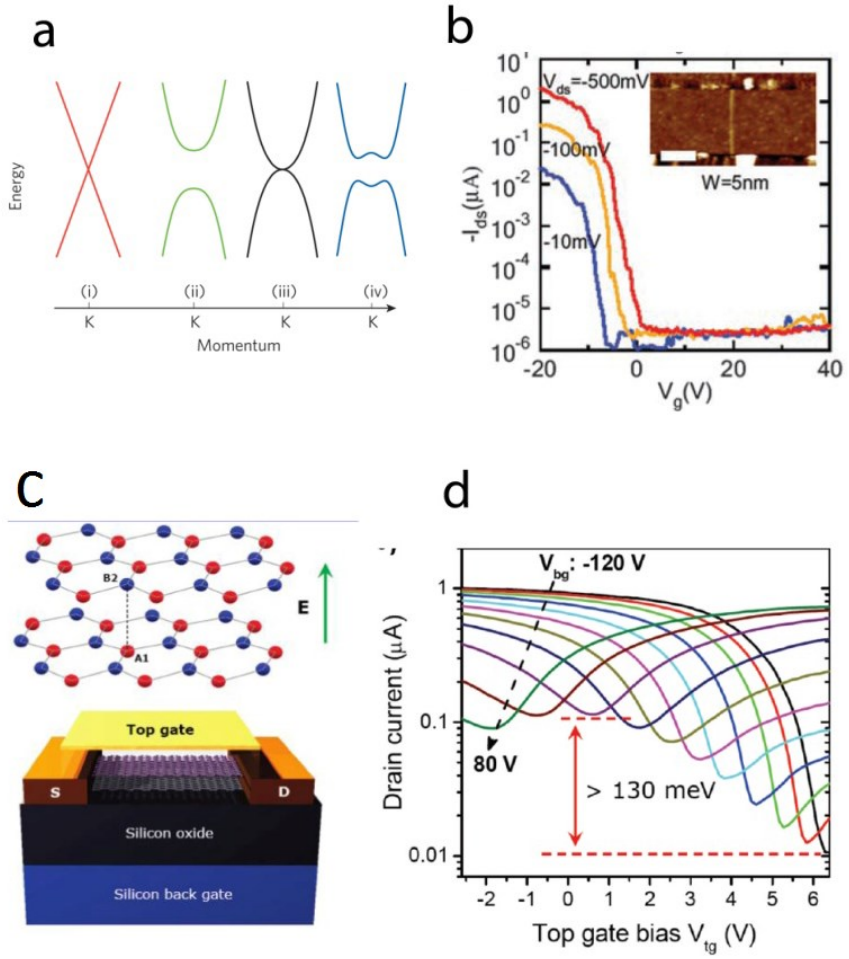


Fig. 2.4.1.1 - a) Band dispersion around the K point for single layer graphene (i), graphene nanoribbon (GNR) (ii), unbiased bilayer graphene (BLG) (iii), and BLG with vertically applied electric field (iv) [233], b) Transfer characteristics of a GNRFET for different drain voltage. Inset: AFM image of the GNRFET (scale bar = 100 nm) [236], c) Lattice structure of BLG with Bernal stacking and schematic of a BLGFET with a top gate to enable the application of a vertical electric field to induce a band gap [http://www.slideshare.net/Askalany/graphene-field-effect-transistor], d) Transfer characteristics of a BLGFET (drain current versus top-gate bias, VTG) for different back-gate biases (VBG). Highest on/off ratio (100) is obtained for the largest displacement field (VBG = -120 V, VTG = 6V) [239].

In addition to a band gap, n-type and p-type GFET are needed for CMOS-based graphene digital electronics. GFETs are intrinsically ambipolar but,

unlike CNTs, graphene doping cannot be controlled by varying the work function of the contact metal. In one approach, it is possible to use charged species to move the charge neutrality point to gate bias, but the transfer characteristics remain ambipolar [242-244]. In contrast, chemical modification of graphene with boron and nitrogen could dope graphene n-type and p-type, respectively [245] but it was found that boron and nitrogen tend to segregate to form domains of hexagonal boron nitride within the graphene lattice, reducing the mobilities [246]. For these reasons, several issues remain to be investigated in order to use graphene for CMOS-based digital electronics.

## 2.4.2. Graphene-FET and state of the art in sensing applications

As with the nanotubes, graphene is also sensitive to the surrounding environment, changing its electrical response.

Graphene is an attractive material for gas/bio sensors production. It has a large surface area (2630 $m^2/g$) and all atoms of one graphene sheet can be considered surface atoms that are capable of adsorbing gas molecules [247]. As a result, a small amount of adsorbed molecules change the local carrier concentration in graphene, which is the cause of a change in the resistance [248,249]. As expected, there are different types of graphene devices for sensing applications, but the most common structures are the GFETs. As mentioned in the first chapter, graphene oxide (GO) or reduced graphene oxide (rGO) are often used instead of the pristine graphene. This happens because the graphene with the functional groups is more reactive to the surrounding environment. Furthermore, the synthesis of GO and RGO is less expensive. For these reasons, in many works on sensing, GO and rGO are used.

### GFET for gas sensing application

Several studies for the detection of $NH_3$, $NO_2$, $H_2$, CO, $CO_2$, and VOC have been performed.

For example, Yumeng Liu et al., produced an ammonia GFET sensor on a flexible plastic substrate [250]. In this work, organic materials, including gate dielectric (170nm-thick parylene C layer), channel dopant (PEI), and substrate (40μm-thick polyimide) are used to produce the flexible GFETs.

Experimental sensing measurements show fast adsorption/desorption process of ammonia purged at room temperature under various gas concentrations (Fig. 2.4.2.1)

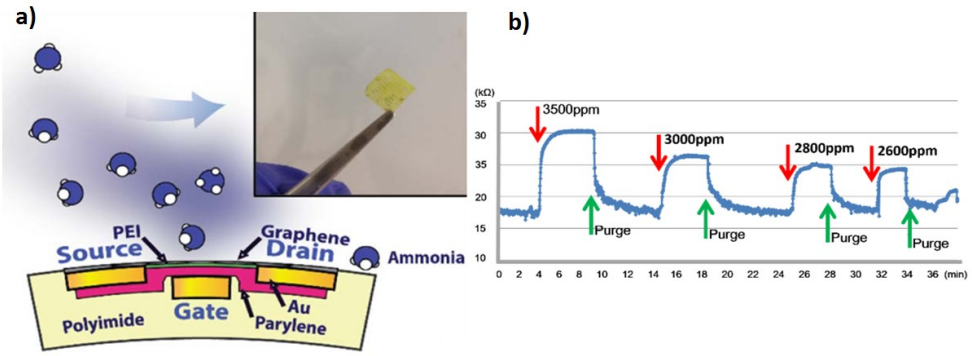


Fig. 2.4.2.1 – a) schematization of the graphene-based device with 170nm-thick parylene and 70nm-thick PEI as gate dielectrics and channel dopant, respectively. Inset shows an array of graphene gas sensors on a flexible polyimide substrate, b) response of a flexible graphene gas sensor under various concentrations of ammonia. The chamber is purged with nitrogen in every cycle [250]

## Graphene Oxide in sensing application

As mentioned several times, the graphene oxide is an excellent choice for sensing applications due to the presence of functional groups. Only in recent years we have seen the first GO-based sensors, for example for the detection of ammonia or hydrogen. One of the key points in the development of these sensors is certainly the cost. For this reason, most of the sensors are composed of a substrate (often plastic to reduce cost) with two electrodes on which GO can be deposited by cheap methods, such as dielectrophoresis. For example, Wang et al. have developed a silicon device with gold electrodes where a GO film was deposited via dielectrophoresis for the detection of hydrogen at room temperature. They have found a good sensing response of

5%, fast response time (<90 s), and fast recovery time (<60 s) for 100 ppm hydrogen gas concentration at room temperature (Fig. 2.4.2.2) [251].

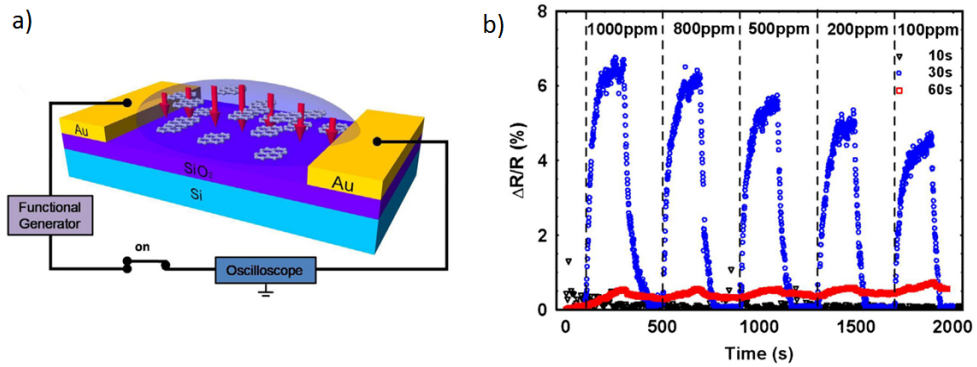


Fig. 2.4.2.2 - Schematic representation of the device and the setup used for the DEP of GO nanostructures in a microgap of a Au electrode during DEP, b) Hydrogen gas sensing response of the GO sensors fabricated by DEP at 500 kHz and 10 V, using various DEP processing times of 10, 30, and 60 s. [251]

Devices based on GO and rGO were also manufactured and used as humidity and temperature sensors. For example, Sun et al., developed a silicon device with two silver electrodes in which GO was deposited using the layer by layer technique (LBL) electrostatic self-assembly. In this work, the authors show how the electrical characteristics of the GO depend on temperature and humidity according to the degree of reduction of the GO, and then the amount and type of functional groups (Fig. 2.4.2.3) [252].

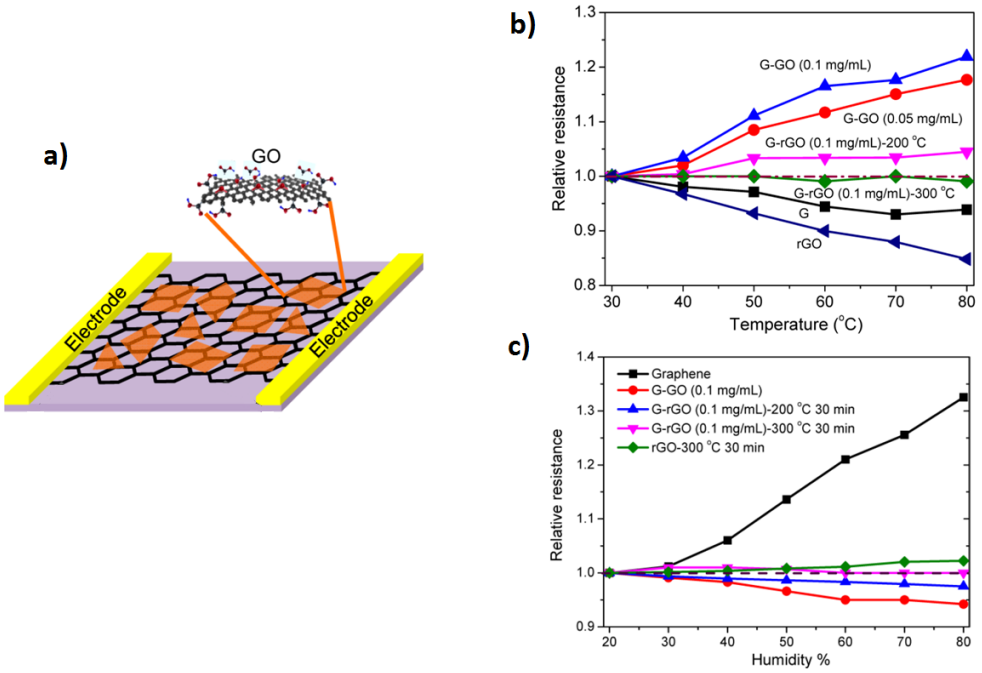


Fig. 2.4.2.3 - a) schematization of the device under investigation b) Relative resistances of graphene−GO (−rGO) hybrid films in the range of 30−80 °C obtained by nomalizing with the resistances at 30°C, c) Relative resistance−humidity curves of graphene and graphene−GO (−rGO) hybrid films [252].

## Graphene-based biosensor

Most of graphene-based electrochemical sensors use reduced graphene oxide (rGO) because its reactivity is much higher than that of pristine graphene and consequently the sensitivity is higher. In general, biosensors for **enzymes, DNA** and **proteins** can be produced.

### Enzyme biosensor

Several works on detection of the glucose oxidase (GOx) enzyme have been performed.

In general, GOx enzyme immobilised on graphene sheets is used as biorecognition element to determination of glucose. GOx oxidises glucose to produce gluconic acid and hydrogen peroxide ($H_2O_2$). The oxidation current produces by $H_2O_2$ affects the electronic structure of the graphene and provides a measurement on the concentration of glucose. For example, Wu et al. [253] reported a GOx–rGO modified electrode that exhibited a limit of detection of 0.01 mM and a sensitivity of 110 mA/mM*cm$^2$.

Also a graphene FET sensor to detect glucose has been produced. For example, Huang et. Al, showed a detection of 0.1 mM, comparable to the commonly used electrochemical sensor, in as-grown CVD grapheneFET [254] (Fig. 2.4.2.4).

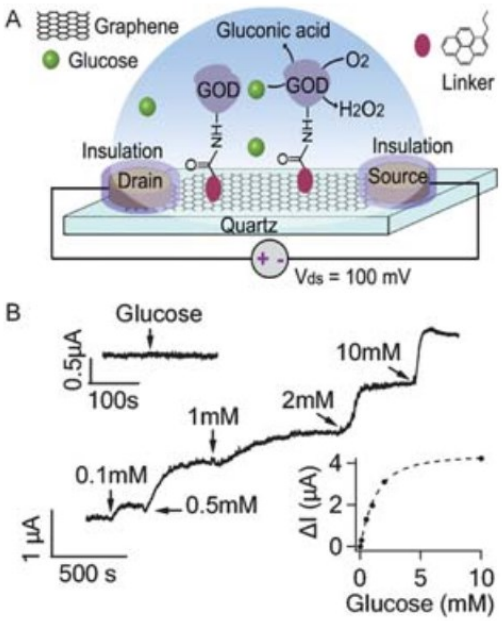


Fig. 2.4.2.4 – a) Schematic illustration of glucose oxidase (GOD) functionalized graphene FET, b) Current responses to the addition of glucose to various concentrations. The upper inset shows that GOD free graphene FET is not responsive to 10 mM glucose. The lower inset shows the response curve of the graphene FET to glucose fitted by an exponential function [254].

**DNA sensors**

Graphene materials have been used also for detection of DNA. For example, Huang et al. used rGO and –COOH groups to electrochemically detect simultaneously guanine and adenine. The direct electrooxidation behaviours of adenine and guanine on the graphene – COOH modified glassy carbon electrode were investigated by cyclic voltammetry and differential pulse voltammetry. The results indicated a detection of 50 and 25 nM, for guanine and adenine, respectively [255].

Also graphene FET sensors have been used for detection of DNA molecules. Dong et al. produced a graphene transistor by transferring the as-grown CVD graphene films from Ni to glass substrates. They show the detection of the hybridisation of target DNAs to the probe-DNAs pre-immobilised on graphene with detection sensitivity of 0.01 nM [256].

**Immunosensors**

The principle of operation is the same as already described for the CNT-based immunosensor. In this case, we want to immobilise antibodies on graphene to capture the corresponding antigens. The selectivity depends on the specific interaction between antibodies and antigens. Graphene sheets are used to improve the loading of biorecognition elements on the electrode and that the sensitivity can be improved by using nanoparticles entrapped with antibodies that allows to amplify the response. For example, Xie et al. reported a graphene-based immunosensor for quantification of phosphorylated p53 on serine 15 (phospho-p53$^{15}$) tumour suppressor protein (Fig. 2.4.2.5). The results showed that the current response is proportional to

the phospho-p53[15] concentration in the range of 0.2–10 ng/mL, with detection limit of 0.1 ng/mL [257].

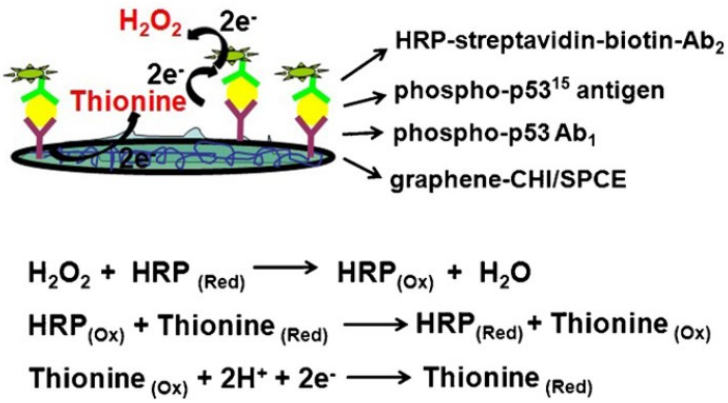


Fig. 2.4.2.5 – Schematic illustration of sandwich immunoassay of phospho-p53[15][257]

Mao et al. developed a FET biosensor using thermally reduced GO (rGO) sheet decorated with AuNP-antibody conjugates for the detection of anti-immunoglobulin G (anti-IgG). The antibody is labelled on the surface of the rGO sheet through AuNPs and detection of the protein binding (immunoglobulin G and anti-IgG) is obstained by electrical measurements. Results indicated that the response increases with the increase of the protein concentrations and saturates at 0.02 mg/mL, with a detection limit of 2 ng/mL (~13 pM) [258]. (Fig. 2.4.2.6)

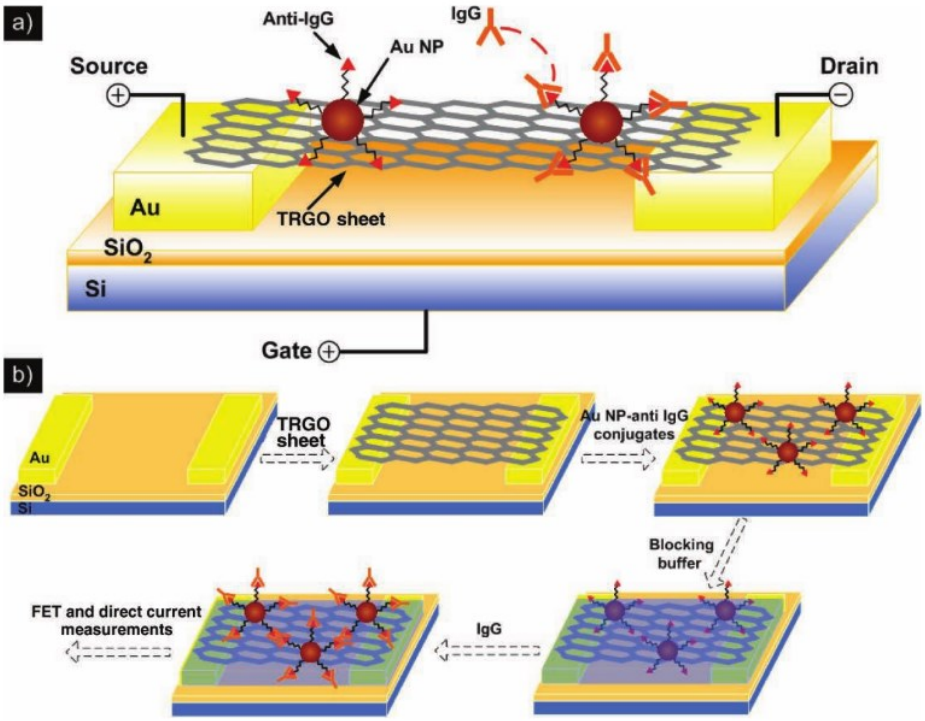


Fig. 2.4.2.6 - a) Schematic of a rGO FET. Anti-IgG is linked to the rGO sheet surface through AuNPs and functions as a specific recognition group for the IgG binding. The electrical detection of protein binding (IgG to anti-IgG) is performed by current measurements. b) Schematic illustration of the rGO FET biosensor fabrication process. Thermally reduced GO (TRGO) sheets were firstly dispersed on the electrodes and then decorated with AuNP-antibody conjugates through noncovalent attachmen [258].

# CHAPTER 3

# Applications and results

## 3.1. Carbon-based devices development

As mentioned in the introduction, the purpose of this thesis was the development of the carbon-based devices for sensing applications. In particular, back-gated CNTFET/GOFET have been produced, using optical lithography techniques and electrophoresis/dielectrophoresis techniques. The devices can be used as resistors just by setting to zero the gate potential. Most of the characterizations at zero gate were performed for reasons that will be described later. The devices based on CNT have been developed as biosensors, while those based on GO were used to investigate the electrical properties of the material, with the purpose of using them for humidity and gas sensing applications. Special attention to the manufacture methods was given. For example, the choice was to deposit the active nanostructured material by electrophoresis/dielectrophoresis on the metal contacts already present on the substrate and not vice versa. As we will see below, this allows to obtain devices in a simple and low-cost way and with a large choice of possible substrates (also plastic substrates). Moreover, MWCNTs were used instead of SWCNTs because MWCNTs are more resistant and less expensive than SWCNTs, and show similar performances

The back-gated CNTFET production process consists of three different phases: the design of the masks with CAD software, optical lithography and chemical/physical processes, controlled deposition of the nanomaterials by electrophoresis/dielectrophoresis and the packaging. (Fig. 3.1.1.)

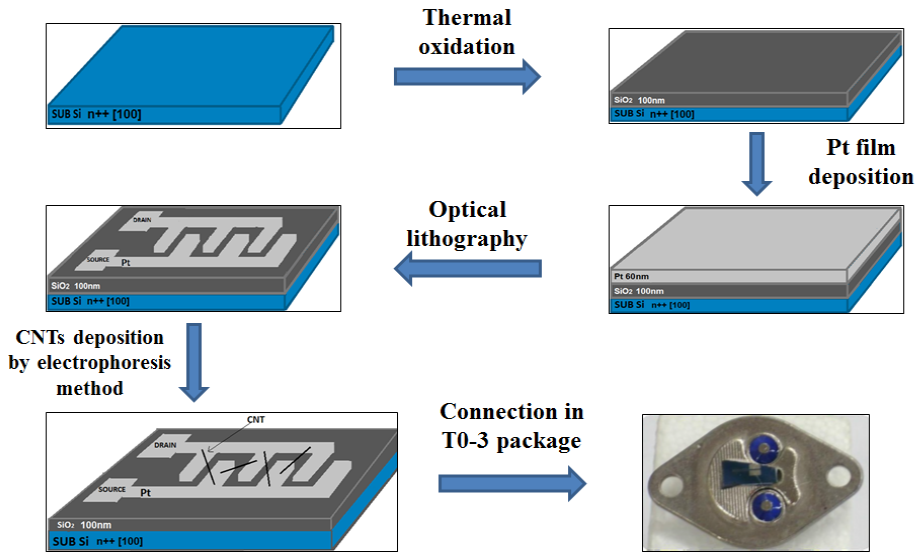


Fig. 3.1.1 – Scheme of the device development. The interdigitated electrodes width and the distance between them varies from 5 to 10 μm

The shape of the electrodes can be chosen in different ways. Typically, interdigitated geometry allows a good electrical contact between the electrodes and the nanomaterial. Moreover, parasitic capacitances are reduced. This geometry is chosen especially when nanomaterials are grown directly on the substrate or when they are deposited by electrophoresis, for reasons which will be described later.

As shown in Fig. 3.1.1., the device preparation starts from a heavily doped silicon substrate (n++) with [100] direction. Subsequently a 100nm silicon dioxide ($SiO_2$) layer is thermally grown on the substrate and, finally, drain and source electrodes are defined by optical lithography (see appendix),

using a 20 nm Ti / 100 nm Pt layer. The interdigitated width and the distance between them are ranging between 5 to 10 μm. The substrate is heavily doped n++ in order to use it as back-gate. Obviously, if the substrate is not connected, a CNTs-based resistor is obtained in which the resistive element is formed by the nanotubes.

In order to explore alternative inexpensive technologies, during the doctorate also glass and plastic devices were produced. In both cases, low-cost optical lithographic technique was used, creating the mask on transparent paper with a laser printer, using a bromograph for the UV irradiation and using the lift off technique (see appendix), which allows the electrodes production (Aluminum) on plastic devices without use of acids. Microscope glass slides were used as a glass substrate while a common transparent paper for printer was used as plastic substrate. In Figure 3.1.2 two examples of these devices are shown. Both glass and plastic devices are resistor devices because the substrates are insulators.

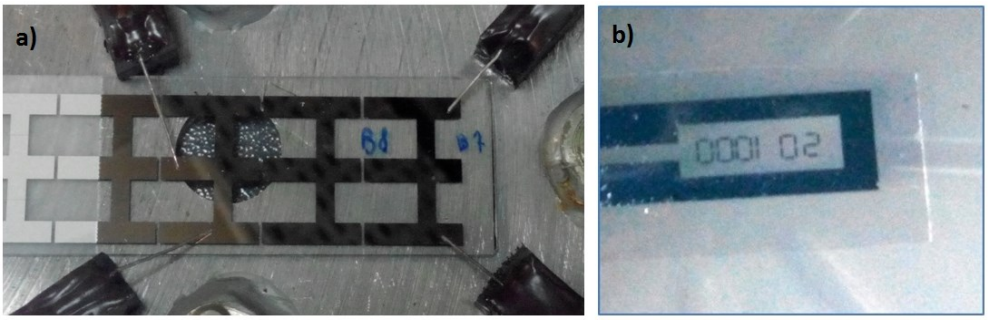


Fig. 3.1.2 – (a) Several Al flat electrodes produced with different interelectrode distances ranging from 20 μm to 150 μm on a glass substrate. In this picture the devices are connected to the electrical instruments through four tips; (b) an example of a plastic device with two flat Al electrodes with an interelectrode distance of 20 μm and length of 1000 μm.

## 3.1.1. Electrophoretic deposition

The term electrophoresis indicates the movement of particles due to a constant electric field. Specifically, **the electrophoretic deposition (EPD)** is a technique based on the movement of electrically charged particles in a fluid, induced by an electric field applied between two electrodes in the same fluid. If the particles have a positive charge they move to the cathode (cataphoresis), if they have negative charge to the anode (anaphoresys) (Fig. 3.1.1.1.).

EPD is a very simple technique which allows to perform the deposition of particles at room temperature and without the use of vacuum systems.

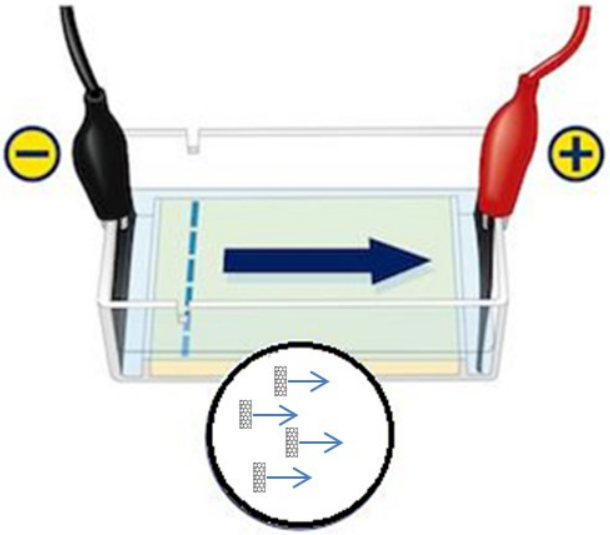

Fig. 3.1.1.1. - Electrophoresis process [http://www.ncbe.reading.ac.uk]

As can be understood, the particles motion in solution (typically water, acetone, ethanol) takes place if they own a charge. As described in the previous paragraphs, the pristine nanotubes, especially SWCNTs, for their nanostructured nature tend to aggregate in solution, and this can affect negtively the deposition process. For this reason, the choice of oxidized

MWCNTs can help: the surface of the nanotubes is negatively charged, due to the the creation of -COOH and $OH^-$ groups induced by oxidation process on the surface of CNTs, and the CNTs repel each other, remaining well dispersed in the solution. Furthermore, the deposition by electrophoresis is possible since the negative charged CNTs are driven towards the positive electrode (anaphoresys).

The deposition process has been done by contacting source and drain electrodes both to the positive potential and placing in front of the device a molybdenum electrode connected to the negative potential. Both the device and the molybdenum electrode have been plunged in a solution (acetone or water) containing CNTs previously prepared (sonicated for 10 min) (fig. 3.1.1.2). The CNTs deposition on the device depends on several factors: deposition time, CNTs type and concentration in the solution, distance and voltage between the device and molybdenum electrode.

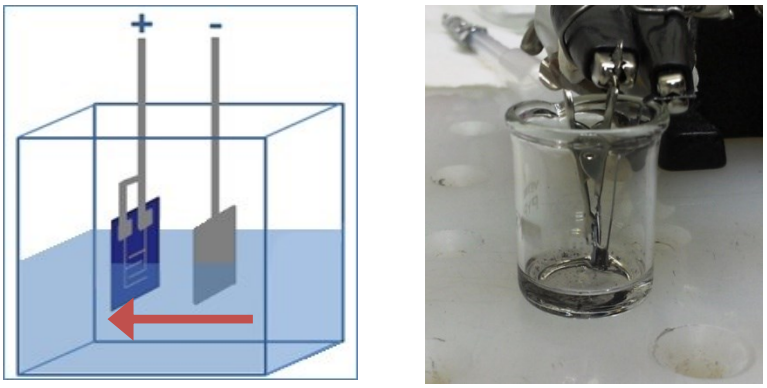


Fig. 3.1.1.2. – Electrophoresis process

Several tests have been made by varying the mentioned parameters. As example, Fig. 3.1.1.3 shows SEM images (using ZEISS SUPRA 35 FE-SEM system, described in Appendix) of two different devices with two different types of CNT. In particular, Fig. 3.1.1.3.a shows a device with MWCNTs

from Sigma Aldrich (synthesized by CVD and subsequently oxidized to eliminate the catalytic particle (see Chapter 1, CNT synthesis), while Fig. 3.1.1.3b shows a device with MWCNTs synthesized by arc discharge in liquid nitrogen and subsequently treated in $H_2O_2$. In both cases, the devices are formed by a silicon n++ substrate with a gate oxide of 150nm and Pt interdigitated electrodes of 5 μm.

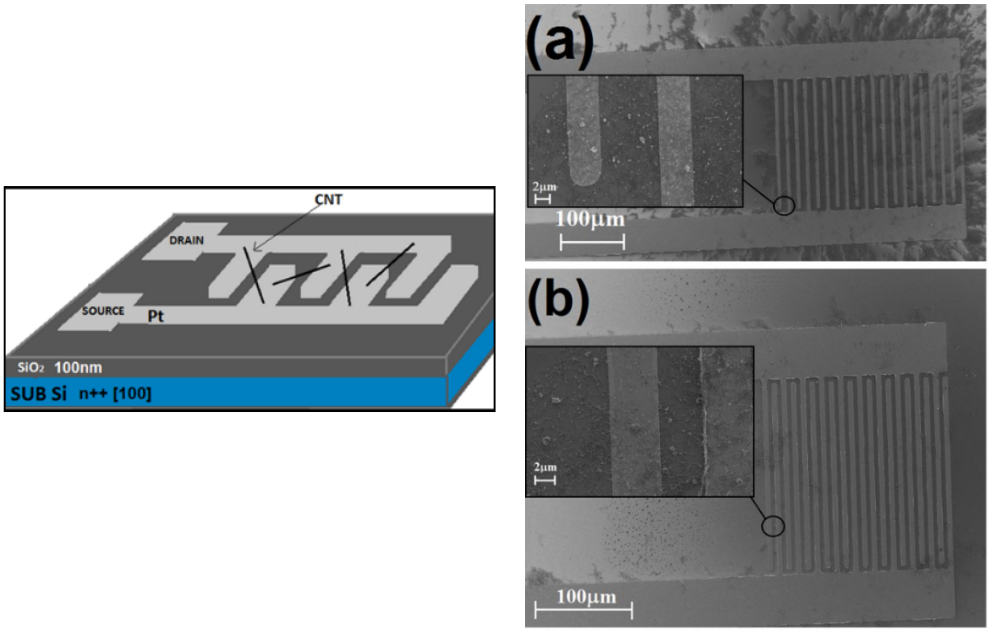


Fig. 3.1.1.3 – SEM images of interdigitated devices with MWCNTs deposited by electrophoresis. (a) device with commercial MWCNTs, (b) device with MWCNTs synthesized by arc discharge in liquid nitrogen and subsequently treated in $H_2O_2$.

The MWCNTs shown in Fig. 3.1.1.3b were produced by arc discharge in liquid nitrogen between two graphite rods, applying a voltage of 25V, and fixing the current at 80A [259,260], and oxidized in $H_2O_2$ (diluted at 30 %) for 2 h in a ultrasonic bath. This mild oxidation method is sufficient to introduce only a low surface charge that allows deposition of a CNTs network on a substrate by EPD. The oxidation method does not introduce

relevant damage on the outer walls of the CNT or the rupture of the caps, as confirmed by Raman and TEM analyses [261]. Therefore, MWCNTs were dispersed in acetone (5 mg/ml) for 10min in ultrasound and then EPD was perfomed by supplying a constant voltage of 30V for 20 min between the cathode (molybdenum 0.5 mm large and 0.25 mm thick) and the interdigitated electrodes of the device (both source and drain), at a distance of 2.5 mm.

It is possible to observe that, for the same deposition time, voltage and CNT concentration, the deposited amount of CNTs is greater in the case of oxidized MWCNTs from Sigma Aldrich. This is explainable because the arc discharge MWCNTs treated in $H_2O_2$ have a mild oxidation and therefore present less negative charges on the surface than the commercial MWCNTs.

In Fig. 3.1.1.4, the electrical characterization of the device in Fig. 3.1.1.3a is shown. The measure was performed in common source configuration using a source meter unit (SMU) Keithley 6430. As can be seen, the characteristic is almost linear, showing a typical metallic behavior of the MWCNTs.

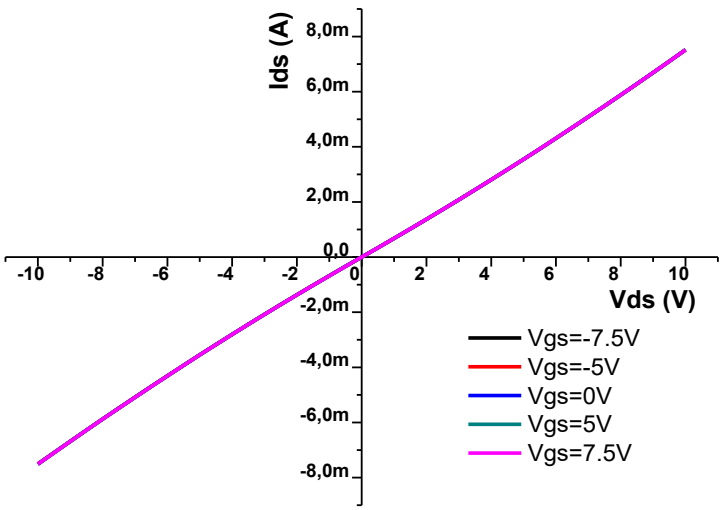


Fig. 3.1.1.4 – Electrical characterization of the device shown in Fig. 3.1.1.3a. The I-V curve shown a linear behavior.

The deposition by electrophoresis does not allows a precise localization of CNT that, instead, are deposited on the entire device area. For this reason, EPD can be used for deposition on large areas using interdigitated electrodes suitably designed.

By various tests, it was observed that the electrical conductivity of the CNT film is directly proportional to the amount of CNT deposited. In this way, through a calibration table, it is possible to define in advance the electrical resistance of the CNT film by suitably calibrating the parameters of the deposition process. This is an important result, because it allows to produce many devices with the same electrical characteristics, in a reliable and repeatable way. However, it remains an indirect measure. Furthermore, as already described, during the EPD it is difficult to determine the CNTs position in the device. This limits the use of the EPD to the deposition of large amounts of the CNT. Instead, it could be useful to find a technique that allows the localized deposition of few CNTs on specific confined regions of the device.

For these reasons, dielectrophoresis, another kind of deposition based on the use of non-uniform electrical fields, was taken into account in the present thesis work.

## 3.1.2. Dielectrophoretic deposition

Dielectrophoresis (DEP) involves the use of high frequency alternating electric fields for the controlled deposition of particles in solution. In particular, the non-uniform electric field induces an electric dipole on the particles that will move along the lines of the electric field. Unlike the electrophoresis, in this case we have the possibility to deposit neutral particles, because the DEP induces an electric dipole on the particle. The dielectrophoretic force depends on the intensity of the electric field, the frequency, the shape of the particles, the interactions between the particles and the difference between the electrical permittivity of the particles and that of the medium in which the particles are suspended.

Approximating the particle to an ellipsoid of radius r and length l, with complex permittivity $\epsilon_p$* and immersed in a solution of complex permittivity $\epsilon_m$*, the dielectrophoretic force is:

$$F_{\mathrm{DEP}} = \frac{\pi r^2 l}{3} \varepsilon_m \mathrm{Re}\left\{ \frac{\varepsilon_p^* - \varepsilon_m^*}{\varepsilon_m^*} \right\} \nabla \left| \vec{E} \right|^2$$

where the permittivity $\epsilon$* is given by $\varepsilon^* = \varepsilon + \frac{\sigma}{j\omega}$, where $\epsilon$ is the dielectric constant, σ is the electrical conductivity, ω is the frequency of the electric field and j is the imaginary unit.

The factor in brackets is known as **Clausius-Mossotti term** and contains all the frequency dependence in the dielectrophoretic force. In particular, this term may also include the particle-particle interactions, making the formula more complex.

The dielectrophoretic deposition is performed by dipping the device in the solution containing the material to be deposited. Unlike electrophoretic processes, it is not necessary to place an electrode in front of the device but the non-uniform electric field (a sinusoidal signal) is applied directly between the source and drain electrodes. In this way, the particles will be deposited directly in an ordered way between the electrodes, enabling the creation of the active channel. At this point we understand the power of this technique: by suitably changing the geometry of the electrodes it is possible to deposit materials at specific points, i.e. the points where the dielectrophoretic force is greater. In Fig. 3.1.2.1. a scheme of the dielectrophoretic deposition process is reported: the oxidized MWCNTs (Sigma Aldrich) dispersed in water (1µg/ml, sonicated for 10min before of the process) are deposited on a device with two flat electrodes one in front of the other at a distance of 10µm. In this way, the nanotubes will tend to align along the electric field lines, depositing between the source and drain electrodes.

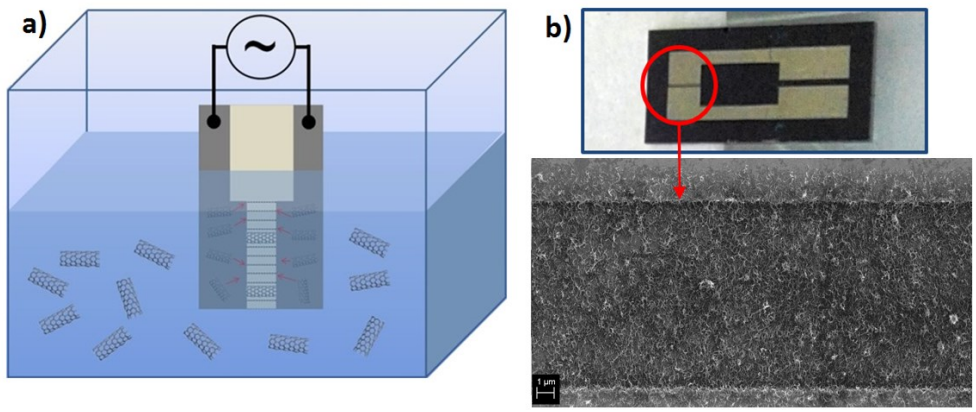


Fig. 3.1.2.1 – (a) a scheme of the dielectrophoretic deposition process: the nanotubes in water are attracted by the dielectrophoretic force between the flat electrodes (connected for 10min to a sine generator, 15Vpp, 100kHz). (b) photo of a CNTFET device and a SEM image of the CNT layer deposited between the electrodes.

Fig 3.1.2.1b, shows a SEM image of a device with a homogeneous film of nanotubes deposited between the two electrodes. This result can be obtained if the nanotubes are well dispersed in water and this is possible, as already said, using oxidized nanotubes, due to the presence of negative charge on their surface.

In Fig. 3.1.2.2, other examples of CNTs deposition between interdigitated electrodes are shown. The deposition occurs only at points where the dielectrophoretic force is greater. In particular, Fig. 3.1.2.2 a,b,c shown the deposition on silicon devices while Fig. 3.1.2.2 d reports the deposition on a glass device.

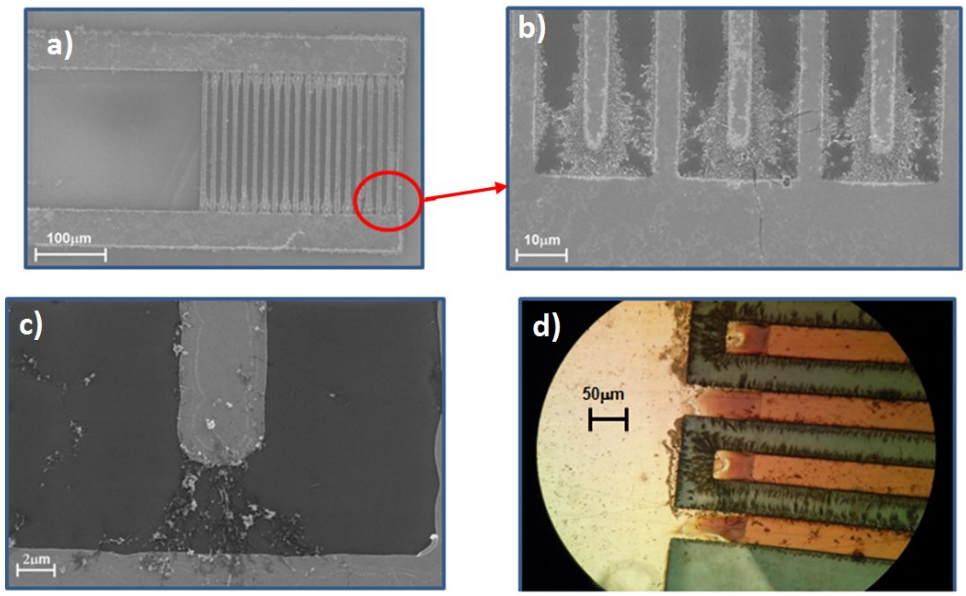


Fig. 3.1.2.2 – Examples of DEP of CNTs on (a),(b),(c) silicon devices and on (d) a glass device with interdigitated electrodes. The nanotubes are deposited in the point where the $F_{DEP}$ is maximum.

As shown by the dielectrophoretic force expression, the deposition also depends on the medium in which the nanotubes are immersed. In addition to water, various deposition also in acetone were performed, in order to study the behavior of the nanotubes in different solvents.

In Fig. 3.1.2.3 examples of deposition of CNTs dispersed in acetone on flat electrodes-based devices are reported. In this case, compared with the water solution, the nanotubes tend to aggregate, but their tendency to align along the electric field lines can be also observed.

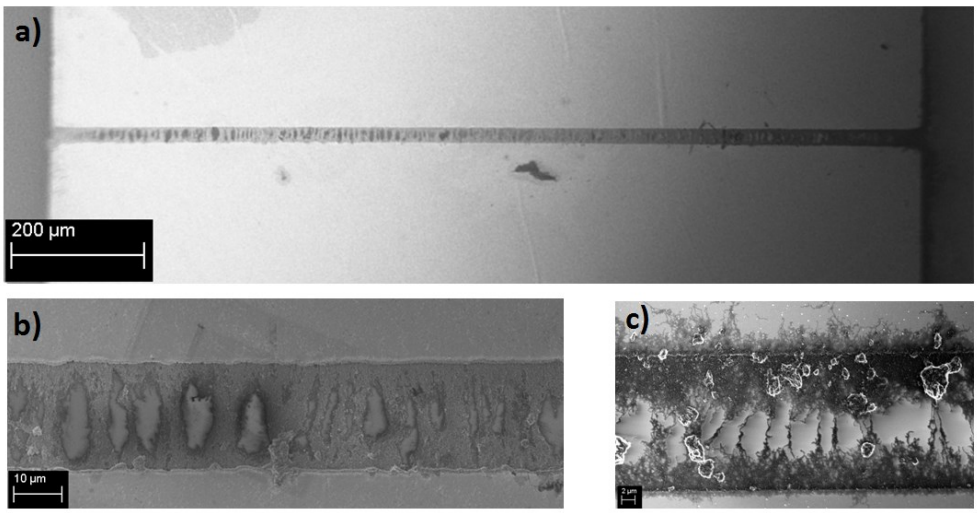


Fig. 3.1.2.3 – Examples of SEM images of devices with MWCNTs deposited between two flat electrodes

The electrical characterization of the device in Fig. 3.1.2.3c is shown in Fig. 3.1.2.4. In particular, in this device, oxidized MWCNTs were deposited between the electrodes (at distance of 20µm) using the dielectrophoresis in acetone, at 100KHz with a voltage of 40Vpp for 5min. The characterization with a Source Meter Unit (SMU) Keithley 6430 in common source configuration was carried out. The figure shows that the MWCNTs in this case have a non linear electrical behavior. This response can be explained by

considering the nanotube-electrode contacts and the low density of nanotubes that connects the source and drain electrodes (see Fig. 3.1.2.3.c). In fact, between each CNT and an electrode a Schottky barrier forms and induces the nonlinearity. It is therefore clear that the linearity depends on the type of CNT, their amount and the type of metal used as electrode (platinum in this case).

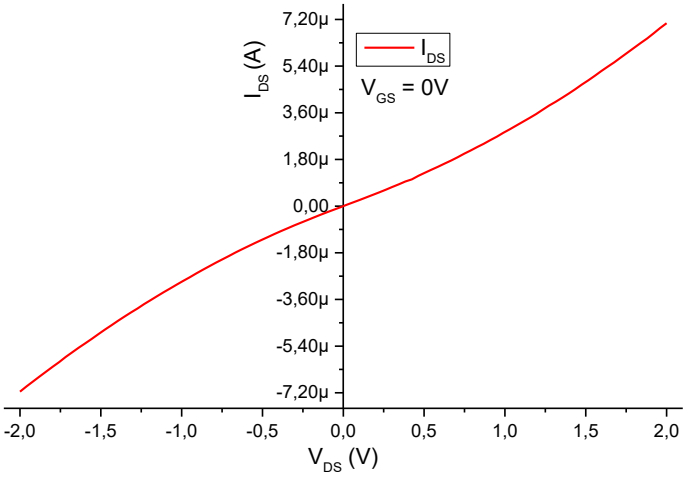


Fig. 3.1.2.4 – Electrical characterization of a device in Fig. 3.1.2.3c with oxidized MWCNTs deposited in acetone.

### 3.1.3. Development of silicon devices in collaboration with STMicroelectronics

During the PhD, within the PON HIPPOCRATES Project "Sviluppo di Micro e Nano-tecnologie e Sistemi avanzati per la salute dell'uomo", several back-gated silicon devices have been developed also in collaboration with STMicroelectronics, Catania. In particular, a mask for the devices by varying type and distances between the electrodes has been designed and, using optical lithography techniques, wafers containing different types of devices were produced. In order to connect the devices to the deposition system, a special PCB was created in such a way that it was possible to perform the dielectrophoretic deposition keeping the device in vertical position dipped in the solution, with its PCB. In Fig. 3.1.3.1 .the design of the mask (a), the wafer with the different devices (b), the single device (c) and the device on the PCB (d) are reported.

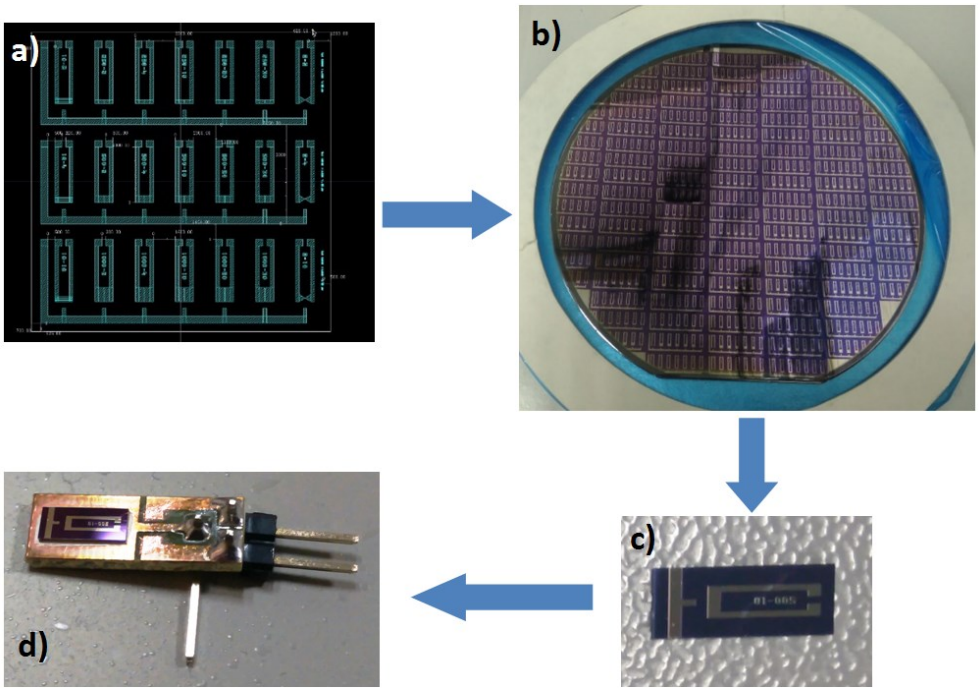


Fig. 3.1.3.1 – Back-gated devices production: (a) mask development using CAD software; b) silicon wafer with the devices produced; c) example of a device produced; (d) a device mounted on a homemade PCB used to easily connect the device to the DEP system.

### Setup for the dielectrophoretic deposition

The deposition process is carried out vertically, i.e., the device is immersed in the solution from top downwards. The setup used for the DEP is formed by a sinusoidal generator (Agilent 33500B), a homemade amplifier and an oscilloscope (Agilent DSOX2014A) to control the process. The system is shown in Fig. 3.1.3.2.

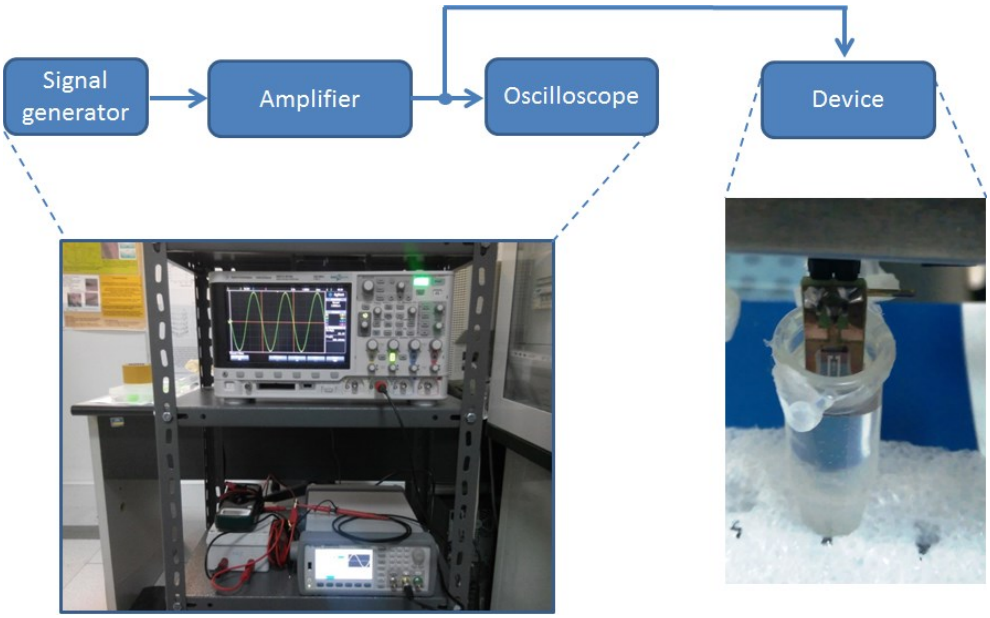


Fig. 3.1.3.2 – Setup for the dielectrophoretic deposition process

It is also possible to perform a horizontal DEP, i.e. placing a drop of solution (containing the material to be deposited) on the region containing the source and drain electrodes, that are connected to the sinusoidal generator by two tips of a probe station. (Fig. 3.1.3.3)

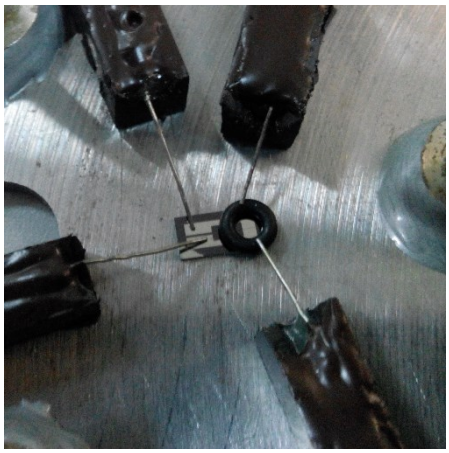

Fig. 3.1.3.3 – Dielectrophoretic process performed by dropping the CNT solution on the electrodes, without dipping the device in the solution. The o-ring is used to maintain the drop in a confined region. The tips are used to perform the electrical characterization.

Both the methods have advantages and disadvantages. In the case of vertical deposition, the process occurs by immersing the device in solution. This involves the production of a special connector for keeping the device in the right position and electrically connected. In the case of the horizontal deposition, instead, the device can be placed on a horizontal support and connected with the tips to the sine generator. In this case, a special connector is not necessary because the deposition take place pipetting a drop over the electrodes. However, in this case it is necessary to remove the drop (for example with a syringe) at the end of the DEP, and this can damage the deposition, while, in the case of vertical DEP, the device has just to be drawn out from the solution.

For all these reasons, in the present thesis work mainly the vertical DEP was used, obtaining a more controlled and repeatable process.

## 3.1.4. The issue of the parasitic capacitances in the dielectrophoresis process

By SEM analysis the devices were characterized and an equivalent electrical model was carried out (Fig. 3.1.4.1). The devices have a gate oxide thickness between 250nm – 300nm, Pt electrodes thickness of 150nm and different possible distances between the electrodes, ranging from 2µm to 30µm depending on the specific device (Fig. 3.1.4.2. a,b).

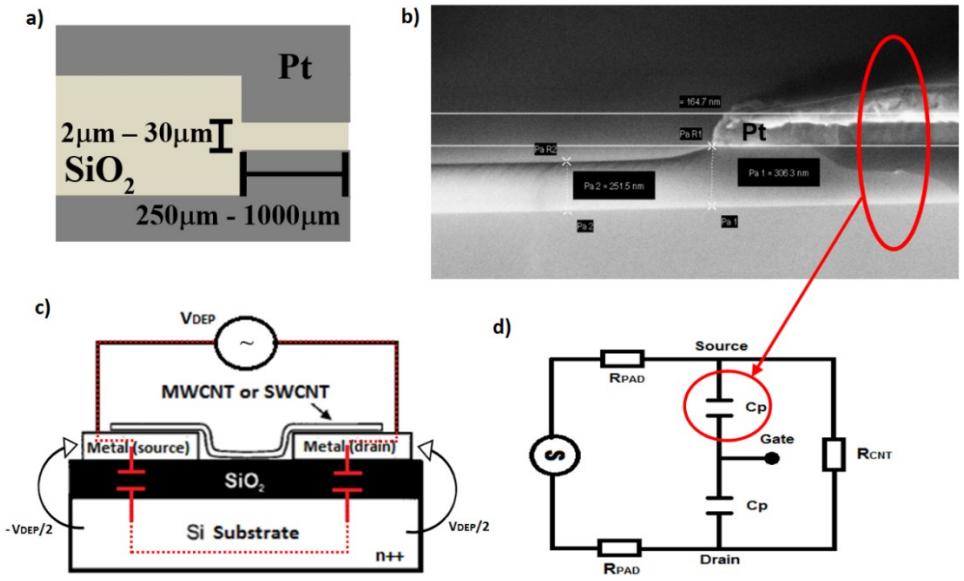


Fig. 3.1.4.2 – Analysis of the parasitic capacitances of the devices produced. (a) Schematization of the device, (b) SEM analysis of the device cross section. It is possible to note the zone of the parasitic capacitances, modeled in (c) and (d)

As shown in Fig. 3.1.4.2, the back-gate structure, having a conductive substrate, has very high parasitic capacitances (source-substrate and drain-substrate capacitances). These capacitances create many problems during the dielectrophoretic process. In particular, when the sinusoidal signal is applied between source and drain ($V_{DEP}$), a current flows through the parasitic capacitances. This causes a voltage between source-substrate and drain-

substrate that, assuming a symmetrical device, is equal to $V_{DEP}/2$. Clearly, this phenomenon depends on the frequency of the applied signal (high frequencies involve high eddy currents, because the impedance of the capacitance is inversely proportional to the frequency), the geometry of the electrodes and the gate oxide thickness.

Therefore, when the sinusoidal voltage is applied, the dielectrophoretic force appears not only between source and drain but also between the substrate and the source/drain. This behavior leads to several problems in the deposition process. For example, in Fig 3.1.2.3c, there is a greater concentration of nanotubes all around the electrodes. This happens because in addition to the dielectrophoretic force between source and drain, there is also a force between the electrodes and the substrate, and it is very big since the distance between the electrodes and the substrate is only 250 nm (the thickness of the gate oxide). Moreover, as the distance between the source and drain electrodes increases, the electrode-substrate $F_{DEP}$ will be greater than that between the two electrodes. This phenomenon is even clearer in Fig. 3.1.4.3, where the deposition occurs also along the entire perimeter of the electrodes, and not only between the source and drain. Clearly this is an unwanted effect that disappears using insulating substrates, as in the case of the glass devices, and in that case the deposition can take place only between source and drain.

For this reason, a trade off in needed and, in the case of silicon devices under investigation in this thesis, all depositions were carried out at 100KHz, a good compromise to reduce eddy current and maintain the effectiveness of deposition.

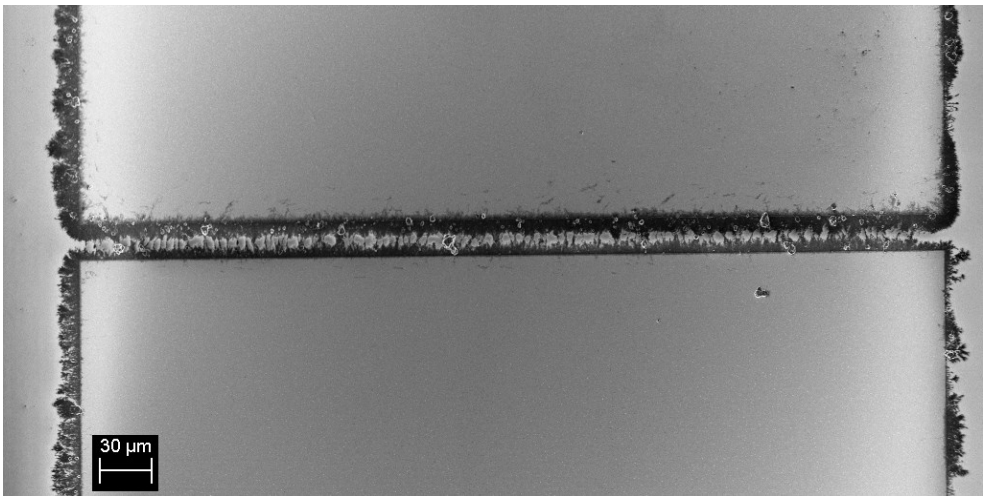


Fig. 3.1.4.3 – Example of dielectrophoretic deposition of MWCNTs in acetone on a silicon device with a highly doped substrate. The deposition all around the electrodes is due to the $F_{DEP}$ between each electrode and the substrate. This unwanted force depends on the presence of the parasitic capacitances.

## 3.1.5. Repeatability of the deposition process

One of the big issues in the sensor field is the repeatability, both in their production processes and in the sensing response. In the first case, it is necessary to achieve devices with similar electrical characteristics, i.e., in our case this could be achieved by depositing the same type, and quantity of CNTs.

To this aim, a system able to perform simultaneously the dielectrophoresis on four devices (**MultiDEP System**) was designed and a prototype was made. In this way, a reduction of the time production and an increase of the repeatability can be achieved (Fig. 3.1.5.1)

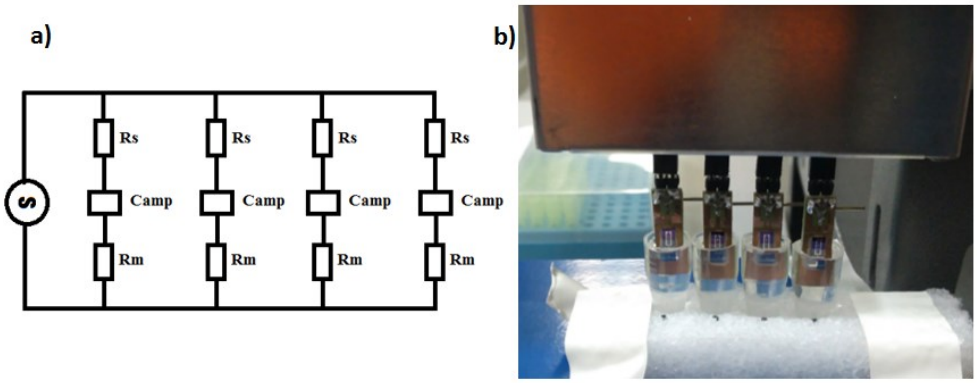


Fig. 3.1.5.1 – (a) electrical model of the four channel DEP system, (b) picture of the DEP process performed on four devices simultaneously.

As shown in Fig 3.1.5.1a, for each channel two resistors in series were included: the first (Rs) is used to limit the current flowing through the nanotubes during the deposition, while the other (Rm) is used to measure the current. The sine generator has a current limiter in order to obtain the same voltage in the four channels also in case of different current demands. Regarding the current measurement, it should be remembered that as the nanotubes are deposited between the electrodes, an electric current begins to

flow through them. This current increases as the quantity of deposited nanotubes increases. In this way it is possible to control the amount of deposited nanotubes just by measuring the current flowing through them during deposition. This is another very useful method for improving the repeatability of production, because it is possible to stop the deposition when the desired resistance value is reached.

In particular, an electronic system has been produced able to measure the electrical resistance during the deposition and to transfer the data to a PC. The system is composed of a homemade amplifier, a filter, an analog-digital converter (Adafruit ADS1115 16Bit) and an Arduino microcontroller (Fig. 3.1.5.2). In particular, the amplifier and the filter were designed to decouple the AC signal deposition with the DC measurement.

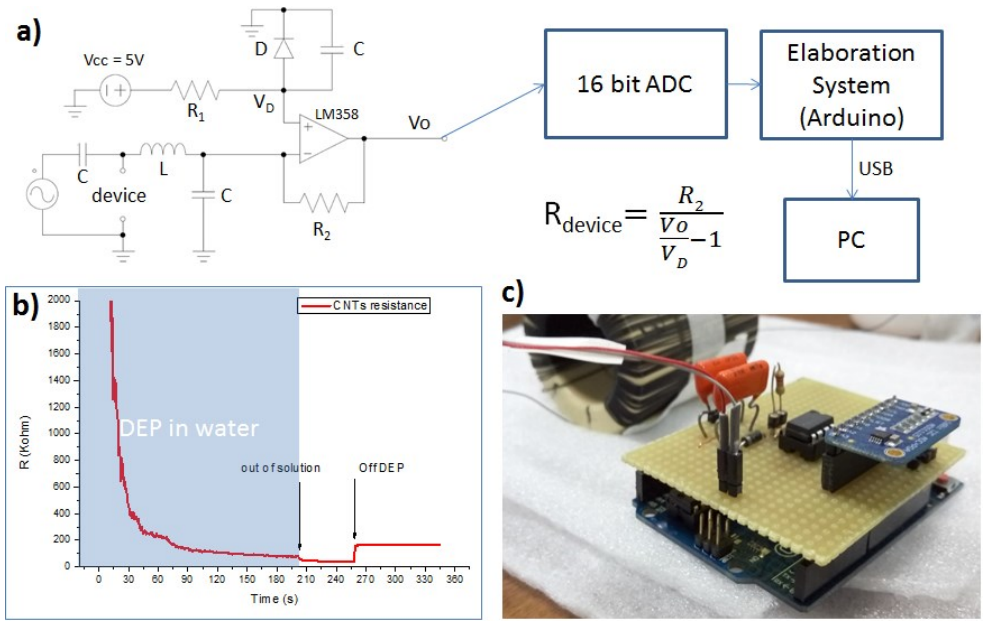


Fig. 3.1.5.2 – (a) Electrical scheme of the amplifier produced to measure the resistance of the CNT layer during the dielectrophoresis process. The resistance value is calculated by the Arduino microcontroller according to the formula shown in figure; (b) resistance profile of the CNTs acquired by the system during the dielectrophoresis process; (c) picture of the electrical system for the deposition control.

In Fig. 3.1.5.2b a typical CNTs resistance profile acquired during the dielectrophoretic deposition process is shown. At time $t_0$=0s, the resistance is infinity because there are no CNTs between the electrodes. As the time goes by, the dielectrophoretic force attracts the CNTs from the solution (water in this case) towards the electrodes and a channel is formed, with current flowing through the CNTs. Therefore, as the CNT density increases between the electrodes, the resistance begins to decrease tending to zero value. In order to obtain a fixed resistance value, the device has to be removed from the solution just when it reaches that value, and then the sine generator can be switched off. As shown, after the generator is switched off, the resistance increases slightly. This happens because the current-voltage response of the device is not linear (Fig. 3.1.2.4) and then the resistance changes according to the voltage value used to measure it. In our case, the resistance is always measured at a fixed DC voltage (Vd) to which the RMS value of the DEP AC voltage has to be added. When the AC sine generator switched off, the AC value disappears and then an increase in the resistance measurement occurs.

## 3.2. Graphene oxide-based devices development

Similarly to CNTs-based devices, graphene oxide (GO)-based devices were also produced. The procedure is identical to the one already reported above. Several silicon and plastic devices, with different shape and distance between the electrodes, were produced. GO, purchased at Sigma-Aldrich, was diluted in water at 1µg/ml concentration and sonicated for 5 min. Therefore, the device was immersed in solution and then, by applying the sine wave to the electrodes (dielectrophoresis), the material deposits between the electrodes (Fig. 3.2.1)

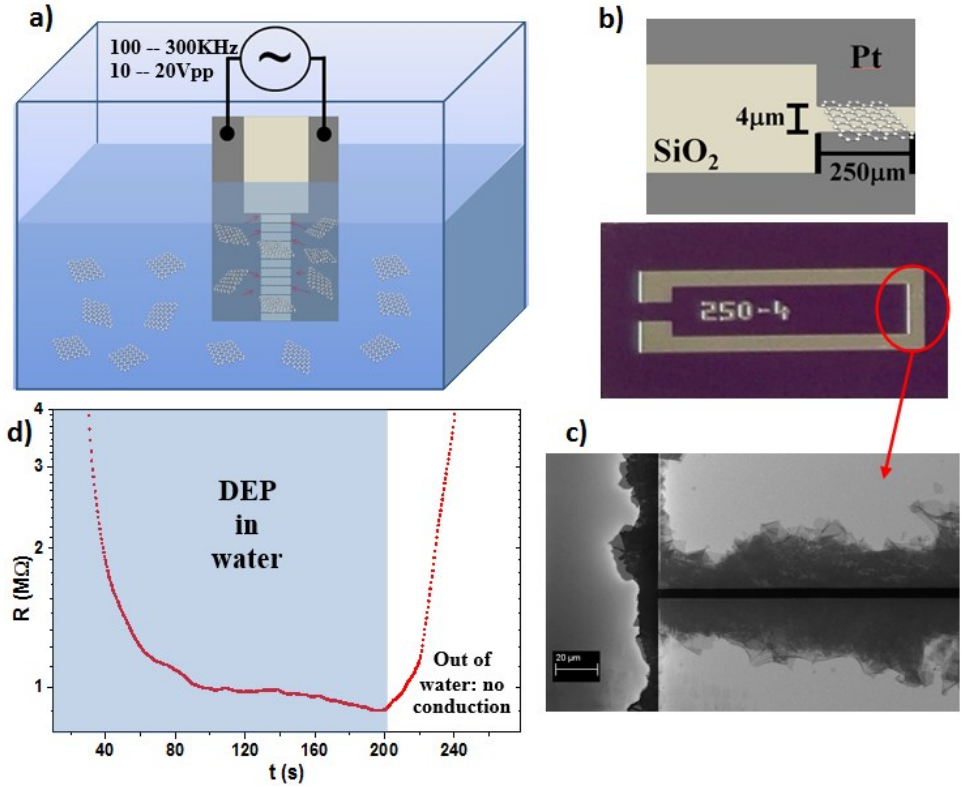


Fig. 3.2.1 – Dielectrophoresis process for GO-based devices: a) DEP process in water. The sheets of the graphene oxide are attracted between the electrodes; (b) Scheme and picture of the device produced; (c) SEM image of the GO sheets deposited between the electrodes; (d) Resistance profile of the GO layer forming during the dielectrophoretic process in water. Graphene oxide exhibits a very high resistance out of the water.

As for the CNTs, also GO tends to follow the $F_{DEP}$. In Fig. 3.2.1c it is possible to note that the deposition takes place between the electrodes but also between each electrode and the substrate. This unwanted behaviour is due to the parasitic capacitances present in this structure, as already explained for the CNTs-based devices.

Several electrode geometries were considered in order to investigate the GO dielectrophoretic behaviour. For example, Fig. 3.2.2.a, shows an optical image of GO deposited between four pairs of small electrodes formed by eigth Pt strips with an interelectrode distance of 4µm. Fig. 3.2.2b reports a SEM image of a single pair of electrodes after GO deposition.

The optical image of a device with a different electrode geometry is shown in Fig. 3.2.2c,d. GO sheets deposited between the electrodes are clearly visible.

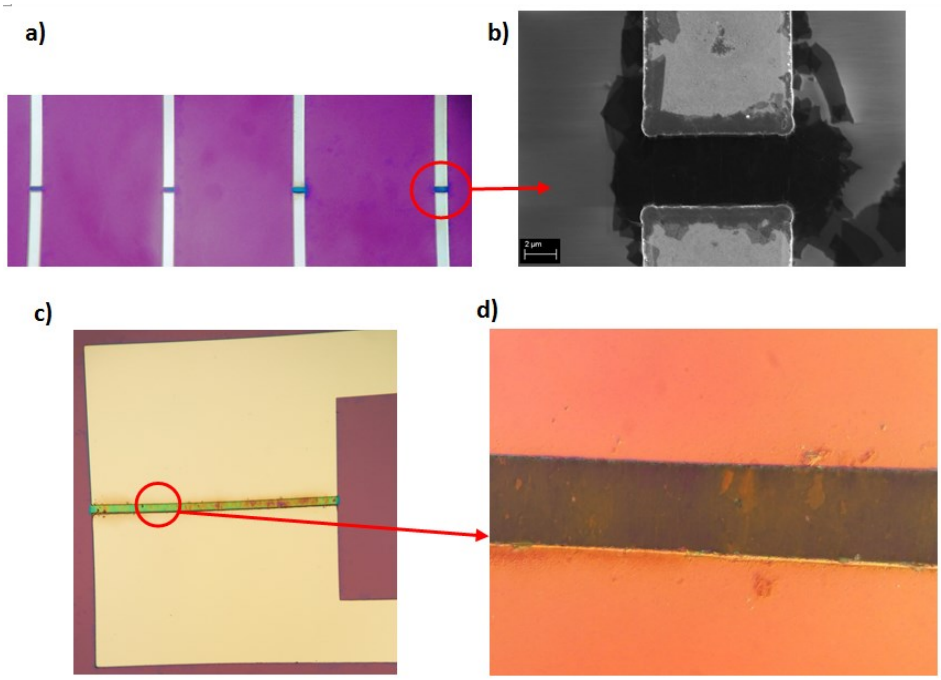


Fig. 3.2.2 – (a) Optical image of GO deposited between four pairs of electrodes; (b) SEM image of a single pair of electrodes with GO deposited in between; (c) overview of a device with flat electrodes with an inter-electrode distance of 10µm. Is possible to note the uniform deposition of GO; (d) zoom of a zone of the device shown in (c). The use of optical filters allows to improve the image contrast and distinguish the areas with a different number of GO sheets.

## 3.3. Development of CNT-based immunosensors for Human Arginase-1 detection

A biomarker is a traceable substance that, in an organism, can indicate a healthy or a pathological condition, depending on the concentration. Several proteins are often used as biomarkers of the risk or progression of a particular disease. As already mentioned in the introduction and in the previous sections, the traditional methods such as ELISA and RIA for the detection of proteins are expensive and time-consuming, requiring special equipment and devices. Furthermore, for some types of proteins, the sensitivity is too low. Therefore, new methods to achieve simpler, faster and cheaper detection systems are required.

As already discussed, CNT-based devices, could detect a specific protein by a simple electrical measurement and therefore can be considered a good alternative to the conventional analytical methodologies. .

In this thesis work the use of CNT-based devices for the detection of the **human Arginase 1 (ARG-1 or liver-type arginase)** was investigated. ARG-1 is a 35 kDa protein circulating in blood probably as a homotrimer. It is most abundant expressed in mammalian liver, but it is also found in non-hepatic tissues, for instance red blood cells, lactating mammalian glands, and the kidney. In addition to its involvement in ammonia detoxification via the urea cycle, arginase plays a role in other processes, for instance macrophage-mediated cytotoxicity due to arginase release and inhibition of lymphocyte proliferation. It shows high activity in growing tissues, wound healing, proliferating lymphocytes and tumors. Furthermore, ARG-1 acts as a modulator of the immune response. Besides this, arginase plays a role in allergen challenged lungs, in autoimmune inflammation in the central nervous system and in acute liver injury. In plasma of healthy individuals

ARG-1 is present in levels of 1.8 - 30 ng/ml [262,263] which increases approximately 10 fold during acute phase responses. ARG-1 blood levels elevate in cancerous patients and correlate with cancer stages and poor prognosis. In particular it is detectable in peripheral blood as serum biomarker (Arg-1) for hematological malignancies, including Hodgkin's Lymphoma and Multiple Myeloma (MM) [264-266] and in urine as renal cell carcinoma biomarker [267]. Recent studies by quantitative urinary proteomics have also identified ARG-1 as a potential candidate molecule involved in the development of obstructive nephropathy in newborns [268]. It was shown that an elevation of arginase in a patient's blood is very harmful to the host immune system, more than having effect in the promotion of the tumor cell growth [269].

As mentioned, typically the detection of such proteins can be performed by ELISA (described in the previous chapter) which can be used in the 1 to 300 ng/ml range in serum and culture supernatants [262,263,270]. As seen in the previous chapter, one of the major challenges in the fabrication of CNT-based immunosensors is to attach antibodies to the CNTs. To do so, a molecular recognition function has to be added by a suitable functionalization that allows immobilizing the receptor on the sidewalls of the nanotubes, as will described below. Since this kind of devices is based on the electrical response of functionalized carbon nanotubes to antibody–antigen binding, they can be easily turned to detect other proteins by functionalizing CNTs with appropriate antibodies.

## 3.3.1. Immunosensors development

The first step is to functionalize the CNTs in order to make the interaction with antibodies possible. Multi walled carbon nanotubes (purity > 95%, diameter of 20–30 nm), and all reagents were purchased from Sigma Aldrich. Diazonium salt treatment was used to create $sp^3$ hybridization sites along the nanotube, ending in carboxylic acid groups, following a previously reported procedure [271]. A suspension of MWCNT-COOH (50 mg) in dimethylformamide (DMF) (10 ml) was sonicated in a water bath for 10 min. Then, 1-ethyl-3-(3-dimethylaminopropyl) carbodiimide hydrochloride (EDC·HCl, 12.8 mg, 0.067 mmol) and N,Ndiisopropylethylamine (11 μl, 0.067 mmol) were added and the mixture was left stirring at room temperature for 1 h. Subsequently, Nhydroxysuccinimide (NHS, 6.7 mg, 0.067 mmol) was added and the mixture was stirred at room temperature for 24 h. The MWCNTs–NHS mixture was then filtered under a vacuum, on a 0.1 μm Millipore membrane and the residue was washed several times with DMF, isopropanol and diethyl ether. The obtained nanosystems were dried under a vacuum at 40 °C. The functionalization process is summarized in Fig. 3.3.1.1.

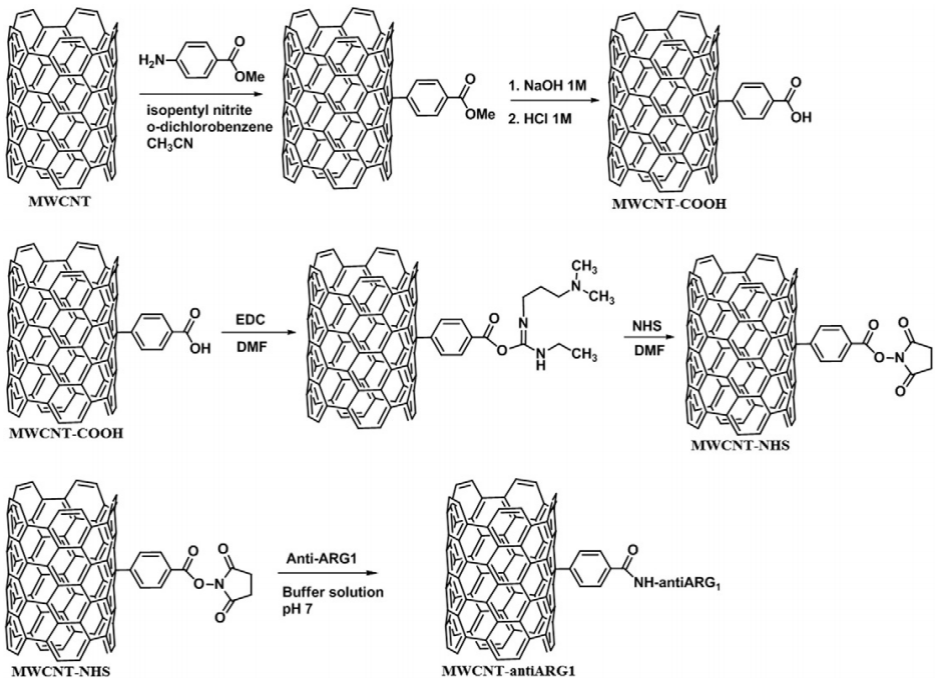


Fig. 3.3.1.1 – Functionalization of MWCNTs in order to link the amino portions of the atibodies

As described in the previous chapter, the antibody can be linked to the CNT through a nucleophilic substitution reaction between the active ester and the amine group of the antibody, forming an amide bond.

The functionalization degree of pristine MWCNTs before functionalization, MWCNTs-COOH and MWCNTs–NHS samples was obtained by comparing the thermogravimetric analysis (**TGA**) data by thermal decomposition of the inserted surface groups, under inert atmosphere. Briefly, TGA is a thermal analysis in which changes in physical and chemical properties of materials are measured as a function of increasing temperature (with constant heating rate), or as a function of time (with constant temperature and/or constant mass loss). In our case, TGA was performed using a temperature ramp of 10 °C/min on a TAQ500 instrument. The pristine MWCNTs do not show any significant weight loss while the weight losses of MWCNT-COOH and

MWCNT–NHS samples, calculated at 700 °C, reached the values of 10% and 14%, respectively (Fig. 3.3.1.2). The difference of weight loss of 4% between MWCNT-COOH and MWCNT–NHS samples, calculated at 700 °C, demonstrated the success of the NHS-ester functionalization reaction. The degree of functionalization is strictly related to the sensor response since it represents the amount of NHS groups which could bind with the anti-ARG1 antibody.

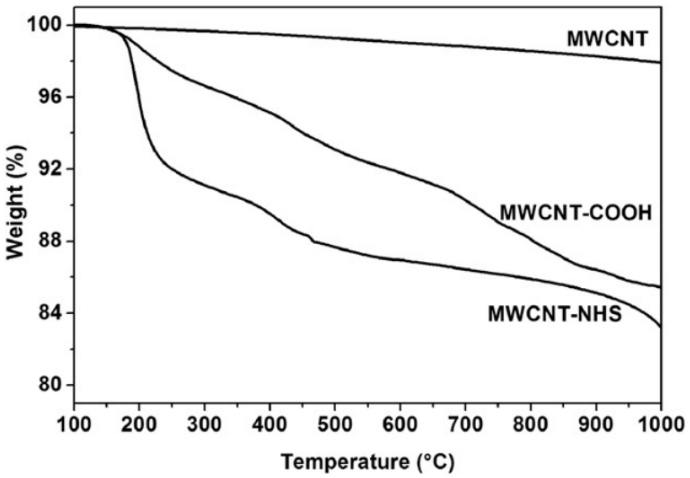


Fig. 3.3.1.2 - TGA for pristine MWCNTs before functionalization, MWCNTs-COOH and MWCNTs-NHS samples.

Functionalized MWCNTs–NHS were deposited between the electrodes, in order to bind the antibodies to the nanotubes. The device geometry, the DEP process and a SEM image of a MWCNT-NHS layer deposited between the electrodes are reported in Fig. 3.3.1.3. In this case, the CNTs concentration in water solution was 1 μg/ml. A voltage of 20 V and a frequency of 100 kHz were set, with a deposition time of 300 s, obtaining a CNT layer resistance of 22 kΩ. Higher resistance values obtained for the other devices under investigation were achieved by reducing the deposition time without changing the other parameters. In particular, 100 kΩ was reached after a deposition time of 120 s and 115 kΩ after 90s. For deposition processes

performed with the same experimental parameters we achieved the same CNT film resistance values within a 2% error. SEM analysis is useful to observe the homogeneity and uniformity of the CNT film (Fig. 3.3.1.3b).

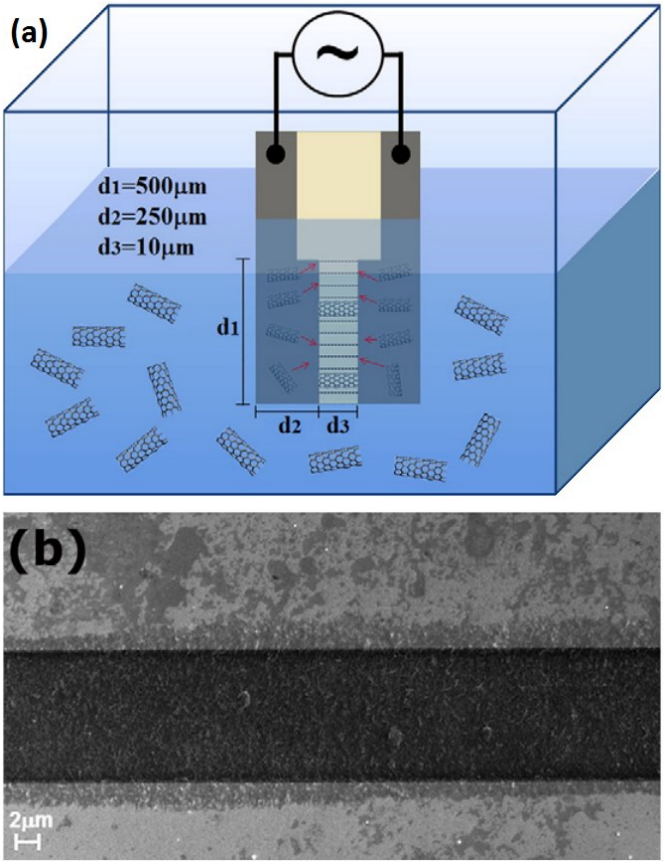


Fig. 3.3.1.3 - (a) Scheme of the DEP system and geometrical features of the device; (b) SEM image of the CNT film region between the electrodes in the sensing device.

**Electrical characterization after the MWCNT-NHS deposition**

Several devices were produced with different CNT layer resistance values. Electrical characterization was performed by a Source Meter Unit (SMU), Keithley 6430, and the current values were acquired for a voltage range

between −1 V and 1 V. The stability of the devices, after DEP deposition, was verified in dry state by repeating the electrical characterization more times consecutively and after 12 h. As an example, in Fig. 3.3.1.4 the I-V characteristics of one device is reported, showing shelf stability and indicating that CNT-NHS functionalization is not changing in the time interval investigated in dry state.

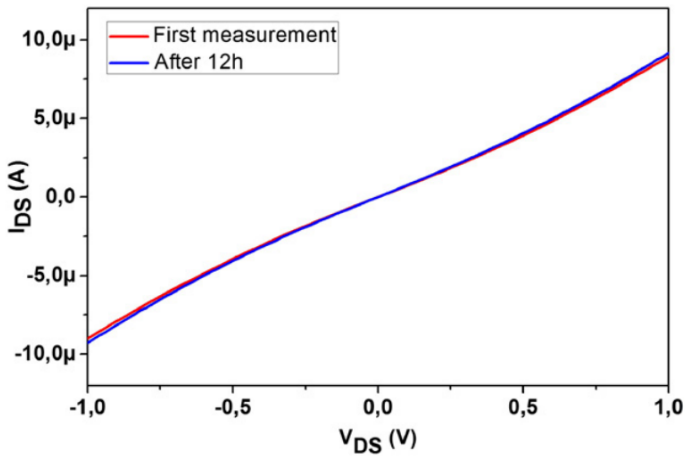


Fig. 3.3.1.4 – I-V characteristics of a typical CNT-based device, just after CNT-NHS dielectrophoretic deposition and after 12 h, showing the stability of the device.

Furthermore, the resistance values of the devices just after DEP deposition and after some days were tested, showing no significant variation. This means that the devices can be prepared with a CNT-NHS film and stored at least for some days before they are used as biosensors, without any visible change in the electrical properties. This is more convenient in terms of time when the sensor has to be used, by avoiding to waste time for the functionalization of CNTs between DEP deposition and the biological steps. Furthermore, for the voltage range here explored and the quantity of CNT deposited, it is evident that the behavior is almost linear, since MWCNTs can be considered almost metallic.

## 3.3.2. Human Arginase-1 detection

The principle of operation of an immunosensor is related to the interaction between antibody and antigen which in this case produces a change of electrical resistance in the nanotubes. To improve the specificity of the sensor, **BSA (Bovine Serum Albumin)** was also used. BSA is a protein derived from cows. It is often used as a protein standard in lab experiments. In our case, BSA (Sigma Aldrich, 05470-1G) is used to block other CNT sites where antigen may bind non-specifically, that is without direct interaction between antibodies and antigens. The procedure used for the arginase detection is described below.

Anti-ARG1 antibody (Ab) (Sigma Aldrich, SAB 4200510) with a 1 μg/ml concentration was dispersed in a dilution buffer solution and a 10 μl droplet was placed on the MWCNT–NHS sensitive layer and left to incubate for 2 h in humid environment. The buffer solution composition used for this experiment is: PBS + TWEEN20 0.05% + BSA 0.4%, where PBS (Phosphate-buffered saline, Euroclone ECB4004L) is a water-based salt solution, commonly used in biological research, because it is a suitable environment for biological interactions; Tween 20 (Sigma Aldrich, P9416) is a detergent (surfactant) commonly added to the buffers in order to enhance the reagents spreading.

The functionalized device was rinsed out in washing buffer (PBS + TWEEN20 0.05%) to remove antibodies not chemically bound, and incubated for further 2 h with a 5 μl droplet of dilution buffer containing ARG-1 (from a Kit ELISA Bio Vendor) with known concentration values in the range of 22–360 ng/ml, followed by a careful rinsing out with DI water. The process is schematically illustrated in Fig. 3.3.2.1. The choice of this concentration range has been done keeping into account the ARG-1 values in

serum observed in normal (<30 ng/ml) or in pathologic conditions in the case of MM disease (>100 ng/ml).

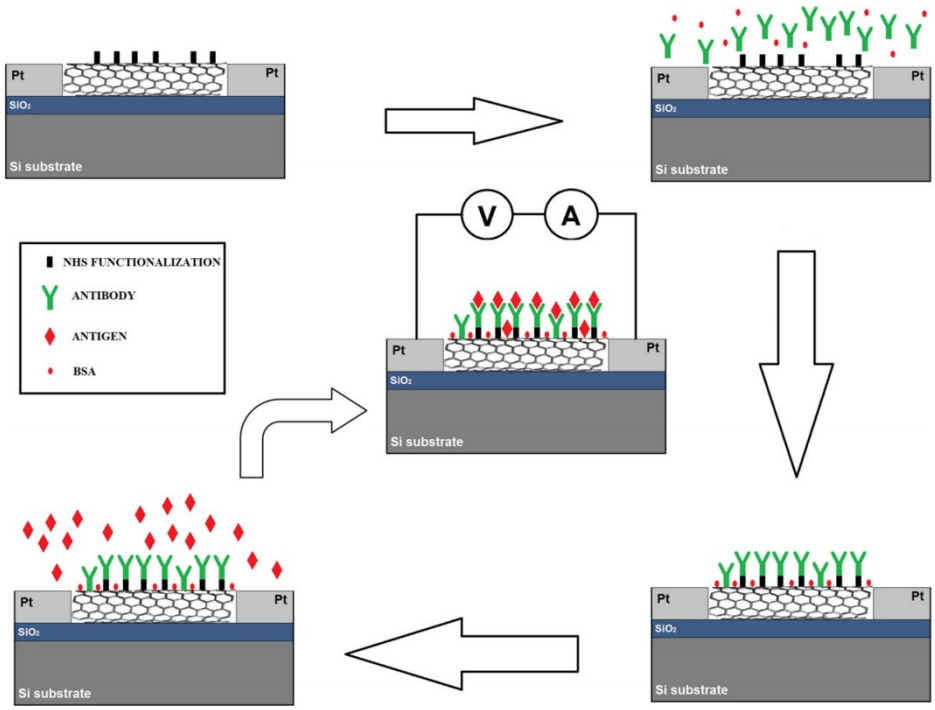


Fig. 3.3.2.1 - Schematization of the CNT–antibody–antigen binding reactions and final electrical characterization.

Electrical characterization was carried out and compared with the initial I-V characteristics of the device (before both CNT–antibody and antibody–antigen interactions). The current–voltage (I-V) characteristic of the CNT-devices was measured before and after Ab incubation and Ab - ARG-1 binding reaction. Each device was used only for a single measurement for a fixed ARG-1 concentration.

It is important to underline that the devices produced are CNTFET and then they may also be characterized by tuning the gate voltage. However, the salt ions in the buffer of the proteins (PBS) penetrate the gate oxide creating an unwanted current path between the gate and source/drain. Therefore, all

electrical characterizations were carried out by imposing a gate voltage equal to zero, operating the device as a CNT-resistor. This problem should not be necessarily seen as a disadvantage, because the use of resistor instead of a FET is much simpler and cheaper, also giving the possibility to use non-conductive plastic substrates.

Fig. 3.3.2.2 shows the I-V characteristics obtained for three groups of devices, after drying, each group showing the same initial CNT layer resistance ($R_0$ = 115 kΩ, 100 kΩ, 22 kΩ). The devices were exposed to AntiARG1 with 1 μg/ml concentration, followed by antibody–antigen binding reaction. In particular, in Fig. 3.3.2.2a and b the investigated antigen concentration values are 180 ng/ml and 360 ng/ml, whereas in Fig. 3.3.2.2c lower ARG-1 concentrations were used, 22 ng/ml and 45 ng/ml. For comparison, the curves obtained in the absence of ARG-1 (0 ng/ml) are reported for each kind of device. Generally, the addition of the protein determines a decrease of the current measured in the CNT layer and the higher is the protein concentration the larger is the current decrease (resistance increase). The current (resistance) changes with respect to the initial value, for a given voltage $V_{DS}$, therefore, it is related to the protein concentration present in the solution drop poured on the sensitive layer of the device. Two sets of each kind ($R_0$) of devices were tested and a reproducibility within a variation below 10% was observed.

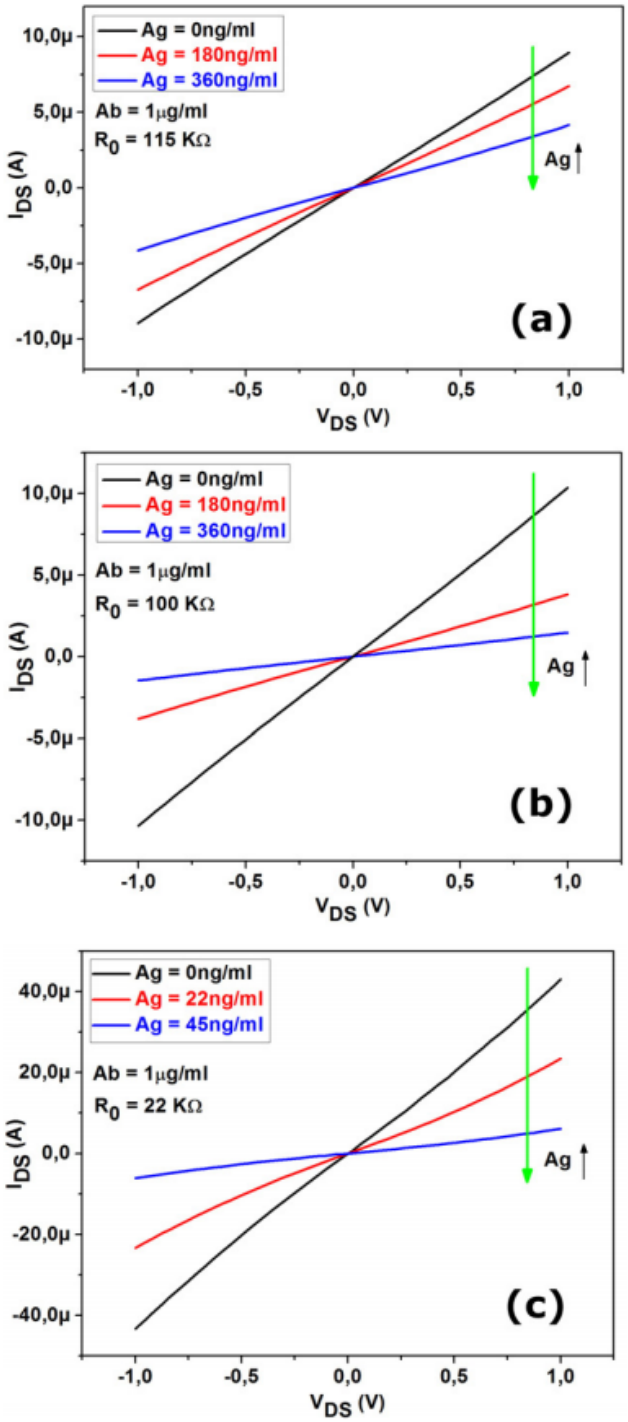


Fig. 3.3.2.2 - . I–V characteristics of CNT-based sensors with different initial resistance values: (a) 115 kΩ, (b) 100 kΩ, and (c) 22 kΩ. Each kind of sensor was tested in a specific range of ARG-1 concentrations.

In Fig. 3.3.2.3 we report a summary of the bio-sensing results that can be extracted from the I–V curves shown in Fig. 3.3.2.2. In particular, for each device the normalized change of the resistance $\Delta R/R_0 = (R - R_0)/R_0$ was calculated, were $R_0$ and R are the CNT film resistance values at V = 1V, respectively, before and after the addition of ARG-1 antigen and its binding with the antibody.

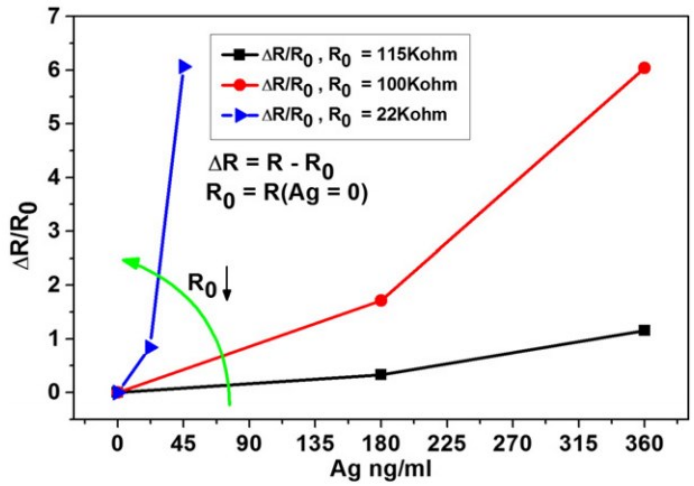


Fig. 3.3.2.3 - Changes of the CNT film resistance observed after antibody-antigen binding reaction, for different ARG-1 concentration values, for each group of devices. The plotted results are calculated using the current values at V = 1 V reported in Fig. 3.3.2.2.

The results reported in Fig. 3.3.2.3 clearly show that the sensitivity range depends on the initial resistance of the device: in order to detect very low ARG-1 concentrations it seems more convenient to use devices with low initial resistance of the CNT layer, whereas for detection of large protein concentration devices with higher initial resistance should be preferred. Indeed, a lower initial resistance means (if the same kind of CNTs are used) that a larger CNT density is present between the electrodes and on the whole layer a larger number of functional groups is available for antibody–antigen binding. This allows to reach a higher sensitivity for low antigen concentration values. In general, a calibration curve can be obtained for

sensors with different initial $R_0$ and in the case of unknown concentrations, as in real samples, it could be useful to use an array of sensors with different initial I-V characteristics and compare their responses. This method would allow to perform a cross check of the results given by the different sensors.

An electronic system based on Arduino microcontroller has been developed in order to obtain a cheap and portable system for the protein detection. The details are shown in the following paragraph.

### 3.3.3. Arduino microcontroller-based system for protein detection

One of the fundamental points of the biosensors production is that they can be easily used with low-cost systems. For this reason, during this thesis work, within PON Hippocrates Project, a measurement system for the developed sensors based on an Arduino microcontroller was produced. In particular, the system is composed of a signal conditioning board, an analog-digital converter, an Arduino UNO Rev3 microcontroller, a display and an SD memory card (Fig. 3.3.3.1).

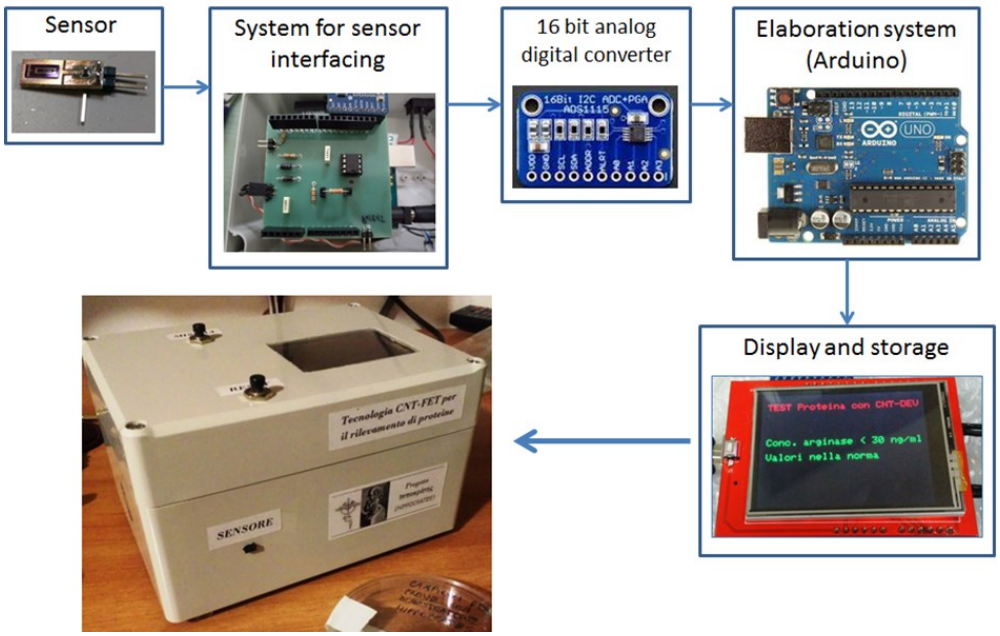


Fig. 3.3.3.1 – Scheme of the Arduino system developed at CNR-IMM, Catania

The conditioning board is composed of a home-made amplifier circuit that takes care of measuring the electrical resistance of the biosensor. The layout of the PCB was developed in order to connect the board with the Arduino microcontroller (Fig. 3.3.3.2).

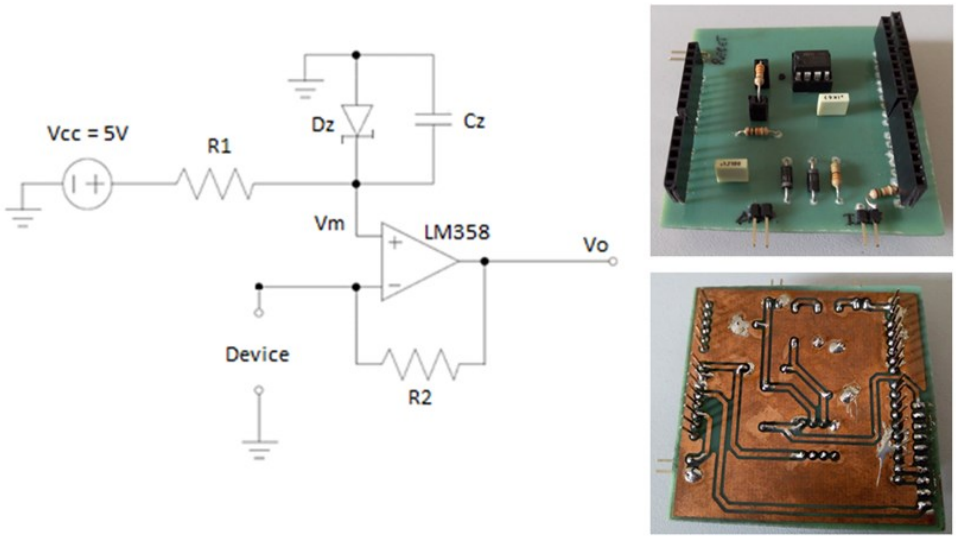


Fig. 3.3.3.2 – Home-made amplifier to measure the resistance of the device under investigation. The voltage Vo is proportional to the resistance value of the device.

The output voltage of the amplifier is linked with the device resistance throught this law:

$$R_{DEVICE} = \frac{R_2}{\frac{V_0}{V_m} - 1}$$

Finally, all circuits were placed in a box with a battery power.

The system works in this way:

- The sensor is connected to the system that measure its initial resistance (that of the CNT-NHS after the dielectrophoresis). Therefore the device can be removed and used to peform the bio-measurement, with the steps shown in the chapters 3;

- After that the interaction with the protein, the sensor can be reconnected with the system and the resistance can be measured again. The resistance change depends on the amount of protein detected;
- The resistance change is compared with a calibration curve stored in the microcontroller that will show in the display the concentration level of arginase detected in the sample.

The code for programming the Arduino microcontroller was developed in C language and is reported in Appendix.

## 3.4. Graphene oxide-based sensors

In the present work, graphene oxide (GO) and thermally reduced GO (rGO) were taken into account as innovative materials for sensing applications. In particular their electrical, chemical and structural properties were investigated. The effect of the environment and temperature on the electrical properties of GO and rGO was evaluated and the correlation, with type and concentration of oxygen functionalities was investigated. Moreover, a preliminary gas sensing test, in particular the detection of ethanol, was performed.

GO was deposited between two Pt electrodes by dielectrophoresis and then characterized, as described for CNTs.

Most devices with different geometries were developed, among which devices with two 250 x 4 μm flat electrodes (Fig. 3.4.1a). GO (from Sigma Aldrich, code 763705) was diluted in DI water to obtain 1μg/ml concentration and deposited between two electrodes using a sine voltage of 10Vpp, frequency of 100 kHz and a deposition time of 240 s. SEM analysis, was performed to study the homogeneity and uniformity of the GO film. (Fig. 3.4.1b).

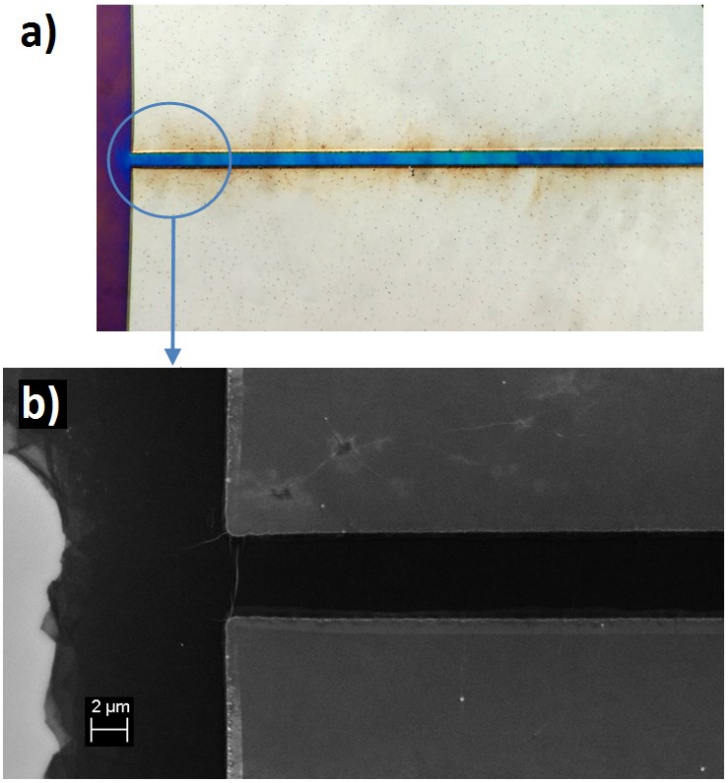


Fig. 3.4.1 – a) optical image of the GO film deposited between the flat electrodes by dielectrophoresis, b) SEM image of the GO film

Several similar devices were produced and some of them underwent a thermal treatment at 200°C for 30min in air environment on a hotplate in order to have rGO as channel layer between the electrodes. In this way, devices with GO and rGO were obtained.

## 3.4.1. Electrical behavior for GO and rGO based devices in air and nitrogen environment

The electrical characterization of GO and rGO devices was performed by a SMU Keithley 6430, with a voltage range between -2V and 2V, at different temperatures, between 25°C and 15°C, placing the device in contact with a Peltier cell, in a home-made system. The electrical behaviour was found to depend on the temperature and measure environment (air or $N_2$).

Since GO contains $sp^3$- bonded hybridized carbon atoms, GO can capture water vapor from external environment easily, owing to its notable hydrophilicity. If the temperature is varied, keeping the device in the air environment, the humidity value also changes in the proximity of the device. For example, as the temperature decreases, below room temperature, there will be a local rise of the humidity. In Fig 3.4.1.1a we report the electrical characterization of the device shown in Fig. 3.4.1: in air environment the current increases as the temperature decreases, while in $N_2$ environment the current is almost zero and does not depend on the temperature. This suggests a humidity effect on the conductivity of GO.

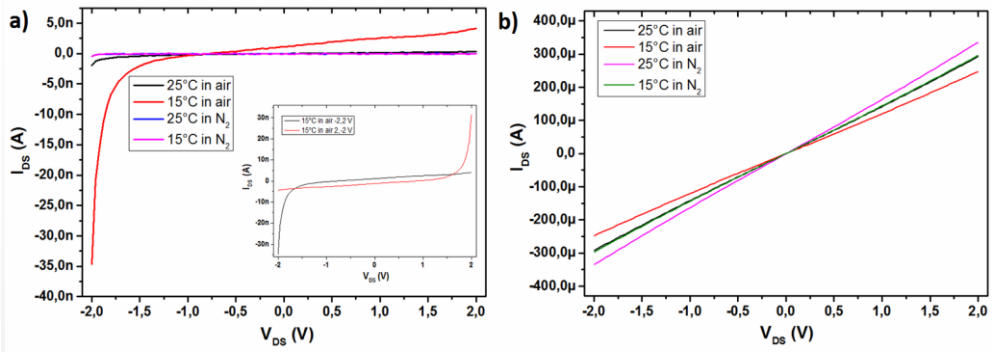


Fig. 3.4.1.1 – electrical characterization of a device with GO (a) and rGO after 200°C for 30min (b) in air and $N_2$ environment

The inset in Fig. 3.4.1.1a shows an opposite electrical response of the device with GO when the measurement is performed from -2V to 2V or from 2V to -2V, due to the insulating nature of the GO and some charging effect.

A different behaviour was observed in the case of rGO. Both in air and $N_2$ environment, the current decreases when the temperature decreases. In particular, the current is higher in $N_2$ then in the air environment, showing that humidity and lower temperature affect negatively the conduction in rGO (Fig. 3.4.1.1b). Results are summarized in Fig. 3.4.1.2a and 3.4.1.2b, where the data are extracted from the graphs in Fig. 3.4.1.1 at V=1V.

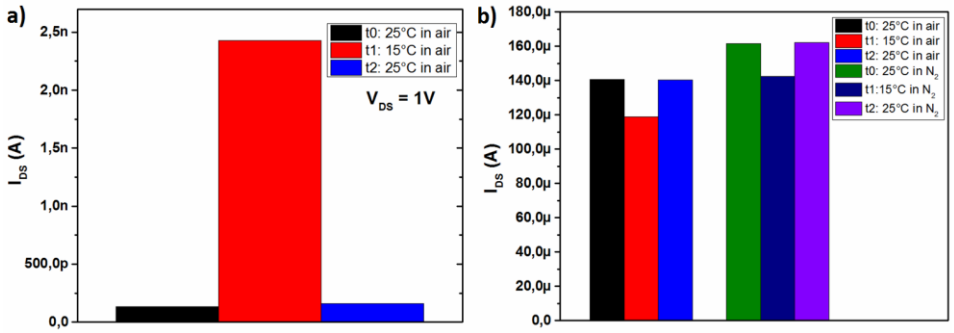


Fig. 3.4.1.2 – Electrical behaviour in the devices with GO (a) and rGO (b)

An electrical characterization over the time was also performed in order to investigate the repeatability of the response. In particular, in Fig. 3.4.1.3a the electrical behaviour of the device with as deposited GO is shown. In this case a small current increase is observed as the temperature decreases in air environment (from 25°C to 15°C), as shown previously. Vice versa in the case of rGO (Fig. 3.4.1.3b) the current decreases as the temperature is reduced (as shown previously), both in air and in $N_2$ environment, with good repeatability and stability in both cases.

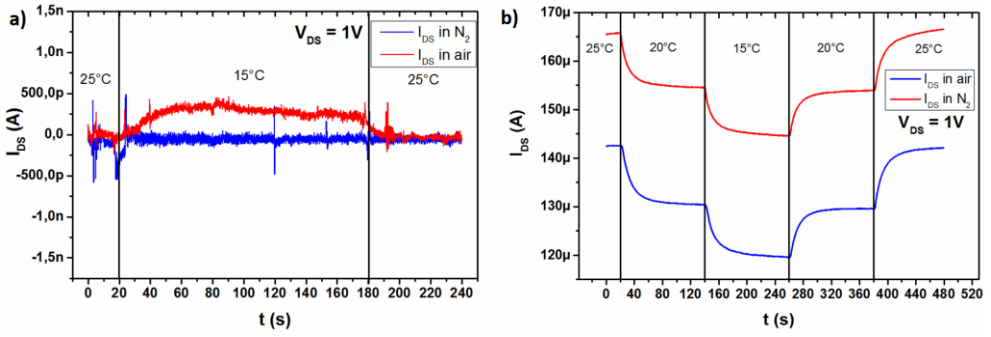


Fig. 3.4.1.3 – Time electrical characterization of the device with GO (a) and rGO (b)

According to the theory of proton transport described in the first chapter, the electrical behaviour depends on the thermal reduction degree of GO (time/temperature) because it is related to a change in the quantity and the type of the functional groups. A further confirmation comes from measurements carried out on a device with GO thermally reduced for 1min at 200°C (low reduction). In this case, a borderline behaviour was noted: both in air and in nitrogen, the sample behaves like the rGO, i.e. the current decreases with decreasing temperature, but in air, over time the trend changes and the current begins to increase (Fig. 3.4.1.4).

This different electrical behaviour, certainly due to the possibility to capture humidity in the air environment, was correlated with the quantity of oxygen and the type of functional groups present in rGO.

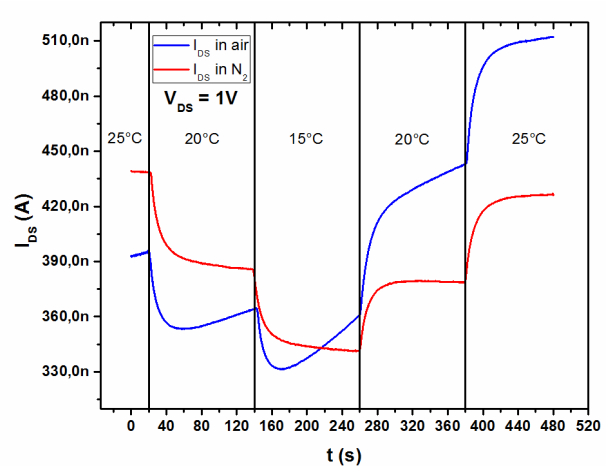


Fig. 3.4.1.4 – Electrical response over the time in the device with GO reduced at 200°C for only 1min. It is possible to note the borderline behaviour due to the low reduction degree

## 3.4.2. AC analysis: Impedance characterization

To further investigate the electrical behavior of the GO, an evaluation of the electrical impedance in AC voltage was carried out. In fact it is possible to associate the AC response with the GO reduction degree. In order to eliminate the parasitic capacitances (that in AC have a big contribute), the measure was done in a glass device with GO deposited between two Al electrodes as described in the dielectrophoretic section. GO was deposited and subsequently thermally reduced for 30min at 60°C, 130°C and 200°C. The impedance measurement was performed using an LCR Meter (HP 4284a), in a frequency range of 20Hz – 1MHz at 0.5V. In Fig. 3.4.2.1a the Nyquist plots of the impedance is shown.

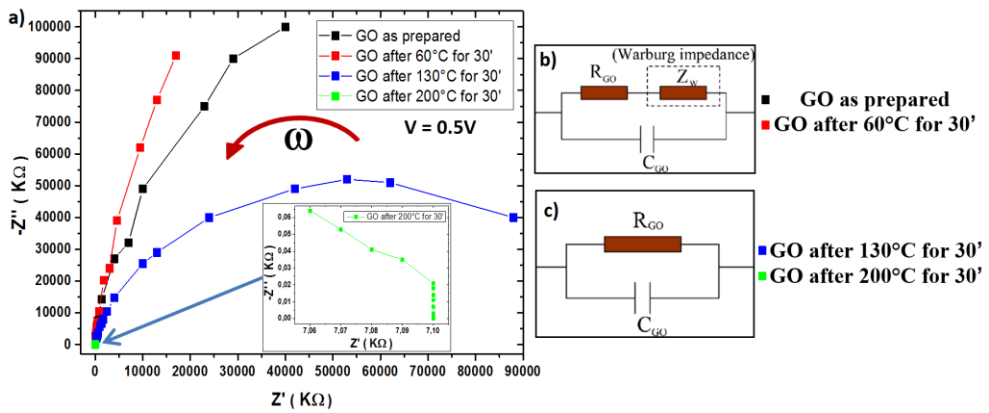


Fig. 3.4.2.1. – a) Nyquist plot of the GO electrical impedance from 20Hz to 1MHz at 0.5V, b) electrical model in the case of GO as prepared and after the thermal process at 60°C for 30min, c) electrical model in the case of GO after a thermal process at T > 130°C for 30min

As prepared GO shows a response with very high impedance at low frequency. This behavior can be explained using the electrical model shown beside the graph, where the Warburg impedance [80] takes into account the

diffusion of ions across the interface between the GO films and the electrodes (Fig. 3.4.2.1b).

After a thermal process at 60°C for 30min, part of water molecules adsorbed in the GO during the deposition process (dielectrophoresis takes place in water) is desorbed leading to a further increase of the impedance, because the conduction due to proton transport is partially decreased. In fact, annealing at 60°C is not sufficient to remove oxygen functional groups but only some adsorbed water. Instead, after a thermal process at T > 130°C for 30min, the reduction of O-functionalities induces a decrease of impedance value and the Nyquist plot shows a behaviour similar to parallel RC (Fig. 3.4.2.1c).

In order to understand what are the functional groups involved at different reduction temperatures, IR characterization was performed. As shown in Fig. 3.4.2.2., 3000 -3700 $cm^{-1}$ in the spectra are related to hydroxyl, carboxyl and water contribution; in the region 800 – 1330 $cm^{-1}$ there is an overlap of different derivatives of ethers (C-O) and epoxides (C-O-C), with epoxides usually found at larger wavenumbers (1220-1320 $cm^{-1}$) and also at about 850 $cm^{-1}$. Another band in the range 1500-1600 $cm^{-1}$, not related to oxygen functionalities, is due to the stretching mode of $sp^2$-hybridized C=C. In the same region vibrational modes related to ketons (C=O) are also present. Higher frequency modes (in the region 1700-1850 $cm^{-1}$) are due to other derivatives of keton groups.

As the temperature is increased the feature between 3000 and 3700$cm^{-1}$ is reduced, as expected due to water removal, and finally at 200°C it is completely removed. The peak at 2400 $cm^{-1}$ associated to the CH and $CO_2$ species is also decreasing as the temperature increases. The variation of the bands in the 1700-1850 $cm^{-1}$ and the 1040-1320 $cm^{-1}$ regions indicate respectively the formation of C=O and C-O / C-O-C when the temperature is raised up to 130°C; a loss of both kinds of bonds is evident when the

temperature is raised up to 200°C and then to 300°C. The C=C bonds starts to be visible after thermal treatments at temperatures higher than 130°C, when the shape of the band in the region 1500-1750 $cm^{-1}$ changes and the feature is shifted towards lower wavenumbers (1500-1600 $cm^{-1}$) (Fig. 3.4.2.2).

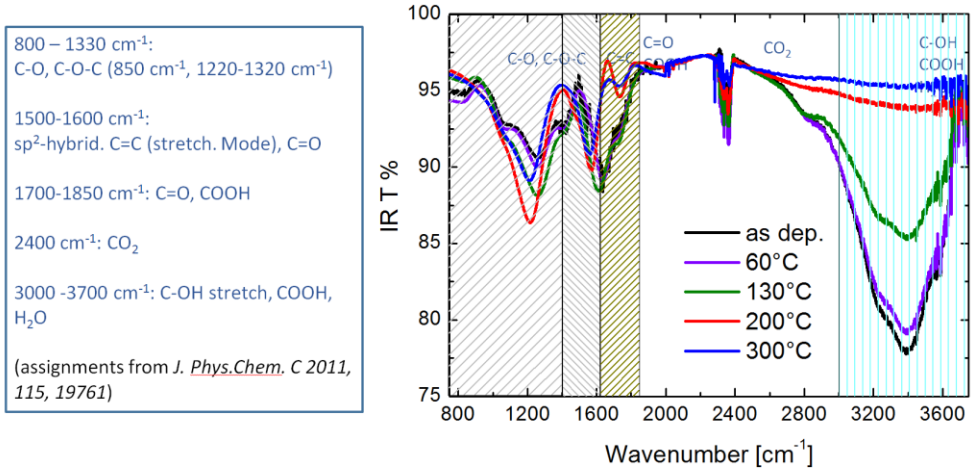


| RT → 60°C → 130°C | 130°C → 200°C | 200°C → 300°C |
|---|---|---|
| **Formation**: $CO_2$, C=O and C-O / C-O-C<br>**Loss**: OH, COOH, $H_2O$ | **Formation**: C=C, C-O<br>**Loss**: OH, COOH, $H_2O$, $CO_2$, C-O-C<br>**Remaining**: C=O | **Loss**: OH, COOH, $H_2O$, $CO_2$, C=O, C-O / C-O-C |

Fig. 3.4.2.2 – IR characterization of the GO at different reduction temperatures

## 3.4.3. Gas detection test: the case of the ethanol

In order to understand the influence of the functional groups on the sensing mechanism, a detection test of ethanol at high concentrations was performed on two devices containing GO reduced by thermal treatment at 200°C or 300°C, respectively. An opposite electrical behavior in these two devices was noted: in the first case (rGO 200° C), in the presence of ethanol there is a reduction of the electrical resistance, while in the second case (rGO 300°C) an increase is observed. The change in response type is attributed to the reduction of oxygen containing functional groups with the thermal treatment. This modifies the interaction of the target gas with the GO samples, leading to a different sensing mechanism. A similar behavior has been observed for $SnO_2$ (bandgap 3.6 eV, R=2.8MOhm) and SnO (bandgap 2.9 eV, R=30kOhm).

Probably a role is played not only by the lower amount of functional groups after thermal treatment, but also on the type of functional groups which ethanol reacts with (Fig. 3.4.3.1).

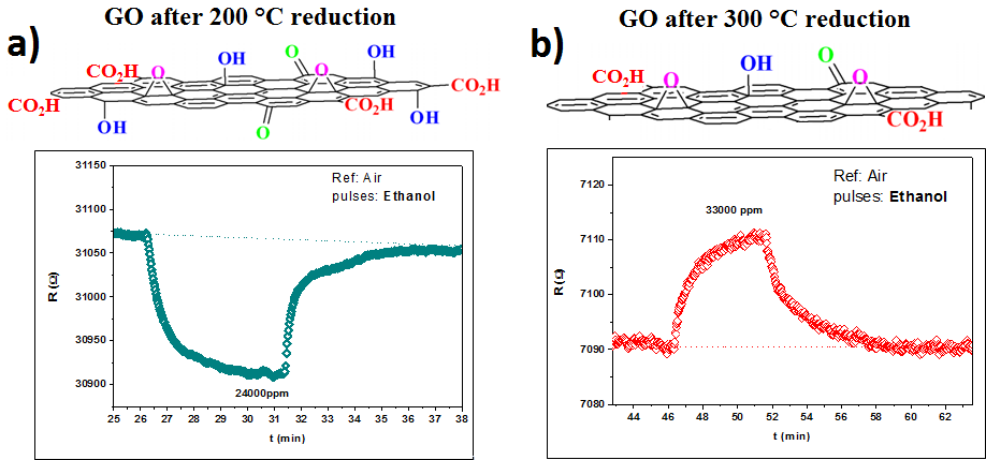


Fig. 3.4.31 – Electrical response to the ethanol of the devices with rGO after 200°C for 30min (a) and after 300°C for 30min (b)

This phenomenon is still under investigation. It has to be noticed that the **sensitivity shown in Fig. 3.4.3.1 can be hugely increased by depositing GO on a larger electrode region**. Indeed the active area of the device considered here is 1 $mm^2$, that has to be compared with areas > 1 $cm^2$ for devices generally used in other literature works.

Another aspect to be taken into account when evaluating the sensitivity of GO is the size of the gas molecules that have to be detected by the GO-based device. Depending on the size, the molecule can penetrate the GO layers or remain on the external surface and this could affect the sensitivity limit.

# Conclusions

In this work, CNT- and GO-based devices were produced and, respectively, used as biosensors (CNT-device) or evaluated as temperature/humidity and VOC sensors (GO-device). The production method of the devices proposedin this thesis work is cheap, involves only low temperature processes, like dielectrophoretic deposition of CNTs, and, therefore, it is compatible with plastic substrates and with the production of disposable biosensors.

In the biosensing case, the detection of ARG-1, a biomarker related to various pathologies, including hematological malignancies like myeloma and lymphoma was performed. For the specific application in hematological malignancies, the sensitivity of the proposed devices is appropriate to detect all the protein concentration ranges from normal values present in serum of healthy individuals (<30 ng/ml), up to higher concentration typical of pathologic conditions (>100 ng/ml). It is comparable to the concentration range detected by commercial ELISA methodology, with the advantage of being less expensive in terms of cost and time-waste. The sensitivity of each sensor can be tuned by using suitable CNT deposition parameters and, therefore, the use of an array of sensors with different initial electrical characteristics can be exploited for reliable protein detection throughout a very large concentration range.

In the case of devices based on GO, the electrical characterization was performed by varying the environmental conditions and the reduction degree of the GO. A dependence on humidity and on the amount of functional groups present on the material was observed and this effect can be exploited for the use of GO in humidity sensing applications. Finally, a preliminary

ethanol detection test has been carried out, showing the promising GO sensitivity for VOC detection applications.

# Appendix

## A1. Moore's Law

Moore's Law is the observation (done in 1965 by Gordon Moore, co-founder of Intel) that the number of transistors per square inch on integrated circuits had doubled every year since the integrated circuit was invented.

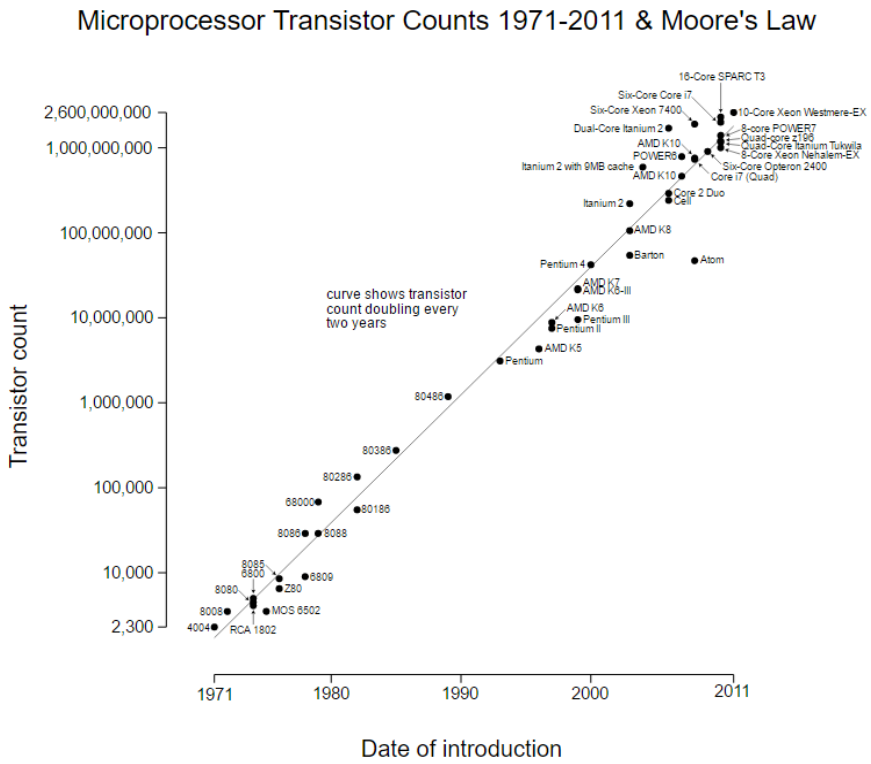


Fig. A1.1 – Trend of the number of the transistor in the ICs from 1971 to 2011 [wikipedia.org]

Moore predicted that this trend would continue for the future. However, in subsequent years, the trend slowed down a bit, but data density has doubled approximately every 18 months, and this is the current definition of Moore's Law, which Moore himself has accepted. Unfortunately, in recent years a decrease in the trend was observed, inevitably due to the technological limits of the silicon. For this reason, technologies based on nanostructured materials are being developed, in order to ensure the trend imposed by Moore's law.

# A2. Scanning electron microscopy (SEM)

A **scanning electron microscope (SEM)** is a type of electron microscope that produces images of a sample by scanning it with a focused beam of electrons. The electrons interact with atoms in the sample, producing various signals that can be detected and that contain information about the sample's surface topography and composition. The electron beam is generally scanned in a raster scan pattern, and the beam's position is combined with the detected signal to produce an image. SEM can achieve resolution better than 1 nanometer. Specimens can be observed in high vacuum, in low vacuum, and (in environmental SEM) in wet conditions. The most common detection mode is by secondary electrons emitted by atoms excited by the electron beam. The secondary electrons number is a function of the angle between the surface and the beam. On a flat surface, the plume of secondary electrons is mostly contained by the sample, but on a tilted surface, the plume is partially exposed and more electrons are emitted. By scanning the sample and detecting the secondary electrons, an image displaying the tilt of the surface is created. In figure A2.1 a SEM basic scheme is shown. The SEM used in the present thesis work is a high resolution SEM (Zeiss Supra 35), with a Schottky field emitter. The electron beam energy is ranging between 0.1 and 30 keV and this wide energy range allows to probe different volumes of the sample. Low energy ($\leq$ 2keV) electron beam can be used for the observation of insulating samples, in order to reduce the charging during the analysis, and for samples that deteriorate easily under the electron beam, like polymers. The resolution that can be reached is about 1 nm at 20 kV and 2.1 nm at 1kV, using a work distance of 2 mm, even though the final resolution depends on the kind of material analyzed. Three detectors are present in the SEM chamber: in-lens SE detector, in chamber Everhart-Thornley detector and a

backscattered electron detector. The latter one is sensitive to the compositional contrast, due to the dependence of the backscattering process on the atomic number of the probed samples.

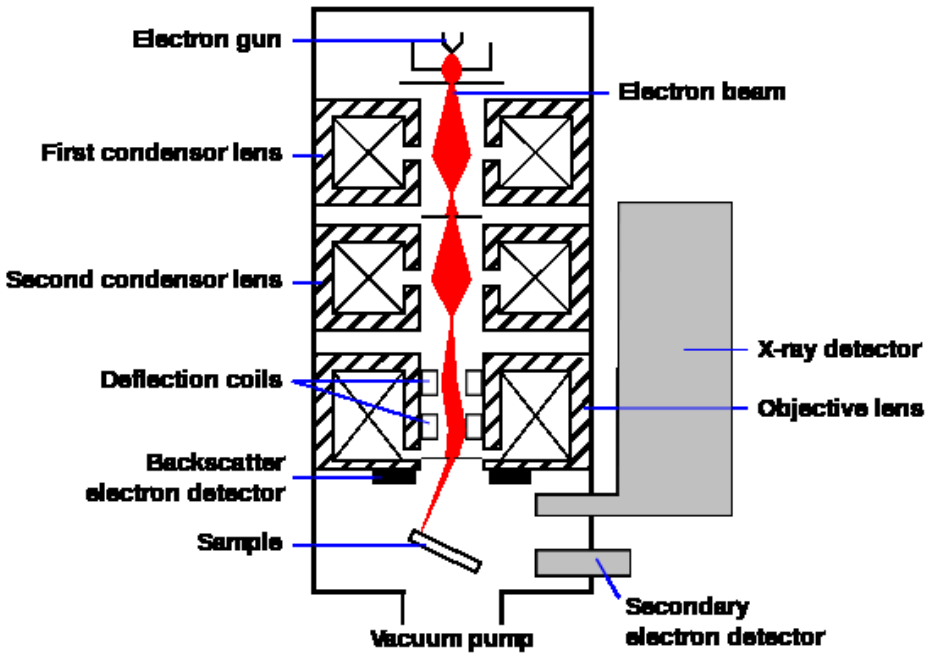


Fig. A2.1 - SEM basic scheme [www.wikipedia.org]

# A3. Optical lithography

**Photolithography**, also termed **optical lithography** or UV lithography, is the process of transferring geometric shapes on a mask to the surface of a substrate. It uses light to transfer a geometric pattern from a photomask to a light-sensitive chemical "**photoresist**", or simply "resist," on the substrate. In the process of transferring on the silicon wafer, the steps involved in the photolithographic process are wafer cleaning, barrier layer formation, photoresist application, soft baking, mask alignment, exposure and development and hard-baking.

## Wafer Cleaning, Barrier Formation and Photoresist Application

In the first step, the wafers are chemically cleaned to remove particulate matter on the surface as well as any traces of organic, ionic, and metallic impurities. After cleaning, silicon dioxide, which serves as a barrier layer, is deposited on the surface of the wafer. After the formation of the $SiO_2$ layer (thermally grown or deposited), photoresist is applied to the surface of the wafer. High-speed centrifugal whirling of silicon wafers is the standard method for applying photoresist coatings in IC manufacturing. This technique, known as "Spin Coating," produces a thin uniform layer of photoresist on the wafer surface.

## Positive and Negative Photoresist

There are two types of photoresist: positive and negative. For positive resists, the resist is exposed with UV light wherever the underlying material is to be removed. In these resists, exposure to the UV light changes the chemical structure of the resist so that it becomes more soluble in the developer.

The exposed resist is then washed away by the developer solution, leaving windows of the bare underlying material. In other words, "whatever shows, goes." The mask, therefore, contains an exact copy of the pattern which is to remain on the wafer.

Negative resists behave in just the opposite manner. Exposure to the UV light causes the negative resist to become polymerized, and more difficult to dissolve. Therefore, the negative resist remains on the surface wherever it is exposed, and the developer solution removes only the unexposed portions. Masks used for negative photoresists, therefore, contain the inverse (or photographic "negative") of the pattern to be transferred. The figure A3.1 shows the pattern differences generated from the use of positive and negative resist.

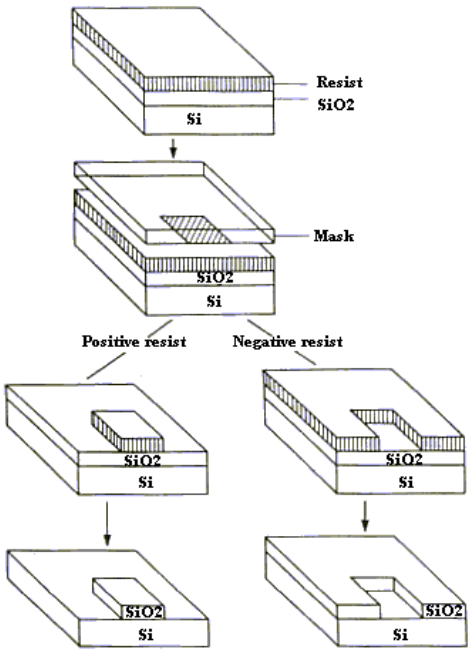


Fig. A3.1 - Pattern differences generated from the use of positive and negative resist [http://www.ece.gatech.edu/]

Negative resists were popular in the early history of integrated circuit processing, but positive resist gradually became more widely used since they offer better process controllability for small geometry features. Positive resists are now the dominant type of resist used in VLSI fabrication processes.

## Soft-Baking

Soft-baking is the step during which almost all of the solvents are removed from the photoresist coating. Soft-baking plays a very critical role in photo-imaging. The photoresist coatings become photosensitive, or imageable, only after softbaking. Oversoft-baking will degrade the photosensitivity of resists

by either reducing the developer solubility or actually destroying a portion of the sensitizer. Undersoft-baking will prevent light from reaching the sensitizer. Positive resists are incompletely exposed if considerable solvent remains in the coating. This undersoft-baked positive resists is then readily attacked by the developer in both exposed and unexposed areas, causing less etching resistance.

## Mask Alignment and Exposure

One of the most important steps in the photolithography process is mask alignment. A mask or "photomask" is a square glass plate with a patterned emulsion of metal film on one side. The mask is aligned with the wafer, so that the pattern can be transferred onto the wafer surface. Each mask after the first one must be aligned to the previous pattern. Once the mask has been accurately aligned with the pattern on the wafer's surface, the photoresist is exposed through the pattern on the mask with a high intensity ultraviolet light. There are three primary exposure methods: **contact, proximity, and projection.** They are shown in the figure A3.2.

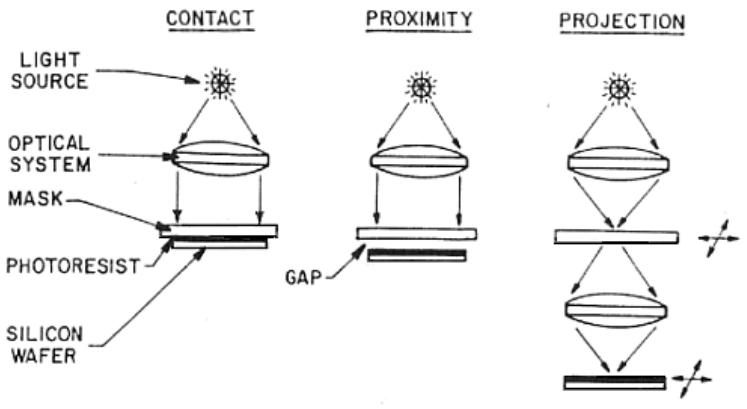


Fig. A3.2 - Photolithography exposure methods [http://www.ece.gatech.edu/]

## Contact Printing

In contact printing, the resist-coated silicon wafer is brought into physical contact with the glass photomask. The wafer is held on a vacuum chuck, and the whole assembly rises until the wafer and mask contact each other. The photoresist is exposed with UV light while the wafer is in contact position with the mask. Because of the contact between the resist and mask, very high resolution is possible in contact printing (e.g. 1-micron features in 0.5 microns of positive resist). The problem with contact printing is that debris, trapped between the resist and the mask, can damage the mask and cause defects in the pattern.

## Proximity Printing

The proximity exposure method is similar to contact printing except that a small gap, 10 to 25 microns wide, is maintained between the wafer and the mask during exposure. This gap minimizes (but may not eliminate) mask damage. Approximately 2- to 4-micron resolution is possible with proximity printing.

## Projection Printing

Projection printing, avoids mask damage entirely. An image of the patterns on the mask is projected onto the resist-coated wafer, which is many centimeters away. In order to achieve high resolution, only a small portion of the mask is imaged. This small image field is scanned or stepped over the surface of the wafer. Projection printers that step the mask image over the wafer surface are called step-and-repeat systems. Step-and-repeat projection printers are capable of approximately 1-micron resolution.

## Development

One of the last steps in the photolithographic process is development. The figure A3.3 shows response curves for negative and positive resist after exposure and development.

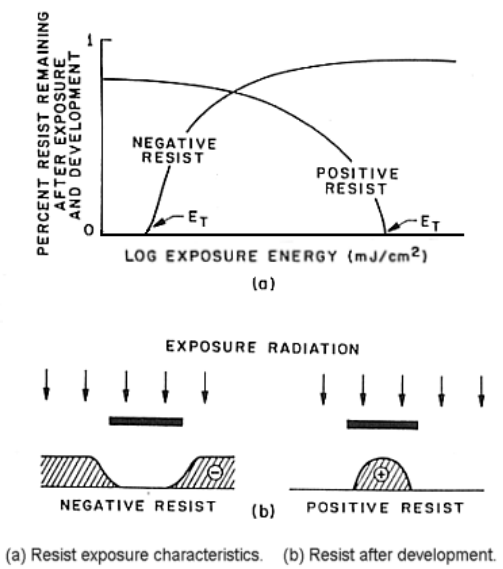


Fig. A3.3 – Resist exposure characteristics and after development [http://www.ece.gatech.edu/]

At low-exposure energies, the negative resist remains completely soluble in the developer solution. As the exposure is increased above a threshold energy Et, more of the resist film remains after development. At exposures two or three times the threshold energy, very little of the resist film is dissolved. For positive resists, the resist solubility in its developer is finite even at zero-exposure energy. The solubility gradually increases until, at some threshold, it becomes completely soluble. These curves are affected by all the resist processing variables: initial resist thickness, prebake conditions, developer chemistry, developing time, and others.

## Hard-Baking

Hard-baking is the final step in the photolithographic process. This step is necessary in order to harden the photoresist and improve adhesion of the photoresist to the wafer surface.

## Lift-OFF technique

The lift-off is a technique that avoids the acid etching of the metal at the end of the manufacturing process of the devices. In particular, with this system, the metal to be deleted is located on the resist that can be removed with a simple etching in acetone place in ultrasound. In Fig. A3.4 an example of the lift off technique is shown.

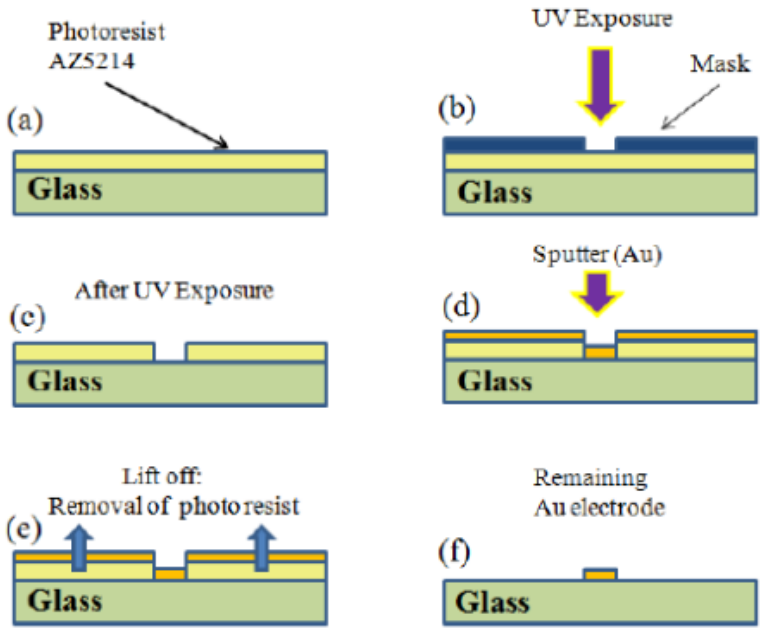


Fig. A3.4 - Lift off fabrication process of electrodes. (a) AZ5214 photoresist coating on the glass surface. (b) UV exposure on the mask. (c) Object is ready for sputtering. (d) Gold (Au) sputtering on the surface. (e) Removal of the AZ5214 photorest by ultrasonic cleaner. (f) Remaining Au electrode on the glass surface [Md. Habibur Rahman et al., 2014, DOI: 10.11113/jt.v70.3467]

# A4. Immunoassay in biosensing field

An immunoassay is a biochemical test that measures the concentration of molecules in a solution through the use of **antibodies**. The molecules detected by the immunoassay, named **Antigen**, are in many cases protein, although may be other kinds of molecules, of different size and types. The test, much used in medicine and research, is frequently carried out in biological liquids such as serum, urine or PBS (Phosphate-buffered saline).
The principle of operation consists on the ability of an antibody to recognize and bind a specific macromolecule (antigen) in a complex mixture of macromolecules. In other words, for each antigen exists a specific antibody able to bind only with it. The bond is non-covalent, typically hydrogen or electrostatic bond that involves the Van der Waals forces. In Fig. A4.1 a schematics of the interaction between antibody and antigen is reported.

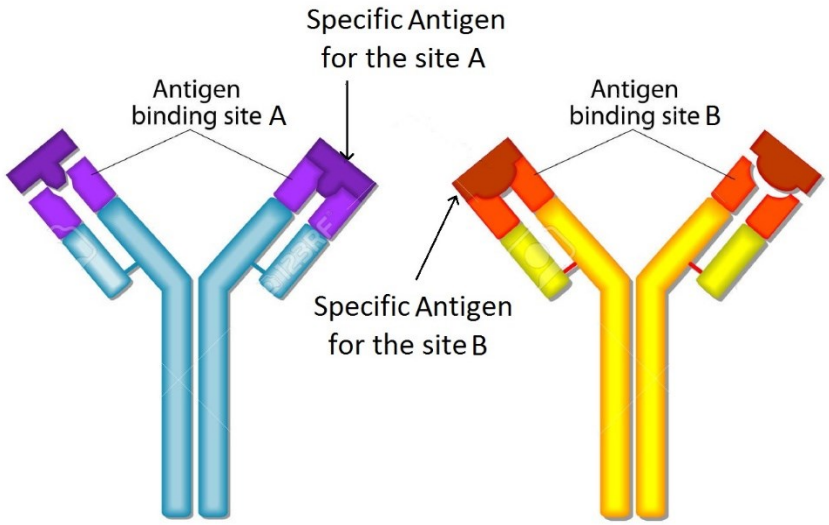


Fig. A4.1- Schematization of antigens-antibodies interaction [http://www.123rf.com/]

There are many techniques that use this specific interaction, and in biology the most common are the **Immunofluorescence**, the **ELISA (Enzyme-Linked Immunosorbent Assay)** and the **RIA (Radio Immunoassay)**. These techniques will be briefly described below.

## Immunofluorescence

Immunofluorescence is a technique used to detect in a sample the presence of specific antigens or antibodies unknown where the note counterpart (the one available to the researcher) is linked to a marker (or label). The marker is a fluorochrome (typically the **fluorescein**), an ultraviolet absorbing dye that emits in the visible (green light). A schematization of immunofluorescence process in Fig. A4.2 is shown.

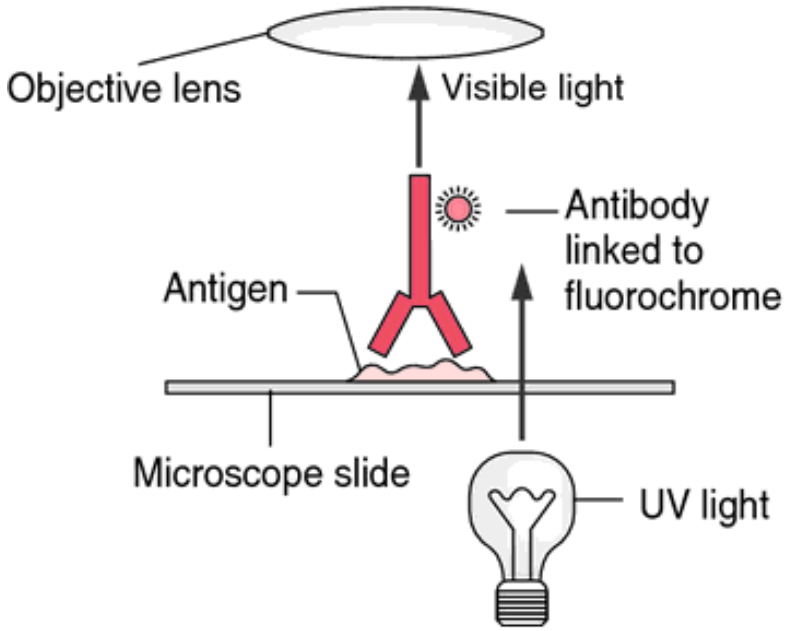


Fig. A4.2 – Schematization of immunofluorescence process [http://medical-dictionary.thefreedictionary.com/immunofluorescence].

## ELISA (Enzyme-Linked Immunosorbent Assay)

ELISA is an immunological analysis method used in biochemistry to detect the presence of a substance (usually an antigen) in liquid (PBS, Serum) using antibodies linked to an enzyme.

ELISA is typically used to detect the presence of antibodies against a given antigen in the blood plasma of a patient to see if there has been exposure to a given pathogen. This takes place in the test for HIV to see if the immune system of the subject was confronted with the AIDS virus.

There are two types of the ELISA test: **direct and sandwich** (Fig. A4.3)

In the direct test, unknown antigens from the sample are attached to a surface. Then, a specific primary antibody (linked to an enzyme) is applied over the surface. If the antibody is the right one, it will bind with the antigen. Finally, a substrate is added and, reacting with the enzyme linked to the antibody, produces a detectable signal, most commonly a colour change in the substrate. In this way, the colour intensity is linked to the quantity of the antigen.

In the sandwich test, instead, the primary antibodies are attached to a surface. Then, unknown antigens is applied over the surface. If the antibody is the right one, the antigen will bind with the antibody. At this point, secondary antibodies, linked to an enzyme (labelled antibodies) are applied. These antibodies will bind to the primary antibody-antigen complex. Finally, a substrate is added and, reacting with the enzyme linked to the antibody, produces a detectable signal.

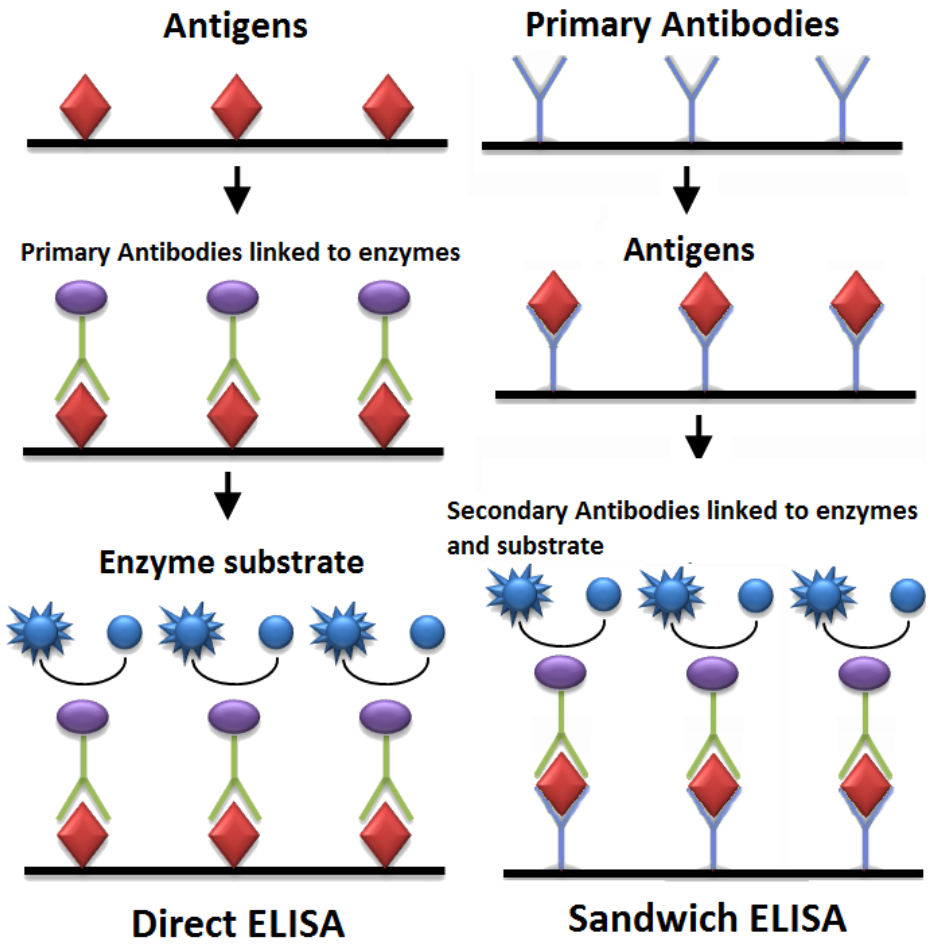


Fig. A4.3 – Schematization of the ELISA test [wikpedia.org]

ELISA is used for several antigens detection. The limits of detection depend on the type of antigen but usually can be detected up to nanograms/millilitres. However, most of the reagents used in immunoassays such as antibodies, enzymes, and fluorescence labels are very expensive. Moreover, is necessary to collect several samples because the test is performed on several samples in parallel.

## Radioimmunoassay (RIA)

**Radioimmunoassay (RIA)** is a technique that measures the presence of an antigen with very high sensitivity. Basically any biological substance for which a specific antibody exists can be measured, even in minute concentrations. RIA has been the first immunoassay technique developed to analyze picomolar concentrations of hormones in biological fluids. The principle of operation is always based on antigen-antibody binding. The target (antigen) is labeled radioactively and bound to its specific antibodies (a limited and known amount of the specific antibody has to be added). A sample, for example a blood-serum, is then added in order to initiate a competitive reaction of the labeled antigens from the preparation, and the unlabeled antigens from the serum-sample, with the specific antibodies. The competition for the antibodies will release a certain amount of labeled antigen. This amount is proportional to the ratio of labeled to unlabeled antigen. A binding curve can then be generated which allows the amount of antigen in the patient's serum to be derived. That means that as the concentration of unlabeled antigen is increased, more of it binds to the antibody, displacing the labeled variant. The bound antigens are then separated from the unbound ones, and the radioactivity of the free antigens remaining in the supernatant is measured. A binding curve can be generated using a known standard, which allows the amount of antigens in the patient's serum to be derived (Fig. A4.4).

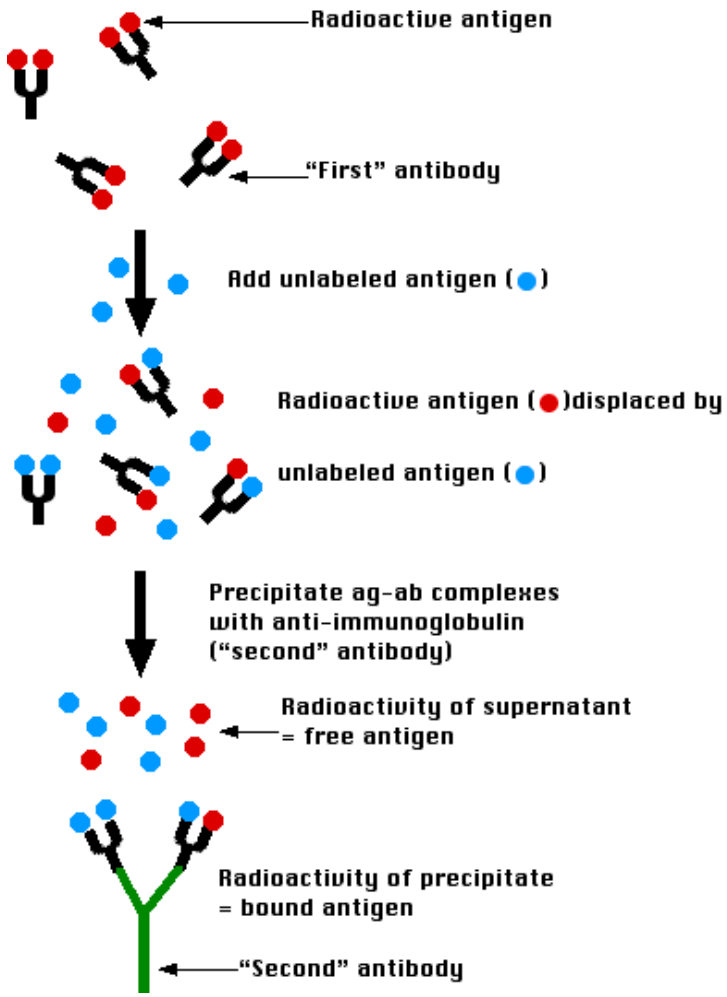


Fig. A4.4 – Schematization of radioimmunoassay [http://www.biology-pages.info/R/Radioimmunoassay.html].

Radioimmunoassay is an old assay technique but it is still a widely used assay and continues to offer distinct advantages in terms of simplicity and sensitivity. However, this technique require sophisticated instrumentation and time-consuming procedures and most of the reagents employed are expensive.

# A5. Code developed in “C” language for the Arduino microcontroller -based system

```
#define LCD_CS A3
#define LCD_CD A2
#define LCD_WR A1
#define LCD_RD A0
// you can also just connect RESET to the arduino RESET pin
#define LCD_RESET A4
//Duemilanove/Diecimila/UNO/etc ('168 and '328 chips) microcontoller:
// Color definitions
#define         BLACK          0x0000
#define         BLUE           0x001F
#define         RED            0xF800
#define         GREEN          0x07E0
#define CYAN           0x07FF
#define MAGENTA        0xF81F
#define YELLOW         0xFFE0
#define WHITE          0xFFFF
#include "SPI.h"
#include "Adafruit_GFX.h"
#include "Adafruit_ILI9341.h"
#include <Adafruit_ADS1015.h>
#define TFT_DC 9
#define TFT_CS 10
//TFTLCD tft(LCD_CS, LCD_CD, LCD_WR, LCD_RD, LCD_RESET);
Adafruit_ILI9341 tft = Adafruit_ILI9341(TFT_CS, TFT_DC);
```

```
Adafruit_ADS1115 ads;
void setup(void) {

Serial.begin(9600);
  pinMode(0, INPUT);
  pinMode(1, OUTPUT);
  //uint16_t identifier = tft.readRegister(0x0);
  Serial.print("ID=");
  //Serial.println(identifier, HEX);
  delay(1000);
  tft.begin();
  ads.setGain(GAIN_ONE);
  ads.begin();

  }

void loop(void) {

  digitalWrite(1, HIGH);
  int16_t adc0;
  float Res=0;
  float Res_i=0;
  float Res_m=0;
  float Rf=32620.00; // resistenza di retroazione (ohm), sostituibile in base al
range di resistenze da misurare
  float Vdz=1062.00; // tensione di misura
  float Vo=0;
  boolean D0;
```

```
int x, i;
tft.begin();
tft.setRotation(1);
tft.fillScreen(BLACK);
tft.setCursor(40,30);
tft.setTextColor(RED);
tft.setTextSize(2);
tft.println("  HIPPOCRATES PROJECT");
tft.println("  ");
tft.setCursor(70,50);
tft.println("  CNT-BIOSENSOR");
tft.setTextColor(WHITE);
tft.setTextSize(3);
tft.println("  ");
tft.setTextSize(2);
tft.println("    Inserisci il sensore e");
tft.println("    mantieni premuto il");
tft.println("  ");
tft.println("    tasto misura per 3s...");
tft.setTextSize(2);
tft.println("  ");
x=0;

 for(;;){
   if(digitalRead(0)==LOW && x==5){
     delay(500);
     for(i=0;i<200;i++){
     adc0 = ads.readADC_SingleEnded(3);
```

```
    Vo=adc0*0.125;
     if(Vo<2000.00){
       ads.setGain(GAIN_TWO);
       adc0 = ads.readADC_SingleEnded(3);
       Vo=adc0*0.0625;
       ads.setGain(GAIN_ONE);
     }
    Res=Rf/(1000*((Vo/Vdz)-1));
    Res_i=Res+Res_i;
   }

Res=Res_i/200.00;
delay (500);
tft.begin();
tft.setRotation(1);
tft.fillScreen(BLACK);
tft.setCursor(40,30);
tft.setTextColor(RED);
tft.setTextSize(2);
tft.println("  HIPPOCRATES PROJECT");
tft.println("  ");
tft.setCursor(70,50);
tft.println("  CNT-BIOSENSOR");
tft.setTextColor(WHITE);
tft.setTextSize(3);
tft.println("  ");
tft.setTextSize(2);
tft.println("    Resistenza sensore:");
```

```
tft.setTextSize(2);
tft.println("  ");
tft.print("    ");
tft.print(Res);
tft.println(" kohm");
Res_m=Res;
Res=0.00;
Res_i=0.00;
tft.println("  ");
tft.println("    Valore memorizzato!");
delay(5000);
tft.begin();
tft.setRotation(1);
tft.fillScreen(BLACK);
tft.setCursor(40,30);
tft.setTextColor(RED);
tft.setTextSize(2);
tft.println("  HIPPOCRATES PROJECT");
tft.println("  ");
tft.setCursor(70,50);
tft.println("  CNT-BIOSENSOR");
tft.setTextColor(WHITE);
tft.setTextSize(3);
tft.println("  ");
tft.setTextSize(3);
tft.setTextSize(2);
tft.println("    Rimuovi il sensore,");
tft.println("  ");
```

```
tft.println("    esegui l'interazione ");
tft.println("  ");
tft.println("    biologica e quindi ");
tft.println("  ");
tft.println("    riesegui la misura...");
tft.setTextSize(2);
tft.println("  ");
tft.setTextSize(2);
x=0;

   for(;;){
    if(digitalRead(0)==LOW && x==5){
     delay(500);
     for(i=0;i<200;i++){
     adc0 = ads.readADC_SingleEnded(3);
     Vo=adc0*0.125;
      if(Vo<2000.00){
        ads.setGain(GAIN_TWO);
        adc0 = ads.readADC_SingleEnded(3);
        Vo=adc0*0.0625;
        ads.setGain(GAIN_ONE);
      }
     Res=Rf/(1000*((Vo/Vdz)-1));
     Res_i=Res+Res_i;
     }

Res=Res_i/200.00;
Res_i=(Res-Res_m)/Res_m;
```

```
tft.begin();
tft.setRotation(1);
tft.fillScreen(BLACK);
tft.setCursor(40,30);
tft.setTextColor(RED);
tft.setTextSize(2);
tft.println("  HIPPOCRATES PROJECT");
tft.println("  ");
tft.setCursor(70,50);
tft.println("  CNT-BIOSENSOR");
tft.setTextColor(WHITE);
tft.setTextSize(2);
tft.println("  ");
tft.println("     Resistenza sensore:");
tft.setTextSize(2);
tft.println("   ");
tft.print("     ");
tft.print(Res);
tft.println(" kohm");
tft.println("  ");
tft.print("     DeltaR: "); tft.print(Res_i*100);tft.println(" %");
tft.setTextSize(2);
tft.println("  ");
x=0;
delay(5000);

if((Res_m<50 && Res_i<1.96)||(Res_m>50 && Res_i<0.10)){ //Res_m è il
```
valore di resistenza misurato prima della fase bio mentre Res_i è il

deltaR/Res_m. I valori di confronto possono essere modificati in base alla retta di taratura

```
  tft.begin();
  tft.setRotation(1);
  tft.fillScreen(BLACK);
  tft.setCursor(40,30);
  tft.setTextColor(RED);
  tft.setTextSize(2);
  tft.println("  HIPPOCRATES PROJECT");
  tft.println("  ");
  tft.setCursor(70,50);
  tft.println("  CNT-BIOSENSOR");
  tft.setTextColor(GREEN);
  tft.setTextSize(3);
  tft.println("  ");
  tft.setTextSize(2);
  tft.println("  ");
  tft.println("    ARG1 < 30 ng/ml");
  tft.setTextSize(2);
  tft.println("  ");
  tft.println("    Valore nella norma");
  tft.setTextSize(2);
  tft.println("  ");
   }else{
          tft.setRotation(1);
          tft.fillScreen(BLACK);
          tft.setCursor(40,30);
          tft.setTextColor(RED);
```

```
        tft.setTextSize(2);
        tft.println("  HIPPOCRATES PROJECT");
        tft.println("  ");
        tft.setCursor(70,50);
        tft.println("  CNT-BIOSENSOR");
        tft.setTextColor(GREEN);
        tft.setTextSize(3);
        tft.println("  ");
        tft.setTextSize(2);
        tft.println("  ");
        tft.println("    ARG1 > 30 ng/ml");
        tft.setTextSize(2);
        tft.println("  ");
        tft.println("    Valore fuori norma");
        tft.setTextSize(2);
        tft.println("  ");}

 delay(5000);
}
 if(digitalRead(0)==LOW){
     x++;
     delay(200);
     }
    Serial.println(x);
  }
 }
  if(digitalRead(0)==LOW){
      x++;
```

```
      delay(200);
      }
    Serial.println(x);
    }
  delay(1000);
}
```

# References

[1] Q. Zhao, Z. Ganand and Q. Zhuang// Electroanalysis. 14(2002)1609.

[2] M. Musameh, J. Wang, A. Merkoci and Y. Lin // Electochem. Commun. 4 (2002) 743.

[3] J.J. Gooding, R. Wibowo, J.Q. Liu, W. Yang, D. Losic, S. Orbons, F.J. Mearns, J.G. Shapter and D. B. Hibbert// J. Am.Chem. Soc. 125 (2003) 9006.

[4] X. Yu, D. Chattopadhyay, I. Galeska, F. Papadimitrakopoulos and J.F. Rusling, Electochem. Commun. 5 (2003) 408.

[5] Loh KP, Bao Q, Eda G, Chhowalla M: Graphene oxide as a chemically tunable platform for optical applications. Nat Chem 2010, 2:1015–1024.

[6] Eda G, Chhowalla M: Chemically derived graphene oxide: towards largearea thin-film electronics and optoelectronics. Adv Mater 2010, 22: 2392–2415.

[7] Balapanuru J, Yang J, Xiao S, Bao Q, Jahan M, Xu Q, Loh KP: A graphene oxide–organic dye ionic complex with DNA-sensing and optical-limiting properties. Angew Chem 2010, 122:6699–6703.

[8] Si, S., Li, S., Ming, Z. and Jin, L. (2010) Humidity Sensors Based on ZnO Colloidal Nanocrystal Clusters. Chemical Physics Letters, 493, 288-291.

[9] Yamazoe, N. and Shimizu, Y. (1986) Humidity Sensors: Principles and Applications. Sensors and Actuators, 10, 379-398.

[10] Erol, A., Okur, S., Comba, B., Mermer, O. and Arikan, M. (2010) Humidity Sensing Properties of ZnO Nanoparticles Synthesized by Sol-Gel Process. *Sensors and Actuators B*: *Chemical*, 145, 174-180.

[11] Su, P.-G. and Chang, Y.-P. (2008) Low-Humidity Sensor Based on a Quartz-Crystal Microbalance Coated with Polypyrole/Ag/TiO2 Nanoparticles Composite Thin Films. *Sensors and Actuators B*: *Chemical*, 129, 915-920.

[12] Massera, E., Ferrara, V.L.A., Miglietta, M., Polichetti, T., Nasti, I. and Francia, G.D.I. (2011) Gas Sensors Based on Graphene. *Chemistry Today*, 29, 39-41.

[13] Guo, L., Jiang, H.-B., Shao, R.-Q., Zhang, Y.-L., Xie, S.-Y., Wang, J.-N., Li, X.-B., Jiang, F., Chen, Q.-D., Zhang, T. and Sun, H.-B. (2012) Two-Beam-Laser Interference Mediated Reduction, Patterning and Nanostructuring of Graphene Oxide for the Production of a Flexible Humidity Sensing Device. *Carbon*, 50, 1667-1673.

[14] Yao, Y., Chen, X., Guo, H., Wu, Z. and Li, X. (2012) Humidity Sensing Behaviors of Graphene Oxide-Silicon Bi- Layer Flexible Structure. *Sensors and Actuators B*: *Chemical*, 161, 1053-1058.

[15] Yao, Y., Chen, X., Guo, H. and Wu, Z. (2011) Graphene Oxide Thin Film Coated Quartz Crystal Microbalance for Humidity Detection. *Applied Surface Science*, 257, 7778-7782.

[16] Novoselov KS, Geim AK, Morozov SV, Jiang D, Zhang Y, Dubonos SV, et al. Electric field effect in atomically thin carbon films. Science 2004;306(5696):666–9.

[17] Chen JH, Jang C, Xiao S, Ishigami M, Fuhrer MS. Intrinsic and extrinsic performance limits of graphene devices on $SiO_2$. Nat Nanotechnol 2008;3(4):206–9.

[18] Stankovich S, Dikin DA, Dommett GHB, Kohlhaas KM, Zimney EJ, Stach EA, et al. Graphene-based composite materials. Nature 2006;442(7100):282–6.

[19] Schedin F, Geim AK, Morozov SV, Hill EW, Blake P, Katsnelson MI, et al. Detection of individual gas molecules adsorbed on graphene. Nat Mater 2007;6(9):652–5.

[20]. Kim, K. S.; Zhao, Y.; Jang, H.; Lee, S. Y.; Kim, J. M.; Ahn, J. H.; Kim, P.; Choi, J. Y.; Hong, B. H. Large-Scale Pattern Growth of Graphene Films for Stretchable Transparent Electrodes. Nature 2009, 457, 706–710.
[21]. Bae, S.; Kim, H.; Lee, Y.; Xu, X. F.; Park, J. S.; Zheng, Y.; Balakrishnan, J.; Lei, T.; Kim, H. R.; Song, Y. I. Roll-To-Roll Production of 30-Inch Graphene Films for Transparent Electrodes. Nat. Nanotechnol. 2010, 5, 574–578.
[22] Novoselov, KS, *et al.*; *Science* 306, 666-669 (2004)
[23] Casiraghi C, *et al.*; *Nano Letters* 7, 2711-2717 (2007)
[24] LotyaM, *et al.*; *ACS Nano* 4, 3155-3162 (2010)
[25] Su CY, *et al.*; *ACS Nano* 5, 2332-2339 (2011)
[26] Forbeaux I, *et al.*; *Phys. Rev. B* 58, 16396-16406 (1998)
[27] Enderlein, C; Dissertation: *Graphene and its Interaction with Di erent Substrates Studied by Angular-Resolved Photoemission Spectroscopy*, Freie Universitaet Berlin (2010)
[28]. Ma, J., et al., Phys Rev B (2009) 80, 033407.
[29]. Bhowmick, S., et al., Phys Rev B (2010) 81, 155416.
[30]. Banhart, F., et al., ACS Nano 5, 26 (2011).
[31] Peter W. Sutter, Jan-Ingo Flege & Eli A. Sutter, Epitaxial graphene on ruthenium, *Nature Materials* 7, 406 - 411 (2008)
[32] Joshua D. Caldwell et al., TECHNIQUE FOR THE DRY TRANSFER OF EPITAXIAL GRAPHENE ONTO ARBITRARY SUBSTRATES,
[33] Kim KS, *et al.*; *Nature* 457, 706-710 (2009)
[34] Xuesong L, *et al.*; *Science* 324, 1312-1314 (2009)
[35] Xuesong Li, Weiwei Cai, Jinho An, Seyoung Kim, Junghyo Nah, Dongxing Yang, Richard Piner, Aruna Velamakanni, Inhwa Jung, Emanuel Tutuc, Sanjay K. Banerjee, Luigi Colombo, and Rodney S. Ruoff. Large-area

synthesis of high-quality and uniform graphene films on copper foils, 05/11 2009.
[36] Sukang S. Bae. Roll-to-roll production of 30-inch graphene films for transparent electrodes. Nature nanotechnology, 5(8):574–578, 2010.
[37] Jin M, Jeong HK, Yu WJ, Bae DJ, Kang BR, Lee YH: Graphene oxide thin film field effect transistors without reduction. J Phys D Appl Phys 2009, 42:135109.
[38] Venugopal G, Krishnamoorthy K, Mohan R, Kim SJ: An investigation of the electrical transport properties of graphene-oxide thin films. Mater Chem Phys 2012, 132:29–33.
[39] Dikin DA, Stankovich S, Zimney EJ, Piner RD, Dommett GHB, Evmenenko G, Nguyen ST, Ruoff RS: Preparation and characterization of graphene oxide paper. Nature 2007, 448:457–460.
[40] Hu NT, Meng L, Gao RG, Wang YY, Chai J, Yang Z, Kong ESW, Zhang YF: A facile route for the large scale fabrication of graphene oxide papers and their mechanical enhancement by cross-linking with glutaraldehyde. Nano-Micro Lett 2011, 4:215–222.
[41] Gilje S, Han S, Wang MS, Wang KL, Kaner RB: A chemical route to graphene for device applications. Nano Lett 2007, 7:3394–3398.
[42] Ekiz OO, Ürel M, Guner H, Mizrak AK, Dâna A: Reversible electrical reduction and oxidation of graphene oxide. ACS Nano 2011, 5:2475–2482.
[43] Teoh HF, Tao Y, Tok ES, Ho GW, Sow CH: Electrical current mediated interconversion between graphene oxide to reduced grapene oxide. Appl Phy Lett 2011, 98:173105.
[44] Guo YL, Wu B, Liu HT, Ma YQ, Yang Y, Zheng J, Yu G, Liu YQ: Electrical assembly and reduction of graphene oxide in a single solution step for use in flexible sensors. Adv Mater 2011, 23:4626–4630.

[45] Wei Z, Wang D, Kim S, Kim SY, Hu Y, Yakes MK, Laeacuente AR, Dai ZT, Marder SR, Berger C, King WP, Heer WAD, Sheehan PE, Riedo E: Nanoscale tunable reduction of graphene oxide for graphene electronics. Science 2011, 328:1373–1376.

[46] Yin KB, Li HT, Xia YD, Bi HC, Sun J, Liu ZG, Sun LT: Thermo-dynamic and kinetic analysis of low-temperature thermal reduction of graphene oxide. Nano-Micro Lett 2011, 1:51–55.

[47] Zhang Y, Guo L, Wei S, He Y, Xia H, Chen Q, Sun HB, Xiao FS: Direct imprinting of microcircuits on graphene oxides film by femtosecond laser reduction. Nano Today 2010, 5:15–20.

[48] Dreyer DR, Park S, Bielawski CW, Ruoff RS. The chemistry of graphene oxide. Chem Soc Rev 2010;39(1):228–40.

[49] Compton OC, Nguyen ST. Graphene oxide, highly reduced graphene oxide, and graphene: versatile building blocks for carbon-based materials. Small 2010;6(6):711–23.

[50] Szabo´, T.; Szeri, A.; De´ka´ny, I. Composite graphitic nanolayers prepared by self-assembly between finely dispersed graphite oxide and a cationic polymer. *Carbon* 2005, *43*, 87–94.

[51] He, H.; Klinowski, J.; Forster, M.; Lerf, A. A new structure model for graphite oxide. *Chem. Phys. Lett.* 1998, *287*, 53–56.

[52] Lerf, A.; He, H.; Forster,M.; Klinowski, J. Structure of graphite oxide revisited. *J. Phys. Chem. B* 1998, *102*, 4477–4482.

[53] Park, S.J.; Ruoff, R.S. Chemical methods for the production of graphene. *Nat. Nanotechnol.* 2009, *4*, 217–224.

[54] B. C. Brodie, On the atomic weight of graphite. Philos. Trans. R. Soc. London 14(1859) 249–259.

[55] Young, R.J.; Kinloch, I.A.; Gong, L.; Novoselov, K.S. The mechanics of graphene nanocomposites: A review. *Compos. Sci. Technol.* 2012, *72*, 1459–1476.

[56] Staudenmaier, L. Verfahren zur Darstellung der Graphitsa¨ure. Ber. Dtsch. Chem. Ges. 31(1898) 1481-1487.

[57]. Ülrich, H.; Rudolf, H. The acid nature and methylation of graphitic oxide. *Ber. Dtsch. Chem. Ges.* 1939, *72*, 754–771.

[58] Ruess, G. Uber das Graphitoxyhydroxyd (Graphitoxyd). *Monatsch. Chem.* 1946, *76*, 381–417.

[59] W. S. Hummers, Offeman, R. E. Preparation of graphitic oxide. J Am Chem Soc 80(1958) 1339-1339.

[60]. Dreyer, D.R.; Park, S.J.; Bielawski, C.W.; Ruoff, R.S. The chemistry of graphene oxide. *Chem. Soc. Rev.* 2010, *39*, 228–240.

[61] Zhu, Y.; Mural, S.; Cai, W.; Li, X.; Suk, J.W.; Potts, J.R.; Ruoff, R.S. Graphene and graphene oxide: Synthesis, properties, and applications. *Adv. Mater.* 2010, *22*, 3906–3924.

[62] Kovtyukhova, N.I.; Ollivier, P.J.; Martin, B.R.; Mallouk, T.E.; Chizhik, S.A.; Buzaneva, E.V.; Gorchinskiy, A.D. Layer-by-Layer assembly of ultrathin composite films from micron sized graphite oxide sheets and polycations. *Chem. Mater.* 1999, *11*, 771–778.

[63] Ma, C.; Liu, W.; Shi, M.; Lang, X.; Chu, Y.; Chen, Z.; Zhao, D.; Lin, W.; Hardacre, C. Low loading platinum nanoparticles on reduced graphene oxide-supported tungsten carbide crystallites as a highly active electrocatalyst for methanol oxidation. *Electrochim. Acta* 2013, *114*, 133–141.

[64] Nikolakopoulou, A.; Tasis, D.; Sygellou, L.; Dracopoulos, V.; Galiotis, C.; Lianos, P. Study of the thermal reduction of graphene oxide and of its application as electrocatalyst in quasi-solid state dye-sensitized solar cells in combination with PEDOT. *Electrochim. Acta* 2013, *111*, 698–706.

[65] Yu, Y; Kang, B.; Lee, Y.; Lee, S.; Ju, B. Effect of fluorine plasma treatment with chemically reduced graphene oxide thin films as hole transport layer in organic solar cells. *Appl. Surf. Sci.* 2013, *287*, 91–96.
[66] D. Luo, G. Zhang, J. Liu, X. Sun, J. Phys. Chem. C 115 (2011) 11327.
[67] S. Saxena, T.A. Tyson, E. Negusse, J. Phys. Chem. Lett. 1 (2010) 3433.
[68] C. Gómez-Navarro, J.C. Meyer, R.S. Sundaram, A. Chuvilin, S. Kurasch, M.Burghard, K. Kern, U. Kaiser, Nano Lett. 10 (2010) 1144.
[69] K.A. Mkhoyan, A.W. Contryman, J. Silcox, D.A. Stewart, G. Eda, C. Mattevi, S.Miller, M. Chhowalla, Nano Lett. 9 (2009) 1058.
[70] G. Eda, C. Mattevi, H. Yamaguchi, H. Kim, M. Chhowalla, J. Phys. Chem. C 113(2009) 15768.
[71] G. Venugopal, K. Krishamoorthy, R. Mohan, S. Kim, Mater. Chem. Phys. 132(2010) 29.
[72] C. Gómez-Navarro, R.T. Weitz, A.M. Bittner, M. Scolari, A. Mews, M. Burghard,K. Kern, Nano Lett. 7 (2007) 3499.
[73] A.B. Kaiser, C. Gómez-Navarro, R.S. Sundaram, M. Burghard, K. Kern, Nano Lett.9 (2009) 1787.
[74] D. Joung, S.I. Khondaker, Phys. Rev. B 86 (2012) 235423.
[75] T.Q. Trung, N.T. Tien, D. Kim, J.H. Jung, O.J. Yoon, N. Lee, Adv. Mater. 24 (2012)5254.
[76] S. Wang, H.E. Lin, H. Lin, K.Y. Chen, K. Tu, C.W. Chen, J. Chen, C. Liu, C. Liang, Y.F.Chen, Nanotechnology 22 (2011) 335701.
[77] B. Fugetsu, E. Sano, H. Yu, K. Mori, T. Tanaka, Carbon 48 (2010) 3340.
[78] Hatakeyama, K., Karim, M. R., Ogata, C., Tateishi, H., Funatsu, A., Taniguchi, T., Koinuma, M., Hayami, S. and Matsumoto, Y. (2014), Proton Conductivities of Graphene Oxide Nanosheets: Single, Multilayer, and Modified Nanosheets. Angew. Chem. Int. Ed., 53: 6997–7000.

[79] Anderson JH, Parks GA: Electrical conductivity of silica gel in the presence of adsorbed water. J Phys Chem 1968, 72: 3662 – 3668.
[80] Yao et al., The effect of ambient humidity on the electrical properties of graphene oxide films, Nanoscale Research Letters 2012, 7:363
[81] M. R. Karim, H. Shinoda, M. Nakai, K. Hatakeyama, H. Kamihata, T. Matsui, T. Taniguchi, M. Koinuma, K. Kuroiwa, M. Kurmoo, Y. Matsumoto, S. Hayami, Adv. Funct. Mater. 2013, 23, 323 – 332.
[82] Meihua Jin, Hae-Kyung Jeong, Woo Jong Yu, Dong Jae Bae,Bo Ram Kang and Young Hee Lee, Graphene oxide thin film field effect transistors without reduction, J. Phys. D: Appl. Phys. 42 (2009) 135109 (5pp)
[83] Schniepp HC, Li J-L, McAllister MJ, Sai H, Herrera-Alonso M, Adamson DH, et al. Functionalized single graphene sheets derived from splitting graphite oxide. J Phys Chem B 2006;110(17):8535–9.
[84] Wang X, Zhi L, Mullen K. Transparent, conductive graphene electrodes for dye-sensitized solar cells. Nano Lett 2008;8(1):323–7.
[85] Becerril HA, Mao J, Liu Z, Stoltenberg RM, Bao Z, Chen Y. Evaluation of solution-processed reduced graphene oxide films as transparent conductors. ACS Nano 2008;2(3):463–70.
[86] Li X, Wang H, Robinson JT, Sanchez H, Diankov G, Dai H. Simultaneous nitrogen doping and reduction of graphene oxide. J Am Chem Soc 2009;131(43):15939–44.
[87] Lopez V, Sundaram RS, Gomez-Navarro C, Olea D, Burghard M, Gomez-Herrero J, et al. Chemical vapor deposition repair of graphene oxide: a route to highly-conductive graphene monolayers. Adv Mater 2009;21(46):4683–6.
[88] Gengler RYN, Veligura A, Enotiadis A, Diamanti EK, Gournis D, Jo´ zsa C, et al. Large-yield preparation of high-electronicquality graphene by a Langmuir–Schaefer approach. Small 2010;6(1):35–9.

[89] Kim MC, Hwang GS, Ruoff RS. Epoxide reduction with hydrazine on graphene: a first principles study. J Chem Phys 2009;131(6):064704.
[90] Gao X, Jang J, Nagase S. Hydrazine and thermal reduction of graphene oxide: reaction mechanisms, product structures, and reaction design. J Phys Chem C 2009;114(2):832–42. Ajayan P. M. et al., "Opening carbon nanotubes with oxigen and implication for filling" - Nature 362, 522-525 (1993).
[91] Xu SC, Irle S, Musaev DG, Lin MC. Quantum chemical study of the dissociative adsorption of OH and H2O on pristine and defective graphite (0001) surfaces: reaction mechanisms and kinetics. J Phys Chem C 2006;111(3):1355–65.
[92] Jeong H-K, Lee YP, Jin MH, Kim ES, Bae JJ, Lee YH. Thermal stability of graphite oxide. Chem Phys Lett 2009;470(4– 6):255–8.
[93] Zhu Y, Murali S, Stoller MD, Velamakanni A, Piner RD, Ruoff RS. Microwave assisted exfoliation and reduction of graphite oxide for ultracapacitors. Carbon 2010;48(7):2118–22.
[94] Hassan HMA, Abdelsayed V, Khder AERS, AbouZeid KM, Terner J, El-Shall MS, et al. Microwave synthesis of graphene sheets supporting metal nanocrystals in aqueous and organic media. J Mater Chem 2009;19(23):3832–7.
[95] Cote LJ, Cruz-Silva R, Huang J. Flash reduction and patterning of graphite oxide and its polymer composite. J Am Chem Soc 2009;131(31):11027–32.
[96] Zhang Y, Guo L, Wei S, He Y, Xia H, Chen Q, et al. Direct imprinting of microcircuits on graphene oxides film by femtosecond laser reduction. Nanotoday 2010;5(1):15–20.
[97] Maria A Buccheri, Daniele D'Angelo, Silvia Scalese, Simon F Spanò, Simona Filice, Enza Fazio, Giuseppe Compagnini, Massimo Zimbone, Maria

V Brundo, Roberta Pecoraro, Anna Alba, Fulvia Sinatra, Giancarlo Rappazzo and Vittorio Privitera, Modification of graphene oxide by laser irradiation: a new route to enhance antibacterial activity, Nanotechnology 27 (2016) 245704 (12pp).

[98] Abdelsayed V, Moussa S, Hassan H M, Aluri H S, Collinson M M and El-Shall M S 2010 Photothermal deoxygenation of graphite oxide with laser excitation in solution and graphene-aided increase in water temperature Phys. Chem. Lett. 1 2804 – 9

[99] Kotov NA, De´ka´ny I, Fendler JH. Ultrathin graphite oxide–polyelectrolyte composites prepared by self-assembly: transition between conductive and non-conductive states. Adv Mater 1996;8(8):637–41.

[100] Stankovich S, Piner RD, Chen X, Wu N, Nguyen ST, Ruoff RS. Stable aqueous dispersions of graphitic nanoplatelets via the reduction of exfoliated graphite oxide in the presence of poly(sodium 4-styrenesulfonate). J Mater Chem 2006;16(2):155–8.

[101] Stankovich S, Dikin DA, Piner RD, Kohlhaas KA, Kleinhammes A, Jia Y, et al. Synthesis of graphene-based nanosheets via chemical reduction of exfoliated graphite oxide. Carbon 2007;45(7):1558–65.

[102] Stankovich S, Dikin DA, Dommett GHB, Kohlhaas KM, Zimney EJ, Stach EA, et al. Graphene-based composite materials. Nature 2006;442(7100):282–6.

[103] Fernandez-Merino MJ, Guardia L, Paredes JI, Villar-Rodil S, Solis-Fernandez P, Martinez-Alonso A, et al. Vitamin C is an ideal substitute for hydrazine in the reduction of graphene oxide suspensions. J Phys Chem C 2010;114(14):6426–32.

[104] Li D, Mu¨ ller MB, Gilje S, Kaner RB, Wallace GG. Processable aqueous dispersions of graphene nanosheets. Nat Nanotechnol 2008;3(2):101–5.

[105] Shin H-J, Kim KK, Benayad A, Yoon S-M, Park HK, Jung I-S, et al. Efficient reduction of graphite oxide by sodium borohydride and its effect on electrical conductance. Adv Funct Mater 2009;19(12):1987–92.
[106] Pei S, Zhao J, Du J, Ren W, Cheng H-M. Direct reduction of graphene oxide films into highly conductive and flexible graphene films by hydrohalic acids. Carbon 2010;48(15):4466–74.
[107] Moon K, Lee J, Ruoff RS, Lee H. Reduced graphene oxide by chemical graphitization. Nat Comm 2010;1(1):73–8.
[108] Williams G, Seger B, Kamat PV. TiO2-graphene nanocomposites. UV-assisted photocatalytic reduction of graphene oxide. ACS Nano 2008;2(7):1487–91.
[109] Zhou M, Wang Y, Zhai Y, Zhai J, Ren W, Wang F, et al. Controlled synthesis of large-area and patterned electrochemically reduced graphene oxide films. Chem Euro J 2009;15(25):6116–20.
[110] Wang Z, Zhou X, Zhang J, Boey F, Zhang H. Direct Electrochemical reduction of single-layer graphene oxide and subsequent functionalization with glucose oxidase. J Phys Chem C 2009;113(32):14071–5.
[111] An SJ, Zhu Y, Lee SH, Stoller MD, Emilsson T, Park S, et al. Thin film fabrication and simultaneous anodic reduction of deposited graphene oxide platelets by electrophoretic deposition. J Phys Chem Lett 2010;1(8):1259–63.
[112] Ramesha GK, Sampath S. Electrochemical reduction of oriented graphene oxide films: an in situ raman spectroelectrochemical study. J Phys Chem C 2009;113(19):7985–9.
[113] Iijima S. et al., “Growth model for carbon nanotubes”, Phys. Rev. Lett., 21,3100-3103, (1992).
[114] Bethune D. S et al.,"Cobalt catalysed growth of carbon nanotubes" - Nature 363, 605 (1993).

[115] Costa et al.,(2002).
[116] Farhat, S. et al., Journal of Chemical Physics, 115, 14, 6752-6759, (2001).
[117] Jung, S. H. et al., Applied Physics A-Materials Science & Processing, 76, 2, 285-286, (2003).
[118] Huang et al.,Nano Letters, 2,10, 1117-1119, (2002).
[119] Park J. B. et al., Journal of Crystal Growth, 244, 2, 211-217, (2002).
[120] Andreas Thess, Roland Lee, Pavel Nikolaev, Hongjie Dai, Pierre Petit, Jerome Robert, Chunhui Xu, Young Hee Lee, Seong Gon Kim, Andrew G. Rinzler, Daniel T. Colbert, Gustavo E. Scuseria, David Tománek, John E. Fischer, Richard E. Smalley, Crystalline Ropes of Metallic Carbon Nanotubes, Science (1996), Vol. 273, Issue 5274, pp. 483-487.
[121] Chang HP et al., Scanning tunneling microscopy studies of carbon oxygen reactions on highly oriented pyrolytic-graphite. J Am Chem Soc;113(15):5588–96 (1991).
[122] Niyogi S. et al., Chemistry of single-walled carbon nanotubes. Acc Chem Res;35(12):1105–13 (2002).
[123] Wilder J. W. G. et al., "Electronic structure of atomically resolved carbon nanotubes". Nature 391, 59-62 (1998).
[124] Schaman-Diamand, Y.; Osaka, T.; Datta, M. & Ohba, T. (2009), Advanced Nanoscale ULSI Interconnects: Fundamentals and Applications, Springer, ISBN 978-0-387-95867-5, United States of America.
[125] Joachim, C.; Gimzewski, J.K. & Aviram, A. (2000), Electronics using Hybrid-Molecular and Mono-Molecular Devices, Nature, Vol. 408, No. 6812, pp. 541-548.
[126] Kang, S.J.; Kocabas, C.; Kim, H.-S.; Cao, Q.; Meitl, M.A.; Khang, D.-Y. & Rogers, J. A. (2007), Printed Multilayer Superstructures of Aligned

Single-Walled Carbon Nanotubes for Electronic Applications, Nano Letters, Vol. 7, No. 11, pp. 3343-3348.
[127] Krompiewski, S. (2005), Spin-Polarized Transport through Carbon Nanotubes, Physica Status Solidi B: Basic Solid State Physics, Vol. 242, No. 2, pp. 226-233.
[128] Kanungo, M.; Malliaras, G.G. & Blanchet, G.B. (2010), High Performance Organic Transistors: Percolation Arrays of Nanotubes Functionalized with an Electron Deficient Olefin, Applied Physics Letters, Vol. 97, No. 5, pp. 053304(3).
[129] Landauer R., in Nanowires, edited by P. A. Serena and N. Garcia (Kluwer, Dordrecht), p. 1 (1998).
[130] White C. T. et al., "Carbon nanotubes as long ballistic conductors" - Nature 393, 240-242 (1998).
[131] Frank et al., Science 280, 1744 (1998).
[132] "Nanotubes make tiny diodes" (1999).
[133] Walt A. de Heer et al., “A Carbon Nanotube Field-Emission Electron Source” Science: Vol. 270 no. 5239 pp. 1179-1180 (1995).
[134] Dagani R., "Much ado about nanotubes" - C&EN 1, 31-34 (1999).
[135] Treacy M. M. J. et al., - Nature 381, 678 (1996).
[136] Erik T. et al., Composites Science and Technology 61 1899–1912 (2001).
[137] Tomànek D., “Thermal and elecctrical conductance of carbon nanotubes”.
[138] Philip G. et al.,Science, 390:68, (2001).
[139] Pederson M. R. et al., "Nanocapillarity in fullerene tubules" - Phys. Rev. Lett. 69, 2689 (1992).

[140] P. M. Ajayan, T. W. Ebbesen, T. Ichihashi, S. Iijima, K. Tanigaki & H. Hiura, Opening carbon nanotubes with oxygen and implications for filling, *Nature* 362, 522 - 525 (1993).

[141] Chen P. et al., "High $H_2$ uptake by alkali-doped carbon nanotubes under ambient pressure and moderate temperatures" - Science 285, 91-93 (1999).

[142] Stone A. J., Wales D. J. "Theoretical studies of icosahedral C60 and some related structures". Chemical Physics Letters 128 (5-6): 501–503 (1986).

[143] Valentini et al., "Role of defects on the gas sensing properties of carbon nanotubes thin films: experiment and theory". Chemical physics, (2004).

[144] Grujicic et al., Appl. Surf.Sci. 211 166 (2003).

[145] Xu, G.; Liu, F.; Han, S.; Ryu, K.; Badmaev, A.; Lei, B.; Zhou, C. & Wang, K.L. (2008), Low-Frequency Noise in Top-Gated Ambipolar Carbon Nanotube Field Effect Transistors, Applied Physics Letters, Vol. 92, No. 22, pp. 223114(3).

[146] Behnam, A.; Johnson, J.L.; Choi, Y.; Ertosun, M.G.; Okyay, A.K.; Kapur, P.; Saraswat, K.C. & Ural, A. (2008), Experimental Characterization of Single-Walled Carbon Nanotube Film-Si Schottky Contacts using Metal-Semiconductor-Metal Structures, Applied Physics Letters, Vol. 92, No. 24, pp. 243116(3).

[147] Chen, P.-C.; Shen, G.; Sukcharoenchoke, S. & Zhou, C. (2009), Flexible and Transparent Supercapacitor based on In2O3 Nanowire/Carbon Nanotube Heterogeneous Films, Applied Physics Letters, Vol. 94, No. 4, pp. 043113(3).

[148] Jia, Y.; Cao, A.; Bai, X.; Li, Z.; Zhang, L.; Guo, N.; Wei, J.; Wang, K.; Zhu, H.; Wu, D. & Ajayan, P.M. (2011), Achieving High Efficiency Silicon-

Carbon Nanotube Heterojunction Solar Cells by Acid Doping, Nano Letters, Vol. 11, No. 5, pp. 1901-1905

[149] Hur, S.-H.; Khang, D.-Y.; Kocabas, C. & Rogers, J.A. (2004), Nanotransfer Printing by Use of Noncovalent Surface Forces: Applications to Thin-Film Transistors that Use Single-Walled Carbon Nanotube Networks and Semiconducting Polymers, Applied Physics Letters, Vol. 85, No. 23, pp. 5730-5732.

[150] Ferry, D.K.; Goodnick, S.M. & Bird, J. (2009), Transport in Nanostructures, Second Edition, Cambridge University Press, United States of America.

[151] Geim, A.K. & Novoselov, K.S. (2007), The Rise of Graphene, Nature Materials, Vol. 6, No. 3, pp. 183-191.

[152] Geim, A.K. (2009), Graphene: Status and Prospects, Science, Vol. 324, No. 5934, pp. 1530-1534.

[153] Cho, H.; Koo, K.-H.; Kapur, P. & Saraswat, K. C. (2008), Performance Comparisons between Cu/Low-κ, Carbon-Nanotube, and Optics for Future on-Chip Interconnects, IEEE Electron Device Letters, Vol. 29, No. 1, pp. 122-124.

[154] Hosseini, A. & Shabro V. (2010), Thermally-aware Modeling and Performance Evaluation for Single-Walled Carbon Nanotube-based Interconnects for Future High Performance Integrated Circuits, Microelectronic Engineering, Vol. 87, No. 10, pp. 1955-1962.

[155] Nojeh, A. & Ivanov, A. (2010), Wireless Interconnect and the Potential for Carbon Nanotubes, IEEE Design & Test of Computers, Vol. 27, No. 4, pp. 44-52.

[156] Andriotis, A.N.; Menon, M.; Srivastava, D. & Chernozatonskii, L. (2001), Rectification Properties of Carbon Nanotube "Y-Junctions", Physical Review Letters, Vol. 87, No. 6, pp. 066802(4).

[157] Goel, A. K. (2007), High-Speed VLSI Interconnections, Second Edition, John Wiley & Sons, ISBN 978-0-471-78046-5, United States of America.

[158] Dekker et al., Verschueren, Alwin R. M.. Nature 393 (6680): 49 (1998).

[159] S. Heinze, J. Tersoff, R. Martel, V. Derycke, J. Appenzeller and P. Avouris, Phys. Rev. Lett., 2002, 89, 106801.

[160] A. Javey, J. Guo, Q. Wang, M. Lundstrom and H. J. Dai, Nature, 2003, 424, 654–657.

[161] Wind S. J. et al., "Vertical scaling of carbon nanotube field-effect transistors using top gate electrodes". Applied Physics Letters 80 (20) (2002).

[162] A. Javey, J. Guo, D. B. Farmer, Q. Wang, D. Wang, R. G. Gordon, M. Lundstrom and H. Dai, Nano Lett., 2004, 4, 447–450.

[163] Kenzo Maehashi * and Kazuhiko Matsumoto, Label-Free Electrical Detection Using Carbon Nanotube-Based Biosensors, *Sensors* 2009, *9*(7), 5368-5378;

[164] Chen et al.,"Externally Assembled Gate-All-Around Carbon Nanotube Field-Effect Transistor". IEEE Electron Device Letters 29 (2) (2008).

[165] Farmer DB, Gordon RG. "Atomic layer deposition on suspended single-walled carbon nanotubes via gas-phase non-covalent functionalization". Nano letters 6 (4): 699–703 (2006).

[166] Cao J. et al.,"Electron transport in very clean, as-grown suspended carbon nanotubes". Nature materials 4 (10): 745–9 (2005).

[167] Lin Yu-Ming et al., "Impact of oxide substrate on electrical and optical properties of carbon nanotube devices". Nanotechnology 18 (29) (2007).

[168] Sangwan, V. K. et al., "Facile fabrication of suspended as-grown carbon nanotube devices". Applied Physics Letters 93 (11) (2008).

[169] Appenzeller, J.; Lin, Y.M.; Knoch, J.; Chen, Z. & Avouris, P. (2005), Comparing Carbon Nanotube Transistors – The Ideal Choice: A Novel Tunneling Device Design, IEEE Transactions on Electron Devices, Vol. 52, No. 12, pp. 2568-2576.

[170] L. Crockett, "Carbon Nanotube Transistor Fabrication and Reliability Characterization," Intel Archived July 23, 2011, at the Wayback Machine.

[171] Pop Eric et al., Avalanche, joule breakdown and hysteresis in carbon nanotube transistors. p. 405 (2009).

[172] Changxin C. and Yafei Z., "Nanowelded Carbon Nanotubes: From Field-Effect Transistor to Solar Microcells" Nano Science and Technology series, pp. 63 (2009).

[173] Chang-Jian et al., "Characterization of developing source/drain current of carbon nanotube field-effect transistors with n-doping by polyethylene imine". Microelectronic Engineering 87 (10): 1973 (2010).

[174] A. Bachtold, P. Hadley, T. Nakanishi and C. Dekker, Science, 2001, 294, 1317–1320

[175] V. Derycke, R. Martel, J. Appenzeller and P. Avouris, Nano Lett. , 2001, 1, 453–456.

[176] L. Ding, Z. Zhang, S. Liang, T. Pei, S. Wang, Y. Li, W. Zhou, J. Liu and L.-M. Peng, Nat. Commun., 2012, 3, 677.

[177] S. R. Forrest, Nature, 2004, 428, 911.

[178] E. S. Snow, J. P. Novak, P. M. Campbell and D. Park, Appl. Phys. Lett., 2003, 82, 2145–2147.

[179] Wang et al., NanoLett. 2012, 12, 1527 – 1533.

[180] S. Kumar, J. Y. Murthy and M. A. Alam, Phys. Rev. Lett., 2005, 95, 066802.

[181] V. K. Sangwan, A. Behnam, V. W. Ballarotto, M. S. Fuhrer, A. Ural and E. D. Williams, Appl. Phys. Lett., 2010, 97, 043111

[182] M. S. Fuhrer, J. Nygard, L. Shih, M. Forero, Y. G. Yoon, M. S. C. Mazzoni, H. J. Choi, J. Ihm, S. G. Louie, A. Zettl and P. L. McEuen, Science, 2000, 288, 494–497.

[183] S. J. Kang, C. Kocabas, H. S. Kim, Q. Cao, M. A. Meitl, D. Y. Khang and J. A. Rogers, Nano Lett., 2007, 7, 3343–3348.

[184] S. J. Kang, C. Kocabas, T. Ozel, M. Shim, N. Pimparkar, M. A. Alam, S. V. Rotkin and J. A. Rogers, Nat. Nanotechnol., 2007,2, 230–236.

[185] C. Kocabas, S. H. Hur, A. Gaur, M. A. Meitl, M. Shim and J. A. Rogers, Small, 2005,1, 1110–1116.

[186] G. Zhang, P. Qi, X. Wang, Y. Lu, X. Li, R. Tu, S. Bangsaruntip, D. Mann, L. Zhang and H. Dai, Science, 2006, 314, 974–977.

[187] M. S. Arnold, S. I. Stupp and M. C. Hersam, Nano Lett., 2005, 5, 713–718.

[188] Hoël Guerinet et al., Carbon nanotube resistors as gas sensors: Towards selective analyte detection with various metal-nanotubeinterfaces, 2013, DOI: 10.1109/ESSDERC.2013.6818884

[189] M. Penza et al., SAW Gas Sensors with Carbon Nanotubes Films2008, DOI: 10.1109/ULTSYM.2008.0455

[190] M. Alvisi et al., Organic Vapor Detection by QCM Sensors Using CNT-Composite Films, 2012

[191] J. Kong, N. R. Franklin, C. Zhou, M. G. Chapline, S. Peng, K. Cho and H. Dai, Science, 2000, 287,622-625.

[192] Y. Shimizu and M. Egashira, MRS Bulletin, 1999, 24, 18-24.

[193] O'connell, M. J., Boul, P., Ericson, L. M., Huffman, C., Wang, Y. H., Haroz, E., et al. (2001). Reversible water-solubilization of single-walled carbon nanotubes by polymer wrapping. Chem. Phys. Lett. 342, 265–271. DOI: 10.1016/S0009- 2614(01)00490-0

[194] T. Someya, J. Small, P. Kim, C. Nuckolls and J. T. Yardley, Nano Lett., 2003, 3, 877-881.

[195] C. P. W. Paul, M. Natacha, T. Zhenni, M. Yoji, J. D. Carey and S. R. P. Silva, Nanotechnology, 2007,18, 175701.

[196] J. Kong, M. G. Chapline and H. Dai, Adv. Mater., 2001, 13, 1384-1386.

[197] S. Auvray, J. Borghetti, M. F. Goffman, A. Filoramo, V. Derycke, J. P. Bourgoin and O. Jost, Appl.Phys. Lett., 2004, 84, 5106-5108.

[198] B. R. Goldsmith, J. G. Coroneus, V. R. Khalap, A. A. Kane, G. A. Weiss and P. G. Collins, Science, 2007, 315, 77-81.

[199] P. Qi, O. Vermesh, M. Grecu, A. Javey, Q. Wang, H. Dai, S. Peng and K. J. Cho, Nano Lett., 2003, 3, 347-351.

[200] A. T. C. Johnson, S. Cristian, C. Michelle, K. Sam, J. Robert, M. L. Klein and A. Gelperin, Semiconductor Science and Technology, 2006, 21, S17.

[201] C. Staii, A. T. Johnson, M. Chen and A. Gelperin, Nano Lett., 2005, 5, 1774-1778.

[202] M. Ganzhorn, A. Vijayaraghavan, S. Dehm, F. Hennrich, A. A. Green, M. Fichtner, A. Voigt, M. Rapp, H. von Löhneysen, M. C. Hersam, M. M. Kappes and R. Krupke, ACS Nano, 2011, 5, 1670-1676.

[203] Ferrari, M. (2005). Cancer nanotechnology: opportunities and challenges. Nat. Rev. Cancer 5, 161–171. doi: 10.1038/nrc1566

[204] Portney, N. G., and Ozkan, M. (2006). Nano-oncology: drug delivery, imaging, and sensing. Anal. Bioanal. Chem. 384, 620–630. doi: 10.1007/s00216-005-0247-7

[205] Wang, Z., and Dai, Z. (2015). Carbon nanomaterial-based electrochemical biosensors: an overview. Nanoscale 7, 6420–6431. doi: 10.1039/C5NR00585J

[206] Lin, Y., Lu, F., Tu, Y., and Ren, Z. (2004). Glucose biosensors based on carbon nanotube nanoelectrode ensembles. Nano Lett. 4, 191–195. doi: 10.1021/nl0347233

[207] Patolsky, F., Weizmann, Y., and Willner, I. (2004). Long-range electrical contacting of redox enzymes by SWCNT connectors. Angew. Chem. Int. Ed. Engl. 43, 2113–2117. doi: 10.1002/anie.200353275

[208] Santos, R. M., Rodrigues, M. S., Laranjinha, J., and Barbosa, R. M. (2013). Biomimetic sensor based on hemin/carbon nanotubes/chitosan modified microelectrode for nitric oxide measurement in the brain. Biosens. Bioelectron. 44, 152–159. doi: 10.1016/j.bios.2013.01.015

[209] Kress, G. J., Shu, H. J., Yu, A., Taylor, A., Benz, A., Harmon, S., et al. (2014). Fast phasic release properties of dopamine studied with a channel biosensor. J. Neurosci. 34, 11792–11802. doi: 10.1523/JNEUROSCI.2355-14.2014

[210] Fei, S., Chen, J., Yao, S., Deng, G., He, D., and Kuang, Y. (2005). Electrochemical behavior of l-cysteine and its detection at carbon nanotube electrode modified with platinum. Anal. Biochem. 339, 29–35. doi: 10.1016/j.ab.2005.01.002

[211] Okuno, J., Maehashi, K., Matsumoto, K., Kerman, K., Takamura, Y., and Tamiya, E. (2007). Single-walled carbon nanotube-arrayed microelectrode chip for electrochemical analysis. Electrochem. Commun. 9, 13–18. doi: 10.1016/j.elecom.2006.07.046

[212] C. Morgan, D. Newman, C. Price, Immunosensors: technology and opportunities in laboratory medicine, Clin. Chem. 42 (1996) 193–209.

[213] D.J. Shirale, M.A. Bangar, M. Park, M.V. Yates, W. Chen, N.V. Myung, A. Mulchandani, Label-free chemiresistive immunosensors for viruses, Environ. Sci. Technol. 44 (2010) 9030–9035

[214] M. Bhattacharya, S. Hong, D. Lee, T. Cui, S.M. Goyal, Carbon nanotube based sensors for the detection of viruses, Sensors Actuators B Chem. 155 (2011) 67–74.
[215] Li, G.; Liao, J.; Hu, G.; Ma, N.; Wu, P. Study of carbon nanotube modified biosensor for monitoring total cholesterol in blood. Biosens. Bioelectron. 2005, 20, 2140-2144.
[216] Banerjee, S.; Kahn, M. G. C.; Wong, S. S. Rational chemical strategies for carbon nanotube functionalization. Chem. Eur. J. 2003, 9, 1898-1908.
[217] Wang, J.; Musameh, M.; Lin, Y. Solubilization of carbon nanotubes by Nafion toward the preparation of amperometric biosensors. J. Am. Chem. Soc. 2003, 125, 2408-2409.
[218] Tzeng, Y.; Huang, T. S.; Chen, Y. C.; Liu, C.; Liu, Y. K. Hydration properties of carbon nanotubes and their effects on electrical and bio-sensor applications. New Diamond Front. Carbon Technol. 2004, 14, 193-201.
[219] Moore, V. C.; Strano, M. S.; Haroz, E. H.; Hauge, R. H.; Smalley, R. E. Individually suspended single-walled carbon nanotubes in various surfactants. Nano Lett. 2003, 3, 1379-1382.
[220] Fei, B.; Lu, H.; Hu, Z.; Xin, J. H. Solubilization, purification and functionalization of carbon nanotubes using polyoxometalate. Nanotechnology 2006, 17, 1589-1593.
[221] Kam, N. W. S.; Dai, H. Carbon nanotubes as intracellular protein transporters: generality and biological functionality. J. Am. Chem. Soc. 2005, 127, 6021-6026.
[222] Lenihan, J. S.; Gavalas, V. G.; Wang, J.; Andrews, R.; Bachas, L. G. Protein immobilization on carbon nanotubes through a molecular adapter. J. Nanosci. Nanotechnol. 2004, 4, 600-604.
[223] O'Connor, M.; Kim, S. N.; Killard, A. J.; Forster, R. J.; Smyth, M. R.; Papadimitrakopoulos, F.; Rusling, J. F. Mediated amperometric

immunosensing using single walled carbon nanotube forests. Analyst 2004, 129, 1176-80.

[224] Kam, N. W. S.; Dai, H. Carbon nanotubes as intracellular protein transporters: generality and biological functionality. J. Am. Chem. Soc. 2005, 127, 6021-6026.

[225] Chen, R. J.; Zhang, Y.; Wang, D.; Dai, H. Noncovalent sidewall functionalization of single-walled carbon nanotubes for protein immobilization. J. Am. Chem. Soc 2001, 123, 3838-3839.

[226] Jiang, K.; Schadler, L. S.; Zhang, R. W. S. X.; Zhang, H.; Terrones, M. Protein immobilization on carbon nanotubes via a twostep process of diimide -activated amidation. J. Mater. Chem. 2004, 14, 37-39.

[227] Yu, X.; Kim, S. N.; Papadimitrakopoulos, F.; Rusling, J. F. Protein immunosensor using single-wall carbon nanotube forests with electrochemical detection of enzyme labels. Mol. BioSyst. 2005, 1, 70-78.

[228] Wohlstadter, J. N.; Wilbur, J. L.; Sigal, G. B.; Biebuyck, H. A.; Billadeau, M. A.; Dong, L.; Fischer, A. B.; Gudibande, S. R.; Jameison, S. H.; Kenten, J. H.; Leginus, J.; Leland, J. K.; Massey, R. J.; Wohlstadter, S. J. Carbon nanotube based biosensor. AdV. Mater. 2003, 15, 1184-1187.

[229] Elkin, T.; Jiang, X.; Taylor, S.; Lin, Y.; Gu, L.; Yang, H.; Brown, J.; Collins, S.; Sun, Y. P. Immuno-carbon nanotubes and recognition of pathogens. ChemBioChem 2005, 6, 6403.

[230] Ostuni, E.; Chapman, R. G.; Holmlin, R. E.; Takayama, S.; Whitesides, G. M. A Survey of structure-property relationships of surfaces that resist the adsorption of proteins. Langmuir 2001, 17, 5605-5620.

[231] Chen, R. J.; Bangsaruntip, S.; Drouvalakis, K. A.; Kam, N. W.; Shim, M.; Li, Y.; Kim, W.; Utz, P. J.; Dai, H. Noncovalent functionalization of carbon nanotubes for highly specific electronic biosensors. Proc. Natl. Acad. Sci. U.S.A. 2003, 100, 4984-4989.

[232] Shim, M.; Wong Shi Kam, N.; Chen, R. J.; Li, Y.; Dai, H. Functionalization of carbon nanotubes for biocompatibility and biomolecular recognition. Nano Lett. 2002, 2, 285-288.
[233] F. Schwierz, Nat. Nanotechnol., 2010,5, 487–496.
[234] Y.-W. Son, M. L. Cohen and S. G. Louie, Phys. Rev. Lett.,2006,97, 216803.
[235] L. Brey and H. A. Fertig, Phys. Rev. B: Condens. Matter Mater. Phys., 2006,73, 235411.
[236] X. Li, X. Wang, L. Zhang, S. Lee and H. Dai, Science, 2008,319, 1229–1232.
[237] D. C. Elias, R. R. Nair, T. M. G. Mohiuddin, S. V. Morozov, P. Blake, M. P. Halsall, A. C. Ferrari, D. W. Boukhvalov,M. I. Katsnelson, A. K. Geim and K. S. Novoselov,Science,2009,323, 610–613.
[238] R. R. Nair, W. Ren, R. Jalil, I. Riaz, V. G. Kravets, L. Britnell, P. Blake, F. Schedin, A. S. Mayorov, S. Yuan, M. I. Katsnelson, H.-M. Cheng, W. Strupinski, L. G. Bulusheva, A. V. Okotrub, I. V. Grigorieva, A. N. Grigorenko, K. S. Novoselov and A. K. Geim, Small,2010,6, 2877–2884.
[239] F. Xia, D. B. Farmer, Y.-m. Lin and P. Avouris, Nano Lett.,2010,10, 715–718.
[240] K. S. Novoselov, E. McCann, S. V. Morozov, V. I. Fal'ko, M. I. Katsnelson, U. Zeitler, D. Jiang, F. Schedin andA. K. Geim,Nat. Phys., 2006,2, 177–180.
[241] E. V. Castro, K. S. Novoselov, S. V. Morozov, N. M. R. Peres, J. M. B. L. dos Santos, J. Nilsson, F. Guinea, A. K. Geim and A. H. C. Neto,Phys. Rev. Lett., 2007,99, 216802.
[242] E. McCann,Phys. Rev. B: Condens. Matter Mater. Phys.,2006,74, 161403.

[243] J. H. Chen, C. Jang, S. Adam, M. S. Fuhrer, E. D. Williams and M. Ishigami,Nat. Phys., 2008,4, 377–381.

[244] W. J. Yu, L. Liao, S. H. Chae, Y. H. Lee and X. Duan, Nano Lett., 2011,11, 4759–4763.

[245] A. Lherbier, X. Blase, Y.-M. Niquet, F. Triozon and S. Roche,Phys. Rev. Lett., 2008,101, 036808.

[246] Ci, L. Song, C. Jin, D. Jariwala, D. Wu, Y. Li, A. Srivastava, Z. F. Wang, K. Storr, L. Balicas, F. Liu and P. M. Ajayan, Nat. Mater., 2010,9, 430–435.

[247] Pumera, M., Ambrosi, A., Bonanni, A.,et al.:'Graphene for electrochemical sensing and biosensing',Trends Anal. Chem., 2010,29, pp. 954–965.

[248] Novoselov, K.S., Geim, A.K., Morozov, S.V., et al.:'Electric field effect in atomically thin carbon films',Science, 2004,306, pp. 666–669.

[249] Ratinac, K.R., Yang, W., Ringer, S.P.,et al.:'Toward ubiquitous environmental gas sensors – capitalizing on the promise of graphene ',Environ. Sci. Technol.,2010,44, pp. 1167 1176.

[250] Yumeng Liu et al., Microelectronic Engineering, 132, 2014.

[251] Wang et al., Dielectrophoresis of graphene oxide nanostructures for hydrogen gas sensor at room temperature, Sensors and Actuators B: Chemical, 194, 2014, pp 296–302.

[252] Sun et al., Small Temperature Coefficient of Resistivity of Graphene/Graphene Oxide Hybrid Membranes, ACS Appl. Mater. Interfaces 2013, 5, 9563−9571.

[253] Wu, P., Shao, Q., Hu, Y., et al.:'Direct electrochemistry of glucose oxidase assembled on graphene and application to glucose detection', Electrochim. Acta , 2010, 55 , pp. 8606 –8614.

[254] Huang et al., Nanoscale, 2010,2, 1485–1488

[255] uang, K.J., Niu, D.J., Sun, J.Y., et al.:‘Novel electrochemical sensor based on functionalized graphene for simultaneous determination of adenine and guanine in DNA’, Colloids Surf., B, 2011,82, pp. 543–549.

[256] Dong, X., Shi, Y., Huang, W., et al.:‘Electrical detection of DNA hybridization with single-base specificity using transistors based on CVD-grown graphene sheets’, Adv. Mater., 2010, 22, pp. 1649–1653.

[257] Xie, Y., Chena, A., Dua, D., et al.:‘Graphene-based immunosensor for electrochemical quantification of phosphorylated p53 (S15)’,Anal. Chim. Acta,2011,699, pp. 44–48.

[258] Mao, S., Lu, G., Yu, K., et al.:‘Specific protein detection using thermally reduced graphene oxide sheet decorated with gold nanoparticle-antibody conjugates’, Adv.Mater., 2010,22, pp. 3521–3526.

[259] Bagiante S, Scalese S, Scuderi V, D’Urso L, Messina E, Compagnini G, Privitera V (2010) Role of the growth parameters on the structural order of MWCNTs produced by arc discharge in liquid nitrogen. Phys Stat Sol B 247:884–887. doi:10.1002/pssb.200982957

[260] Scalese S, Scuderi V, Bagiante S, Gibilisco S, Faraci G, Privitera V (2010) Order and disorder of carbon deposit produced by arc discharge in liquid nitrogen. J Appl Phys 108:064305. doi:10.1063/1.3475726

[261] Scuderi V., Tripodi L., Piluso N. et al., J Nanopart Res, (2014), 16, 2287, doi:10.1007/s11051-014-2287-4.

[262] M. Kimura, K.I. Tatsumi, H. Tada, M. Ikemoto, Y. Fukuda, A. Kaneko, M. Kato, Y. Hidaka, N. Amino, Enzyme immunoassay for autoantibodies to human liver-type arginase and its clinical application, Clin. Chem. 46 (1) (2000) 112–117

[263] M. Ikemoto, S. Tsunekawa, M. Awane, Y. Fukuda, H. Murayama, M. Igarashi, A. Nagata, Y. Kasai, M. Totani, A useful ELISA system for human

liver-type arginase, and its utility in diagnosis of liver diseases, Clin. Biochem. 34 (6) (2001) 455–461

[264] C. Vetro, A. Romano, F. Ancora, F. Coppolino, M.V. Brundo, S.A. Raccuia, F. Puglisi, D. Tibullo, P. La Cava, C. Giallongo, N.L. Parrinello, Clinical impact of the immunome in lymphoid malignancies: the role of myeloid-derived suppressor cells, Front. Oncol. 5 (2015) 104.

[265] A. Romano, C. Conticello, M. Cavalli, C. Vetro, A. La Fauci, N.L. Parrinello, F. Di Raimondo, Immunological dysregulation in multiple myeloma microenvironment, BioMed Res. Int. 2014 (198539) (2014) 1–10.

[266] A. Romano, C. Vetro, G. Caocci, M. Greco, N.L. Parrinello, F. Di Raimondo, G. La Nasa, Immunological deregulation in classic hodgkin lymphoma, Mediterr. J. Hematol. Infect. Dis. 6 (1) (2014), e2014039.

[267] P.C. Rodriguez, M.S. Ernstoff, C. Hernandez, M. Atkins, J. Zabaleta, R. Sierra, A.C. Ochoa, Arginase I-producing myeloid-derived suppressor cells in renal cell carcinoma are a subpopulation of activated granulocytes, Cancer Res. 69 (4) (2009) 1553–1560.

[268] C. Lacroix, C. Caubet, A. Gonzalez-de-Peredo, B. Breuil, D. Bouyssié, A. Stella, L. Garrigues, C. Le Gall, A. Raevel, A. Massoubre, J. Klein, S. Decramer, F. Sabourdy, F. Bandin, O. Burlet-Schiltz, B. Monsarrat, J.P. Schanstra, J.L. Bascands, Label-free quantitative urinary proteomics identifies the arginase pathway as a new player in congenital obstructive nephropathy, Mol. Cell. Proteomics 13 (12) (2014) 3421–3434.

[269] S.R. Wang, S. Hou, A. Wang, Y.J. Chang, C.T. Liu, G.J. Tsay, C.C. Wei, The significance of arginase 1 administration on the survival of mice bearing NS-1 myeloma cells, J. Surg. Res. 151 (1) (2009) 28–32

[270] L.-W. Huang, H.-W. Liu, K.-L. Chang, Development of a sandwich ELISA test for arginase measurement based on monoclonal antibodies, Hybridoma 20 (1) (2001) 53–57.

[271] A. Pistone, A. Piperno, D. Iannazzo, N. Donato, M. Latino, D. Spadaro, G. Neri, Fe3O4- MWCNT PhCOOH composites for ammonia resistive sensors, Sensors Actuators B 186 (2013) 333–342.

# List of publications

- S. Baldo, S. Buccheri, A. Ballo, M. Camarda, A. La Magna, M.E. Castagna, A. Romano, D. Iannazzo, F. Di Raimondo, G. Neri, S. Scalese: “Carbon nanotube-based sensing devices for human Arginase-1 detection”, Sensing and Bio-Sensing Research, 7 (2016), pp 168-173;

- R. Di Martino, M. Camarda, M. Cascio, M. Gallo, S. Baldo, A. Magliano, A. Romano, L. Minafra, G. Forte, G. Russo, M. Gilardi, F. Di Raimondo, S. Scalese, A. La Magna, “Analysis of the role of elution buffers on the separation capabilities of dielectrophoretic devices”, Sensing and Bio-Sensing Research, 7 (2016), pp 162-167;

- S. Baldo, V. Scuderi, L. Tripodi, A. La Magna, S.G. Leonardi, N. Donato, G. Neri, S. Filice, S. Scalese: “Defects and gas sensing properties of carbon nanotube-based devices”, J. Sens. Sens. Syst., 4 (2015), pp 25-30;

- S. Baldo, S. Scalese, V. Scuderi, L. Tripodi, A. La Magna, L. Romano, S.G. Leonardi, N. Donato: "Correlation between structural and sensing properties of carbon nanotube-based devices", Sensors - Lecture Notes in Electrical Engineering, 319 (2015), pp 207-210;

- M. Camarda, S. Baldo, G. Fisicaro, R. Anzalone, S. Scalese, A. Alberti, F. La Via, A. La Magna, A. Ballo, G. Giustolisi, L. Minafra, F. P. Cammarata, V. Bravatà, G. I. Forte, G. Russo and M. C. Gilardi: "Study of the role of particle-particle dipole interaction in dielectrophoretic devices for biomarkers identification", Sensors - Lecture Notes in Electrical Engineering, 319 (2015), pp 9-12;

- M. Camarda, S. Baldo, S. Scalese, A. Ballo, G. Giustolisi, A. Romano, F. Di Raimondo, M. Pucci, F. Vicari, L. Minafra, F.P. Cammarata, V. Bravata, G.I. Forte, G. Russo, M.C. Gilardi, A. La Magna, "Theoretical and experimental study of the kinetics of particle chains near electrodes in dielectrophoretic devices", Nanotechnology Materials and Devices Conference (NMDC), 2014 IEEE 9th, pp.58-61;

# Acknowledgements

During these three years many things have happened: I moved to Catania, I met many people, and I learned new things.
There are many people that I would like to thank.
First I would like to thank Dr. Silvia Scalese, researcher at the CNR-IMM in Catania and my mentor during my journey. Always available and ready for anything, Silvia has been a key person. I'd like also to thank Prof. Giuseppe Falci, for his support during these years. A special thank goes to my colleague Dr. Simona Filice, which helped me during laboratory testing sessions: She was always ready to give me great advices and She also have been a real friend. Unforgettable will be our coffee breaks and all the time spent together during the scientific conferences.
Surely, I would like to thank Dr. Daniele D'angelo, Dr. Salvo Buccheri and all the people which worked with me at the CNR-IMM in Catania, They whole have been fundamental.
I will never forget all the moments spent with them both at work or in the evening just for a pizza to enjoy togheter.
A special thanks also goes to Dr. Antonino La Magna, always ready for any clarification and scientific advice. Last but not least, I'd like to thank my girlfriend Altea, all my family and friends, fundamental people which supported me during this wonderful period.

Thanks to all.
Salvatore